UNIVERSITY OF SOUTHAMPTON

Faculty of Engineering and the Environment

School of Engineering Sciences

CFD modelling of the gas-solid flow dynamics and thermal conversion processes in fluidised beds.

by

Lindsay-Marie Armstrong

Thesis for the degree of Doctor of Philosophy

June 2011

UNIVERSITY OF SOUTHAMPTON

Abstract

Faculty of Engineering and the Environment
School of Engineering Sciences

Doctor of Philosophy

by Lindsay-Marie Armstrong

The increasing application of bubbling fluidised bed (BFB) and circulating fluidised bed (CFB) technology in industry means optimum reactor designs are required to improve efficiency and reduce emissions. The reduction of greenhouse emissions is vital due to its noticable effects on climate change. The excellent thermal and mixing properties in fluidised beds allows for the complete burn out of excess carbon and improved mixing of gases leading to potentially a more efficient method of combustion and gasification over standard fixed bed combustors.

Computational fluid dynamic modelling has proven to be a viable tool for simulating the processes that take place in fluidised beds. Increased computational power allows for non-invasive simulations for complex geometries and wide parameter ranges to be carried out which would be difficult and expensive to perform experimentally. Whilst Eulerian-Lagrangian modelling of the gaseous and particulate phases provides detailed information of the particle dynamics on a microscale its application to fluidised bed technologies is computationally exhaustive due to the large number of particles present within the bed. Eulerian-Eulerian modelling reduces computational time and expense significantly and the inclusion of the kinetic theory of granular flow provides information on the particle collisions thus proving to be a viable tool for the modelling of fluidised beds.

The present work applies Eulerian-Eulerian modelling to capture the hydrodynamic and heat transfer processes that take place in different fluidised bed reactors. The reaction kinetics for the gasification of coal in a bubbling fluidised bed are incorporated and the results are validated with published experimental data. An extensive parametric review is carried out which had not been carried out previously for the gasification of coal using this model. Finally, limestone calcination is introduced to the model. During the work, extensive code writing was carried out not only to allow for the interactions between the solid and gaseous phases but also to extend on current built in models in the commercial software FLUENT 12.0 to update with additional, more complex models.

Acknowledgements

There are so many people who deserve a thank you for their insight and encouragement during the course of the last three years.

I owe a massive thank you to my supervisors, Dr Sai Gu and Professor Kai H. Luo for their help and support. Their advice and encourage throughout the last three years has been invaluable. I would also like to thank some people who helped me prior to this course who got me where I am now. Dr Charles Fall from Northumbria University who introduced me to the fascinating subject of fluid dynamics during my mathematics degree and the staff at Leeds University during my MSc who helped me to expand my knowledge in this area.

There are too many people I would like to thank for their friendship during this period. There are so many to mention but I would like to start with the colleagues in my office whose company during the last three years has not only provided me with interesting conversations but an excellent environment to spend the majority of my day working in. To all my friends at aerobics, I would like to thank them for some fantastic times which has proven to be an excellent distraction during the difficult times. I would especially like to thank Nazila Soleimani and Angela Camerlingo whose lunch time conversations have been not only interesting but very entertaining. I will miss those get togethers so much.

Last but definitely not least I would like to thank all my family. In particularly, my parents and brother for their much appreciated support during my studies. For their encouragement over the years as they push me to be the first Dr. in the family. Also I would like to give a huge thank you to my fiancée, David, for his love and friendship and for generally putting up with me during this project, especially the last few stressful months. I love you all so much!

Declaration of Authorship

I, Lindsay-Marie Armstrong, declare that this thesis titled, 'CFD MODELLING OF THE GAS-SOLID FLOW DYNAMICS AND THERMAL CONVERSION PROCESSES IN FLUIDISED BEDS' and the work presented in it are my own. I confirm that:

- this work was done wholly or mainly while in candidature for a research degree at this University.
- where any part of this thesis has previously been submitted for a degree or any other qualification at this University or any other institution, this has been clearly stated.
- where I have consulted the published work of others, this is always clearly attributed.
- where I have quoted from the work of others, the source is always given. With the exception of such quotations, this thesis is entirely my own work.
- I have acknowledged all main sources of help.
- where the thesis is based on work done by myself jointly with others, I have made clear exactly what was done by others and what I have contributed myself.
- parts of this work have been published as given in the list of publications.

Signed: _____

Date: _____

Publications

Journal Articles

Published manuscripts

Armstrong, L.M.; Luo, K.H. & Gu, S. (2011) *A parametric study of gasification processes in a BFB coal gasifier*; Ind. Eng. Chem. Res., 50:5959-5974

Armstrong, L.M.; Luo, K.H. & Gu, S. (2011) *Effects of limestone calcination on the gasification processes in a BFB coal gasifier*; Chem. Eng. J., 168:848-860

Armstrong, L.M.; Luo, K.H. & Gu, S. (2010) *The influence of multiple tubes on the tube-to-bed heat transfer in a fluidised bed*; Int. J. Multiphase Flow, 36:916-929

Armstrong, L.M.; Luo, K.H. & Gu, S. (2010) *Parameter study of the wall-to-bed heat transfer in a gas-solid bubbling fluidised bed using the Kinetic Theory of Granular Flow*; Int. J. Heat Mass Tran., 53:4949-4959

Armstrong, L.M.; Luo, K.H. & Gu, S. (2010) *Two-dimensional and three-dimensional computational studies of hydrodynamics in the transition from bubbling to circulating fluidised bed*; Chem. Eng. J., 160:239-248

Conference Papers

Armstrong, L.M.; Luo, K.H. & Gu, S. *CFD modelling of the co-gasification of biomass and coal particles in fluidised beds*; In Proceedings of the Bioten Conference, Birmingham, UK, Sept 2010

Armstrong, L.M.; Luo, K.H. & Gu, S. *CFD modelling of the gasification of coal particles in fluidised beds*; In Proceedings of the International Heat Transfer Conference, Washington DC, USA, Aug 2010

Armstrong, L.M.; Luo, K.H. & Gu, S. *Three-dimensional modelling on the hydrodynamics of a circulating fluidised bed*; In Proceedings of the Inaugural US-EU-China Thermophysics Conference, Beijing, China, May 2009

Contents

List of Figures

List of Tables

Nomenclature

Dimensionless Numbers

Ar	Archimedes number
Nu	Nusselt number
Pr	Prandtl number
Re	Reynolds number
Sc	Schmidt number
Sh	Sherwood number

Greek Symbols

ϵ	Dissipation rate of turbulent kinetic energy	$\mathrm{m}^{-2}/\mathrm{s}^{-3}$
γ_i	Collisional dissipation of energy	$\mathrm{W/m}^3$
λ_i	Thermal conductivity	W/mK
μ_i	Shear viscosity	kg/s m
$\overline{\overline{\tau}}_i$	Stress-Strain tensor	Pa
ϕ	Angle of internal friction, Equation 3.30	$^\circ$
ρ_i	Density	$\mathrm{kg/m}^3$
σ_ε	Turbulent Prandtl numbers for ε	
σ_k	Turbulent Prandtl numbers for k	
Θ	Particle phase pseudo-temperature	$\mathrm{m/s}^2$
υ_i	Velocity	m/s
ε_i	Volume fraction	
φ	Specularity coefficient	

ξ_i	Bulk viscosity	kg/s m
k	Turbulent kinetic energy	m^2/s^2

Roman Symbols

$\overline{\overline{I}}$	Stress tensor	Pa
A	Pre-exponential factor	1/s
C_i	Concentration of species i	$kmol/m^3$
C_D	Drag coefficient	$kg/m^3.s$
C_{fr}	Coefficient of friction	
C_p	Specific heat	J/kgK
D_i	Diffusion coefficient for species	m^2/s
d_i	Particle diameter	m
E	Activation energy	J/mol
e	Coefficient of restitution	
g	Acceleration due to gravity	m/s^2
G_k	Shear production	
g_0	Radial distribution coefficient	
h	Height	m
H_i	Enthalpy,	J/kg
h_i	Heat transfer coefficient	W/m^2K
I_{2D}	Second invariant of deviatoric stress tensor, Equation 3.30	Pa
J_i	Diffusion flux of species i	kg/m^2s
k_{Θ_s}	Diffusion coefficient for granular energy	kg/m s
K_a	Kinetic rate constant	kg/m^3s
K_b	Diffusion rate constant	kg/m^3s
K_i	Momentum interface exchange coefficient	kg/m^3s
p	Gas pressure	Pa
p_i	Phase pressure	Pa

Q_i	Interphase Heat transfer coefficient	W/m^2K
R	Universal gas constant	J/mol K
r	Radius	m
$R_{g,i}$	Net rate of production of homogeneous species i	
$R_{s,i}$	Heterogeneous reaction rate	
S_i	Mass source term	kg/m^3s
t	Time	s
T_i	Temperature	K
U_{mb}	Minimum bubbling velocity	m/s^2
U_{mf}	Minimum fluidised velocity	m/s^2
V_t	Terminal velocity	m/s
w_i	Species molecular weight,	kg/kmol
X_i	Molar fraction of species	
Y_i	Mass fraction of species	

Subscripts

Arr	Kinetic rate
b	Bubble
c	Char
$Diff$	Diffusive rate
Edd	Eddy-dissipation rate
g	Gas
i	General index, i^{th} species
mb	Minimum bubbling velocity, U_{mb}
mf	Minimum fluidisation velocity, U_{mf}
p	Particles
q	Phase
s	Solids

w	Wall

Superscripts

$bulk$	Bulk porosity
kin	Kinetic contribution
mol	Molecular contribution

Mathematical Notation

$\cdot$	Vector dot product
δt	Finite difference time step
δx	Finite difference mesh size in the x-direction
δy	Finite difference mesh size in the y-direction
δz	Finite difference mesh size in the z-direction
∇	Gradient
$\nabla\cdot$	Divergence
$\otimes$	Vector cross product
$\sum$	Summation
$\mathbf{n}$	Normal unit vector

Acronyms

2D	Two Dimensional
3D	Three Dimensional
BFB	Bubbling Fluidised Bed
BFBC	Bubbling Fluidised Bed Combustion
BFBG	Bubbling Fluidised Bed Gasification
CFB	Circulating Fluidised Bed
CFD	Computational Fluid Dynamics
EMMS	Energy Minimisation Multiscale
FBT	Fluidised Bed Technology
FCC	Fluid Catalytic Cracking

IHTC	International Heat Transfer Conference
IPCC	Intergovernment Panel on Climate Change
KTGF	Kinetic Theory of Granular Flow
LBM	Lattice Boltzmann Method
LDA	Laser Doppler Anemometry
PCSIMPLE	Phase Coupled Semi-Implicit Method for Pressure Linked Equations
RMS	Root Mean Square
SIMPLE	Semi-Implicit Method for Pressure Linked Equations
TFM	Two Fluid Model
UDF	User Defined Function
UECTC	US-EU-China Thermophysics Conference

Chapter 1

Introduction

This chapter provides introductory comments about the current climatic concerns whilst providing an insight into the available fuels and technologies utilised in industry for the generation of energy. The objective of this thesis is discussed along with the novelties that have been carried out. Finally, the progress of the work carried out is provided along with a break down of the chapters covered in the thesis.

1.1 Climate change and energy sources

Over the recent years, major concerns have been raised with regards to the effect increasing emissions is having on the world's climate. The greenhouse effect occurs when light from the sun enters the atmosphere but the reflected heat off the surface of the earth becomes absorbed by the greenhouse gases and trapped within the atmosphere. It is thought that consequences of this effect over time will show dramatic effects on the climate, including increasing temperature, sea levels, storm severity and changes in precipitation patterns. The Intergovernment Panel on Climate Change (IPCC) have suggested that there has been a 0.6-0.9°C increase in the Earth's temperature over the past 100 years [6]. Whilst natural events such as volcanic erupts can also introduce greenhouse gases to the atmosphere it is likely that the major contributions have been made during the recent 50 years since the industrial age. During this period, additional anthropogenic greenhouse gases have been produced, especially carbon dioxide, CO_2, through the increased burning of fossil fuels which prior to this had remained at constant levels for thousands of years [6].

Unfortunately, the global population has become highly dependent on the production of energy through the industrial burning of fossil fuels. Therefore if greenhouse gas emissions are to be reduced then research needs to focus on the development of low-carbon technologies through the usage of low-carbon sources and/or technologies capable

of capturing and storing emissions; whilst ensuring that the increasing energy demands continue to be maintained.

The fossil fuels that contribute towards the global generation of energy include oil, natural gas and coal. Oil and natural gas products account for approximately 37% and 21% of the global energy consumption [6], respectively. They are formed naturally in geological formations beneath the surface of the Earth through the degradation of organic matter by high pressures and temperatures; deep under accumulated sediment. Oil is extracted through a drilling process where it is then refined and separated into different fuel products e.g. petroleum. Natural gas, however, is released during the extraction of oil as the pressure reduction releases light hydrocarbon gases from the oil. Before the natural gas can be used as an effective fuel most of the components must be removed to leave highly combustible methane. It was estimated that there was approximately 50 years supply of oil at the consumption rates in 2009, whereas the predicted supplies for natural gas was given at approximately 60 years remaining [7]. These values could vary however as the possibility of undiscovered resources being found over the next few decades remains hopeful.

Coal accounts for around 25% of the global consumption of energy and is the most abundant fossil fuel [6]. Research has suggested that there is over 847 billion tonnes of proven coal sources world wide and continuation of its consumption at the same rate would mean reserves would last for a further 120 years [7]. Unfortunately, as with oil and natural gas, the consumption rate of coal is faster than the production rate. The formation of coal began millions of years ago; when plants died and gradually over the years layers formed upon another with more plants and soils. Additional layers led to compression and restriction of excess air which prevented decomposition. Over time the heat and pressure draws out the oxygen and hydrogen leaving carbon rich deposits, namely, coal.

The molecular structure of coal is classified by its rank depending on the amount of carbon content. Figure 1.1 displays the four major types, in order of increasing carbon content are lignite, sub-bituminous, bituminous and anthracite [1]. The longer the coal is compressed, the higher the carbon content and the lower the moisture within the coal.

Since fossil fuel sources are limited, the utilisation of renewable sources of energy has become a viable solution. Renewable sources of energy come in many forms such as wind, solar, hydro, geothermal and biomass and as a whole they account for over 15% of the global energy supply [6].

Biomass is a mature renewable technology which has been used utilised for energy production for many years; it is also a viable option for the substitution of coal in industrial combustors and gasifiers it is a large sustainable energy resource. Moreover, biomass is regarded by many as a carbon neutral source due to it low carbon content and the

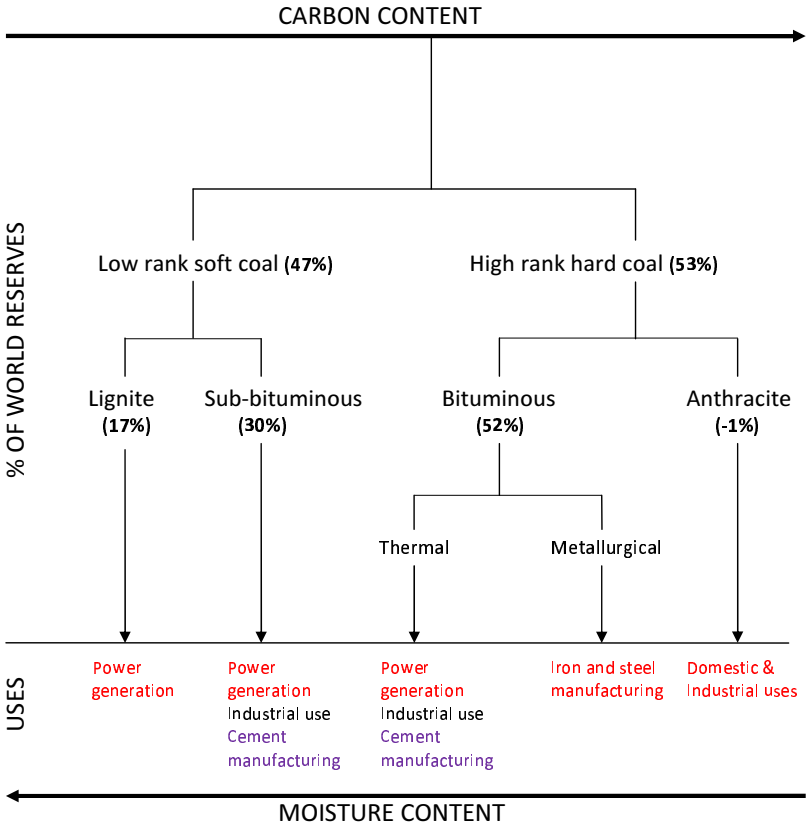

FIGURE 1.1: Different ranks of coal, their percentage of world supplies and uses [1].

process of photosynthesis during its growth means the plants absorb carbon dioxide from the atmosphere. Its chemical structure consists primarily of lignin, cellulose and hemicellulose with small amounts of nitrogen, sodium, potassium and chlorine. Unfortunately in biomass fuels, as with low rank coals, there is a significant amounts of water present so without a drying out period which requires time and expense the fuel is not effective. Furthermore, the increased levels of potassium in biomass compared to coal causes early reactor degradation, therefore it is not as simple as switching from one fuel to another. Furthermore, issues with regards to transportation, storage and energy density needs to be overcome before considering its utilisation into the industrial energy production industry can be increased [1].

The variation of fuels is not the only solution to reduce harmful emissions. Other options include different conversion processes and variation in the technologies carrying out such conversions. A conversion process that has dominated in the production of energy from burning fuels is the combustion process which converts fuels into high temperature gaseous emissions through exothermic reactions with oxygen. Such processes have been carried out in fixed bed combustors and has developed significantly since the industrial revolution. Earlier technologies had uncontrolled inflows of air from under the grates resulting in inefficient burning [8]; however, over the years reactors were improved to gain better efficiencies with modified boiler designs and controlled airflows. Furthermore,

fixed bed reactors varied to help improve the coal surface area contact with the air more effectively by the introduction of moving and traveling grates in the reactors. The introduction of pulverised coal in the 1890s resulted in a vast increase in the combustion intensity and heat transfer rates [9]. This was due to the smaller pulverised particles having a much faster reaction rate resulting in a significant increase in temperature.

Another conversion process is gasification which is a recent technology that is carried out at slightly lower temperatures than combustion; in an oxidating mixture of air and/or steam. This method leads to a reduction in carbon dioxide, CO_2, emissions compared to combustion due to the limited amount of oxygen, O_2, and reduced temperatures. The O_2 initiates the reaction sequences by reacting with the fuel to produce energy and carbon monoxide, CO, which drives the subsequent reactions producing a gaseous solution predominantly consisting of carbon monoxide, CO, and hydrogen, H_2, also known as synthetic gas or syngas. Syngas is a useful fuel source itself with its combustible properties but it is also helpful in obtaining specific chemicals like hydrogen for the generation of hydrogen fuel cells.

In the 1920s, Fritz Winkler developed a conversion technology, which utilised coal gasification, that offered even higher efficiencies than the fixed bed technologies. The fluidised bed works by suspending fuel particles and mixing them thoroughly allowing for good air-particle contact whilst the good mixing behaviour promotes excellent heat transfer. Small fuel particles in the bed allow for faster reaction rates which can, along with the excellent mixing behaviour, enhance the thermal conversion of the particles to ensure that all the carbon has combusted. This continues to be an issue in fixed bed combustors where unburned carbon can remain in the ash.

However, before fluidised bed gasifiers can be considered as a major energy technology in the industry sector further understanding needs to be established into optimum conditions that produce the most efficient energy production whilst maintaining low emissions. Carrying out gasification experiments is expensive and requires time and resources. This makes it difficult and expensive to establish optimal reactor designs and operating conditions, especially if the modifications turn out to be unsuccessful. However, computational modelling has proven to be a viable option over recent years and with the continual enhancement of computational capabilities it is capable of carrying out such modifications to determine optimum design and operating conditions before experimental modifications can be carried out.

1.2 Project objectives

The primary objective of this project is to simulation the gasification processes in a fluidised bed using computational fluid dynamics (CFD) modelling. The model will take into account the different gas-solid behaviours, heat transfer and thermal conversion

processes using multiphase flow modelling from the commercial software package ANSYS 12.0. A clear understanding of the gas-particle and particle-particle interactions will be obtained through the investigation of benchmark cases from the literature. The Eulerian-Eulerian model, or two-fluid model (TFM), is utilised with particle interactions being considered through the incorporation of the kinetic theory of granular flow (KTGF).

Initially, isothermal hydrodynamic models will analyse the gas-solid behaviour in different types of fluidised beds and heat transfer will be considered from two different type of heat sources that can be found in fluidised bed reactors. Research into the hydrodynamic and heat transfer behaviours in fluidised beds continues to dominate this area of research as researchers endeavour to develop more detailed models for the flow behaviours. The author feels, however, that current models already capture adequate flow behaviours; therefore it is worth considering the incorporation of reaction models. C-Subroutines are written for the reaction kinetics which take into account the release of volatiles - also known as devolatilisation; the interaction of char with the surrounds gases - known as heterogeneous reactions; and the reaction of the different gaseous species with each other - known as homogeneous reactions.

Although reaction kinetic modelling within fluidised beds by means of the TFM has only recently been acknowledged and implemented with basic reaction kinetics, the reasonable results obtained could be further improved if the computer models were to include all the reactants used within the experimental set up, e.g limestone. The use of multiple solid phases to represent the different materials in the bed is generally avoided due to the added computational time required to solve for an additional phase and the modification of the code to incorporate additional phases. However, with improved computational performances compared to recent years such issues could be regarded as negligible.

Providing an extensive review of the gasification process for different operating conditions is a step towards finding optimum reactor designs which could potentially lead to improved emissions. Furthermore, given the wider utilisation of coal in industry compared to biomass it would be easier to validate the models with a wider range of data already available. Upon successful validation with coal, this work can be extended to the field of biomass gasification which could help to encourage the utilisation of this sustainable energy source more widely into the industrial sector.

1.3 Project novelty

The present work expands on previous research carried out in the fields of multiphase flow dynamics, heat transfer and reaction kinetics which are carried out using Eulerian-Eulerian multiphase flow modelling.

Whilst extensive work has already been carried out in the field of hydrodynamic modelling it was during a revision of previous works that a gap became apparent which enabled me to produce a paper in this area. The use of Eulerian-Eulerian modelling to capture the flow behaviour and transition from a bubbling regime to a fast fluidising regime was absent therefore different gas velocities set within the region of the terminal velocity were tested for different particle properties which lead to a publication in this field. The advantage of an Eulerian-Eulerian model being able to capture this transition means that should the variation of phase diameters or densities be included in such models due to the reaction processes, i.e., particle shrinkage, then appropriate inlet velocities can be chosen to avoid potential entrainment.

A couple of papers were also produced in the field of heat transfer modelling for a wall-to-bed and an immersed tube bubbling bed. The effects that multiple immersed tubes had on the flow distribution, heat transfer and the temperature in a bubbling bed were explored, particularly at different distances from the tubes which had not been observed previously. A heated wall reactor was also modelled and comparisons of the heat transfer within different regions of the bed, i.e., in bubbles and in a packed bed region, were made. Furthermore, the simulation time was expanded over those previously carried out to highlight the periodic effects that occurred.

The major contribution from this project comes from the mathematical modelling of the gasification chemical reactions through the incorporation of C-subroutines into Eulerian-Eulerian modelling using the KTGF. The modelling approach differed from previous models carried out in coal gasification modelling by introducing multiple phases for the different solid species, namely coal, char and limestone. Such results led to a more realistic flow distribution compared to previous models which used a multi-component solid phase which integrated coal and sand together in the same phase. The present model was able to capture the different segregation effects due to a variation in the material properties which previous models could not.

The model carried out an extensive review of the gasification processes in a bubbling fluidised bed with coal. This included a parametric study on the important factors including temperature, heat transfer coefficients, bed material, bed height and extended time periods. Such an extensive study has not been carried out previously using TFM on a bubbling fluidised bed coal gasifier. The present work also introduced limestone calcination to the reaction kinetics which has also not been carried out using Eulerian-Eulerian modelling with the KTGF.

The gasification model can be applied to the Eulerian-Eulerian model in both bubbling and circulating beds. With the continual research into the advancement and incorporation of multiscale modelling to circulating fluidised beds, this model can also be applied to large-scale circulating reactors. Although the present work was carried out for the gasification of coal the model can be modified easily to accommodate combustion

processes and also different fuel properties through the incorporation of the relevant reaction kinetics required. Such a model is invaluable in the future research of fluidised bed technologies as preliminary simulations are cheaper than experimental modifications to determine optimal reactor designs and operating conditions.

1.4 Progress of work

Before the reaction kinetics could be implemented a clear understanding was required of the fundamental hydrodynamic and heat transfer processes that take place in fluidised bed technologies. The first year was spent gaining insight into the concept of granular phase modelling by carrying out isothermal models of both bubbling and circulating fluidised beds. Whilst substantial work had already been carried out in these areas there was a gap observed in the literature looking at an Eulerian-Eulerian model's ability to capture the transition from a bubbling to a circulating regime. The initial results lead to the development of a conference paper which was submitted, reviewed and accepted at the US-EU-China Thermophysics Renewable Energies Conference (UECTC) in China [10]. The results from the conference paper were expanded to include three-dimensional results to produce a journal which was accepted in the Chemical Engineering Journal [11]. During the first year, regular meetings were carried out to ensure tasks were being met and after 9 months a formal assessment was carried out which reviewed the achievements up to that point.

Time period	**Task**	**Description**
Nov 2007 - Ongoing	Literature reading	Fluidised beds
Feb 2008 - Jan 2009	Hydrodynamics modelling	Bubbling fluidised beds
Jun 2008 - Jan 2009	Hydrodynamics modelling	Circulating fluidised beds
Jun 2008 - Aug 2008	9 month report	
Feb 2009 - Mar 2009	Journal writing	BFBs and CFBs modelling [11]
Mar 2009 - May 2009	Heat transfer modelling	Wall-to-bed BFB
Apr 2009 - May 2009	Journal writing	Wall-to-bed heat transfer [12]
May 2009	Conference	UECTC, China [10]
May 2009 - Jul 2009	Heat transfer modelling	Tube-to-bed BFB
Apr 2009 - Aug 2009	18 month report	
Jun 2009 - Jul 2009	Journal writing	Tube-to-bed heat transfer [13]
Jul 2009 - Oct 2010	Reaction modelling	Coal BFBG simulations
Jun 2010 - Aug 2010	Reaction modelling	Wood BFBG simulations
Aug 2010	Conference	IHTC, Washington, USA [14]
Sept 2010	Conference	BioTen, Birmingham, UK [15]
Sept 2010 - Oct 2010	Journal writing	Limestone reaction modelling [16]
Oct 2010 - Nov 2010	Journal writing	Parameter reaction modelling [17]
Nov 2010 - Feb 2011	Thesis writing	

TABLE 1.1: Table showing tasks that were completed with start and completion dates.

The first six months of the second year were dedicated to the incorporation of heat transfer modelling in different designed fluidised beds. Both wall-to-bed and immersed tube reactors were simulated using the KTGF where each bed design led to the production of a paper in the International Journal of Heat and Mass Transfer [12] and the International Journal of Multiphase Flow [13], respectively. The UECTC in China took place during this period which allowed me to orally present my hydrodynamic results before an audience which was well received. This time period was finalised with the transfer viva which reviewed the work that was carried out to that date.

The final 18 months was dedicated to the incorporation of reaction kinetics into a lab-scale bubbling fluidised bed. Current CFD packages do not incorporate the reaction kinetics required for gasification into multiphase modelling however through the development of source codes via User-Defined Functions (UDFs) the devolatilisation, heterogeneous and homogeneous reactions were incorporated. Within the first few months, initial coal gasification results were submitted to the International Heat Transfer Conference (IHTC) in Washington which was accepted and presented in the form of a poster [14]. The code was also modified to incorporate the reaction kinetics of wood for the submission to the BioTen conference in Birmingham which was also well received [15]. The incorporation of the reaction kinetics into Eulerian-Eulerian models has grown in interest recently however an extensive review of different parameters that influence coal gasification had not been carried out. This study was carried out over the last year and led to the production of two journal papers. The first paper validated the model to experimental results presented in the literature and was accepted for publication in the Chemical Engineering Journal [16]. The second paper is an expansion of the first paper to consider a range of important parameters that affects the gasification process and is currently under review in the Industrial and Engineering Chemistry Research journal [17].

A table reviewing the overall work that was carried out through out this project is provided Table 1.1.

1.5 Thesis structure

This thesis comprises of the following chapters:

Chapter 1: Introduction

The introduction provides introductory comments about the current climatic concerns whilst providing an insight into the available fuels and technologies utilised in industry for the generation of energy. The objective of this thesis is given along with the novelties that have been carried out. Finally, the progress of the work carried out is discussed along with a break down of the chapters covered in the thesis.

Chapter 2: Literature Review

The literature review recaps the work that has previously been carried out in the field of fluidised bed modelling using computational fluid dynamics approaches. The review covers the hydrodynamic modelling which has been extensively covered, the heat transfer processes that are an important aspect to fluidisation and finally a review of the reaction kinetics and their recent interest and incorporation into Eulerian-Eulerian modelling.

Chapter 3: Computational Fluid Dynamic Modelling

This chapter provides information about the various constitutive equations and closure models used within Eulerian-Eulerian modelling. The heat transfer models and reaction kinetics are also provided.

Chapter 4: Hydrodynamics

The hydrodynamics section carries out a number of parametric studies on bubbling and circulating fluidised beds. The effects of drag, particle diameter, inlet velocity and coefficient of restitution are explored and both two-dimensional and three-dimensional beds are considered. The results are compared to experimental results from the literature.

Chapter 5: Heat Transfer

Two types of bubbling fluidised beds are considered in this section, one designed for wall-to-bed heat transfer and another for immersed tube heat transfer. The instantaneous local heat transfer coefficient near the wall and tubes are validated with experimental results whilst variations to model parameters highlight the influences such parameters have on the flow dynamics, heat transfer and temperatures within the bed.

Chapter 6: Reaction Modelling

A two-dimensional Eulerian-Eulerian model implementing the KTGF is applied to a simple coal gasification model which includes the devolatilisation, homogeneous and heterogeneous reactions and introduces limestone calcination via UDFs. An extensive study is carried out looking at the influences of different parameters including temperature, bed material, bed height and heat transfer coefficients. The model is extended to a three-dimensional model where further operating conditions are compared to experimental data. Finally the model tests the variation of fuel properties through the inclusion of an additional biomass phase.

Chapter 7: Conclusion

A summary of the conclusions drawn throughout the thesis is given and the novelties made as a result of this work are highlighted. Finally, suggestions are made for the future application of this work to the field of fluidisation technologies.

Appendix A: Momentum Interphase Equations

There are a number of momentum interphase equations, otherwise known as drag models, utilised within the present work therefore to keep the continuity of the main text they are given in the appendix.

Appendix B: Discretisation

The discretisation process is described for a basic case for the benefit of readers who are relatively new to the field of computational fluid dynamics.

Chapter 2

Literature Review

This chapter provides information on the work that has already been carried out in the modelling of fluidised beds. The chapter initially introduces the concept of fluidisation and some of the fundamental phenomena that occurs during different fluidising regimes. A brief discussion on the development of significant computational fluid dynamic models is given along with an insight in to how they have been applied by previous researchers to fluidised beds. A section on heat transfer highlights different heat transfer sources and various modelling techniques carried out to model them. Finally, the reaction kinetics which have previously been carried out are presented.

2.1 Fluidised bed technologies

The term fluidisation comes from the fluid-like characteristics that can be observed in a bed of suspended particles under certain conditions. Different regimes of fluidisation occur depending on the velocity of air supply, particle diameter and particle density. To visualise some of the different processes of fluidisation, Figure 2.1 shows the transitional regimes that taken place for different inlet velocities.

A bed of particles sits over a porous plate distributor where gas is introduced at different velocities. For zero to low velocities the particles remain stationary in the bed and if a low velocity gas is introduced then it traverses slowly through the small gaseous spaces between the spherical particles, also known as voidages. This bed is termed a fixed bed reactor as the particles appear fixed. However, should the gas velocity be increased this allows for the particles to move around more. Eventually the particles in the bed appear to be suspended as the weight of the particles equals the frictional forces between the particles and the gas. The velocity at which this occurs is called the minimum fluidisation velocity, U_{mf}, which occurs when the pressure drop within the bed remains constant and equals the weight of the bed [18]. Figure 2.2 shows how the

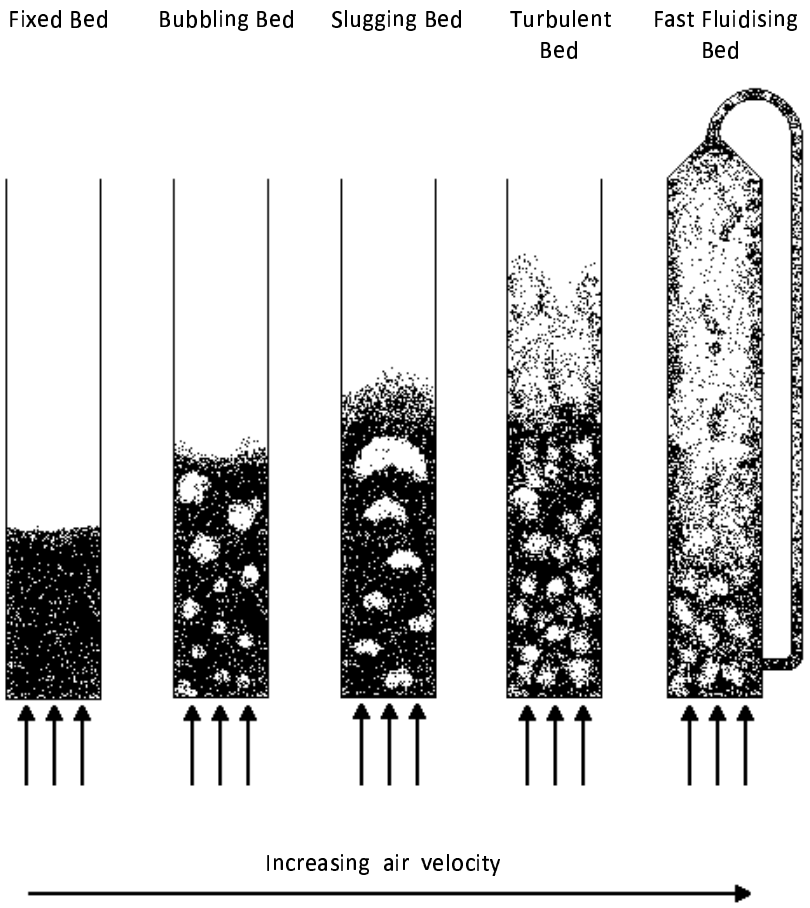

FIGURE 2.1: The transitional regimes of fluidsation

determination of the minimum fluidisation velocity can be shown by the intersection of the pressure drop versus the superficial velocity curve, where the superficial gas velocity is the hypothetical fluid velocity of the phase in terms of the cross-sectional area.

The minimum fluidisation velocity can be determined by Equation 2.1 for smaller particles and equation Equation 2.2 for larger particles [18].

$$U_{mf} = \frac{d_s^2 \left(\rho_s - \rho_g\right) g}{1650\mu}, \quad Re_{mf} < 20 \tag{2.1}$$

$$U_{mf}^2 = \frac{d_s^2 \left(\rho_s - \rho_g\right) g}{24.5\rho_g}, \quad Re_{mf} > 1000 \tag{2.2}$$

Wen and Yu [19] had proposed the following correlation which determines the Reynolds number at minimum fluidisation velocity which is related to the Archimedes number (Ar) which determines the motion of the fluids due to density differences (Equation 2.3):

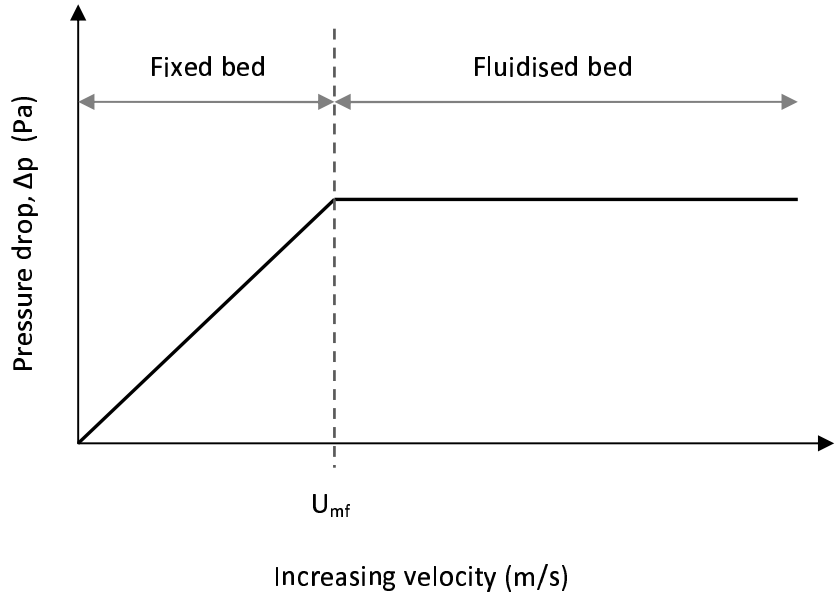

FIGURE 2.2: The determination of the minimum fluidisation velocity by the intersection of pressure drop and superficial velocity

$$Re_{mf} = \sqrt{[33.7^2 + 0.0408Ar]} - 33.7 \tag{2.3}$$

Increasing the air velocity further leads to the appearance of bubbles within the bed which is termed a heterogeneous or bubbling fluidised bed. The point at which bubbling occurs is called the minimum bubbling velocity and is generally about $3U_{mf}$ [20]. In deep reactors which have a narrow diameter and reactors containing large particles, a slugging behaviour is observed where the bubbles ascend the tube which is spread across the diameter of the tube.

Increasing the inlet velocity of the gas for smaller particles further leads to a turbulent bubbling behaviour where particles are forced into the freeboard of the reactor. Some particles descend back down towards the bed however, should the terminal velocity of the particles be exceeded, where $V_t = (d_s^2 (\rho_s - \rho_g) g)/18\mu$, then particle entrainment takes place where the particles are carried with the flow and are generally circulated back into the base of the bed through the utilisation of a cyclone and downcomer tube, otherwise known as fast fluidisation which is seen in circulating fluidised beds (CFBs).

A number of parameters including particle size and density alter the behaviour of gas-solid fluidising flows. The Geldart classification system was developed by Geldart [21] to categorise particles into four categories depending on their mean particle size and the density difference between the gas and solid phase. A visual representation of the Geldart's classification system of powders is given in Figure 2.3.

Group A: The first category, group A (Aerated) contains very small mean particles with sizes ranging between $30\mu\text{m} < d_p < 100\mu\text{m}$ and a density falling below $\rho_s < 1400\text{kg/m}^2$. When fluidised by air with ambient conditions, there is a steady non-bubbling fluidisation between the minimum fluidising velocity U_{mf} and the minimum bubbling velocity U_{mb}.

Group B: The second category, group B (Bubbling) contains a mean particle size ranging between $40\mu\text{m} < d_p < 500\mu\text{m}$ and a density $1400\text{kg/m}^2 < \rho_s < 4000\text{kg/m}^2$. The flow starts bubbling from minimum fluidisation and the bubbles continue to grow in size. Gidaspow et al. [22] showed through numerical simulations that the use of a continuous jet produced small bubbles which rise a lot slower than the jet speed.

Group C: The third category, group C (Cohesive) contains very fine particles that are very difficult to fluidise. This is due to the interparticle forces being significantly larger than the inertial forces from the fluid on the particle. Instead of bubbling, the gas channels through the powdered particles.

Group D: The last category, group D (Spoutable) contains very large or very dense particles which produce deep spouting beds; examples include rice. Liu et al. [23] reported that Group D powders can be fluidised with a homogeneous bed expansion like a Group A powder.

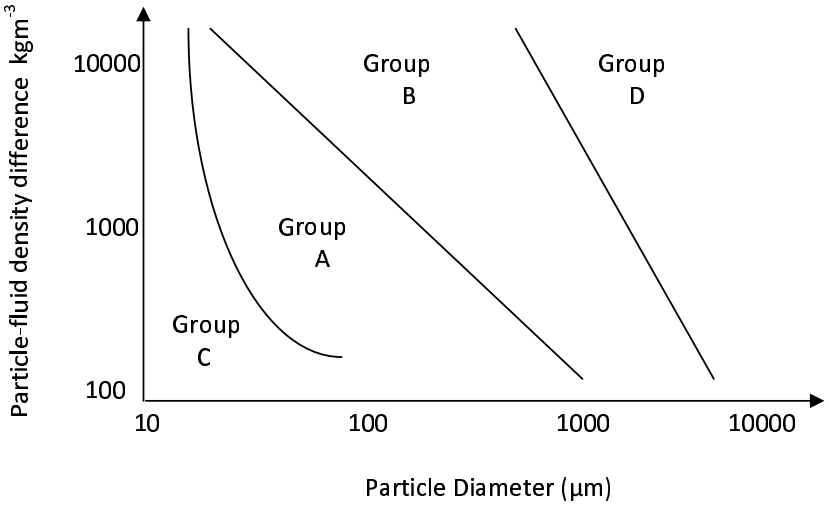

FIGURE 2.3: The Geldart classification system of powders for Groups A, B, C and D

2.2 Computational fluid dynamic modelling

Computational fluid dynamic modelling uses a numerical method to simulate the behaviour of a flow. As will be discussed further in Chapter 3, governing equations are solved that are based on the fundamental physical principles; the conservation of mass,

momentum and energy. Computational modelling for the flow behaviours in a fluidised bed can be carried out using both Lagrangian and Eulerian methods.

Lagrangian models track the individual granular particles which offers a great advantage in determining their individual specific properties, e.g., positions and velocities. Such models have been carried out in fluidised beds previously [24–27]. However, fluidised beds contain a vast number of particles and to individually track each one incurs huge computational expenses with regards to computational time and memory storage.

A different and more preferred approach is to treat the gas and particles as an inter-penetrating continuum which is known as the Eulerian-Eulerian approach, or two-fluid modelling (TFM). Both the gas and the particulate phase are treated with its own fluid phase where the introduction of a volume fraction specifies the volume of the cell which is occupied by each individual phase. Since this method treats the particulate phase as a continuum, it does not display the accuracy that Lagrangian modelling does as the particle properties, i.e., velocities, densities etc., are averaged over the control volume hence losing the ability to track individual particles.

A combination of the Eulerian-Eulerian model and the Eulerian-Lagrangian model was recently considered by Papadikis et al. [28–36] where one or two Lagrangian biomass particles were introduced to an Eulerian-Eulerian bubbling bed of inert sand. Although their approach is highly beneficial for the investigation at an individual particle dynamic scale, the simulation was limited to up to 5.0 s in physical time. Hence, their method does not prove to be computationally viable for realistic industrial reactors which contain far more fuel particles and require simulations over a longer period to allow for the achievement of possible steady state conditions and the statistical convergence of averaged results.

Whilst the Eulerian-Eulerian method is the cheaper method its treatment of the solid phase as a fluid is not representative of actual particle behaviour despite the fluid motion observed in a fluidised bed. Assumptions need to be made to appropriately model the particle interactions. The kinetic theory of granular flow (KTGF) was developed based on an analogy of the particles to the molecules in dense gases which is extensively discussed by Chapman and Cowling [37]. The random oscillating behaviour of the particles are measured in terms of the granular temperature. If particles are involved in inelastic collisions then kinetic energy is dissipated. The initial development of the KTGF started with the works of Bagnold [38] who derived an expression for the repulsive pressure of uniform shear flow from an expression for the collision frequency of the particles. Ogawa et al. [39] later suggested that the internal energy of the granular flow was suggested to occur from the dissipation of random particle motion.

The loss of energy due to particle collisions was recognised through the development of the coefficient of restitution by Jenkins and Savage [40]. The coefficient quantifies the elasticity of the particle collisions where a value of 0 indicates the collision is fully

inelastic whilst a coefficient of 1 represents a fully elastic collision. However, the energy lost due to the collisions was not accounted for in the kinetic theory model by Savage and Jeffrey [41] but they later extended this work with a correction being applied which considered the inelastic collisions of particles by introducing the coefficient of restitution [42].

Goldschmidt et al. [43] found that decreasing the coefficient of restitution led to less elastic particle collisions resulting in a higher dissipation of energy as more fluctuating energy was generated. The higher the coefficient of restitution suggests that nearly all the energy is conserved during the collisions of particles which results in an active movement of the particles [44]. Kim and Arastoopour [45] extended the kinetic theory of granular flow to incorporate the cohesiveness of the particles. Whilst Sun and Battaglia [46] modified it to account for the rotation of rough particles.

One of the first applications of the kinetic theory of granular flow was applied to fluidisation for the core-annular regime within a riser by Sinclair and Jackson [47] but further research has been and continues to be carried out for both CFBs [2, 43, 48–50, 50–57] and BFBs [27, 44, 46, 57–63].

The drag models are important in simulating the interphase momentum transfer between the gas and particle phases and researchers continue to develop and improve their capabilities in order to improve the accuracy of simulations. Ergun [64] began looking at the momentum interphase transfer, i.e., drag between for phases, by creating an experimental method looking at a packed bed of particle which led to the development of the Ergun equation. Unfortunately, fluidised regimes consist of particle rich and gas rich regions so a model needed to be developed that considered regions of low particle volume fractions, i.e., bubbles and the freeboards above the bed. Wen and Yu [19] developed this drag model which has been widely accepted. A standard model which has been used for many fluidised bed simulations incorporates the two drag models for the dense and dilute regions of the bed and is the Gidaspow model [65]. Unfortunately, there is a discontinuity in the Gidaspow model during the transition from a dense regime to a dilute regime, i.e., when $\varepsilon_g = 0.8$. This discontinuity increases in magnitude with increasing Reynolds number. Further drag models have also been developed over the years [66–72].

Although these drag models have provided reasonable results with applications to two-fluid models, such drag models can not be called ab initio methods as the constitutive closure models whilst showing dependence on parameters such as the Reynolds number of the flow and the particle volume fraction, they neglect other important parameters such as particle shape and roughness. Furthermore, the development of the above drag models were determined by analysis of experimental data hence limiting the complete theoretical understanding.

However, a drag model has been developed recently using numerical-experimental data from Lattice Boltzmann modelling (LBM). The terminology numerical-experimental is justified by the fact that LBM uses first principle calculations [73]. Therefore, the derivation of a drag model given by Hill et al. [74, 75] provides the most extensive numerical-experimental data reported to date [73]. A number of different formulas for the drag function at varying Reynolds numbers and particle volume fraction were developed; however, the transition of the drag values for the different equations were very sudden and contained gaps between values which causes problems when trying to model the transitions. Benyahia et al. [73] extended their work further to develop a single formula that smoothly covers the varying range of Reynolds numbers and volume fraction without jumps or gaps such that it can be applied to multiphase models.

Circulating fluidised beds behave differently to bubbling fluidised beds as the flow contains dense clustering regions to the base of the riser and near the walls and dilute regions at higher heights and within the core. Whilst the use of some of the aforementioned drag models have produced similar results compared to experimental data for this fast fluidising regime, they do not take into account the structure of particle clusters at different scales. Figure 2.4 (a) and (b) displays an example of how standard drag models average the particles in a control volume (Fig. 2.4(a)) thus being unable to pick up on small clustering structures which could occur within the control volume (Fig. 2.4(b)) leading to a variation in the drag. The drag is overpredicted as the drag coefficients are determined through the local slip velocities and average gaseous volume fractions hence they do not display the overall structural effects. This was determined by Gunn and Malik [76] who showed that grouped clusters of particles display a decrease in the measured drag coefficient due to the increase of gas flowing around the clusters and decrease gas flow penetrating them. O'Brien and Syamlal [77] stated that the importance of the clustering of particles needs to be accounted for in current drag correlations.

The energy minimisation multiscale (EMMS) approach is a filtered model that was developed by Li et al. [78] which identified the different multiple scales present in the circulating fluidised bed. Figure 2.4 (c) displays the different scales that can occur in a circulating fluidised bed [78]. The micro-scale considered the discrete individual particles which were located in either a dense phase or a dilute phase; the meso-scale which considered the interaction between the particle clusters and the surrounding dilute broth and the macro-scale which considered the full global system of the gas-particle suspension within its boundaries. This filtered model was applied by Li et al. [79] later to show the heterogeneous flow including the axial and radial heterogeneity caused by the boundaries. It is these heterogeneous structures that cause issues when using standard average-based drag models as the disparity between the dilute core annulus and dense wall regions is so dramatic.

The EMMS drag model has been applied by key researchers within the field of fluidisation hydrodynamics [57, 78–82], calculations were made and compared for the slip

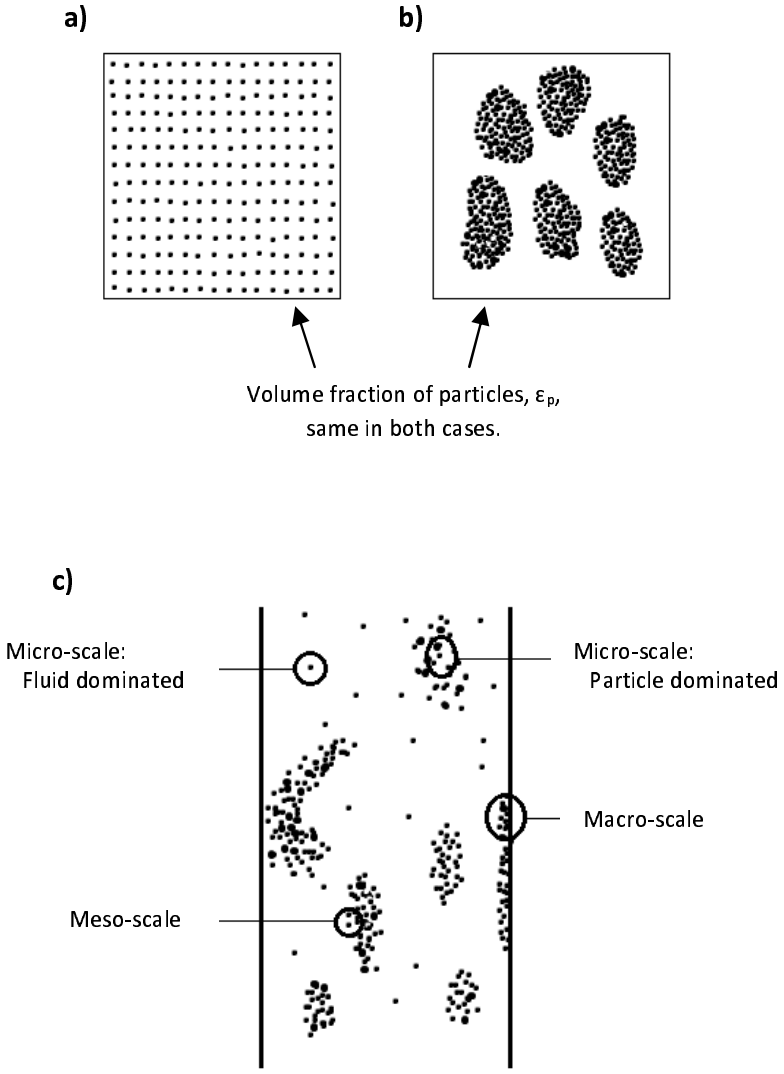

FIGURE 2.4: a) The averaging behaviour of a standard drag model and b) the realistic clustering behaviour of particles in a control volume of a circulating bed simulation along with c) the different multiple-scales they exhibit.

velocities and drag coefficients for the different interaction phases of dense clusters, dilute phases and interactions between them both [78]. This was further extended to show the strong dependence of the drag coefficient on simple structural differences [80] and later a decrease in drag coefficient due to local and global structural changes.

Unfortunately, TFMs have issues with regard to scaling. In order to obtain sufficient information for all the particle interactions and structures, small control volumes are required. This method has shown reasonable results for small scale models with a height of around 1-2m as the control volumes are small. However, increasing the dimensions of the reactor would require an increase in the cell sizes to prevent excessive computational time and expenses. This would result in the model's inability to capture the full particle structures [83]. The advantage of the filtered drag model is that it can be applied to

coarser grids which could reduce the computational time and costs for potential large-scale models.

The Reynolds numbers for the multiphase flows within CFB risers are high so additional turbulence models to the kinetic theory have been applied for many years [2, 50, 51, 72]. Cruz et al. [72] and Almuttahar and Taghipour [51] carried out a simulation comparing the use of turbulence models against laminar models which suggested that the laminar models showed more consistent results over the turbulence models. However, these comparative models for turbulence were carried out in 2D simulations and since turbulence fluctuations always have three-dimensional spatial character then 3D comparative studies are required to draw a firm conclusion.

The incorporation of multiple solid phases into a TFM with the KTGF was carried out by Mathiesen et al. [84] who applied the kinetic theory to one gas phase and three solid phases with good agreement. They later extended their work to include three solid phases [85] which was later extended further by Ibsen et al. [86] to extend the number of solid phases to six thus creating a more realistic display of the particles which would be present in a reactor.

Three-dimensional modelling has been carried out by several researchers [87–91] with results confirming 3D models to be superior over the 2D models. However, 2D modelling still takes preference over 3D modelling due to the excessive computational time and expense that 3D modelling incurs. With the increase in computational performance and introduction of parallel computing systems, the issues with computational time for 3D modelling are reduced.

2.3 Heat transfer modelling

Single particle models were the simplest form which looked at a continuous fluidising medium, i.e., either gas or air, and a discrete particle. Botterill and Williams [92] developed the simplest model which considered the heat transfer from a heated surface to an isolated particle surrounded a fluid which was in contact with the surface for a certain time. After the application of this to a finite difference technique and comparing with experimental data they found the results deviated considerably. They further extended the model to consider the presence of a gas film set to approximately $0.1d_p$ and the results agreed the experimental results. However, Schlünder [93] explained that this gas film assumption did not represent the physical reality as it only considered the heat exchange for short residence times and if the heat transfer were to extend further than the first layer of particles, i.e., during longer residence times, than the model would fail.

The introduction of emulsion-phase models was proposed by Mickley and Fairbanks [94]. In such models the emulsion-phase is considered as the continuous phase and the bubbles are the discrete phases. Their model suggested that the heat was transferred by emulsion 'packets' which were periodically replaced from the heated surface by bubbles.

Unfortunately, such empirical correlations are not attractive in the application of heat transfer modelling as they do not provide a clear understanding of the fundamental mechanisms that take place [95]. Kuipers et al. [95] carried out a TFM approach which successfully managed to calculate the heat transfer coefficient values through the solution of the mass and momentum conservations resulting in no empirical parameters being used which were required in the single and emulsion phase modelling.

Zehner and Schlünder [96] had previously described the thermal conductivity from the bulk of a packed bed as being a function of the solid volume fraction and the thermal properties of both the gaseous and solid phases. An effective thermal conductivity for the gas phase and solid phase was adapted by Kuipers et al. [95] and carried out [95, 97] which was based on the molecular properties. However, Natarajan and Hunt [98] proposed the effective thermal conductivity of the solids phase to also include a kinetic contribution caused by the streaming of particles. A model for the kinetic contribution was derived by Hunt [99] as a function of the kinetic energy of random particle fluctuations, i.e., granular temperature. However, the incorporation of this kinetic contribution led to a strong over estimation in the heat transfer coefficient due to large granular temperatures [97].

The voidage variation within the near region of the heated wall or immersed tube needs to also be considered. The local porosity relative to the bulk porosity of a packed bed of particles was measured as a function of the relative distance away from a wall or an immersed surface by Korolev et al. [100]. Their experimental results showed that the local porosity was dependent on the fluidising velocity. Furthermore, they found that the measured local porosity distribution near the wall and that around the immersed tube differed as the distribution near a wall is similar to a packed bed at low fluidisation whereas that of a tube varied to a much greater degree.

Martin [101] produced a porosity model that agreed well with the packed bed results for a heated wall. However, a fluidised bed is exerted to a higher bulk porosity compared to packed beds which was not taken into account. Patil et al. [97] modified the model produced by Martin [101] to take this into account by proposing the minimum porosity be related to the bulk porosity of the fluidised bed. Their effective gas porosity correlation agreed well with the experimental results from Korolev et al. [100].

Another important aspect to consider in modelling heat transfer is the interphase heat transfer coefficient which transports heat from one phase to another. The Nusselt number is the ratio of convective and conductive heat transfer within the boundary of a flow.

Gunn [102] developed a model that considered the interaction of convection, thermal conduction and interphase heat and mass transfer. Analytic results were applied to the convection and diffusion within randomly-packed beds and the experimental results for single particles, fixed beds and fluidised beds were well described with a single equation which contained both experimental and analytical conditions for both heat and mass transfer. The correlation relates the Nusselt number to the Prandtl number for the heat transfer within a porosity range of 0.35-1.00 with the experimental data being correlated up to a particle Reynolds number Re = 1 x 10^5.

2.4 Reaction kinetics

The combustion and gasification processes have been considered for a number of decades. An early comprehensive mathematical model was produced starting with simplified chemical reactions to determine emission predictions by Smoot [103]. The first model to be regarded as a fully complete model considered fluidisation modelling (FM) which models the emulsion phase and the bubbles through to the mass balance of the drying and devolatilisation processes [104]. Work has continued to be carried out using an emulsion phase rather than a particulate phase by a number of people [105–108]. Huilin et al. [105, 107] carried out a FM on a circulating fluidised bed combustor whilst Yan et al. [106] carried out several simulations of a bubbling fluidised bed coal gasifier with different scales. de Souza-Santos [104] also introduced limestone calcination to FM which was also adopted by Chejne and Hernandez [108]. Furthermore, the product of limestone calcination, calcium oxide, CaO, was active in the absorption of sulphur dioxide, SO_2, from the surrounding gases [104, 107–109].

Unfortunately, fluidisation models (FM) so far do not consider the fully complex gas-particle dynamics that CFD considers but they still maintain the multiphase flow dynamics with the inclusion of semi-empirical fluid-dynamic correlations, e.g., bubble diameter correlations, for the gas and an emulsion phase.

Lagrangian modelling has been carried out to perform more detailed simulations of the gasification processes [28–34, 36, 110–112]. The pyrolysis works by Papadikis et al. [28–34, 36], as discussed previously in Section 2.2, incorporated a limited number of Lagrangian biomass particles into an Eulerian-Eulerian bubbling bed of inert sand. This method is advantageous with regards to obtaining individual reacting particle dynamics but is not a viable solution as realistic reactors which contain more fuel particles and require longer periods of time to allow for the achievement of possible steady state conditions. This reason also applies to the works from Zhou et al. [111] who carried out a Lagrangian model of a bubbling fluidised bed for only 2.0s utilising 20 coal particles and a bed of 2000 sand particles.

Although Eulerian-Eulerian modelling has been recognised as the preferred method for fluidised bed modelling it has only been recently that the incorporation of reaction kinetics has been considered. This is because researchers continue to focus primarily on the improvement of the flow behaviour models. Yu et al. [63] carried out a two-dimensional model of a bubbling fluidised bed which included the gasification of Colombian coal based on experimental data from the literature [5]. Their model included the pyrolysis, heterogeneous reactions and homogeneous reactions and produced reasonable results for a sand bed. The work by Yu et al. [63] was further extended to three-dimensions by Wang et al. [113], who also obtained reasonable results. However, both their models considered a single solid phase which composed of coal and sand together. Whilst this is computationally more efficient it is unrealistic.

Recently, Eulerian-Eulerian modelling was carried out in a bubbling fluidised bed for biomass by Gerber et al. [114]. They considered a bed of char over the commonly carried out bed of inert bed material. Advantages of its use include reduced pressure loss due to its density being lower than other catalysts, i.e., limestone and olivine; and it is the byproduct of the devolatilisation process so it will be continually regenerated [114].

Separate phases for different solid phases has been carried out [16, 114] and it was found that the use of multiple phases better represents the bed behaviour due to its segregative tendencies as a result of different material properties. Limestone calcination was also introduced to Eulerian-Eulerian CFD modelling [16]. The results suggested that residence times needed to be increased significantly in order to observe an almost complete conversion as found by [115] who investigated the effects of temperature and residence time on the decomposition of limestone of similar sized particles in a CO_2 atmosphere and found that with a BFB temperature of 920°C, the residence time for over 73% conversion of $CaCO_3$ to CaO was approximately 70mins. Unfortunately, due to low levels of sulphur in the fuel our work did not consider the effects of sulphur absorption.

The gasification process includes the release of volatiles and char from the coal, i.e., devolatilisation; the reactions between the char with oxygen through heterogeneous combustion reactions and the reaction of char with gasifying species, H_2O, H_2 and CO_2; known as heterogeneous gasification reactions. Finally, gaseous components react with each other during homogeneous reactions.

The time required for the devolatilisation process to take place was investigated by Ross et al. [116] who found that over a range of temperatures, 750-950°, particles with a diameter of less than 6.0 mm the time required was less than 10.0 s. Chejne and Hernandez [108] considered the devolatilisation processes to be instantaneous since drying and devolatilisation take place very quickly in fluidised beds. de Souza-Santos [104] on the other hand carried out a simulation which considered these processes as non-instantaneous.

A number of devolatilisation models have been implemented previously including the constant model [117, 118], single rate model [119] and the Kobayashi model [120, 121]. The most basic devolatilisation model assumes the release of volatiles to occur at a constant rate [117], where the rate was later suggested to be 12.0 1/s [118]. The single rate model [119] assumes the rate of the volatile release is first-order dependent based on the amount of volatiles remaining in the coal. The Kobayashi model [120, 121] handles the devolatilisation of coal and volatiles release through the implementation of two equations. An equation for low temperatures where the volatiles would asymptotically approach a yield value whereas the second equation was developed for higher temperatures where it was assumed that the volatile yields could be much larger [121].

Unfortunately, these devolatilisation models rely on data which would be specific to different coals therefore the general utility of the models would be limited to the available data extracted from the coals. Due to the wide variation in the properties of coal it would be difficult to develop a universal devolatilisation model that can be applied without the use of the fuel's proximate and ultimate analysis data, i.e., the fuels composition in terms of moisture, volatiles, char and ash; and the fuels weight composition in terms of hydrogen, oxygen, carbon etc.

The yield of the volatile products is required to determine the composition of the volatile gases that are released. A number have been developed including [122–126]. The correlations developed by Loison and Chauvin [122] have been widely utilised for predicting the volatile yields as it estimates the important gaseous products based on the proximate analysis of the coal. Unfortunately, their model does not account for temperature effects. Correlations were later developed by Goyal and Rehmat [124] which predicted the composition of the tar, methane as a function of temperature but considered the remaining species as independent of the temperature. Correlations have also been considered which specify all the yields to be determined as a function of time [123, 125].

Song et al. [126] carried out a study comparing all these correlations for bituminous coals and found that the yields produced by Loison and Chauvin [122] produced better results than the completely temperature dependant models. Their own correlations, which were also dependant on the temperature, produced very good results however they only considered the release of H_2, CO, CO_2 and CH_4, therefore a more general relationship is required.

The heterogeneous reactions take place between the char and the surrounding gases. The oxidation of char has been considered to be influenced by a number of factors including pore structures, ash films, particle swelling, etc [127, 128]. For Lagrangian modelling such influences can be considered more easily due to the detailed information available for the particles. However, Eulerian modelling of the char phase restricts this information that can be accessed, e.g., the particles are treated with the same diameters therefore particle swelling can not be incorporated. However, the unreacted-core model considers

the effects of resistance due to the diffusion of the gases through an external surface of the char. This approach has been carried out successfully in fluidisation modeling [104, 108, 129] and Eulerian modelling [63, 113, 114].

The gasification heterogeneous reactions take place much slower than the combustion heterogeneous reactions and they have a longer residence time within the bed. The diffusion of the reactants into the char is therefore not dominated by the fast external surface reactions that take place during combustion instead the reaction is control through the kinetic rate constant [127]. Hobbs et al. [129] highlighted that based on the experimental data from several researchers [130, 131] that the gasification rate of steam and carbon dioxide takes place with the same rate whilst the hydrogen reaction rate is three orders of magnitude slower than the other gasification rates.

The homogeneous reactions take place between the species in the gaseous phase. The kinetic reaction rates have been established over the recent decades and are provided by a number of researchers [104, 108, 109]. Such reactions are not only driven by the kinetic forces but also by the turbulent motions of the gas. Yu et al. [63] considered the effects of turbulence by incorporating the finite-rate/eddy-dissipation model which determines whether the kinetic rate is dominating the local reactions or the turbulent mixing therefore chooses the appropriate model accordingly. This model has also been applied by Wang et al. [113] and Gerber et al. [114].

Chapter 3

Computational Fluid Dynamic Modelling

The flow of fluid through a region is calculated by numerically solving specific governing equations. These equations are based on three of the fundamental physical principles; the conservation of mass, momentum and energy. FLUENT 12.0 is a computational package which solves these governing equations by integrating them over all the control volumes in a domain; converting the resulting integral equations into a system of algebraic equations which will then be solved by an iterative method. This process will be described in Appendix B.

FLUENT 12.0 can be used to model flows with Lagrangian and Eulerian methods. Eulerian modelling takes a control volume and fixes it to a reference framework relative to a coordinate system and allows the fluid to flow through. All particles that flow through the framework can be observed and treated as a general fluid by averaging properties such as velocities, etc. Lagrangian modelling tracks each of the individual particles without a fixed reference frame. Unfortunately, Lagrangian modelling can be computationally expensive depending on the number of particles being tracked as simulations can take much longer to run and require more storage space for the data. The work carried out is a multiphase Eulerian-Eulerian model, treating the gas and solids as a dispersed continuous flow. The interactions between particulate phase is incorporated using the kinetic theory of granular flow (Section 3.1.1). The relevant equations for the models are presented in the next section.

3.1 Multiphase modelling

To model the behaviour of a fluid flow the governing equations must obey the conservation laws of physics: 1) The mass of the fluid must be conserved, 2) the rate of change

of the momentum must equal the sum of all the forces acting upon the fluid and 3) the rate of change of energy must equal the sum of the rate of heat added to and the rate of work done on the fluid. The behaviour of the fluid is regarded as a continuum and given in terms of the properties: density, velocity, pressure and temperature; which are modelled over varying spatial and time derivatives. Multiphase flow modelling treats both the gaseous and the solid phases as interpenetrating continua therefore the concept of the volume fraction, ε_i, is introduced indicating the volume that each phase occupies within the control volume.

3.1.1 Kinetic theory of granular flow (KTGF)

Before the treatment of the particulate phase can be considered on a macroscopic basis, it is important to highlight its microscopic origins. Its development, mentioned previously in Section 2.2, is analogous to the kinetic theory of gases which considers the behaviour of molecular particles in a fluid that traverse and collide in a fixed space. Using information about the atoms and molecules within the fluid, the theory can provide information about the fluids properties, such as pressure and temperature. Unfortunately, considering the individual molecules in the fluid incurs extensive computational costs and time, therefore an averaging technique is required that is still small enough to be considered microscopic yet large enough to contain enough molecules to obtain reasonable averaging statistics for the macroscopic properties. The Boltzmann method considers a number of particles of mass, m, within a volume at position, $\mathbf{x}$, with velocity, $\mathbf{u}$ and at time, $\mathbf{t}$; and their values at time, $t + dt$, after experiencing an external force, $\mathbf{F}$:

$$f(\mathbf{x}, \mathbf{u}, t)\mathrm{d}\mathbf{x}\mathrm{d}\mathbf{u}, \tag{3.1}$$

and

$$f(\mathbf{x} + \frac{\mathbf{u}}{m}\mathrm{d}t, \mathbf{u} + \mathbf{F}\mathrm{d}t, t + \mathrm{d}t)\mathrm{d}\mathbf{x}\mathrm{d}\mathbf{u}. \tag{3.2}$$

Subtraction of Equation 3.2 and Equation 3.1 produces the Liouville equation:

$$f(\mathbf{x} + \frac{\mathbf{u}}{m}\mathrm{d}t, \mathbf{u} + \mathbf{F}\mathrm{d}t, t + \mathrm{d}t)\mathrm{d}\mathbf{x}\mathrm{d}\mathbf{u} - f(\mathbf{x}, \mathbf{u}, t)\mathrm{d}\mathbf{x}\mathrm{d}\mathbf{u} = 0. \tag{3.3}$$

However, it is likely that collisions between particles occur therefore the number of particles in the volume, $\mathrm{d}\mathbf{x}\mathrm{d}\mathbf{u}$, would change. Therefore, an additional term is required to account for the effects of these collisions:

$$f(\mathbf{x} + \frac{\mathbf{u}}{m}\mathrm{d}t, \mathbf{u} + \mathbf{F}\mathrm{d}t, t + \mathrm{d}t)\mathrm{d}\mathbf{x}\mathrm{d}\mathbf{u} - f(\mathbf{x}, \mathbf{u}, t)\mathrm{d}\mathbf{x}\mathrm{d}\mathbf{u} = \left.\frac{\partial f\,(\mathbf{x}, \mathbf{u}, t)}{\partial t}\right|_{\mathrm{coll}} \mathrm{d}\mathbf{x}\mathrm{d}\mathbf{u}\mathrm{d}t. \tag{3.4}$$

Finally, manipulation of Equation 3.4 leads to:

$$\frac{\partial f}{\partial t} + \frac{\partial f}{\partial \mathbf{x}} \cdot \frac{\mathbf{u}}{m} + \frac{\partial f}{\partial \mathbf{u}} \cdot \mathbf{F} = \left.\frac{\partial f}{\partial t}\right|_{\mathrm{coll}}. \tag{3.5}$$

Granular particles portray similar kinetic and collisional behaviours to the molecules considered in the above equations, however, the scale of the particles is much larger. Since the probability densities can be found using the above equations at different times we can develop transport equations to determine the average fluid properties on a macroscopic scale. This has been carried out and explained extensively by Gidaspow [18] but comes about through the multiplication of the above Boltzmann equation by an arbitrary value, ψ, and integrating over the velocity domain to produce Maxwell's equation. The Maxwellian transport equation can then be used to determine the macroscopic mass, momentum and kinetic energy equations through the substitution of ψ with m, mu and $1/2mc^2$, respectively.

Differing from the Boltzmann equations, the kinetic theory of granular flow needs to consider the different stages of particle loading that take occur, especially in fluidised beds, kinetic, collisional and frictional. Therefore, closure terms are developed and explained with the progression of this chapter which accounts for these different phenomena. However in most cases, particularly kinetic and collisions driven regimes, random oscillations occur between the particles, leading to inelastic collisions and the dissipation of energy. The granular temperature, Θ_s, measures these random oscillations of the particles and is defined as the average of the three variances of the particle's velocities, $1/3(u^2+v^2+z^2)$. A full mathematical description of the kinetic theory is provided by Gidaspow [18]. The kinetic theory of granular flow is modelled using the following equation:

$$\frac{3}{2}\left[\frac{\partial}{\partial t}\left(\varepsilon_s\rho_s\Theta_s\right)+\nabla\cdot\left(\varepsilon_s\rho_s\vec{v}_s\Theta_s\right)\right]=\left(-p_s\cdot\overline{\overline{I}}+\overline{\overline{\tau}}_s\right):\nabla\vec{v}_s+\nabla\cdot\left(k_{\Theta_s}\cdot\nabla\Theta_s\right)$$
$$-\gamma_{\Theta_s}-3K_{gs}\Theta_s. \tag{3.6}$$

The first term on the right-hand side represents the production of fluctuations due to pressure and shearing forces. The second term in Equation 3.6 is the granular heat flow vector and the granular conductivity, k_{Θ_s}, [18] is comprised of a kinetic component and two collisional components accounting for the transport of energy by particle velocity fluctuations and by particle collisions, respectively:

$$k_{\Theta_s}=\frac{150\rho_s d_s\sqrt{\Theta_s\pi}}{384\left(1+e\right)g_0}\left[1+\frac{6}{5}\,\varepsilon_s g_0\left(1+e\right)\right]^2+2\varepsilon_s^2\rho_s d_s\left(1+e\right)g_0\sqrt{\frac{\Theta_s}{\pi}}. \tag{3.7}$$

The kinetic component dominates the flow in dilute regimes whereas the collisional terms dominates in dense flows as collisions take place more readily. The dissipation of energy due to inelastic collisions is taken into account in Equation 3.6 by the collisional dissipation term, γ_{Θ_s}. It is taken from Ding and Gidaspow [132] and is given as follows:

$$\gamma_{\Theta_s}=\frac{12\left(1-e^2\right)g_0}{d_s\sqrt{\pi}}\,\varepsilon_s^2\rho_s\Theta_s^{3/2}. \tag{3.8}$$

For elastic particles, $e = 1$, there would not be any loss of energy due to the collisions therefore γ_{Θ_s} would equal zero.

The final term in Equation 3.6 represents the dissipation of fluctuating kinetic energy due to the interaction of the particles with the surrounding fluid.

3.1.2 The conservation of mass

Although the previous section explained that the conversation of mass and momentum equations could be derived by the Maxwell transport equation, it is also interesting to show the derivation of the multiphase conservation equations in comparison to single phase modelling. The conservation of mass for a single fluid is obtained when the rate of increase of the mass within the volume is equated to the net rate of mass entering and leaving the volume through its surfaces.

The total mass per unit volume, ρ, over the entire control volume is:

$$m = \int_{\Omega} \rho \, \mathrm{d}\Omega \tag{3.9}$$

The rate of change over the volume including the convective change across the surface of the control volume, S, is:

$$\frac{\mathrm{d}m}{\mathrm{dt}} = \frac{\partial}{\partial t} \int_{\Omega} \rho \, \mathrm{d}\Omega + \int_{\mathrm{S}} \rho \left(\vec{v} \cdot \mathbf{n} \right) \, \mathrm{ds} = \sum (\text{external influences}) \tag{3.10}$$

Applying Gauss' theorem, also known as the divergence theorem, relates the net mass flow across the surfaces of the volume to its behaviour within the volume, thus producing:

$$\int_{\Omega} \left[\frac{\partial \rho}{\partial t} + \nabla \cdot (\rho \vec{v}) \right] \mathrm{d}\Omega = \sum (\text{external influences}) \tag{3.11}$$

Finally giving the conservation of mass for a single phase:

$$\frac{\partial \rho}{\partial t} + \nabla \cdot (\rho \vec{v}) = \sum (\text{external influences}) \tag{3.12}$$

Since the present work utilises multiphase flow modelling with a gaseous phase and granular solid phases, each phase would be modelled with its own conservation of mass equation with the inclusion of the volume fraction term, ε_i to specify the volume of the cell occupied by each phase, such as:

$$\frac{\partial \left(\varepsilon_g \rho_g \right)}{\partial t} + \nabla \cdot \left(\varepsilon_g \rho_g \vec{v}_g \right) = S_{gs}, \tag{3.13}$$

and

$$\frac{\partial\left(\varepsilon_s\rho_s\right)}{\partial t}+\nabla\cdot\left(\varepsilon_s\rho_s\vec{v}_s\right)=S_{sg}, \tag{3.14}$$

where

$$S_{sg}=-S_{gs}=w_i\Sigma Y_i R_i. \tag{3.15}$$

The source term, S_i, is the specific rate of production of the mass of phase, i, due to chemical reactions. This source term is important in reaction modelling since chemical reactions lead to a mass exchange from one phase to the other. An example of this would be during heterogeneous reactions where the solid char phase reacts with different gaseous reactants to produce additional gaseous products and a reduction in the mass of the char phase. Where mass exchange is not taking place the source term is taken to be zero.

The sum of all the phases in a control volume equals 1:

$$\sum\varepsilon_i=1. \tag{3.16}$$

3.1.3 The conservation of momentum

The conservation of momentum requires that the rate of change of momentum of the fluid element equals the sum of the forces that act upon it.

The conservation of momentum is determined by the same method as that used to find the conservation of mass, Equation 3.11, however the total momentum per unit volume, $\rho\vec{v}$, is solved instead of the total mass per unit volume. After the application of Gauss' theorem the momentum equation can be written as:

$$\int_\Omega\left[\frac{\partial}{\partial t}\rho\vec{v}\,\mathrm{d}\Omega+\nabla\cdot\left(\rho\left(\vec{v}\otimes\vec{v}\right)\right)\right]\mathrm{d}\Omega=\text{Body forces}+\text{Surface forces}. \tag{3.17}$$

The forces acting upon the control volume for a general single phase case include body forces, i.e., gravitational forces, $\rho\vec{g}$, pressure forces, ∇p, and the surface viscous forces, $\nabla\cdot\overline{\overline{\tau}}$, thus the conservation of momentum equation becomes:

$$\frac{\partial\left(\rho\vec{v}\right)}{\partial t}+\nabla\cdot\left(\rho\left(\vec{v}\otimes\vec{v}\right)\right)=-\nabla p+\nabla\cdot\overline{\overline{\tau}}+\rho\vec{g}. \tag{3.18}$$

Common forces between a single phase and a multiphase flow include surface forces and body forces as shown in Equation 3.18, however multiphase flow modelling requires an additional force that considers the interaction between the different phases, $K_{gs}\left(\vec{v}_g-\vec{v}_s\right)$. Furthermore, in the case of reaction modelling the mass exchange between phases is taken into account in the form of a source term.

The gaseous and solid phases in multiphase flow modelling are modelled with their own momentum equation as follows:

$$\frac{\partial\left(\varepsilon_g\rho_g\vec{v}_g\right)}{\partial t}+\nabla\cdot\left(\varepsilon_g\rho_g\left(\vec{v}_g\otimes\vec{v}_g\right)\right)=-\varepsilon_g\nabla p+\nabla\cdot\varepsilon_g\overline{\overline{\tau}}_g+\varepsilon_g\rho_g\vec{g}+K_{gs}\left(\vec{v}_g-\vec{v}_s\right)+S_{gs}\vec{v}_g, \tag{3.19}$$

and

$$\frac{\partial\left(\varepsilon_s\rho_s\vec{v}_s\right)}{\partial t}+\nabla\cdot\left(\varepsilon_s\rho_s\left(\vec{v}_s\otimes\vec{v}_s\right)\right)=-\varepsilon_s\nabla p-\nabla p_s+\nabla\cdot\varepsilon_s\overline{\overline{\tau}}_s+\varepsilon_s\rho_g\vec{g}-K_{gs}\left(\vec{v}_g-\vec{v}_s\right)+S_{sg}\vec{v}_s. \tag{3.20}$$

The first term on the right-hand side of Equation 3.19 and the first and second term on the right-hand side of Equation 3.20 represent the surface forces acting on the fluid element due to pressure. An additional pressure term is included for the solid phase which is made up from a kinetic and a collisional term as given by Ding and Gidaspow [132]:

$$p_s=\varepsilon_s\rho_s\Theta_s+2\rho_s\left(1+e\right)\varepsilon_s^2g_0\Theta_s. \tag{3.21}$$

The solids pressure is similar to the Van der Waal's equation of state for a gas of which Chapman and Cowling [37] carried out extensive work on non-uniform gases. In granular modelling, the thermal temperature is exchanged for the granular temperature, Θ_s, which was described in Section 3.1.1 and the radial distribution term, g_0, replaces the χ term where a value equal to 1 would represent a gas with molecules distanced far apart and increasing the value towards infinity lead to the compaction of those molecules until eventually they would be regarded motionless. The coefficient of restitution, e, was developed by Jenkins and Savage [40] to account for the loss of energy due to particle collisions. The radial distribution used in the present work was developed by Ogawa et al. [39] and is expressed as:

$$g_0=\left[1-\left(\frac{\varepsilon_s}{\varepsilon_{s,max}}\right)^{1/3}\right]^{-1}. \tag{3.22}$$

The second and third terms on the right-hand side of Equations 3.19 and 3.20, respectively, are the stress-strain tensors for the viscous forces. Each phase has its own equation:

$$\overline{\overline{\tau}}_g=\varepsilon_g\mu_g\left(\nabla\vec{v}_g+\nabla\vec{v}_g^T\right)-\frac{2}{3}\varepsilon_g\mu_g\left(\nabla\cdot\vec{v}_g\right)\overline{\overline{I}}_g, \tag{3.23}$$

and

$$\overline{\overline{\tau}}_s=\varepsilon_s\mu_s\left(\nabla\vec{v}_s+\nabla\vec{v}_s^T\right)+\varepsilon_s\left(\xi_s-\frac{2}{3}\mu_s\right)\left(\nabla\cdot\vec{v}_s\right)\overline{\overline{I}}_g. \tag{3.24}$$

The stress-strain tensor for the solid phase is similar to that of the gaseous phase only an additional term is added for the bulk viscosity, ξ_s, which accounts for the resistance of the granular particles from expansion and compression during particle collisions. The expression used is taken from the works of Lun et al. [133]:

$$\xi_s = \frac{4}{3}\varepsilon_s d_s \rho_s g_0 (1+e) \left(\frac{\Theta_s}{\pi}\right)^{1/2}. \tag{3.25}$$

Equations 3.23 and 3.24 also include the effects of shear viscosity, μ_i. The gaseous viscous term is made up of the gas phase laminar viscosity and the gas phase turbulent viscosity. Turbulence modelling is not a large contributor to the modelling of bubbling fluidised beds as the drag effects dominate. However, in circulating beds where the Reynolds number, Re, is higher and also in reaction kinetic modelling; both of which are considered in the present work; a turbulent model is applied. This will be discussed further in Section 3.1.5 wherein the expression for the gas phase turbulent viscosity, μ_{g_t}, is given in Equation 3.40. The gaseous viscous term is given by the following expression:

$$\mu_g = \mu_{g_l} + \mu_{g_t}. \tag{3.26}$$

The solid shear viscous term is a combination of translational, collisional and frictional momentum exchange:

$$\mu_s = \mu_{s_{col}} + \mu_{s_{kin}} + \mu_{s_{fr}}. \tag{3.27}$$

The translational viscous term is taken from the works of Gidaspow et al. [65] who developed the following expression:

$$\mu_{s_{kin}} = \frac{10 d_s \rho_s \sqrt{\Theta_s \pi}}{96 \varepsilon_s (1+e) g_0} \left[1 + \frac{4}{5}\varepsilon_s g_0 (1+e)\right]^2 \tag{3.28}$$

As flows become more dense more collisions occur between particles therefore the viscosity due to these collisions needs to be accounted for. The collisional viscosity in the present work is taken from Ding and Gidaspow [132].

$$\mu_{s_{col}} = \frac{4}{5}\varepsilon_s d_s \rho_s g_0 (1+e) \left(\frac{\Theta_s}{\pi}\right)^{1/2}. \tag{3.29}$$

For very dense flows, a frictional viscosity is introduced as the volume fraction of the particulate phase approaches the packing limit, which is the maximum volume fraction of particles that can occupy the control volume. Therefore, the friction created between the particles generates a large amount of stress which is modelled by Schaeffer's expression [134]:

$$\mu_{s_{fr}} = \frac{p_s \sin\phi}{\sqrt{I_{2D}}}. \tag{3.30}$$

The friction model was developed based on the von Mises yield function [134] where I_{2D} is the second deviatoric stress invariant and ϕ is the angle of internal friction which varies for different mixture properties, i.e., smooth and rounded particle have low angles of internal friction; whereas sticky or very fine particles have a high angle of internal friction. The values for the angle of internal friction range between 15° and 45°, with 30° the typical value.

The external gravitational forces acting on the fluid element are given by the third and fourth term on the right-hand side of Equations 3.19 and 3.20, respectively. The next term in these equations refers to the momentum transfer due to the interaction of the phases within the fluid element, i.e., drag.

There are a number of drag models for the interaction between the gaseous and solid phases available in the literature as discussed previously in Section 2.2. The following drag models are used in the present work: the Gidaspow [65], Syamlal-O'Brien [68], Hill-Koch-Ladd [73] and the Energy Minimisation Multi-scale (EMMS) [81]. Due to the large number of equations involved, the gas-solid drag models are given in Appendix A.

In simulations where there are multiple solid phases the interaction between them also needs to be considered. An expression was developed by Syamlal [135] which incorporates the different diameters of each phase, the radial distribution and introduces a coefficient of friction term for the friction between different phase particles.

$$K_{s_1 s_2} = \frac{3\left(1+e\right)\left(\frac{\pi}{2} + C_{fr,s_1 s_2}\frac{\pi^2}{8}\right)\varepsilon_{s_1}\varepsilon_{s_2}\rho_{s_1}\rho_{s_2}\left(d_{s_1}+d_{s_2}\right)^2 g_{0,s_1 s_2}}{2\pi\left(\rho_{s_1} d_{s_1}^3 + \rho_{s_2} d_{s_2}^3\right)}\left|\vec{v}_{s_1} - \vec{v}_{s_2}\right|. \quad (3.31)$$

3.1.4 The conservation of energy

The third law of physics requires that the rate of change of energy must equal the sum of the rate of heat added to and rate of work done on the fluid. The enthalpy is the sum of the total energy and the product of its pressure and volume.

The conservation of energy is written in terms of the enthalpy for each phase in the flow, as follows:

$$\frac{\partial}{\partial t}\left(\varepsilon_g \rho_g H_g\right) + \nabla\cdot\left(\varepsilon_g \rho_g \vec{v}_g H_g\right) = \nabla\left(\lambda_g \nabla T_g\right) + Q_{gs} + S_{gs} H_S \quad (3.32)$$

and

$$\frac{\partial}{\partial t}\left(\varepsilon_s \rho_s H_s\right) + \nabla\cdot\left(\varepsilon_s \rho_s \vec{v}_s H_s\right) = \nabla\left(\lambda_s \nabla T_s\right) + Q_{sg} - S_{sg} H_S. \quad (3.33)$$

where H_S represents the source term that includes sources of enthalpy, H_i is the enthalpy for each species in the mixture and λ_g is the mixture thermal conductivity. The specific

enthalpy, H_i, for the individual species in a mixture is defined as follows:

$$H_i = \int_{T_0}^{T} C_{p,i} dT + \Delta H_{f,i} \tag{3.34}$$

The specific heat, $C_{p,i}$, represents the amount of heat required to change that species' temperature by a given amount and the heat of formation, $H_{f,i}$, is the change of enthalpy required for the formation of 1 mole of a substance in its standard state from its constituent elements in their standard states at temperature, T_0. The standard state that data is usually obtained is at a pressure of 1 bar and a temperature of 25°C.

The thermal conductivity of the phase, λ_i, describes a substance's ability to conduct heat. For a gas containing a mixture of species the thermal conductivity is given by:

$$\lambda_g = \sum_j \frac{X_j \lambda_j}{\Sigma_j X_j \phi_{ij}} \tag{3.35}$$

and

$$\phi_{ij} = \left[1 + \left(\frac{\mu_i}{\mu_j}\right)^{1/2} \left(\frac{w_j}{w_i}\right)^{1/4}\right] / \left[8\left(1 + \frac{w_i}{w_j}\right)\right]^{1/2}, \tag{3.36}$$

where X_i represents the mole fraction of the individual species.

The heat exchange between the phases, Q_{gs}, is a function of the temperature difference and given by:

$$Q_{gs} = -Q_{sg} = h_{gs} \left(T_g - T_s\right). \tag{3.37}$$

The interphase heat transfer coefficient, h_{gs}, is discussed in further detail in Section 3.2.1.

3.1.5 Turbulence modelling

In the present work, the k - ϵ turbulence model is used to model the gaseous phase in circulating fluidised beds and during reaction modelling. In bubbling beds, the solid phases are not influenced greatly by the surrounding gases because the influence of drag from the fluidising behaviour of the bed dominates. However, in circulating beds the velocity of the gases at the base of the reactor are much higher than in bubbling beds, as a result the Reynolds number, Re, increases and a fast fluidising behaviour can be observed.

In reaction modelling, turbulent mixing is a large contributor to the mixing of reactants for the homogeneous reactions. In the present work the homogeneous reactions, which will be discussed further in Section 3.3.4, consider the effects of turbulent mixing in addition to chemical kinetic rates with the finite-rate/eddy-dissipation model therefore it is important to consider a turbulent model for the gaseous phase. The transport

equations for turbulent kinetic energy, k, and its dissipation rate, ϵ, are as follows [136]:

$$\frac{\partial\left(\varepsilon_g\rho_g k\right)}{\partial t}+\nabla\cdot\left(\varepsilon_g\rho_g \upsilon_i k\right)=\nabla\cdot\varepsilon_g\left(\mu_{gl}+\frac{\mu_{g_t}}{\sigma_k}\nabla\cdot k\right)+\varepsilon_g G_k-\varepsilon_g\rho_g\epsilon \tag{3.38}$$

and

$$\frac{\partial\left(\varepsilon_g\rho_g \epsilon\right)}{\partial t}+\nabla\cdot\left(\varepsilon_g\rho_g \upsilon_i \epsilon\right)=\nabla\cdot\varepsilon_g\left(\mu_{g_l}+\frac{\mu_{g_t}}{\sigma_\epsilon}\nabla\cdot\epsilon\right)+\frac{\varepsilon_g\epsilon}{k}\left(C_{\epsilon_1}G_k-C_{\epsilon_2}\rho_g\epsilon\right) \tag{3.39}$$

where

$$\mu_{g_t}=\rho_g C_\mu\frac{k^2}{\epsilon}. \tag{3.40}$$

Equation 3.40 defines the gaseous turbulence viscosity which was required previously in Equation 3.26 to determine the gaseous shear viscosites. The model constants are taken from Launder and Spalding [136] to be $C_{\epsilon_1}=1.44$, $C_{\epsilon_2}=1.92$ and $C_\mu=0.09$, whilst the turbulent Prandtl numbers for k and ϵ are $\sigma_k=1.0$ and $\sigma_\epsilon=1.3$, respectively. G_k represents the generation of turbulent kinetic energy due to the mean velocity gradients and is represented by:

$$G_k=-\rho_g\overline{\upsilon_i'\upsilon_j'}\frac{\partial\upsilon_j}{\partial x_i}, \tag{3.41}$$

where

$$-\rho_g\overline{\upsilon_i'\upsilon_j'}=\mu_{g_t}\left(\frac{\partial\upsilon_i}{\partial x_j}+\frac{\partial\upsilon_j}{\partial x_i}\right)-\frac{2}{3}\rho_g k\delta_{ij}. \tag{3.42}$$

3.2 Heat transfer modelling

3.2.1 Heat transfer coefficients

For multiple phases, the interphase heat-transfer coefficient, h_{gs}, which is used in Equation 3.37, is related to the Nusselt number, Nu_s, as it is the product of the specific surface area and the interfacial heat transfer coefficient:

$$h_{gs}=\frac{6\lambda_g\varepsilon_g\varepsilon_s Nu_p}{d_p^2} \tag{3.43}$$

An empirical relation for the interphase heat transfer coefficient was proposed by Gunn [102] which relates the Nusselt number with the particle Reynolds and Prandtl number:

$$\begin{aligned}Nu_s=&(7-10\varepsilon_g+5\varepsilon_g^2)[1+0.7(Re_p)^{0.2}(Pr)^{1/3}]\\&+(1.33-2.40\varepsilon_g+1.20\varepsilon_g^2)(Re_p)^{0.2}(Pr)^{1/3}\end{aligned} \tag{3.44}$$

where the Reynolds number, Re, is calculated as of Equation A.1 and the gas phase Prandtl number, Pr, is calculated as follows:

$$Pr = \frac{C_{p,g}\mu_g}{\lambda_g} \tag{3.45}$$

3.2.2 Thermal conductivities

As discussed previously in Section 2.3, the thermal conductivities of both the gaseous and solid phases are dependent on the local porosity as well as the thermal properties of both phases, λ_g and λ_s. The effective thermal conductivities for the gaseous phase was developed by Zehner and Schlünder [96] and later adopted by Kuipers et al. [95] and is given by:

$$\lambda_g^{eff} = \left(\frac{1-\sqrt{\varepsilon_s}}{\varepsilon_g}\right)\lambda_g. \tag{3.46}$$

Natarajan and Hunt [98] expressed the effective thermal conductivity of the solids phase as the sum of the internal molecular conductivity and the particle kinetic conductivity:

$$\lambda_s^{eff} = \lambda_s^{mol} + \lambda_s^{kin}. \tag{3.47}$$

An effective solid thermal conductivity was also developed by Zehner and Schlünder [96] who suggested that the molecular conductivity of spherical particles takes the form:

$$\lambda_s^{mol} = \frac{1}{\sqrt{\varepsilon_s}}\,\lambda_g\left[\omega A + (1-\omega)\,\Gamma\right] \tag{3.48}$$

where

$$\Gamma = \frac{2}{\left(1-\frac{B}{A}\right)}\left[\frac{(A-1)}{\left(1-\frac{B}{A}\right)^2}\frac{B}{A}\ln\left(\frac{A}{B}\right) - \frac{(B-1)}{\left(1-\frac{B}{A}\right)} - \frac{B+1}{2}\right] \tag{3.49}$$

$A = \frac{\lambda_s}{\lambda_g}$

$B = 1.25\left(\frac{\varepsilon_s}{\varepsilon_g}\right)^{10/9}$

$\omega = 7.26\text{x}10^{-3}$

Hunt [99] derived an expression for the kinetic contribution as a function of granular temperature. It considers the solid kinetic conductivity as the rate of thermal energy which is transported due to the fluctuating motion of particles.

$$\lambda_s^{kin} = \rho_s C_p d_p \sqrt{\Theta_s}\frac{\pi^{3/2}}{32 g_o} \tag{3.50}$$

3.2.3 Porosity modelling

The effective thermal conductivies, λ_g^{eff} and λ_s^{eff} require information about the bulk porosity, ε_g, however in the near wall region, where the scale is in the order of particle diameters, the porosity is dependent on the diameter of the particles and the distance from the wall. Therefore the bulk porosity would not correctly represent the porosity distribution in this near wall region.

Patil et al. [97] modified a model produced by Martin [101] to consider the variation in voidage near a wall in a fluidised bed compared to the previously used packed beds. Fluidised beds display a higher bulk porosity, and hence near-wall, porosities therefore the model was developed to account for this. The effective gas porosity determined from the model is then utilised in the thermal conductivities above. The porosity distribution is given by:

$$\varepsilon_g = \begin{cases} 1.26\varepsilon_g^{bulk} - 0.26 + 1.26\left(1-\varepsilon_g^{bulk}\right)\left(\frac{2x}{d_p}-1\right)^2 & \left(0 \le \frac{x}{d_p} \le \frac{1}{2}\right) \\ \varepsilon_g^{bulk} + 0.26\left(\varepsilon_g^{bulk}-1\right)\exp\left(\frac{1}{4}-\frac{x}{2\,d_p}\right)\cos\left(\frac{2x}{d_p}\frac{\pi}{c}-\frac{\pi}{c}\right)^2 & \left(\frac{x}{d_p} \ge \frac{1}{2}\right) \end{cases} \tag{3.51}$$

where

$$\begin{aligned} \varepsilon_g^{bulk} &= 0.39 \\ c &= 0.816 \end{aligned}$$

3.3 Reaction modelling

3.3.1 Species transport

The mass fraction of each species in a phase, Y_i, is determined from the conservation equation of species transport as follows:

$$\frac{\partial}{\partial t}\left(\varepsilon_g \rho_g Y_i\right) + \nabla\left(\varepsilon_g \rho_g \vec{v}_g Y_i\right) = -\nabla \cdot \varepsilon_g J_i + \varepsilon R_{g,i} + R_{s,i}. \tag{3.52}$$

J_i is the diffusion flux of the individual species, i, as a result of concentration gradients and is calculated using the modified Fick's law for the diffusion flux of chemical species in turbulent flow. The turbulent Schmidt number, Sc_t, is set to 0.7, and $D_{m,i}$ is the mixture diffusion coefficients:

$$J_i = -\left(\rho_g D_{m,i} + \frac{\mu_t}{Sc_t}\right)\nabla Y_i \tag{3.53}$$

where

$$D_{m,i} = \frac{1 - X_i}{\Sigma_{j \neq i} \frac{X_j}{D_{i,j}}}. \tag{3.54}$$

The second and third terms on the right hand side of (3.52) represent the rate of production of species, i, due to the homogeneous reactions between gaseous species and heterogeneous reactions between gas and solid species, respectively.

3.3.2 Devolatilisation modelling

During the devolatilisation process, the coal phase breaks down into a char phase whilst the gaseous volatiles are released:

$$\text{Coal} \rightarrow \text{Volatile} + \text{Char} \tag{3.55}$$

$$\text{Volatile} \rightarrow a_1\text{CO}_2 + a_2\text{CO} + a_3\text{CH}_4 + a_4\text{H}_2 + a_5\text{H}_2\text{O} + a_6\text{Tar} \tag{3.56}$$

The yield of the volatile products released is determined using correlations developed by Loison and Chauvin [122] which estimates the important gaseous products based on the proximate analysis of the coal. The proximate and ultimate analysis of the coal used the present work is given in Section 6 which gives details of the reaction model set up. The yields are calculated as follows:

$$Y_{\text{CO}_2} = 0.135 - 0.900Y_{\text{volatile(daf)}} + 1.906Y^2_{\text{volatile(daf)}}, \tag{3.57}$$

$$Y_{\text{CO}} = 0.428 - 2.653Y_{\text{volatile(daf)}} + 4.845Y^2_{\text{volatile(daf)}}, \tag{3.58}$$

$$Y_{\text{CH}_4} = 0.201 - 0.469Y_{\text{volatile(daf)}} + 0.241Y^2_{\text{volatile(daf)}}, \tag{3.59}$$

$$Y_{\text{H}_2} = 0.157 - 0.868Y_{\text{volatile(daf)}} + 1.388Y^2_{\text{volatile(daf)}}, \tag{3.60}$$

$$Y_{\text{H}_2\text{O}} = 0.409 - 2.389Y_{\text{volatile(daf)}} + 4.554Y^2_{\text{volatile(daf)}}, \tag{3.61}$$

$$Y_{\text{Tar}} = -0.325 + 7.279Y_{\text{volatile(daf)}} - 12.880Y^2_{\text{volatile(daf)}}. \tag{3.62}$$

Badzioch and Hawksley [119] developed a single rate model which assumes the rate of the volatile release to be first-order dependent based on the amount of volatiles remaining in the coal. The model releases char and volatiles as follows:

$$\text{Coal} \xrightarrow{k} \text{Char} + \text{Volatile} \tag{3.63}$$

and the kinetic rate follows the Arrhenius equation,

$$k = A\text{exp}\left(\frac{-E}{RT_p}\right), \tag{3.64}$$

where the pre-exponential factor is $A = 4.92\text{x}10^5$ s^{-1} and the activation energy is $E = 7.4\text{x}10^4$ J/mol.

TABLE 3.1: Heterogeneous reactions with their kinetic rates.

	Reaction	Kinetic Rate	Units
R1	$C + O_2 \rightarrow CO_2$	$K_{Arr_1} = 1.04\text{x}10^5 T_c \exp\left(\frac{-11200}{T_c}\right)$	kg/m^{3}s
R2	$C + H_2O \rightarrow CO + H_2$	$K_{Arr_2} = 342 T_c \exp\left(\frac{-15600}{T_c}\right)$	kg/m^{3}s
R3	$C + CO_2 \rightarrow 2CO$	$K_{Arr_3} = 342 T_c \exp\left(\frac{-15600}{T_c}\right)$	kg/m^{3}s
R4	$C + 2H_2 \rightarrow CH_4$	$K_{Arr_4} = 0.342 \exp\left(\frac{-15600}{T_c}\right)$	kg/m^{3}s

The Kobayashi two-equation method [137] instantaneously handles the devolatilisation of coal and volatiles release:

$$\text{Coal} \begin{cases} \overset{k_1}{\nearrow} & (1 - Z_1)\, S_1 + Z_1 V_1, \\ \overset{k_2}{\searrow} & (1 - Z_2)\, S_2 + Z_2 V_2, \end{cases} \tag{3.65}$$

$$k_i = A_i \exp\left(\frac{-E_i}{R T_p}\right). \tag{3.66}$$

S_i represents the char that is unreacted, V_i is the volatile produced and the yield factors are given by Z_i. Kobayashi et al. [137] recommends that Z_1 be set to the fraction of volatiles determined by the proximate analysis as it represents devolatilisation at lower temperatures. Z_2 should be set close to unity as it is the yield of volatiles at high temperatures. The rate constants k_1 and k_2 are given in Arrhenius form where A_1 =2x10^5 s^{-1}, A_2 =1.3x10^7 s^{-1}, E_1 =1.046x10^5 J/mol, E_2 =1.67x10^5 J/mol, Z_1 = 0.418, $Z_2 = 1.0$ and R is the universal gas constant, 8.314472 J/mol K.

3.3.3 Heterogeneous reactions

Heterogeneous reactions take place between the char and the surrounding gases. The char combustion between the char and O_2 takes place very quickly. The reactions take place on the external surface of the particles therefore models have been created that

consider the kinetic and the diffusive rate constants as follows:

$$R_C = \left((K_{Arr})^{-1} + (K_{Dif})^{-1} \right) C_{O_2} \tag{3.67}$$

$$K_{Arr} = A T_s^n exp\left(\frac{E}{RT_s} \right) \tag{3.68}$$

$$K_{Dif} = \frac{ShD_{gs} w_C}{RT_s d_s} \tag{3.69}$$

$$Sh = 2.0 + 0.6 Re^{1/2} Pr^{1/3} \tag{3.70}$$

$$D_{gs} = \frac{8.34\text{x}10^{-6} T^{1.75}}{p} \tag{3.71}$$

where Sh and D_{gs} are the Sherwood number and diffusion coefficient for the gas, respectively.

The gasification heterogeneous reactions take place much slower than the combustion reaction and have a longer residence time within the bed. The diffusion of the reactants into the char is not dominated by the external surface reactions as seen in combustion therefore such diffusive reactions need not be considered:

$$R_C = K_{Arr}[C_g]. \tag{3.72}$$

The kinetic rates are taken from the literature [129, 138] and are provided in 3.1.

3.3.4 Homogeneous reactions

The homogeneous reactions within the gaseous phase consider the effects of the turbulent flow and chemical reactions. The Arrhenius kinetic rate and the eddy-dissipation rate [139] are calculated using the finite-rate/eddy-dissipation model which takes the minimum of the two rates to be the net reaction rate depending on whether the kinetic rate is dominating the local reactions or if turbulent mixing is dominating:

$$R_{i,r} = min\left(R_{Arr}, R_{Edd}\right), \tag{3.73}$$

$$R_{Arr} = k_a T^z C_A^n C_B^m, \tag{3.74}$$

$$R_{Edd} = 4.0 v'_{i,r} w_i \rho_g \frac{\epsilon}{k} \min\left[\min_R \left(\frac{Y_R}{v'_{R,r} w_R} \right), \frac{\Sigma_P Y_P}{2\Sigma_j^N v''_{j,r} w_j} \right]. \tag{3.75}$$

The homogeneous reactions with their kinetic rates [104, 108] are provided in 3.2.

3.3.5 Limestone calcination

Limestone calcination is the breakdown of limestone, $CaCO_3$, into calcium oxide, CaO, and carbon dioxide, CO_2. The reaction and the kinetic reaction rate (Pa^{-1} s^{-1})[104,

TABLE 3.2: Homogeneous reactions with their kinetic rates.

	Reaction	Kinetic Rate	Units
R5	$CO + 0.5O_2 \rightarrow CO_2$	$K_1 = 1.0\text{x}10^{15}\exp\left(\frac{-16000}{T_g}\right) C_{CO} C_{O_2}^{0.5} \rho_g^{1.5}$	kg/m^{3}s
R6	$H_2 + 0.5O_2 \rightarrow H_2O$	$K_2 = 5.159\text{x}10^{15}\exp\left(\frac{-3430}{T_g}\right) T^{-1.5} C_{H_2}^{1.5} C_{O_2} \rho_g^{2.5}$	kg/m^{3}s
R7	$CH_4 + 2O_2 \rightarrow 2H_2O + CO_2$	$K_3 = 3.552\text{x}10^{14}\exp\left(\frac{-15700}{T_g}\right) T^{-1} C_{CH_4} C_{O_2} \rho_g^2$	kg/m^{3}s
R8	$CO + H_2O \Leftrightarrow H_2 + CO_2$	$K_4 = 2780\exp\left(\frac{-1510}{T_g}\right)\left[C_{CO} C_{H_2O} - \frac{C_{CO_2} C_{H_2}}{0.0265\exp\left(3968/T_g\right)}\right]$	kg/m^{3}s

140, 141] for the limestone calcination are given by:

$$CaCO_3 \overset{k_{cal}}{\rightarrow} CaO + CO_2 \tag{3.76}$$

and

$$k_{cal} = \frac{3.07\text{x}10^{11}}{3.336\text{x}10^7 p \exp\left(-20269/T_l\right)} \exp\left(\frac{-24670}{T_l}\right). \tag{3.77}$$

The CaO is the active solid that absorbs SO_2 producing $CaSO_4$:

$$2CaO + 2SO_2 + O_2 \rightarrow 2CaSO_4; \tag{3.78}$$

however, due to the low amount of sulphur within the coal, the present model does not account for its presence in the chemical processes.

3.3.6 Wood gasification

Although the primary purpose of this study is the gasification of coal, the model is modified to incorporate a biomass model to determine the effects of fuel variation. The biomass model considered in the present work uses the primary step modelling of Thurner and Mann [142] which has been applied previously by Grϕnli and Melaan [143], Larfeldt et al. [144] and Gerber et al. [114]. The primary step considers the degradation of wood into three components, namely gases, tar and char. The kinetic reactions use the standard Arrhenius form taken from Equation 3.66:

$$\text{Wood} \begin{cases} \overset{k_1}{\nearrow} & \text{Gases} \\ \overset{k_2}{\longrightarrow} & \text{Tar} \\ \overset{k_3}{\searrow} & \text{Char.} \end{cases} \tag{3.79}$$

The mass fraction composition of the gaseous products released are taken from the experimental works of Seebauer [145]. The gaseous compositions and the kinetic parameters for the different models are given in Table 3.3.

TABLE 3.3: Kinetic parameters for the biomass model along with the composition of the products released after each reaction.

Reaction Kinetics			**Mass fraction of products**						
$\mathbf{k}_i$	$\mathbf{A}_i$ (1/s)	$\mathbf{E}_i$ (J/mol)	$\mathbf{CO_2}$	**CO**	$\mathbf{CH_4}$	$\mathbf{H_2}$	$\mathbf{H_2O}$	**Char**	**Tar**
k_1	1.43x10^4	88600	0.386	0.270	0.056	0.032	0.256	-	-
k_2	4.13x10^6	112700	-	-	-	-	-	-	1
k_3	7.38x10^5	106500	-	-	-	-	-	1	-

3.4 Boundary conditions

In order to solve the equations for granular flows there needs to be appropriate boundary conditions. For an impermeable wall, a no-slip boundary condition would be given for the gaseous phase however the solids phase would require different boundary conditions for the velocity and granular temperature of the particles. The solid phase velocity component normal to the wall is set to zero but the particles are allowed to slip along the wall. Johnson and Jackson [146] developed a model introducing the specularity coefficient, which quantifies the nature of the particle-wall collisions based on whether the walls are smooth and frictionless, $\varphi = 0$, or very rough, $\varphi = 0$:

$$\vec{u}_{s,w} = -\frac{6\mu_s\varepsilon_{s,max}}{\sqrt{3}\sqrt{\theta}\pi\varphi\rho_s\varepsilon_s g_0}\frac{\partial\vec{v}_{s,w}}{\partial n}. \tag{3.80}$$

The granular temperature is found by equating the granular temperature flux to the wall and the generation of granular temperature at the wall to the energy dissipation due to particle-wall collisions.

$$\theta_w = -\frac{k\theta}{\gamma_w}\frac{\partial\theta}{\partial n} + \frac{\sqrt{3}\pi\varphi\rho_s\varepsilon_s g_0\vec{v}^2_{s,slip}\theta^{\frac{3}{2}}}{6\gamma_w\varepsilon_{s,max}}, \tag{3.81}$$

where

$$\gamma_w = \frac{\sqrt{3}\pi\left(1-e_w^2\right)\varepsilon_s\rho_s g_0\theta^{\frac{3}{2}}}{4\varepsilon_{s,max}}. \tag{3.82}$$

Chapter 4

Gas-Solid Flow Dynamics

This chapter looks at the gas-solid flow dynamics in both bubbling and circulating fluidised beds. The first section carries out a parameter study on a bubbling fluidised bed which also covers the transition from a bubbling, turbulent regime to a circulating regime whereas the second section focuses solely on a fast fluidised regime in a circulating fluidised bed taken from the literature [2]. Variations in the gas velocity and particle diameters are tested to determine their influence on the flow dynamics whilst different model parameters are varied and compared to determine their effects on the models, i.e., drag models, coefficient of restitution and specularity coefficients. Finally, conclusions are drawn based on the results discussed in this chapter. The work carried out in this chapter was published previously in the Chemical Engineering Journal [11].

4.1 Bubbling fluidised beds

The reactor used for the bubbling fluidised bed is the same as that used for the circulating bed in Section 4.2. The reactor is based on the experimental set up given by Samuelsberg and Hjertager [2] and a schematic diagram is given in Fig. 4.1. In the experiment, the root mean square velocities of the particles were taken at three heights, 0.16 m, 0.32 m and 0.48 m in the reactor using laser doppler anemometry (LDA) technology, which measures the direction and speed of the particles in the air. The introduction of a gas exceeding the terminal velocity, would carry the particles up the reactor and into the cyclone. Exhaust gases would exit through the top of the cyclone whilst particles would descend down the downpipe where they are re-introduced back into the reactor, hence completing the cycle.

An initial static bed height of 0.05 m was set for the particles with the secondary air inlet position at the same height. This secondary inlet forces circulating particles back into the reactor with a low constant velocity, set at 0.05 m/s, thus preventing particle build up

in the tube. The particles utilised in the experiment were fluid catalytic cracking (FCC) particles which are widely used in petroleum refineries for the conversion of petroleum crude oils into more valuable products such as gasoline. The particles had a density of 1600 kg/m^3 and a diameter range of 20 μm - 150 μm with the mean diameter taken to be 60 μm. Two superficial gas velocities, 0.71 m/s and 1.42 m/s, were introduced through the primary inlet at an ambient temperature.

For the bubbling fluidised bed model, the focus of this section only, the secondary air inlet is neglected and assumed to be covered up to prevent lose of particles from the riser and to ensure a single gas supply from the primary inlet below the bed. Since the transition from a bubbling to fast fluidising regime is the primary focus of this section of work, the simulations concentrate only on the lower 0.5 m section of the riser where the majority of the bubbling behaviour takes place thus reducing the number of unnecessary cells and hence the computational time.

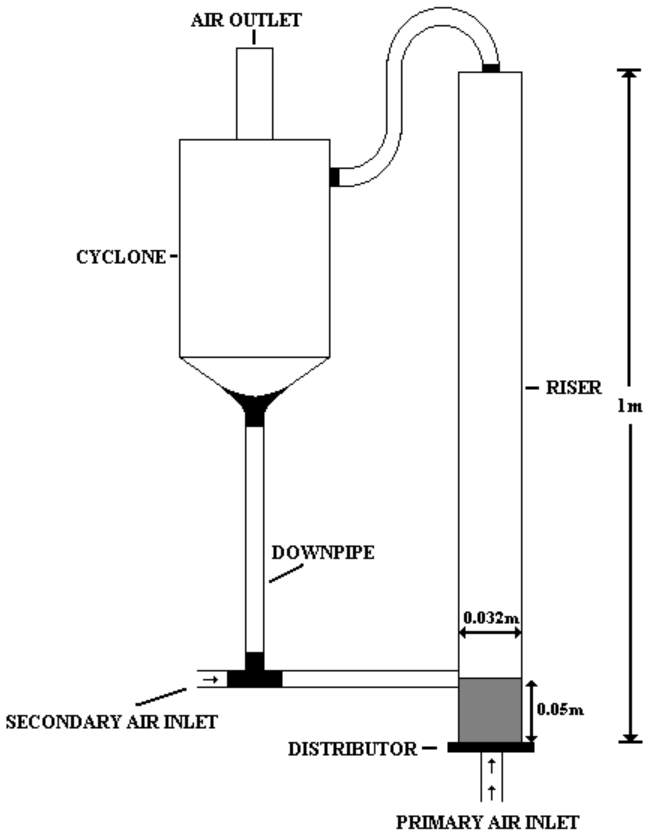

FIGURE 4.1: Sketch of the laboratory scale circulating fluidised bed used in the bubbling and circulating fluidised bed work [2].

TABLE 4.1: Table of Parameters for the bubbling and circulating fluidised bed.

Gas			Units
υ_g	Velocity	0.06-1.42	m/s
ρ_g	Density	1.225	kg/m^3
μ_g	Shear viscosity	1.79x10^{-5}	kg/m s
Particles			
d_p	Particle diameter	40, 60, 80	μm
ρ_p	Particle density	1600	kg/m^3
e	Particle coef. of restitution	0.95	
e_w	Wall coef. of restitution	0.95	
φ	Specularity coefficient	0.25	

4.1.1 Mesh generation

The 2D mesh used for the bubbling fluidised bed reactor contains 18732 cells with cell sizes set to 0.001 m. In order to capture the complex flow behaviours at the walls, the nodes in the radial direction were non-uniformly distributed such that a more refined grid, set to a minimum of 0.0005 m, could accurately model the downflow behaviour within these regions. As previously mention, the secondary inlet is not present in the bubbling bed simulations as the transition from bubbling to fast fluidisation is the main objective therefore the mesh contains only the primary inlet, the riser and a pressure outlet set 0.5 m above the inlet. The 3D mesh contains 733821 cells of width 0.002 m and a height of 0.005 m with a refined mesh at the walls of 0.00075 m to capture the near-wall particle behaviours. The parameters utilised in both the bubbling and circulating beds are given in Table 4.1.

4.1.2 Bubbling characteristics

Figure 4.2 displays the contour plots of the particle volume fraction distribution comparing the Gidaspow and Syamlal-O'Brien drag models at 9.0 s with an inlet velocity of 0.16 m/s. A line graph of the particle volume fraction up the center line of the reactor is also displayed. Both drag models show a bed expansion height around 0.28-0.3 m. The slight increase in volume fraction above this range which can be seen in the Syamlal-O'Brien model is due to the presence of a large voidage along the left wall which will erupt releasing particle spray into the freeboard.

In both models it can be seen that the bubbles appear larger towards the top of the bed due to coalescence of smaller rising voidages. The particle volume fractions towards the top of the reactor appears more dilute compared to lower regions of the bed. This is emphasised in the line graph where the higher particle concentrations reside at the base decreasing with height. This is due to the compromising behaviour of the two phases,

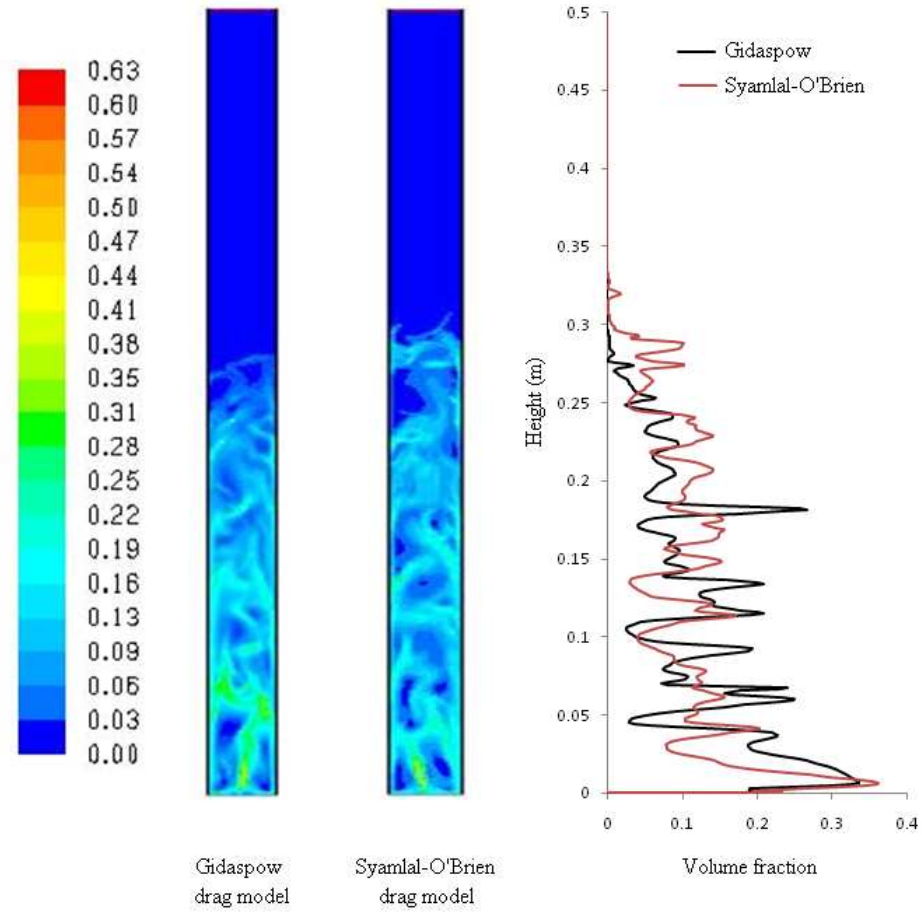

FIGURE 4.2: Contour plots and centre line graph comparing the volume fraction of particles within the lower 0.5 m of the bed for the Gidaspow and Syamlal-O'Brien drag models with velocity 0.16 m/s.

i.e., the air rises whilst the denser particles descend down to the base. This leads to a larger collection of particles at the base of the reactor.

The heterogeneous flow distribution and positioning of the bubbles within the bed leads to the fluctuating particle volume fraction observed in the line graph in Fig. 4.2. The fluctuations decrease with increasing height for both models where the lower regions of the beds hold regions of strong particle collections amongst small dilute bubbles. As bubble coalescence takes place the particles become more evenly dispersed within the bubbles, reducing the opportunity of particle agglomeration which results in smaller fluctuations between the dense regions and voidages with increasing height.

The contour plots in Fig. 4.2 display higher particle volume fractions along the walls compared to the core region. This is due to the segregative tendencies of the particles towards the walls; where they can descend back down towards the base of the reactor without too much resistance from the ascending gas flow.

4.1.3 Effects of inlet velocities

The volume fraction distribution for the particles using the Gidaspow model with four inlet velocities, i.e., 0.1 m/s, 0.16 m/s, 0.18 m/s and 0.36 m/s, are shown in Fig. 4.3(a-d) for particles with a diameter of 60 μm. The terminal velocity, V_t, for particles with a diameter of 60 μm, is 0.175 m/s so inlet velocities were chosen to capture the behaviour of the particles below and above V_t. Although the terminal velocity applies to single particles in suspension, the bursting-bubbles at the top of the particle bed release a small number of particles above the bed where they are effectively suspended. If the gas velocity does not exceed V_t the particles fall back down to the particle bed. This is referred to as a bubbling bed and is displayed in Fig. 4.3 (a)(b). Exceeding V_t means the suspended particles can be carried with the gas phase and continue up the riser. This fast fluidisation state can be seen in Fig. 4.3 (c)(d).

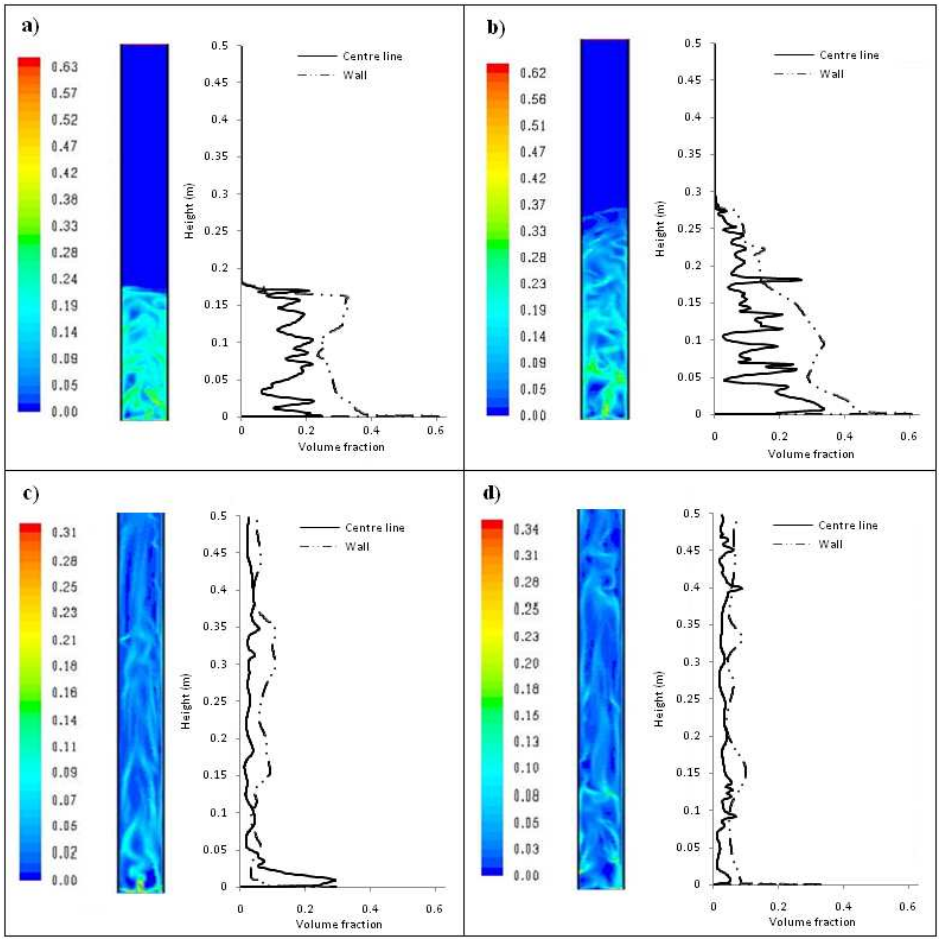

FIGURE 4.3: Particle volume fraction at 9.0s for a range of velocities above and below the terminal velocity. For $d_p = 60$ μm: a) V = 0.1 m/s, b) V = 0.16 m/s, c) V = 0.18 m/s and d) V = 0.36 m/s.

The bed height expansions for the bubbling fluidised states are approximately 0.16 m and 0.3 m for 0.1 m/s and 0.16 m/s, respectively. Their contour plots show bubbles

appear smaller with a more regular shape near the entrance of the riser, increasing in size and distorting with increasing height. As observed in the previous section, this is due to the coalescence of the bubbles with smaller bubbles rising from the base of the reactor. As the velocity increases, the bubble sizes increase and the solid-gas mixture appears more dilute particularly towards the top of the bed. The solids descend to the base of the reactor as the solids and gas compromise. The solids segregate towards the walls which is clearly seen in the line graphs in Fig. 4.3 (a)(b) where the volume fraction against the right walls are significantly higher than in the centre of the reactor.

The fast fluidising states in Fig. 4.3 (c)(d) show very dilute distributions in comparison to the bubbling models. The fluctuations indicating a change from a region of high to low particle volume fraction within the core are less pronounced in the fast fluidising state due to the solids being carried with the flow and more evenly dispersed compared to that in bubbling beds. The volume fraction against the wall remains slightly higher than the core again due to particle segregation.

The lower fast fluidising velocity, 0.18 m/s, shows a higher accumulation of particles nearer the inlet compared to the higher gas velocity of 0.36 m/s. As particles accumulate and denser regions are formed in lower regions of the bed. The local gases are not strong enough to carry a collection of particles with the flow compared to single particles and since the introduced gas in Fig. 4.3 (c) is only slightly higher than the terminal velocity then more agglomeration will take place. Increasing the gas velocity allows for a faster flow of gas to push the collection particles higher up the bed.

4.1.4 Variation in coefficient of restitution

A number of coefficient of restitutions are compared for the Gidaspow model at two velocities 0.1 m/s and 0.16 m/s, i.e., in the bubbling regime. Figure 4.4 and Fig. 4.5 shows the volume fraction of the particles in the centre and against the right wall of the reactor for the inlet velocity 0.1 m/s and 0.16 m/s with a coefficient of restitution of 0.9, 0.95, 0.98 at time 9.0s. A linear line of best fit is provided to show the general trend of the volume fractions at different heights.

The line graphs in Fig. 4.4 and Fig. 4.5 for all three coefficient of restitutions display a higher volume fraction at lower heights which decreases with height. The results within the centre of the reactor for all three coefficients of restitution and both velocities show strong fluctuations from high to low particle volume fraction regions. These fluctuations reduce with height as the particles disperse due to the mixing behaviour and larger bubbles. For both velocities, the model set with a coefficient of restitution of 0.98 shows a steeper incline in particle volume fractions in the centre of the reactor. Furthermore, the lower region of the beds contain a lower particle volume fraction compared with the remaining coefficient of restitution models whilst above the bed it appears to be higher.

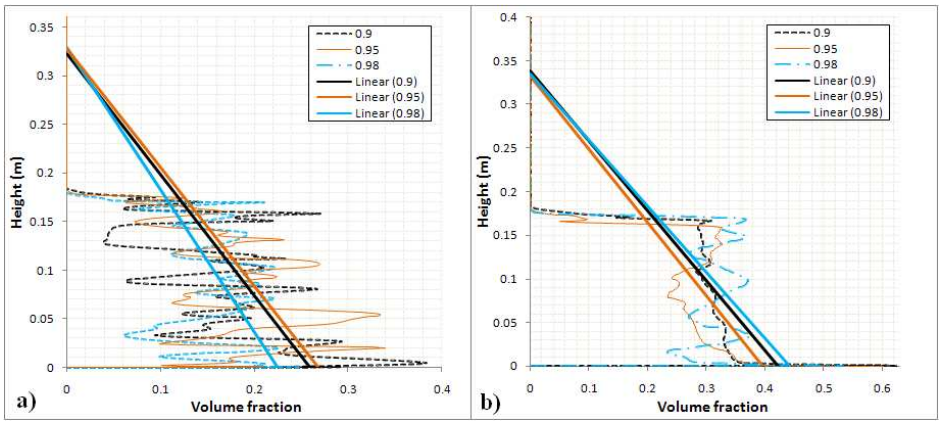

FIGURE 4.4: Variation in coefficient of restitution for velocity 0.1 m/s a) going up the centre line and b) going up the right wall.

This would indicate there in a decrease in the build up of dense particle regions near the base of the reactor compared to lower the coefficients of restitutions, whereas there is a slight increase in particle spray above the bed. This would be due to the conservation of energy during the collisions of particles with higher coefficient of restitutions leading to a more active behaviour of the particles.

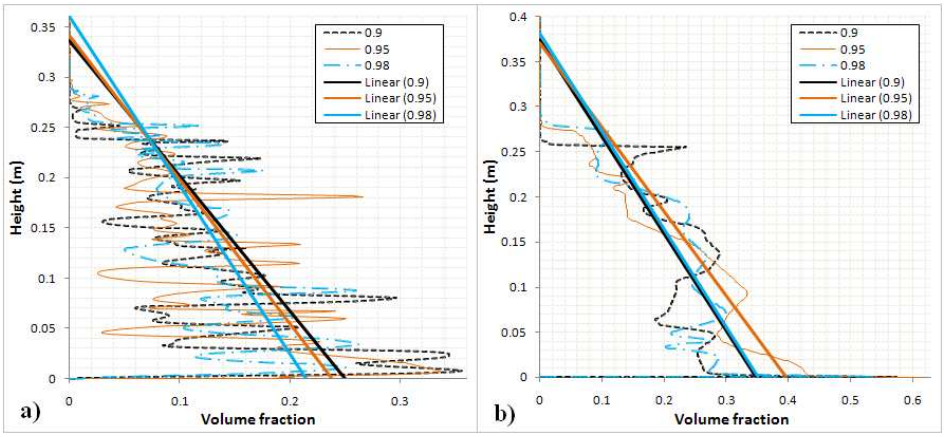

FIGURE 4.5: Variation in coefficient of restitution for velocity 0.16 m/s a) going up the centre line and b) going up the right wall.

The particle volume fractions at the wall are significantly higher than those in the core of the reactor whereas the fluctuating behaviour of the particle volume fractions are minimal in comparison. This confirms that particles segregate towards the wall and accumulate as indicated by the increase in particle volume fraction with descending height. Larger intervals of lower volume fractions can be seen at the wall, particularly with ascending height. This is due to the presence of large air bubbles near the wall which was observed previously in Fig. 4.3, and is due to the elongation of bubbles in the presence of the walls.

4.1.5 Effects of particle diameter

If the particle diameter changes then this results in a different terminal velocity, V_t, since the terminal velocity is dependent on particle diameter. The previous model was carried out using a particle diameter of 60 μm so an additional two diameters were simulated, 40 μm and 80 μm, using the Gidaspow drag model for a period of 9.0 s. The terminal velocities for particle diameters of 40 μm and 80 μm are 0.08 m/s and 0.31 m/s, respectively.

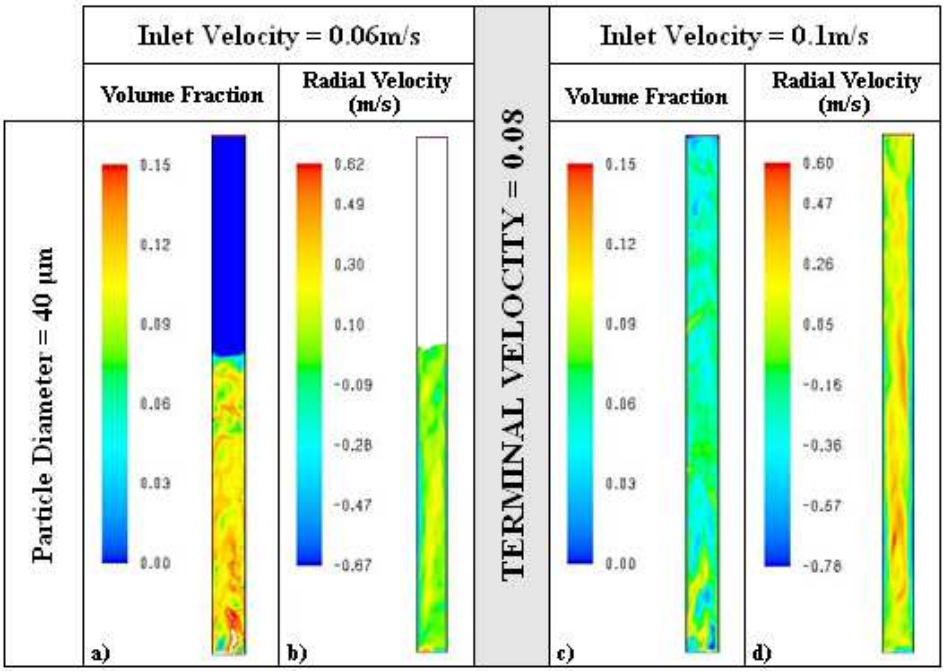

FIGURE 4.6: The particle volume fraction and particle velocity (m/s) from bubbling to fast fluidisation for a particle diameter of 40 μm at 9.0 s.

Figure 4.6 displays the particle volume fraction and particle velocity for the transition from bubbling to fast fluidisation for particle diameter, 40 μm. In both Fig. 4.6 (a) and (c), the maximum scale of the contour plot for the particle volume fraction is reduced to 0.15 from an optimal of 0.42 for a clearer observation hence, the white section in the base of the bubbling reactor (Fig. 4.6 (a)) represents a higher volume fraction than on the scale. The scale for the particle velocities, in Fig. 4.6 (b) and (d), indicates particles ascending the reactor with a positive velocity whereas particles descending the reactor with negative values.

The terminal velocity for a particle with a diameter of 40 μm is 0.08 m/s and the results show that an inlet velocity below this value displays a bubbling regime. The volume fraction results in Fig. 4.6 (a) show a significantly higher accumulation of particles in the lower region of the reactor, which was also observed previously in the 60 μm results, with more bubbles being present at the top of the bed. The velocity of the particles in

the bubbling regime are shown in Fig. 4.6 (b). As expected, the particles travel faster in the core of the bed whereas slower particles are seen descending the reactor near the walls. This explains the continual accumulation of particles near the inlet.

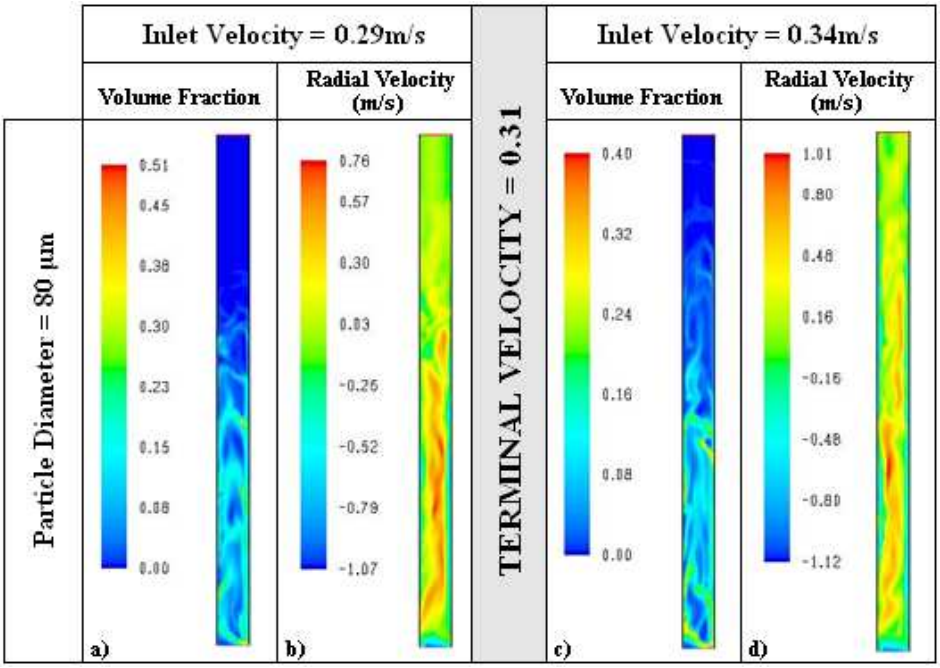

FIGURE 4.7: Contour plots of the volume fraction and vector plots of the radial velocity (m/s) from bubbling to fast fluidisation for particle diameter, 80 μm.

Increasing the particle diameter from 40 μm to 80 μm (Fig. 4.7 (a)) leads to an overall dilute distribution within the bed which would be due to the significant increase in bubble diameter. Furthermore, the bubbles show a clear increase in size with increasing height as coalescencing smaller bubbles form larger ones. The particle velocities in Fig. 4.7 (b) displays the presence of particle as high up as 0.5 m in the reactor. It can be explained by looking at the velocities of the particles within the core of the reactor which appear to be as high as 0.76 m/s. This is over twice as fast as the terminal velocity therefore the particles which are sprayed into the freeboard after bubble eruptions would continue to be influenced by this fast velocity which will carry them higher in the reactor. The velocities show the particles in the centre of the freeboard reducing in velocity with increasing height and, particularly against the walls, circle and descend back down towards the bed.

Above the terminal velocity, a fast fluidising regime is present where the particles continue to travel up through the reactor. The particle volume fraction in Fig. 4.6 (c) displays the typical dilute accumulation of particles at the base of the reactor whilst the top of the riser holds a very dilute dispersed particle distribution. The overall volume fraction is significantly lower in the fast fluidising regime compared to that observed in the bubbling regime. The particle velocities in Fig. 4.7 (d) displays the core-annulus

structure which is commonly observed in fast fluidising regimes where faster upward velocities are observed in the core of the reactor whilst descension is observed at the walls. In regions of low particle volume fraction, the upward velocities are higher since the gas prefers to travel through regions of least resistance, i.e., in the bubbles. Furthermore, the presence of particle build up against the walls leads to a reduction in the area for the gases to pass which leads to a faster gas velocity. Regions of high particle volume fraction have generally a lower velocity particularly at the walls due to increased resistance against the flow.

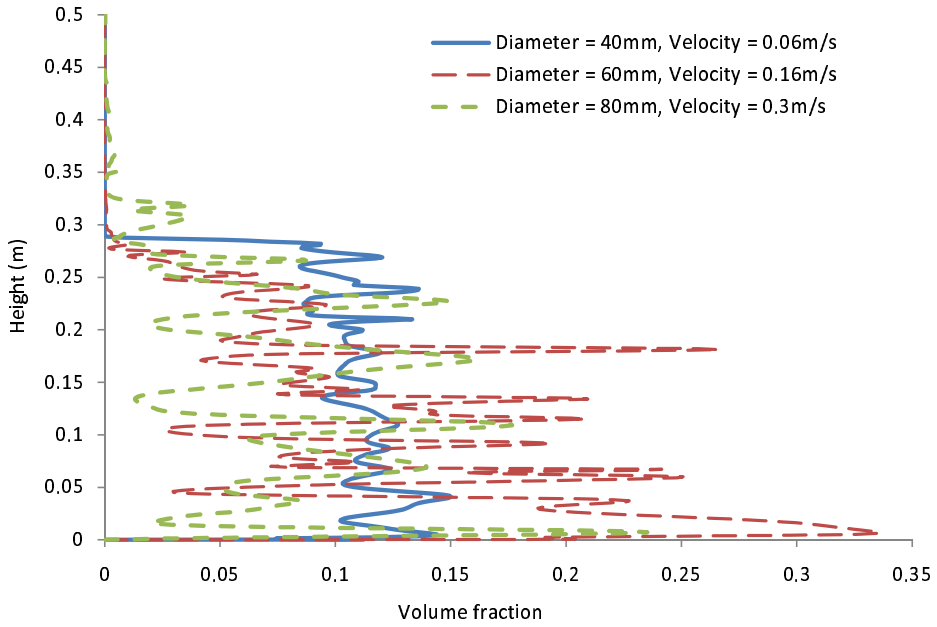

FIGURE 4.8: Volume fraction of particles up the centre of the reactor for different diameter particles in the bubbling regime.

Figure 4.8 displays the particle volume fraction up the centre of the reactor for the three diameter models with a bubbling regime. All three cases displays a clear distinction between the fluidising bed and the dilute region above the bed, i.e., the freeboard. The model with a particle diameter of 80 μm shows more clearly the effects of particle spray as a result of bubbles bursting at the top of the bed. Furthermore, the fluctuations are stronger yet less frequent in comparison to the 60 μm particles, thus indicating the bubbles are significantly larger. The fluctuations of the volume fraction for the 40 μm particles are minimal in comparison to the other two diameters suggesting that the rising air does not form large bubbles but disperses and travels through the bed between particles resulting in the overall dilution of the bed as was seen in Fig. 4.6 (a).

The particle volume fraction up the centre of the reactor is given in Fig. 4.9 for the fast fluidising regimes. Within the lower 0.3 m of the bed, the volume fraction for the 80 μm particles appears higher than the other diameters. This may be due to larger particles colliding more frequently at lower heights and since the terminal velocity does not apply

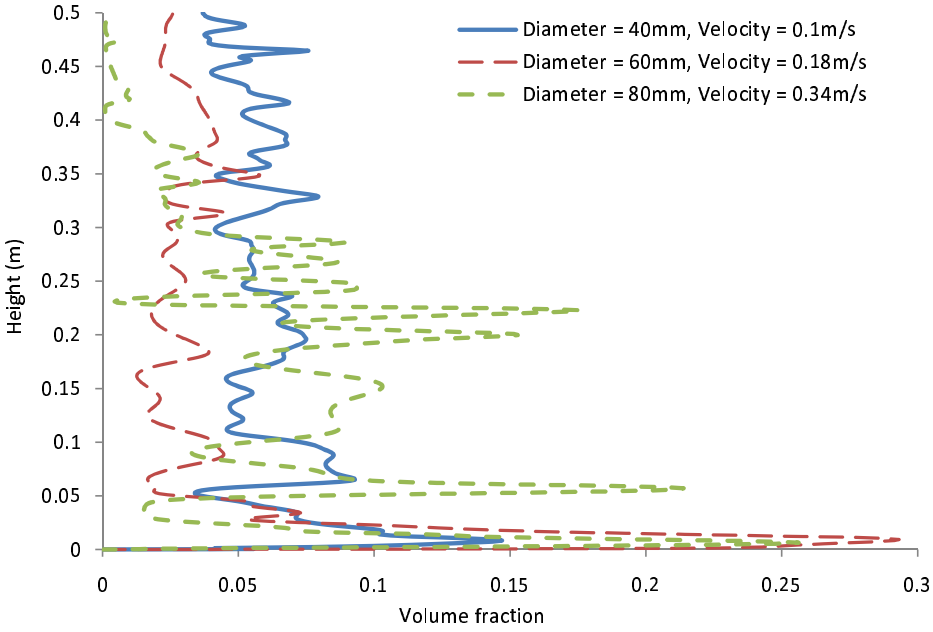

FIGURE 4.9: Volume fraction of particles up the centre of the reactor for different diameter particles in the fast fluidising regime.

to multiple particles in close proximity these would be found closer to the base of the reactor. Above 0.3 m however, the volume fraction is considerably lower than the other diameters due to the majority of particles being situated in the lower bed and those in the free board being more dispersed. The 40 μm particles have a higher volume fraction within the centre compared to the 60 μm particles which suggests more particles are traversing with the gas phase.

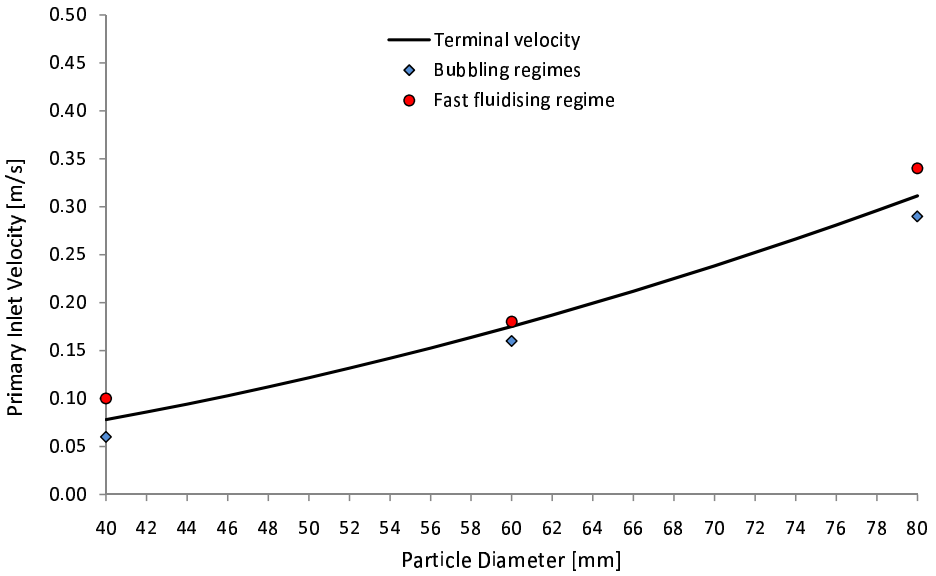

FIGURE 4.10: Fast fluidising regimes observed above the terminal velocity, V_t, and bubbling fluidised regimes below the V_t.

Overall an increase in particle diameter results in an increase in bubble size. Furthermore, simulations showed that increasing the gas velocity past the terminal velocity, V_t, resulted in a fast fluidising regime being seen whereas a velocity lower than this value displayed a bubbling fluidising regime which agrees with the theory. Figure 4.10 displays the graph of the terminal velocity for a range of diameters where the inlet velocities for the three diameter particles are plotted and coloured to show the fast fluidising regimes occurring above V_t and bubbling regimes lying below V_t.

It is worth highlighting that the mesh carried out within these models were generated for a 60 μm particles; of which a grid dependency test was carried out and will be discussed further in Section 4.2.1. Reducing the particle diameter would potentially lead to more particles accumulating within the cell which would reduce the accuracy. For simulations comparing different particle sizes it would be more beneficial to carry out a separate grid dependency test for each particle diameter. Furthermore, the results obtained are given at instantaneous times, however time averaging would give a more representative outlook of the results.

4.1.6 Three-dimensional bubbling fluidised beds

Three dimensional models were performed on three cases exhibiting a bubbling regime, i.e., case 1: $d_p = 40$ μm with V = 0.06 m/s, case 2: $d_p = 60$ μm with V = 0.16 m/s and case 3: $d_p = 80$ μm with V = 0.29 m/s. Figure 4.11 shows a slice taken in the XY plane (Z=0) for all three cases up to the height 0.3 m above the distributor. Five slices were also taken in the XZ plane at different heights depending on the height of the bed in the specific case. As mentioned previously in Section 4.1.1 the three-dimensional mesh was coarser than the two-dimensional mesh to reduce the computational time.

The results for case 1, shown in Fig. 4.11 (a), shows the bed height is approximately 0.12 m. This is much lower than that observed in the two-dimensional models which showed a bed height of approximately 0.28m in Fig. 4.8. This could be due to the spatial advantage 3D modelling has over 2D models as two-dimensional models allow particles to move in unrealistic limited directions whereas in 3D modelling the particles could travel in any direction and consequently affecting the flow dynamics which could lead lower bed heights. However, it is likely that this could be due to the loss of accuracy from using such a coarse grid with such fine particle diameters. It is worth highlighting that the three-dimensional mesh is twice as coarse as the two-dimensional model in the x-direction whereas it is five times coarser in the y-direction thus greatly increasing the number of particles per cell. This would also be the case in Figure 4.11 (b) shows the results for case 2 where the bed shows the bed height is approximately 0.17 m which again is highly underpredicted. The results for case 3 are shown in Fig. 4.11 (c) and displays a bed height of approximately 0.26 m which is similar to that obtained in the

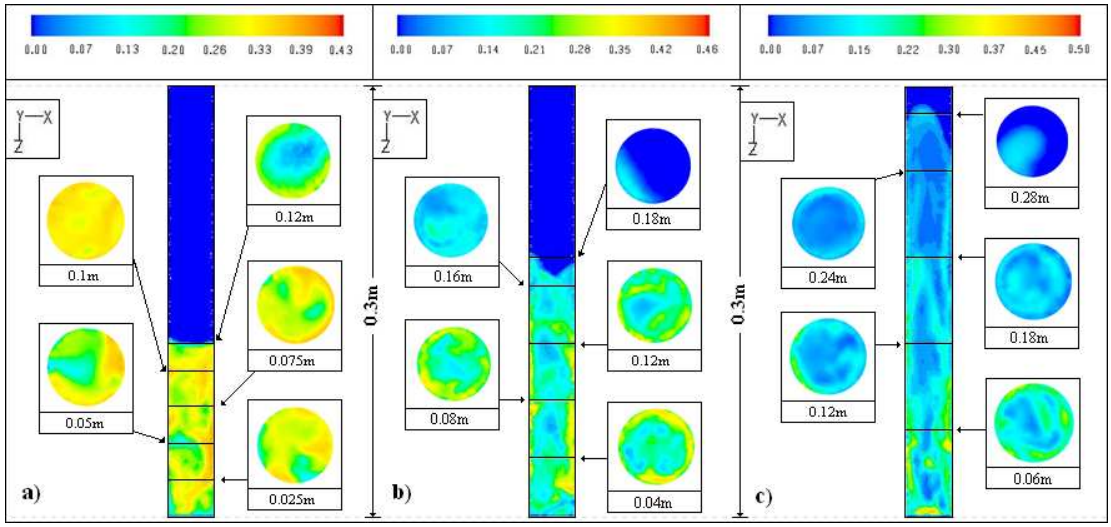

FIGURE 4.11: Contour plots of volume fraction taken through the centre of the reactor and horizontal slices across the reactor at different heights for three cases. a): $d_p = 40$ μm with V = 0.06 m/s, b): $d_p = 60$ μm with V = 0.16 m/s and c): $d_p = 80$ μm with V = 0.29 m/s.

two-dimensional models. This could be due to the particles being larger therefore less would be present in a cell compared to smaller particles.

The horizontal slices were taken at heights 0.025 m, 0.05 m, 0.075 m, 0.1 m and 0.12 m for case 1 showing higher particle volume fractions overall compared to the other two cases. The core-annulus structure can be seen at higher heights however at 0.025 m near the inlet there is an irregular distribution of solid and voidages. This is expected and agrees with previous results (in Fig. 4.3) as the solids and gas compromise for space before coalescence and segregation of particles occurs with increasing height. The horizontal slices for case 2 were taken at heights 0.04 m, 0.08 m, 0.12 m, 0.16 m and 0.18 m. There is generally a more dilute distribution of particle throughout the bed compared to the distribution of the 40 μm particles, further indicating that the bubbles increase in size with increasing particle diameter, also observed previously (in Fig. 4.3). The dilute core is more clearly apparent and there is significant accumulation of particles around the walls particularly at lower heights. This is observed in both case 2 and case 3 as the mixture becomes more dilute with ascending height again due to the coalescence of bubbles. The slice for case 3 at heights 0.06 m, 0.12 m, 0.18 m, 0.24 m and 0.28 m show further dilution of the particulate phase compared to the 60 μm particles. The bubbles are much larger and the core-annulus structure can be clearly seen with a significant segregation against the walls particularly at lower heights.

4.2 Circulating fluidised beds

This section expands on the previous bubbling regime to look at the fast fluidising regime in both two- and three-dimensions. A complete circulating fluidised bed model is based on and validated with the works of Samuelsberg and Hjertager [2] and the experimental set up was discussed in depth previously in Section 4.1.

4.2.1 Mesh generation

The two-dimensional mesh for the circulating fluidised bed comprises of 78934 quadrilateral cells with the cell sizes set to 0.001 m. In order to capture the complex flow behaviours at the walls, the nodes in the radial direction were non-uniformly distributed such that a more refined grid, set to a minimum of 0.0005 m, could accurately model the downflow behaviour within these regions. The nodes in the axial direction were uniformly distributed apart from the region where the secondary inlet joins with the riser which was more refined in order to capture the re-entry behaviour of the particles.

A 2D grid dependency test was carried using four different grid sizes for the Gidaspow model since it requires finer cells to capture the important flow dynamics. The EMMS model, however, is a sub-grid scale model which can be applied to larger cells in order to capture some of the meso-scale structures. This is a good advantage for larger scaled reactors where smaller grid sizes are far too computationally exhaustive. Table 4.2 shows the different grid sizes that were considered. Case I replicates the mesh used by Samuelsberg and Hjertager [2] and the meshes in the other cases are refined further until the results show independency. These tests were carried out using the same set up as that seen in the literature [2] with free slip along the walls, $\varphi = 0$. Time-averaged measurements of the local axial velocities were taken at different points across the riser over a period of 3.0 s once complete circulation had begun. The time step remained at $1\text{x}10^{-4}$ s for the grid checks since the simulations showed convergence in all grid cases. Although reducing the time step could further improve convergence and could result in slight alteration in the flow dynamics, the increase of time for the simulation to reach circulation for the complete bed including cyclone etc. would not be feasible.

Figure 4.12 shows the particle velocities across the 0.16 m height for the four grid sized simulations using an inlet velocity of V = 0.71 m/s. Although the four cases display similar reasonable results, the more refined the mesh the more the results converged, as expected. All subsequent 2D models were carried out using the case III mesh.

To reduce the computational time and cost, the 3D mesh is coarser than the 2D mesh, containing 1620798 cells. The cell sizes in the x-direction were set to 0.002 m whereas the cells in the y-direction were set to 0.005 m, namely case II in Table 4.2. Similarly to the 2D grid, the downcomer region was further refined along with the near-wall cells in the

TABLE 4.2: Table displaying the different grid size cases

	$\Delta x_{\min}$	$\Delta x_{\max}$	Δy
Case I	0.001	0.0034	0.01
Case II	0.00075	0.002	0.005
Case III	0.0005	0.001	0.001
Case IV	0.00025	0.0005	0.0005

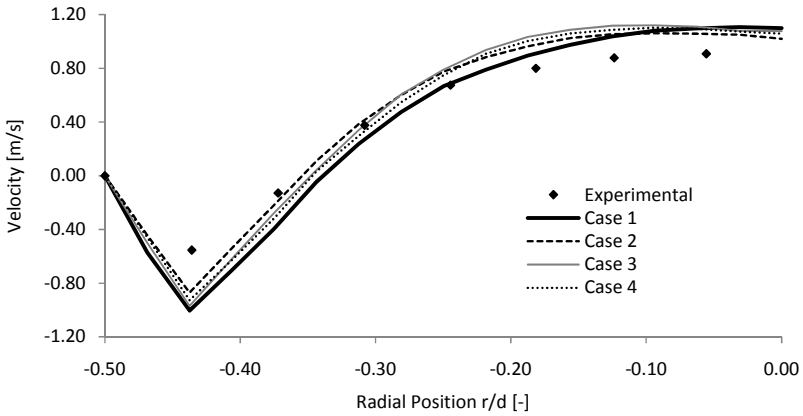

FIGURE 4.12: Particle velocity across the riser at 0.16 m for the four different meshes in Table 4.2 for φ =0, d_p =60 μm and V = 0.71 m/s.

radial direction to a size of 0.00075 m to capture the re-entry and near wall behaviours more effectively.

The two-dimensional circulating fluidised bed models ran for over 14.0 s to allow for complete circulation whereas the three-dimensional models ran for 10.0 s and will be discussed further in Section 4.2.5. The particle diameter d_p was set to 60 μm and the models were tested with inlet velocities of V = 0.71 m/s and V = 1.42 m/s. The same particle properties were used as those for the bubbling fluidised beds and the full set of parameters are given in Table 4.1.

4.2.2 Specularity coefficient

The specularity coefficient, φ, quantifies the nature of the particle-wall collisions based on whether the walls are smooth and frictionless or very rough. In circulating beds, typical behaviour displays the segregation of particles towards the wall where they descend back down towards the base of the reactor. It is difficult to specify a generic condition for wall roughness based on specific wall materials as continual usage would affect the condition of the material over time. Since the condition of the walls in the experimental reactor were not given a preliminary two-dimensional model was carried out to determine a value for the specularity coefficient which agrees well with the experimental results.

The previous model carried out in the literature [2] assumed free slip at the walls and they found that the velocity of particles travelling down the wall was overpredicted. Time-averaged measurements of the local axial velocities were taken at 32 points across the riser at intervals of 0.001 m over a period of 3.0 s once complete circulation had begun. Five specularity coefficients,i.e., 0, 0.25, 0.5, 0.75 and 1.0, were set to account for the different slip boundary conditions for the solids tangential velocity against the wall, where a $\varphi = 0$ is represents a smooth wall and $\varphi = 1$ represents a very rough wall.

The time-averaged results for an inlet velocity, V=0.71 m/s, and particle diameter, d_p =60 μm, across the height 0.16 m are shown in Fig. 4.13. A positive velocity indicates the particles travelling up the riser whereas a negative velocity indicates the particles are descending. A specularity coefficient of 0, representing free slip at the wall, shows an overprediction of the particle velocities travelling down the wall which concurs with the results given in the literature [2]. Increasing the specularity coefficient reduces the slip at the wall leading to a reduction in the downflow velocity of the particles. In all cases, the velocity within the core of the riser are overpredicted as was also observed previously in the literature [2]. The specularity coefficient around 0.25 displays a reasonable reproduction of the experimental data for all the models carried out and for this reason is chosen to be the specularity coefficient for subsequent simulations.

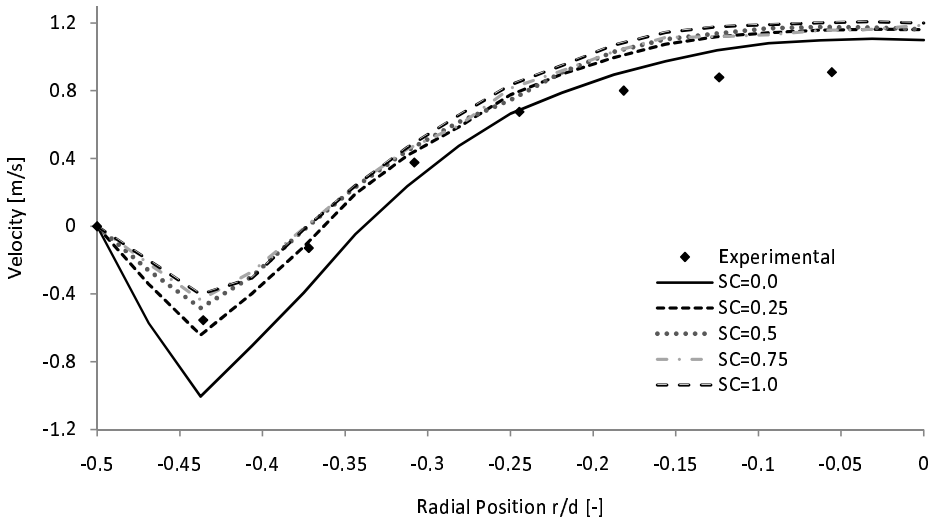

FIGURE 4.13: Specularity coefficient effects on particle velocity predictions across the height 0.16 m for d_p =60 μm and V = 0.71 m/s.

4.2.3 Core-annulus distribution

The two-dimensional particle velocities from three heights in the riser, taken at 14.0 s with an inlet velocity of 1.42 m/s and the Gidaspow drag model, are shown in Fig. 4.14. The results compare well to the experimental results extracted from literature [2]. It

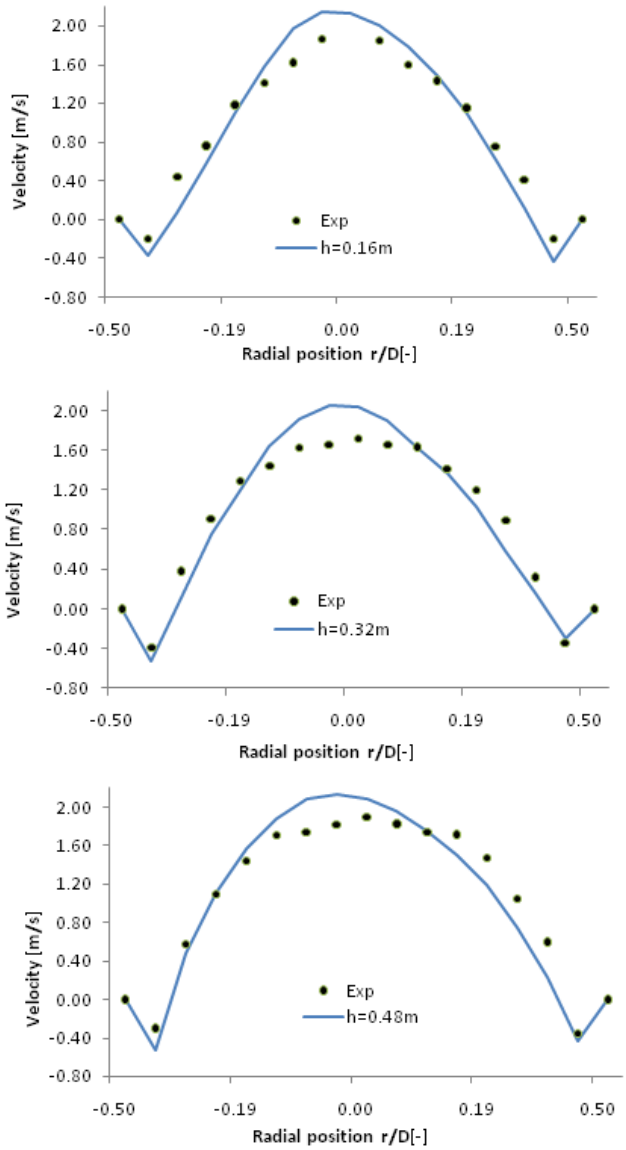

FIGURE 4.14: Experimental and simulated particle velocities at heights 0.16 m, 0.32 m and 0.48 m for d_p =60 μm and V = 1.42 m/s.

is worth mentioning that the experimental data were taken from half the diameter and replicated symmetrically to give the symmetrical results shown. However the velocities obtained during the experiment were averaged over 1000 accepted samples at each of the measuring points, hence is it suitable to assume a symmetrical distribution would be observed over such an extensive sampling period. The simulated results which were given previously in Fig. 4.13 were time-averaged for a period of 3.0 s and the results obtained appeared quite symmetrical. However, the simulated particle velocities displayed in Fig. 4.14 are instantaneous at 14.0 s to display the asymmetry within the core of the riser at this particular instance. There could be a couple of reasons for the skewed distribution within the riser. Firstly, the position of the secondary air inlet could influence the direction of the flow due to recirculated air and particles entering from a side angle

causing the flow to become slightly asymmetric. However this is unlikely to influence the flow greatly as the secondary inlet velocity is only 0.05 m/s compared to a fast inlet velocity of 1.42 m/s. Furthermore, if the secondary inlet were to strongly influence the core flow distribution then the lower height would display a significant skewness which is not obvious in Fig. 4.14. Furthermore, if such skewness from the secondary inlet were to affect the flow it would favour towards one direction which would also be observed in time-averaged results. This was not the case for the time-averaged results given previously in Fig. 4.13 which displays quite a symmetrical distribution at the lowest height for an inlet velocity of 0.71 m/s.

A second factor which would influence the distribution of the core flow is the inlet velocity. Increasing the inlet velocity leads to an increase in the Reynolds number, Re. For the flow of air through the riser with a diameter of 0.032m and inlet velocity 1.42 m/s the Reynolds numbers would be approximately Re = 3110. A flow with Re $<$ 2300 is generally considered to be laminar where viscous effects dominate the flow and a flow with Re $>$ 4000 is regarded as turbulent and displays an unpredictable flow distribution dominated by the inertial effects of the flow. The range between these categories is referred to as a transitional flow and can display both laminar and turbulent behaviours; for example, a turbulent behaviour can be seen within the core of a pipe whilst laminar flow can be observed near the walls. A transitional flow structure would affect the particle distribution as particles are carried along with the flow. Faster particle velocities would be observed in the core where the gas flow is fastest, confirming the results seen in Fig. 4.14, whilst displaying some asymmetric behaviour due to turbulent effects. Furthermore, slower gas velocities would be observed near the walls hence reducing the flows ability to entrain particles leading to the segregation and accumulation of particles near the walls which would descend back down to the base of the reactor, again confirming the results in Fig. 4.14.

The velocity of the particles within the central core is slightly overpredicted compared to the experimental results, however the wall effects show reasonable predictions which are better than those in the literature [2]. Improved wall behaviour is established through the variation of the specularity coefficient accounting for wall roughness, as discussed previously in Section 4.2.2. The increase in the core velocity, however, could be due to the narrowing of the core diameter which is seen at all three heights in Fig. 4.14. When the cross-sectional area available for the upward travelling gas and particle flow to pass through is reduced, the velocity of the flow needs to accommodate for this reduction in area by increasing its velocity.

4.2.4 Particle segregation

To determine the accumulation of particles at the different heights of the riser the particle volume fractions are given across the three heights in Fig. 4.15. As expected, the volume

fraction of the particles at the walls is higher than in the core of the riser. Furthermore, there is an increase in the volume fraction of particles with descending height. This is due to the continual accumulation of particles both travelling down the walls from higher heights but also segregated particles from the core. Within the centre of the riser the volume fraction is very dilute with a particle volume fraction lower than 0.05. At this particular instance, 14.0 s, the particle volume fraction is slightly higher in the core at the higher heights as the dispersed particles are carried with the flow and there is a denser entrainment around the vicinity of 0.32 m. The volume fraction at the highest height, 0.48 m is lower than at 0.32 m which could be due to particle segregation back towards to wall before this height is reached. However it would be more beneficial to analyse these results over a period of time to obtain a general trend. Unfortunately, this was not carried out for this investigation.

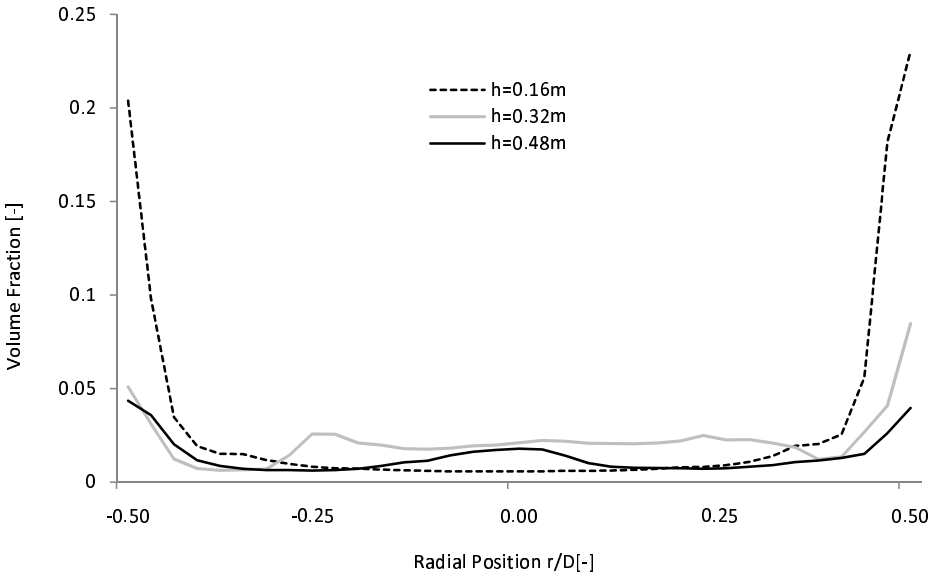

FIGURE 4.15: Radial profiles of particle volume fraction at heights of 0.16 m, 0.32 m and 0.48 m for d_p =60 μm and V = 1.42 m/s.

4.2.5 Three-dimensional circulating fluidised bed

The 3D models were run for 10.0 s to allow for complete circulation using both the Gidaspow and the energy minimisation multiscale (EMMS) drag models. Since the 3D mesh, as discussed in detail in Section 4.2.1, is significantly coarser than the 2D mesh, the accuracy of the Gidaspow model has been greatly reduced. This was highlighted previously by the results in Section 4.1.6. However, the EMMS model, which was introduced in Section 2.2, is a subgrid-scale model which works effectively on coarser grids in order to capture the multiple scales observed in CFBs. As with the two-dimensional model, the particle diameter d_p was set to 60 μm and the models were tested with inlet velocities of V = 0.71 m/s and V = 1.42 m/s.

Figure 4.16 shows contour plots of the particle velocities and volume fraction for the two drag models across the reactor at three heights 0.16 m, 0.32 m and 0.48 m for the velocities 0.71 m/s and 1.42 m/s. Asymmetry is observed more with the faster velocities particularly for the Gidaspow drag model due to the transitional effects influencing the flow structure and particle distribution. The asymmetric velocities for the Gidaspow drag model are more apparent in the 3D results compared to the 2D results as three-dimensional modelling has a better spatial advantage allowing the flow to travel in any direction compared to the two-dimensional models.

The flow starts to centralise with height, as expected. The over estimation of the Gidaspow model would be due to the models inability to capture the clustering effects of the particles correctly but also due to the lack of accuracy by the 3D coarse mesh. The downflow radial velocity of particles against the wall shows the majority of particles are falling at the wall down to -0.532 m/s; whilst the downflow radial velocity of particles for the EMMS model shows a lower velocity of around -0.32 m/s which agrees with the experimental results, as it is more adapt at modelling the particle clusters that form near the wall regions.

The volume fraction distributions in Fig. 4.16 for all cases show the accumulation of particles towards the walls. The lower velocities display an even distribution of particles around the walls of the riser and a lower distribution within the central region where the velocity is fastest. At lower heights the volume fraction of particles against the walls are slightly increased due to the continual collection of descending particles. The Gidaspow drag model at the 1.42 m/s shows a larger cluster of particles situated towards a single area of the wall where the velocity is lower. The EMMS shows a more dilute distribution in particularly for faster velocity due to the majority of particle clusters being present at the base of the riser.

Further comparisons of the radial velocity for the fast EMMS model are shown in Fig. 4.17. A 45°-225° line (Fig. 4.17 (a)) was created through the riser at the heights 0.16 m, 0.32 m and 0.48 m. The radial velocities for the V = 1.42 m/s are taken across the three heights, at 10.0 s, and compared with experimental data from literature [2]. The 3D models show that the EMMS has slight asymmetry due to the transient flow structure however, the magnitude agrees with the experimental results. Contour plots of the radial velocities are also shown to show the asymmetric flow distribution. The downflow at the wall is slightly under predicted however they are much improved over 2D models in literature [2]. Indicating that increasing the specularity coefficient slightly would improve the downflow radial velocity. A value between 0-0.25 should be applied to obtain closer results.

Table 4.3 provides the computational times for the 2D and 3D simulations run over 6 processors for the simulations using the two drag models to reach complete circulation, i.e. 10.0 s. The EMMS model takes slightly longer to run compared to the Gidaspow

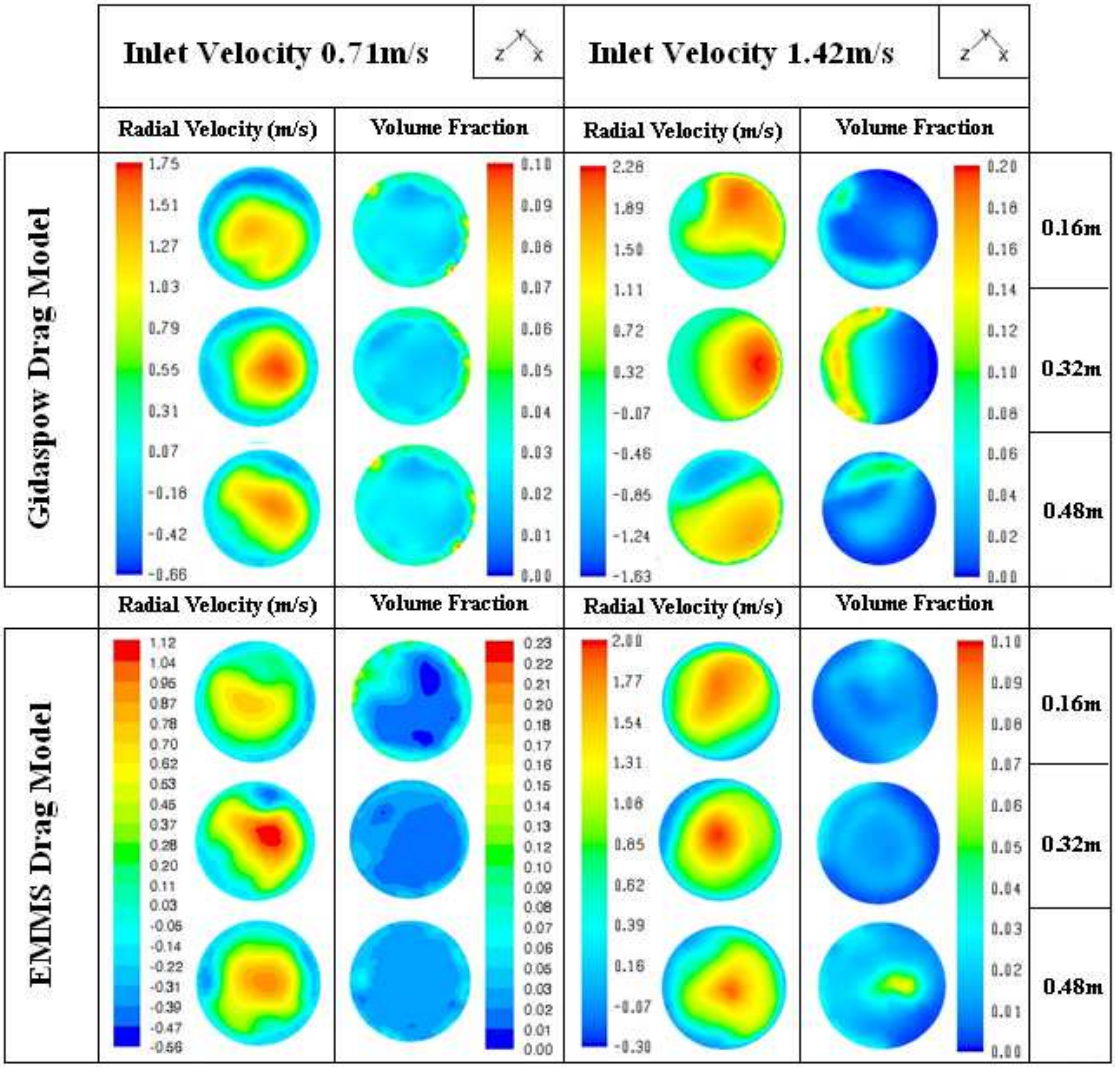

FIGURE 4.16: Comparison of the 3D radial velocities and volume fraction of particles across the heights 0.16 m, 0.32 m and 0.48 m for d_p =60 μm and velocities V = 0.71 m/s and V = 1.42 m/s.

model for both the 2D and 3D simulations. However, should a coarser grid be used this would reduce significantly. Although the grid for the 3D case was coarser than the 2D case the 3D models still took a much longer period to reach complete circulation due to the increase in computational cells.

Although it is computationally exhaustive to repeat three-dimensional models for the benefit of determining grid independency it would be highly beneficial to carry out on three-dimensional test instead of relying on the grid independency results of two-dimensional modelling. Furthermore, a full grid dependency for the EMMS-based model on coarser grids would also be beneficial to capture the meso-scale structures, namely clusters and streamers of particles, since these meso-scale structures can be found up to 100 particle diameters-much larger than the cell sizes used for standard drag models [18, 147, 148].

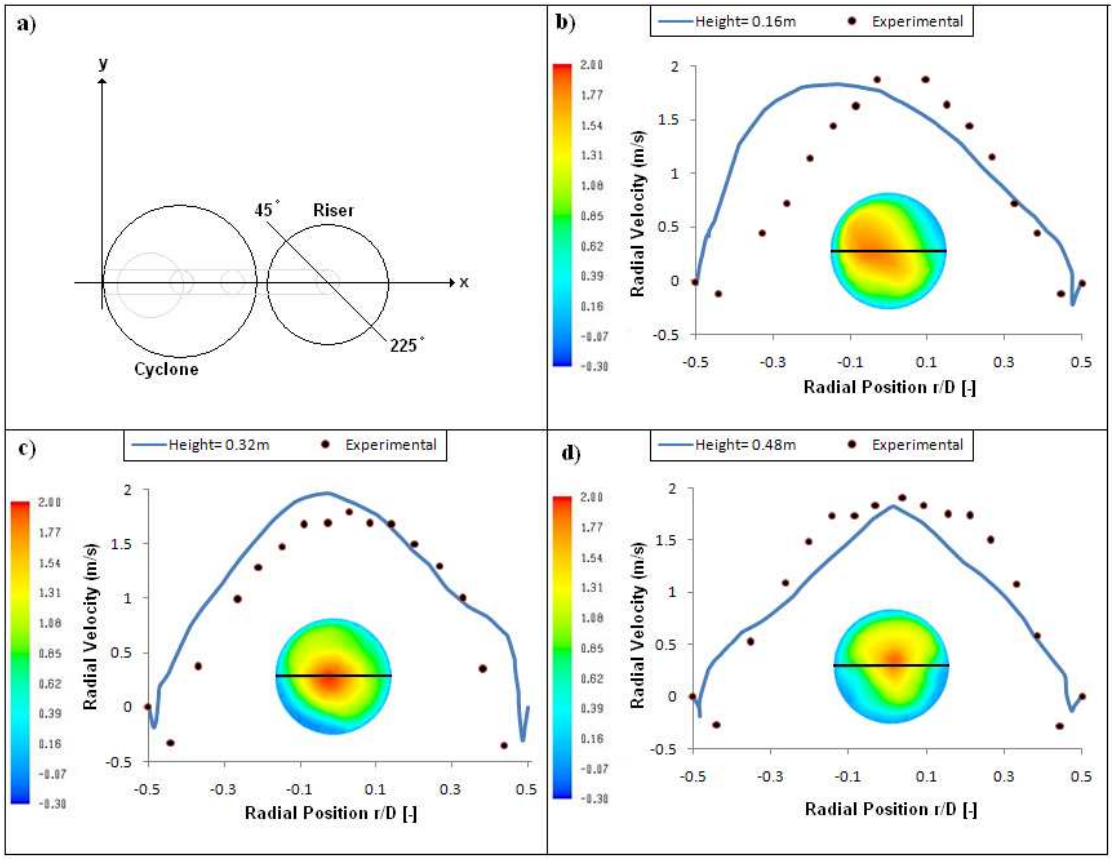

FIGURE 4.17: a) Cross-section of the 3D reactor showing the radial measurement locations and the 3D radial particle velocities for the EMMS model with, V= 1.42 m/s, across the different heights: b) 0.16m, c) 0.32m, and d) 0.48m.

TABLE 4.3: Comparison of the computational times of the two drag models for 2D and 3D simulations.

	Time taken (hrs)	
Drag model	Two-dimensional	Three-dimensional
Gidaspow	≈ 144	≈ 528
EMMS	≈ 192	≈ 720

To reduce the computational time for 2D and 3D simulations further an increase in the number of processors used for calculations could be a sensible and viable solution for future studies.

4.3 Conclusions

Two-dimensional and three-dimensional simulations were carried out on a circulating fluidised bed taken from literature [2]. Initially a parametric study in a riser under a bubbling regime was carried out including drag model comparisons, coefficients of

restitution, inlet velocity variation and particle diameter. Furthermore the transition from a bubbling bed regime to a fast fluidising regime was considered for a variety of inlet velocities. Results were as expected with the transition from bubbling to fast fluidising regimes occurring after the inlet velocity exceeds the terminal velocity. Within the bubbling regime, bubble size increased with height and also as the inlet velocity and particle diameter increased. The lower the velocity, the larger the collection of particles settling back to the base of the riser. The results of the variation in coefficient of restitution showed that the particles with the larger coefficient of restitution, 0.98, displayed reduced particle agglomeration at the base of the bed. Probably since a higher coefficient of restitution conserves more energy during the collisions of particles resulting in an active movement of particles. The volume fraction of particles against the wall was higher than the core in both bubbling and fast fluidising regime showing the segregation of particles towards the wall from the fast flowing core.

The complete CFB geometry was simulated for a fast fluidising regime using two drag models, the Gidaspow and the energy minimisation multiscale (EMMS) model. The EMMS model correctly predicted the particle clusters which the Gidaspow model was unable to take into account. Furthermore, a line taken across the 3D EMMS models showed the magnitude of the results agreed fairly well with the experimental results taken from literature [2]. The 3D Gidaspow results did not show the core-annulus structure and over estimated the velocity due to the incorrect modelling of cluster formation. Improvements were made on the EMMS velocity of the particle downflow at the walls as the shear on the wall was slightly increased compared to previous results in literature which imposed a free slip condition. Further exploration was extended to the volume fraction distribution of particles at three heights within the riser. The results of the volume fraction distribution showed an increase in the volume fraction at the walls due to the segregation of particles from the core towards the walls which further increased down the bed as the particles descend and accumulate. The 3D results agreed that higher volume fractions of particles are found at the walls, as seen experimentally and in the 2D models. Increasing the airflow to a transitional turbulent state along with the presence of the secondary inlet affects the flow of particles within the bed to produce an irregular flow lower down the riser becoming more symmetrical with height.

Chapter 5

Heat Transfer

This chapter focuses on the heat transfer in bubbling fluidised beds from different heat sources. The first section analyses the CFD results from a heated wall model which considers the effects of different parameters like gas velocity, particle diameters and sustained residence times. The results from this section were published in the International Journal of Heat and Mass Transfer [12]. The second section looks at the influence immersed tubes has on the flow dynamics, heat transfer and temperature within the bed. The results from this section were published in the International Journal of Multiphase Flow [13]. Finally, conclusions are made based on the results observed from this chapter.

5.1 Wall-to-Bed heat transfer

The wall-to-bed heat transfer model is based on an experimental investigation by Patil et al. [97]. The purpose of their experiment was to provide extensive, reliable data for validation of their CFD model. The present work continues from their computational work utilising their experimental set up to highlight the effects of model variation, extended residence times and the near-wall dynamics in both dense and dilute conditions.

A two-dimensional wall-to-bed heat transfer fluidised bed with the dimensions 0.2925 m x 1.0 m is modelled. The right wall is heated with a constant temperature of 333 K whilst the remaining bed is initialised with a temperature of 288 K. A pulsating jet is positioned next to the wall which introduces air with varying velocities of 5.0 m/s and 10.0 m/s whilst the remaining inlet continually supplies air with a velocity set at the minimum fluidising velocity hence creating bubbles along the heated wall. The jet is continuously flowing with a pulse length of 0.25 s and the pulse interval of 0.25 s where the pulse interval would be set to a velocity of 0 m/s. The bed is filled to a height of 0.35m with glass bead particles with either 280 μm or 480 μm diameters. Finally, sensors were positioned up the wall to measure the heat flux at the following heights above the inlet: 0.026 m, 0.092 m, 0.175 m and 0.259 m.

TABLE 5.1: Table of Parameters: Bubbling fluidised bed with wall-to-bed heat transfer.

Gas				Units
v_g	Velocity		5, 10	m/s
ρ_g	Density		1.225	kg/m^3
μ_g	Shear viscosity		1.79x10^{-5}	kg/m s
$C_{p,g}$	Specific heat		994	J/kg K
λ_g	Thermal conductivity		0.0257	W/m K
Particles		Case I	Case II	Units
d_p	Particle diameter	280	460	μm
ρ_p	Particle density	2600	2660	kg/m^3
$C_{p,p}$	Specific heat	737	737	J/kg K
λ_p	Thermal conductivity	1.0	1.0	W/m K
e	Particle coef. of restitution		0.9, 0.95, 0.99	
e_w	Wall coef. of restitution		0.9	
φ	Specularity coefficient		0.25	

5.1.1 Mesh generation

A 2D mesh containing 11457 quadrilateral cells was created which contained a uniform 0.01 m grid in the vertical direction and a non-uniform horizontal grid with a minimum size of 5x10^{-5} m normal to the heated wall to a maximum size of 0.005 m. Figure 5.1 displays the geometry and mesh used for the simulation. The parameters used in the model are given in Table 5.1.

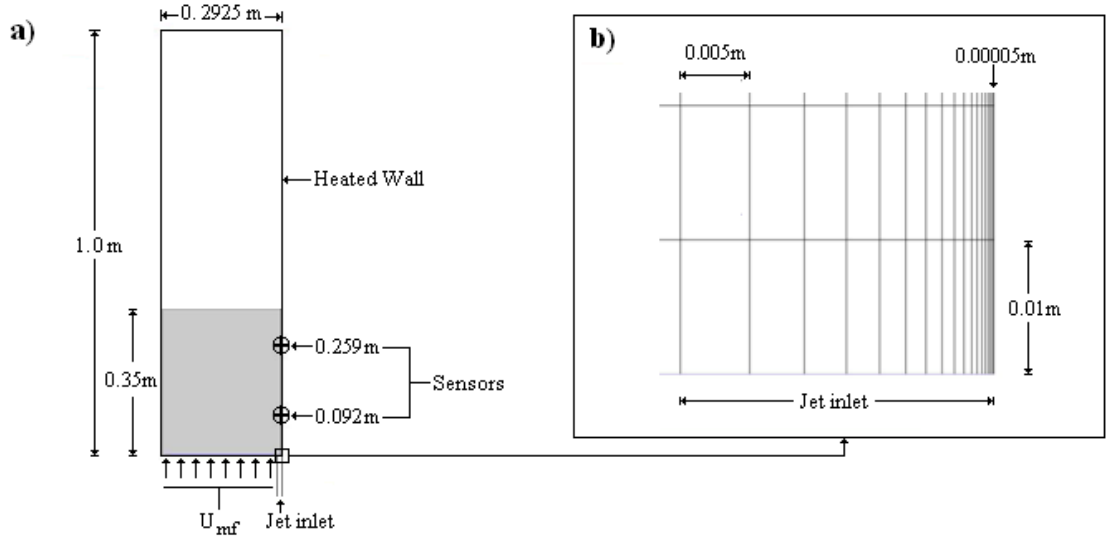

FIGURE 5.1: a) Geometric setup for the bubbling fluidised bed with wall-to-bed heat transfer, b) Close up of the near wall grid at the entrance of the jet inlet.

5.1.2 Drag model comparisons

Figure 5.2 shows the volume fraction contour plots using two different drag models, the Gidaspow (Appendix A.3) and the Syamlal-O'Brien (Appendix A.4) drag models, at the time intervals 0.1 s, 0.3 s, 0.5 s and 0.8 s. For this specific simulation, the pulsating fast inlet velocity was set to 5.0 m/s for a period of 0.25 s, stopped (0 m/s) for a further 0.25 s then this cycle was repeated. The particle coefficient of restitution for this simulation was set to 0.95.

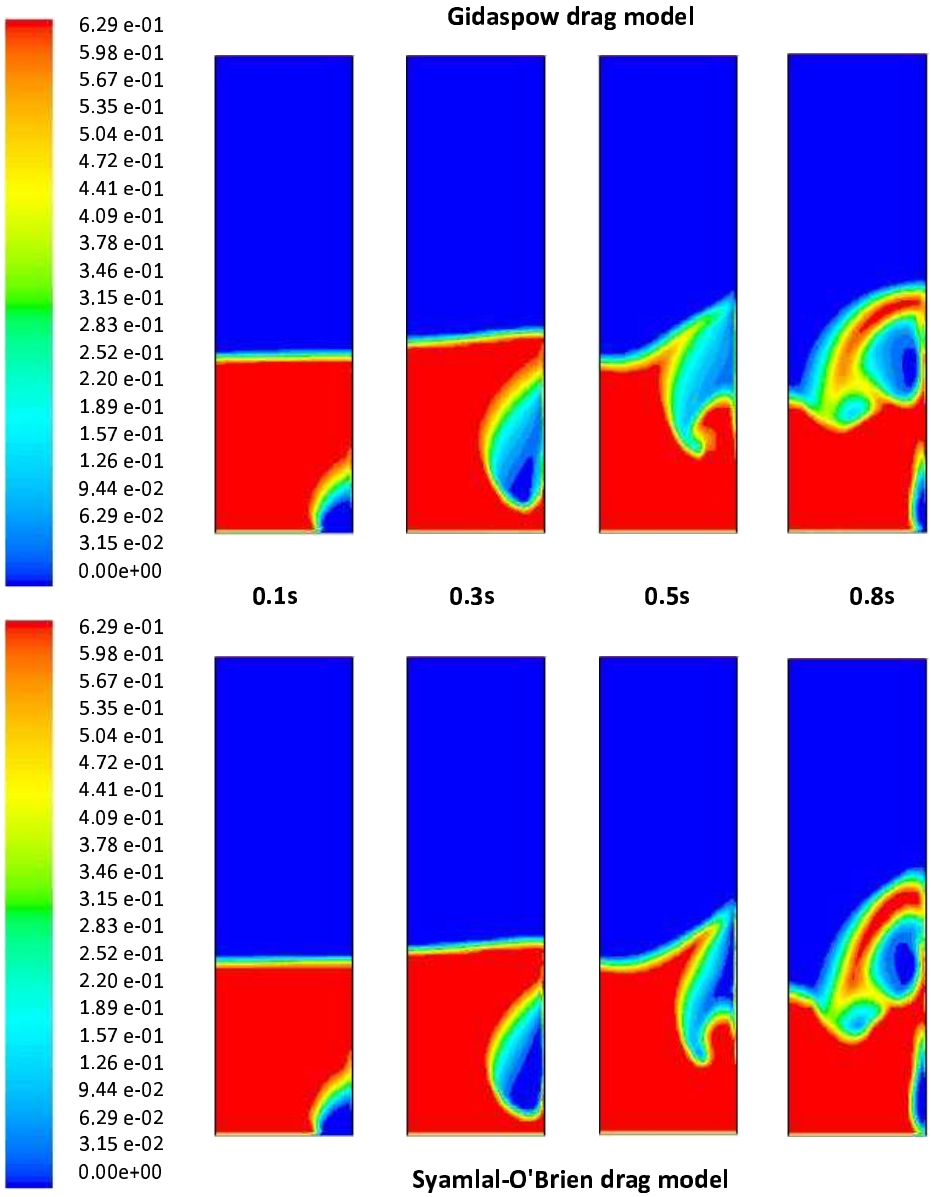

FIGURE 5.2: Contour plots of the instantaneous particle volume fractions at 0.1 s, 0.3 s, 0.5 s and 0.8 s for the Gidaspow and Syamlal-O'Brien drag models.

The transition of the bubble up the wall displays similar features with both drag models. At 0.1 s, a bubble has formed above the inlet due to the fast inlet supplying air at a rate

of 5.0 m/s. At 0.3 s, the bubble continues to rise towards the top of the bed along the wall, however the air supply from the fast inlet stopped 0.05 s prior to this which leads to the circulation of particles under the bubble to occupy the voidage below. At 0.5 s, the bubble is situated at the top of the bed and begins to burst which releases particles into the freeboard of the reactor. The bubble also appears to elongated and circle back round towards the walls under the bubble. This indicates the particles in the bed are moving in a circular motion, influencing and distorting the bubble back towards the wall. This is seen more clearly in Fig. 5.3 which displays the particle velocity vectors on top of, Fig. 5.3 (a) the particle volume fraction and b) the particle velocity distribution. The circulating behaviour of the particles can clearly be seen and the faster velocities are observed directly below the bubble, pushing particles up and causing distortion of the bubble. The particle velocity distribution in Fig. 5.3 (b) also shows the motion of particles above what appears to be the peak of the bed height in Fig. 5.3 (a). This is due to the expulsion of particles that are released as the bubble erupts from the bed. These particles then fall back to the bed as can be seen in Fig. 5.3 (a).

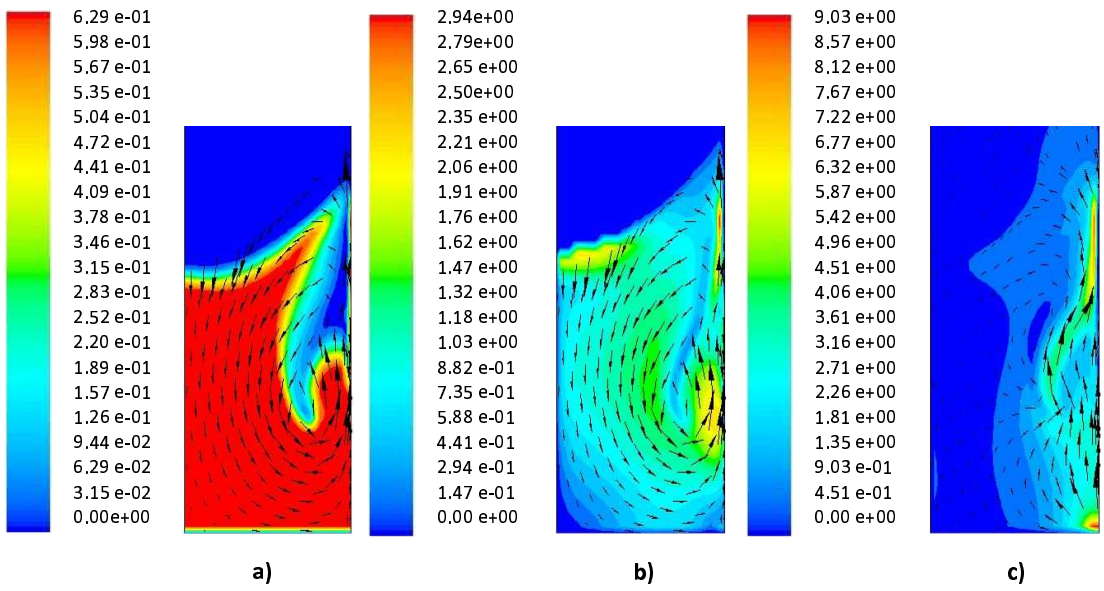

FIGURE 5.3: Velocity vectors on contours plots at 0.5 s showing the a) particle volume fractions with particle velocity vectors, b) particle velocity distribution (m/s) with particle velocity vectors and c) gas velocity distribution (m/s) with gas velocity vectors for the Syamlal-O'Brien drag model.

The gas velocity distribution and gas velocity vectors can be seen in Fig. 5.3 (c). As expected the faster gas velocities are observed near the heated wall. The fast air inlet was switched on at 0.5s but it is still too early for the build up of a bubble directly above the inlet. However, the gas velocity distribution shows a very fast velocity in this region which would be due to an immediate inflow of air at 5.0 m/s following a period of 0.25 s of no flow in this region. Furthermore, the circulatory behaviour of the particles would also influence the gases due to drag hence encouraging the gases in this area to travel

up following the motion of the bed. It is also interesting to see the transition of the gas moving faster through the bubble. This is because the gas would travel the easiest route through the bed, namely that containing the least obstruction due to particles, therefore bubbles provide a faster channel for the air to rise.

After 0.8 s in Fig. 5.2, both drag models capture the presence of a bubble near the top of the bed with the presence of a further smaller bubble. This is created by the recirculation of the particles in the bed. Although the fast inlet is not supplying air at that time, there is still the presence of an air bubble at the base of the wall which is a result of bubble partitioning due to the force of the circulating particles back towards the wall.

Figure 5.4 displays the heat transfer coefficient and the volume fraction of particles along the wall at the time intervals 0.1 s, 0.3 s, 0.5 s and 0.8 s. It can be clearly seen that regions of high particle volume fraction transfer heat more effectively compared to regions of low particle volume fraction. The very low heat transfer coefficients found above the bed, above approximately 0.5 m, confirms that air acts as a strong resistance against heat transfer. Although the gas-solid flow dynamics shown in Fig. 5.2 display a similar resemblance between the two drag models, the detailed volume fraction distributions along the wall reveal significant differences. The Syamlal-O'Brien model displays a strong fluctuating behaviour along the wall capturing both dense and dilute regions in close proximity of the wall. Correspondingly, the heat transfer coefficients predicted by the Syamlal-O'Brien model show much larger variations along the walls than those by the Gidaspow model.

The heat transfer coefficients taken at 0.092 m for both drag models are compared with the experimental data taken from the study of Fig. 5.5. The results in the early stages, before 0.1 s, show a dramatic decrease in the heat transfer coefficient for the simulation which is due to different initial states between the simulation and the experiment. In the simulations, the bed is initially set to room temperature, which is not the case in the experimental setup as the local area heats up whilst the heated wall reaches the required temperature. The subsequent results show the results from 0.1 s to bypass this phenomenon.

Both drag models detect the passage of the bubble against the sensor and the collection of particles against the wall in the wake. The highest heat transfer coefficients occur when the particles circulate back in the wake of the bubble after the air supply has stopped. However, in the high particle concentration regions the heat transfer coefficients are over-predicted by both models and was also seen in previous studies [97].

The Gidaspow model was employed previously [97] and a smaller bubble was detected as a result of partitioning of the initial bubble due to particle circulation. This is present for both drag models in Fig. 5.5, seen as small peaks between dilute phases, however the Syamlal-O'Brien model is less pronounced. The sudden increase in heat transfer

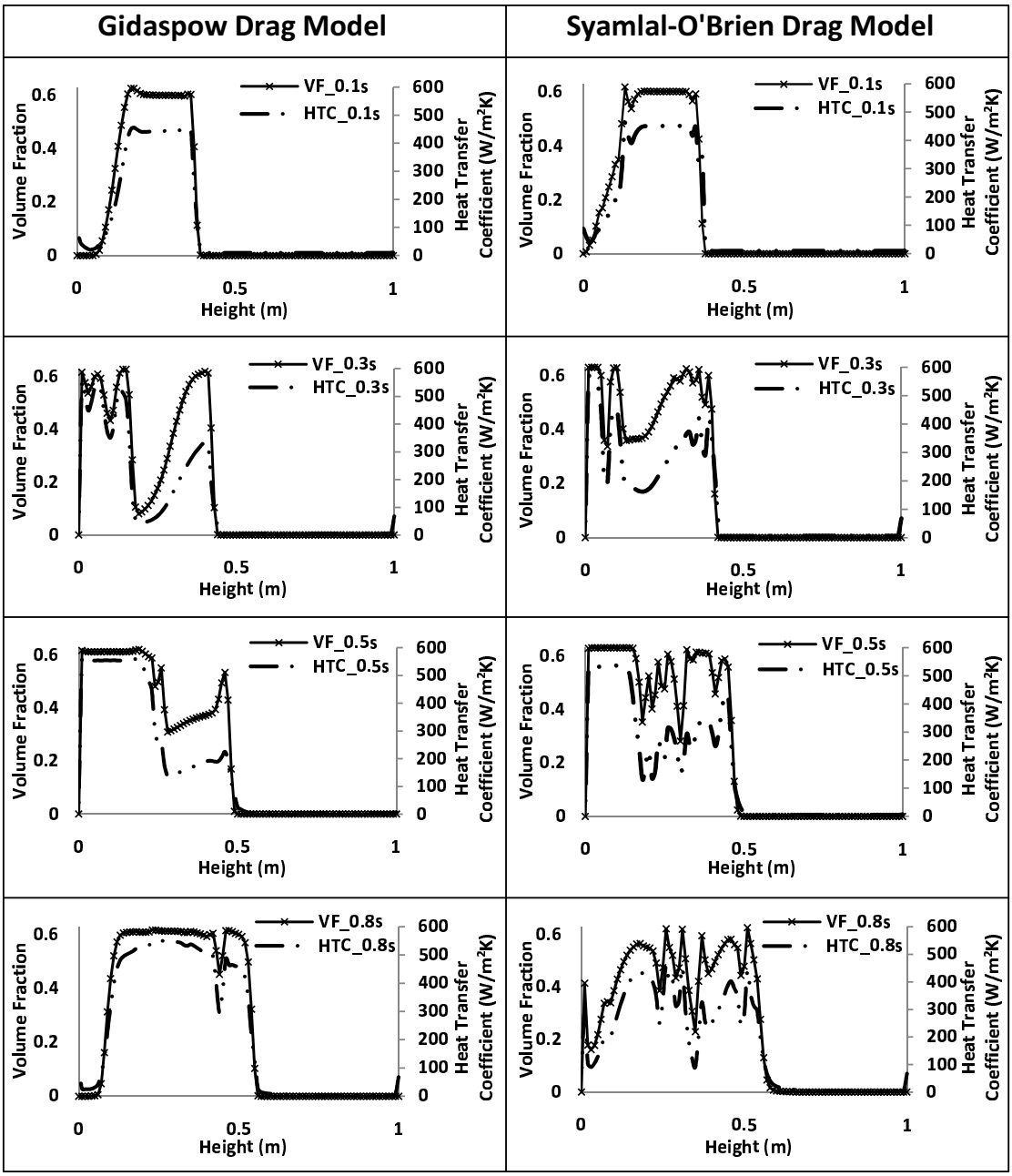

FIGURE 5.4: Local volume fractions and heat transfer coefficients along the wall at 0.1 s, 0.3 s, 0.5 s and 0.8 s for the Gidaspow and Syamlal-O'Brien drag models.

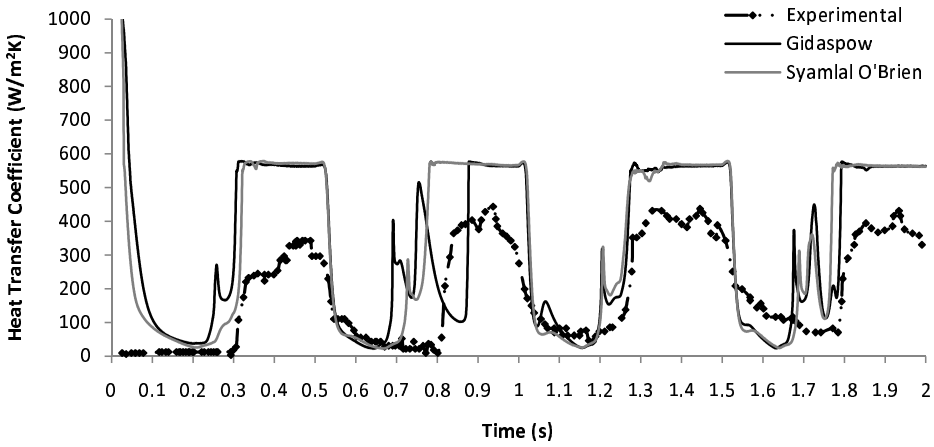

FIGURE 5.5: Comparison of the local heat transfer coefficient for the Gidaspow and Syamlal-O'Brien drag models with experimental data at 0.092 m with d_p = 280 μm and pulsating jet = 5.0 m/s.

coefficient for the Gidaspow model before 0.7 s is where a collection of particles circulate towards the wall. This small collection of particles is pushed by the remaining bubble underneath resulting in the decrease in heat transfer coefficient between 0.75-0.9 s as the secondary bubble passes the sensor. The Syamlal-O'Brien model is delayed highlighting the influence that varying drag models has on flow dynamics. The variation between the drag models could suggest the presence of a thin layer of particles that are clustered near the wall. This would also explain the fluctuations of volume fraction and hence heat transfer coefficient in Fig. 5.4 as a result of varied particle clustering.

The temperature of the particulate and gas phases at 0.8 s within a 5 particle diameter distance from the wall at two heights of 0.092 m and 0.259 m are given in Fig. 5.6 and Fig. 5.7, respectively. The particle volume fractions near the wall are also shown. At 0.8 s, the 0.092 m sensor is situated within a bubble whereas at 0.259 m the area contains a dense particle region in the wake of the larger bubble at the top of the bed (as seen previously in Fig. 5.2).

Within the bubble at 0.092 m in Fig. 5.6, the Syamlal-O'Brien model shows a higher volume fraction at the wall than the Gidaspow model. The Syamlal-O'Brien model also shows a dramatic decrease to the dilute bubble region whereas the Gidaspow model shows a gradual decrease. This suggests there are a tight clustering of particles about 2 particle diameters against the wall whilst the Gidaspow model shows the presence of particles which are not as compact but over a larger distance from the wall.

Within the wake at 0.259 m in Fig. 5.7, the volume fraction of the solids differs significantly to that observed in the bubble. The fluctuation observed by both models within a distance of approximately 2 particle diameters indicates the compaction of particles in the dense phase against the wall. The Gidaspow model shows the volume fraction leveling off to approximately 0.63 whilst the Syamlal-O'Brien model decreases. This can

be explained in Fig. 5.2 where the elongation of the lower bubble in the bed extends slightly further up the wall and closer to the sensor for the Syamlal-O'Brien model, hence slightly reducing the volume fraction locally.

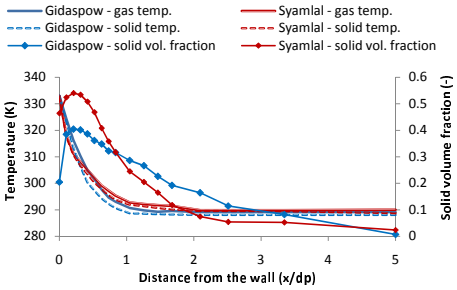

FIGURE 5.6: The near wall simulated gas and solid temperature and particle volume fraction within the bubble at 0.092 m with velocity = 5.0 m/s and time = 0.8 s.

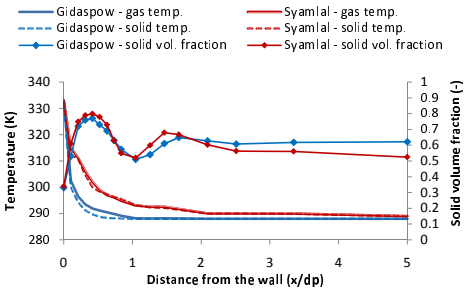

FIGURE 5.7: The near wall simulated gas and solid temperature and particle volume fraction within the dense bed at 0.259 m with velocity = 5.0 m/s and time = 0.8 s.

In both Fig. 5.6 and Fig. 5.7 the temperatures of both phases continue to show the heat transfer takes place within 1-2 particle diameters however, the Syamlal-O'Brien model shows a slightly increase temperature which could be due to the slight increase in local particle volume fraction indicating a slightly lower porosity. The solid and gas temperatures for both models are similar within the dilute and dense regions, however the dilute region shows a higher temperature at a further distance for the Gidaspow model compared in the dense region. This could be due to a dilute region allowing for the movement of particles thus carrying heat further. Furthermore, this would also explain the increased volume fraction of particles observed for the Gidaspow model at a further distance from the wall. The temperatures of the gas and solid phases agree well with the results obtained previously [97] with the heat transfer resistance taking place within the first two particle diameters.

The simulations were carried out for three coefficients of restitutions 0.9, 0.95 and 0.99 for the Gidaspow model with inlet velocity of 5.0 m/s and particle diameter 280 μm. However, varying the coefficient of restitution did not appear to affect the local heat transfer coefficient probably because the wall conditions and frictional effects have a strong effect in the region nearest the wall where particle-particle collisions are less influential.

5.1.3 Velocity variation

Increasing the fast inlet velocity to 10.0 m/s gave the results displayed in Fig. 5.8. Both drag models show a good general agreement with the experimental data. There is a slight over-estimation in the heat transfer coefficient at the beginning but the discrepancies

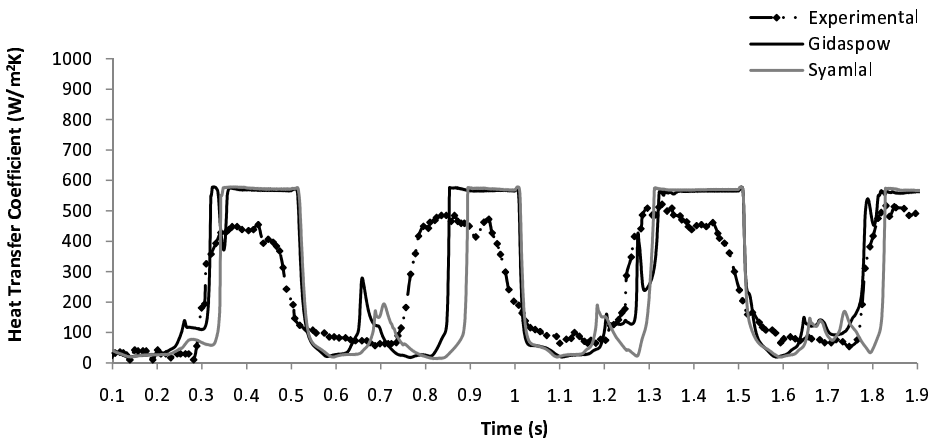

FIGURE 5.8: Comparison of the Syamlal O'Brien and Gidaspow drag models with experimental data with an increased inlet velocity of 10.0 m/s and particle diameter 280 μm.

between model predictions and experimental data decrease with time, partly because the peaks of the experimental data increases with time.

Whilst the heat transfer coefficients for both models descend together to show the presence of a new bubble, a difference is observed once the bubble fully passes the sensors and the particles circulate back towards the walls. The period of bubble contact with the sensor differs with each bubble passage, with a larger bubble being observed between 0.5 s and 0.8 s for both models. The formation of the small peak around 0.65 s for the Gidaspow drag model occurs before the Syamlal-O'Brien model again highlighting the different influences the drag models have on the flow dynamics. The local heat transfer coefficient at the small peaks however reduces which would indicate that the simulation times should be extended to allow for the flow to develop fully.

5.1.4 Diameters

The results of increasing the particle diameter and density to 460 μm and 2660 kg/m^3, respectively, are displayed in Fig. 5.9. The simulated heat transfer coefficients agree very well with the experimental data as found previously [97]. The decrease in heat transfer coefficient at a higher diameter is due to the increase in porosity which is taken into account using the porosity model. The larger air spacing between particles would cause the transfer of heat to be deferred slightly as air resists heat transfer more than particles.

The transition of the bubbles for both drag models is slightly ahead of the experimental results. Suggesting that particles the circulate back towards the wall in the wake of the bubble sooner then observed experimentally. However the regions of lower heat transfer coefficient, indicating the presence of a bubble, would suggest the bubbles observed in

the simulations are of similar diameter to those observed in the experiment. This delay in the experimental data compared to the simulated results was also observed by Patil et al. [97].

The heat transfer coefficient within the bubbles are low as soon as the bubbles are formed, however, the value increases as the bubble ascends. This would suggest that particles within the bubble segregate towards the walls as the bubble rises, increasing the particle volume fraction thus allowing for an increase in heat transfer.

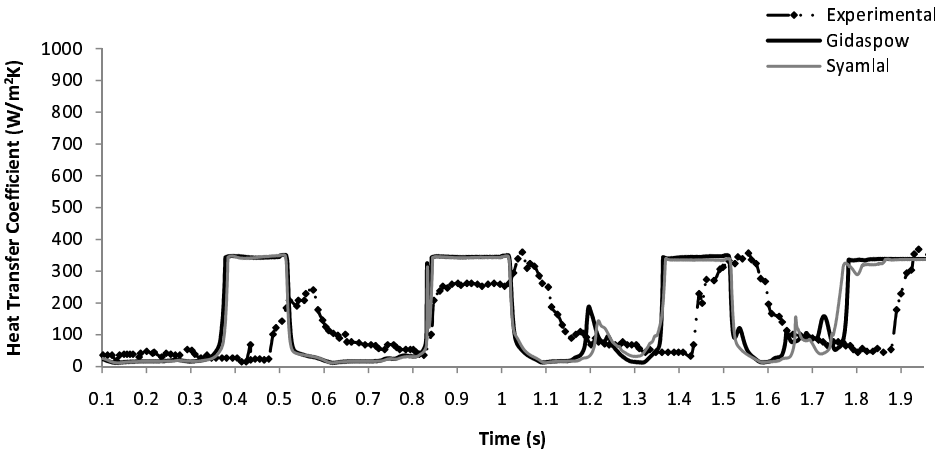

FIGURE 5.9: Comparison of the Syamlal O'Brien and Gidaspow drag models with experimental data with an increased particle diameter 460 μm and inlet velocity 10.0 m/s.

5.1.5 Periodic behaviour

The Syamlal-O'Brien model simulation with particle diameter, density and coefficient of restitution of 280 μm, 2600 kg/m^3 and 0.95, respectively, was continued for a further 6.0 s to observe any periodic effects and the results are displayed in Fig. 5.10.

The results clearly show the heat transfer coefficient periodically peaks soon after the fast inlet has stopped supplying air causing the particles to circulate back to the wall to fill the voidage. The presence of the smaller bubble against the wall is to be seen prior to the seizing of fast inlet air supply. This was also observed previously using the KTGF model [97] due to bubble partitioning. The additional peak is less pronounced at the beginning of the flow but builds up to what appears to be a heat transfer coefficient of approximately 350 W/m^{2}K. This would suggest that the initial 0.0-2.0 s allow the flow to regulate and become fully developed before the achievement of any periodic observations, therefore previous results obtained [97] were not allowed to run long enough for periodicity to be achieved.

Figure 5.10 also displays a variation in the local heat transfer coefficient. The lower values seen during the passing of the bubble show very strong periodicity with heat transfer coefficients as low as 30-100 W/m^{2}K which agrees well with the experimental data from an earlier stage (Fig. 5.5). Furthermore, the peak heat transfer coefficients appear to decrease slightly possibly due to the flow regulation, suggesting that for a more complete analysis to be made longer simulations and experiments would be required. However, it is worth highlighting that although similar patterns in the flow are observed over time, there are still irregular flow distributions due to the unsteady nature of a bubbling bed.

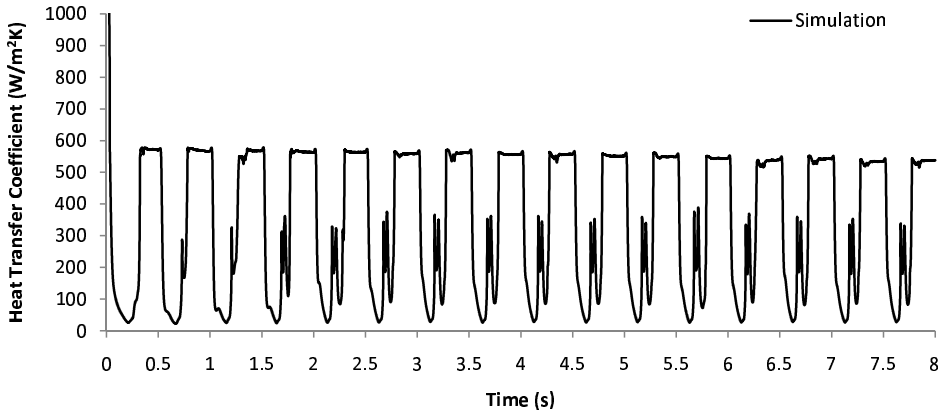

FIGURE 5.10: The Syamlal O'Brien drag model over an extended period of 8.0 s with particle diameter 280 μm and inlet velocity 5.0 m/s.

5.2 Immersed tube heat transfer

A two-dimensional numerical model was set up based on a model from Schmidt and Renz [3]. Three gas fluidised bed reactors were modelled with one, two and three heated immersed tubes as displayed in Fig. 5.11. Glass beads were used with a uniform diameter of 500 μm and density 2660 kg/m^3 whereas the fluidising gas was air with a density of 1.225 kg/m^3 and viscosity of 1.79x10^{-5} kg/m s. The full material properties are given in Table 5.2. Two air velocities were introduced into the reactor, a fast air inlet within the centre of the reactor base to produce air bubbles and a slow velocity introduced through the remaining base of the reactor. The fast air inlet was set to a velocity of 5 m/s whilst the slow inlet was set to the minimum fluidising velocity, 0.25 m/s. The immersed tubes were set to a constant wall temperature of 373 K whilst the remaining reactor walls were assumed adiabatic and the initial bed temperature was set to 293 K.

5.2.1 Mesh generation

For the single immersed tube model a 2D mesh containing 30704 quadrilateral cells was created which contained a uniform 0.0025 m grid in the vertical direction and a horizontal grid of size 0.0025 m. Due to the near-wall interest in the vicinity of the tubes, a boundary layer was set with a minimum size of $6.25\text{x}10^{-5}$ m normal to the heated tube. This minimum cell size represents the initial distance that the results start being extracted. Further distances are considered with distances from the tube increasing with a factor of approximately 1.22. Similarly, the mesh with two immersed tubes contained 32770 quadrilateral cells and the mesh with three immersed tubes contained 34922 cells. Figure 5.11 (a) displays the geometry used for the three models, Fig. 5.11 (b) shows the direction and angular positions from where the data was taken and Fig. 5.11 (c) shows the different distances from the tubes that data was extracted. The parameters used in all models are given in Table 5.2.

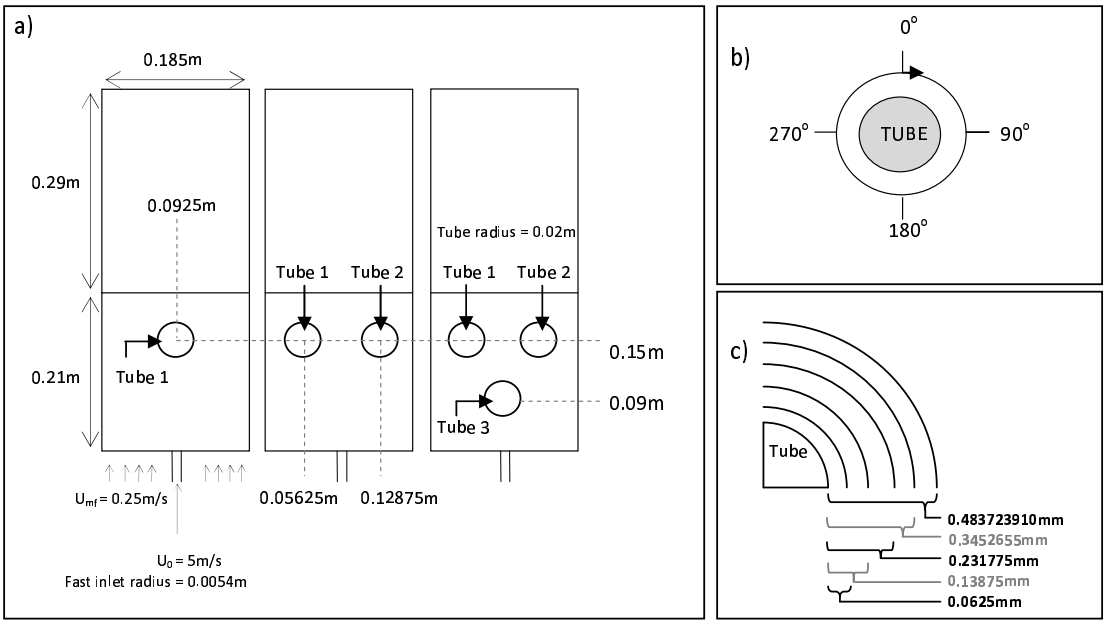

FIGURE 5.11: a) Schematic diagram of the numerical set up, b) the direction and angular positions from where the data was taken and c) the distances from the tube at which data was taken.

5.2.2 Flow distribution

The contour plots of the particle volume fractions within the three reactors are displayed for the first 1.0 s in Fig. 5.12 using the Gidaspow drag model. The 1-tube simulation results agree really well with the simulated and experimental results provided in the literature [3]. In the early stages of the single immersed tube model a collection of air forms below the tube. A large air bubble develops at the inlet and ascends through the bed with time whilst the small air voidage under the tube continues to build up and

TABLE 5.2: Table of Parameters: Bubbling fluidised bed with tube-to-bed heat transfer.

Gas			Units
υ_g	Fast inlet velocity	5	m/s
υ_{mf}	Slow inlet velocity	0.25	m/s
ρ_g	Density	1.225	kg/m^3
μ_g	Shear viscosity	1.79x10^{-5}	kg/m s
$C_{p,g}$	Specific heat	994	J/kg K
λ_g	Thermal conductivity	0.0257	W/m K
Particles			
d_p	Particle diameter	500	μm
ρ_p	Particle density	2660	kg/m^3
$C_{p,p}$	Specific heat	737	J/kg K
λ_p	Thermal conductivity	1.0	W/m K
e	Particle coef. of restitution	0.95	
e_w	Wall coef. of restitution	0.9	
φ	Specularity coefficient	0.25	

blanket round the tube. At 0.3 s, the bubble that built up around the tube comes away to continue up through the bed whilst the larger bubble from the inlet reaches the tube and begins to encase it. Similar trends are seen in the early stages of the 2-tube and 3-tube simulations however, with each addition of a tube there is a delay of the dynamic processes observed. This is due to a longer period of time required for the build up of gas below each additional tube before becoming sufficient enough to encase the tube, separate and continue up the bed.

As expected, the presence of large bubbles within the bed causes a higher bed height expansion which is seen in Fig. 5.12 at 0.3-0.5 s for the 1-tube simulation. Furthermore, Fig. 5.12 suggests that a reactor with a tube position directly above the fast air inlet leads to smaller bubble sizes. This is particularly seen in the 3-tube simulation as the centre tube partitions the bubbles but the additional two tubes breaks up the bubbles further. This presence of the tubes prevents the coalescence of large bubbles resulting in a low bed height expansion. To investigate this further the approximate bed expansions were determined for the three reactors at each time interval and are shown in Fig. 5.13. The bed height peaks in the early stages of the simulation whilst the bed dynamics establishes a regular motion. Once regularity is achieved the bubbles continue to form with similar sizes resulting in very little variation in bed height.

The 2-tube simulation behaves differently compared to the 1-tube and 3-tube simulations. The bed expansion peaks a number of times around 0.7 s, 1.0 s and 1.4 s. This is seen in Fig. 5.14 which displays the volume fraction contour plots of the 2-tube simulations over a longer period. A voidage region lies in the mid-region below the two tubes. As this region expands and the bubbles enlarge they come into contact with the tubes on the outer faces nearer the walls of the reactor and the gas follows this route

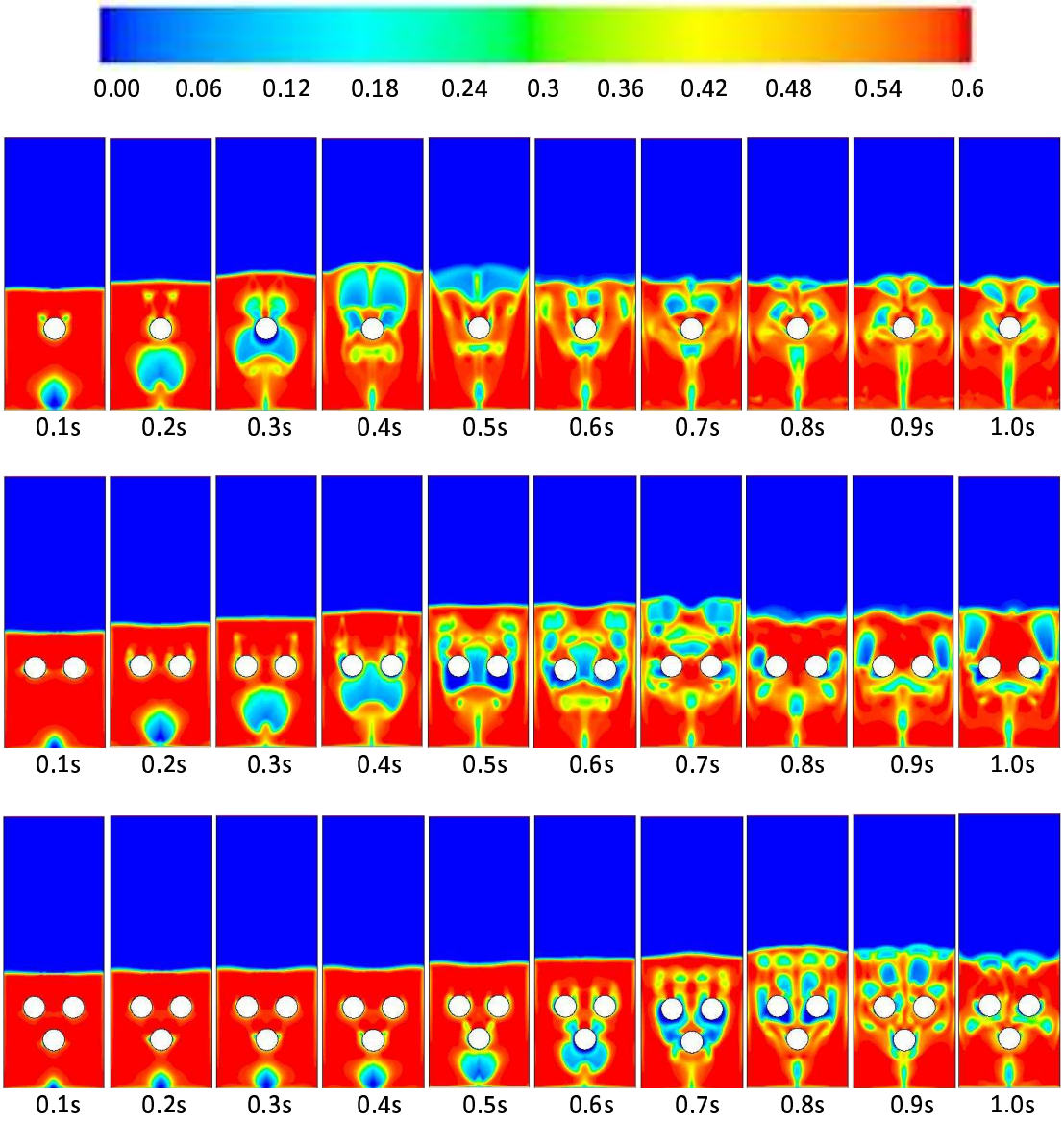

FIGURE 5.12: Contour plots of the particle volume fractions over the initial 1.0 s using the Gidaspow drag model.

through the bed. As the bubbles continue to expand and rise they form larger bubbles than those seen in the 1-tube and 3-tube simulations which results in an increase in bed height.

The release of a bubble from around each tube appears to alternate between the left and right tube. This is due to the flow dynamics, as a large bubble on the left is formed the particles in the bed are forced towards the opposite side of the bed suppressing and delaying the bubble formation on the right. This alternating bubble development is a clear indication that the previous model carried by Schmidt and Renz [3], who applied symmetry by using half the bed for simplicity, was not a viable approach. The asymmetry of the bubble locations in the bed can be seen as early as 1.0 s for all three

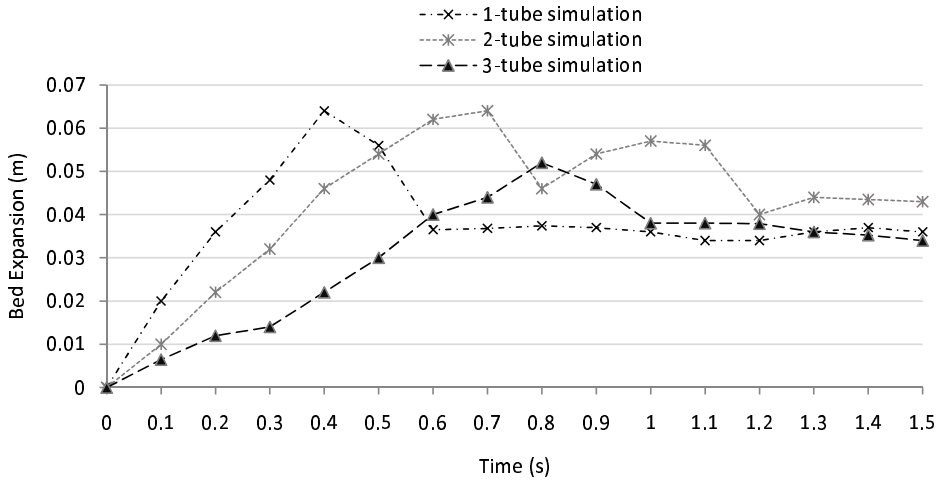

FIGURE 5.13: The approximate bed expansion for all three reactors with increasing time using the Gidaspow drag model.

cases in Fig. 5.12 thus further confirming the previous assumption by Schmidt and Renz [3] that a symmetrical model would not capture the full flow characteristics.

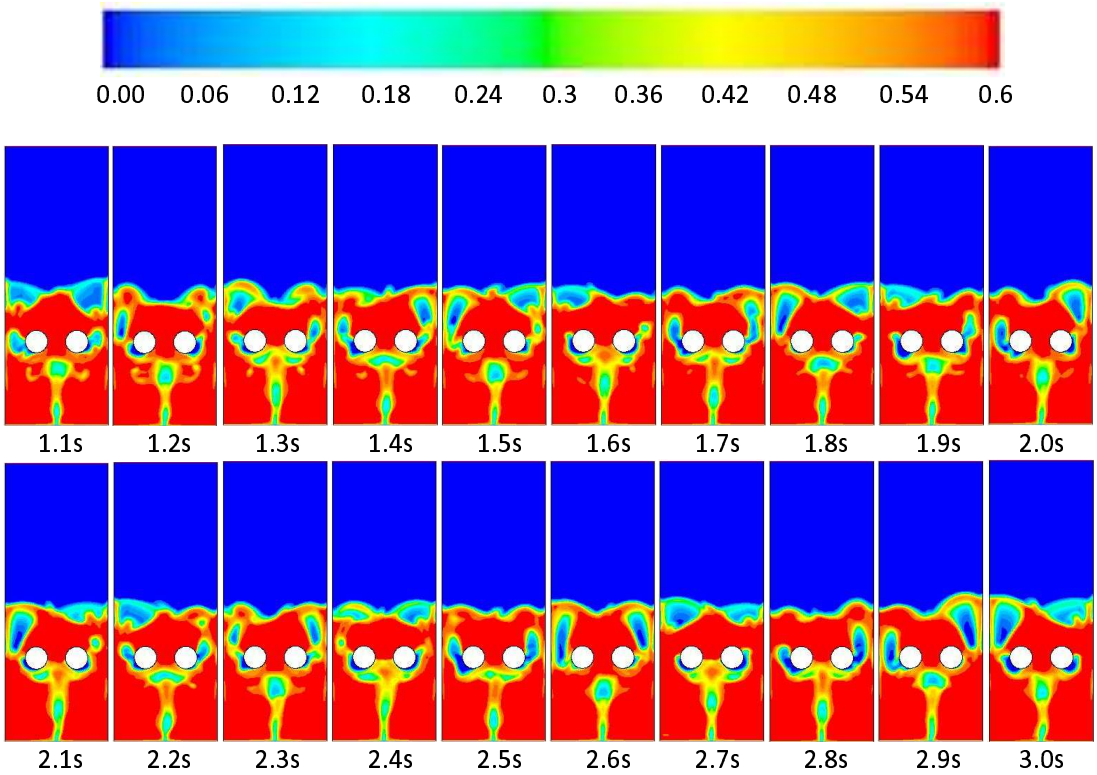

FIGURE 5.14: Contour plots of the particle volume fractions for the 2-tube simulation over the 1.1-3.0 s period using the Gidaspow drag model.

5.2.3 Local heat transfer coefficients

The local heat transfer coefficients were taken close to the tube, 6.25x10^{-5} m away, for the 1-tube simulation at 0.3 s. At this particular instance, seen previously in Fig. 5.12, air bubbles are separating from the top of the tube whilst a larger bubble from the inlet starts to blanket it. As in the previous study [3], where their results were also taken at an instance of similar flow behaviour, the predicted results around the first 180^{o} in Fig. 5.15 (a) use the molecular thermal conductivity model only. All the drag models provide similar trends but different magnitudes near the tube surfaces. At 0.3 s, the contour plot in Fig. 5.12 indicates a collection of particles above the tube leading to an increase in heat transfer since particles are better conductors than air. This is further displayed in a plot of the volume fraction around the tube in Fig. 5.15 (b). As seen previously there is always a region of high volume fraction in contact with the tube so the bubbles do not encase the tube completely [3]. There is a difference observed between the simulated results and the predicted results from Schmidt and Renz [3], particularly between the particle volume fractions. This is because both sets of predictions are given instantaneously and not time-averaged so the variation in the case set up, more specifically the modelling of the complete bed as opposed to the previous symmetrical model, leads to significant differences at specific local times. The low heat transfer coefficients observed from approximately 30^{o} occur due to the large air voidage blanketing the tube.

Time averaged particle volume fraction results were taken over a period of 1.0 s and reported in Fig. 5.16. The results are compared with the experimental results from Di Natale et al. [4], who carried out void fraction profiles around a single tube using 500 μm glass beads. However, their model was carried out using gas velocities ranging from 0.15-0.45 m/s which are significantly lower than that used in this case. A similar trend can be seen between the simulation and experimental results although differences are also clearly observed. The values at the lowest and highest point on the tube agree reasonably well with the experimental results. The particle volume fraction around the side of the tube however appears to be significantly lower. This would be due the significantly higher fast inlet velocity of 5.0 m/s used compared to 0.45 m/s used to obtain the experimental results. The increased velocity could result in the removal of particles around the side of the tube within the vicinity of the tube as the air passes along the tube walls faster. Since the highest point of the tube is seen to have a large collection of particles in contact with the tube this would explain the high particle volume fraction seen both in the simulation and the experiment. This region appears to form later in the simulation due to the increased air velocity continuing around the tube and releasing up in the bed later.

Figure 5.17 shows the full 360^{o} results for one tube for the molecular thermal conductivity model only. It can be seen that as early as 0.3 s the flow displays a non-symmetrical

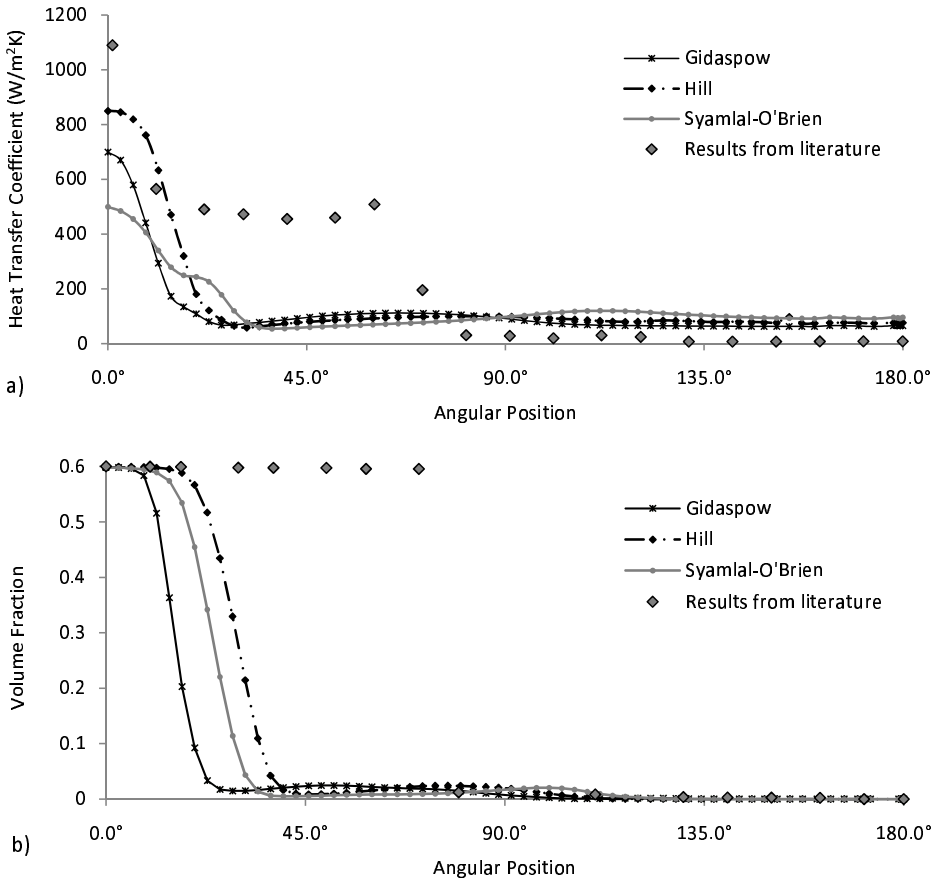

FIGURE 5.15: a) The local heat transfer coefficient using the molecular thermal conductivity model and b) the volume fraction of particles around the tube at 0.3 s for the first 180° comparing the three drag models and the predicted results from Schmidt and Renz [3].

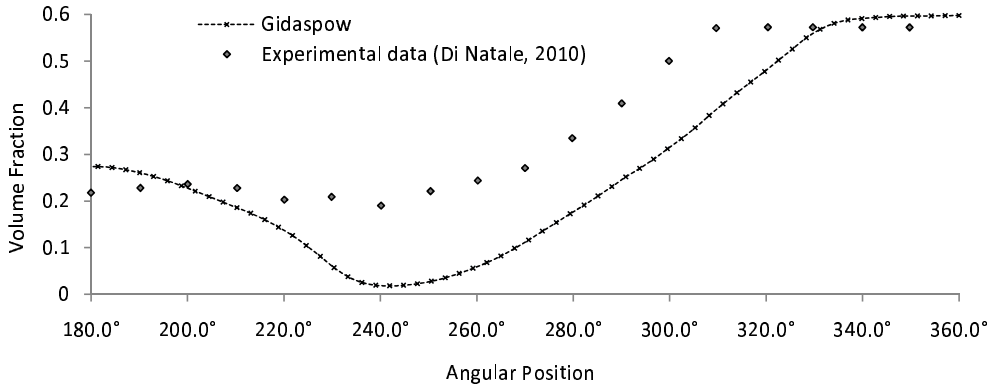

FIGURE 5.16: Time-averaged particle volume fraction compared to experimental results from Di Natale et al. [4] using the Gidaspow drag model.

distribution. The complete effective thermal conductivity, Eqn. 3.47, was also applied for the three drag models and the results are displayed in Fig. 5.18. The results show a dramatic increase in the local heat transfer coefficients due to the strong influence the granular temperature has on the thermal conductivities. The peaks of the heat transfer coefficients do not appear to occur at similar angular positions compared to the molecular contributions only. Stronger heat transfer fluctuations occur in regions which were previously seen to be dilute in 5.15. This is because in dilute regions particles are allowed to travel more freely gaining faster velocities than in dense areas where increased particle presence inhibits the motion of the particles. The granular temperature, Θ_s, which is utilised in the kinetic contribution, Eqn. 3.50, of the effective thermal conductivity, Eqn. 3.47, is taken to be one-third the mean square-velocity of the particles, $\Theta_s = 1/3 < \vec{v}_s^2 >$, therefore the faster the velocity of the particles the stronger the granular temperature contribution to the effective thermal conductivity. This overestimation of the heat transfer coefficient due to the inclusion of the particle kinetic conductivity was also observed previously [97].

Whilst Natarajan and Hunt [98] soundly suggested the effective thermal conductivity would be influenced by the particle kinetic conductivity as well as its molecular contribution, further research needs to carried out to determine a more effective model. It would be interesting to see how the kinetic contribution model differs should the effects of particle rotation be considered in the determination of the granular temperature. Realistically, experimental particles would have a slight roughness causing them to bounce off after collisions in both a translational and rotational manner, therefore the energy released due to both collisional directions could lead to a reduction in the value for the granular temperature.

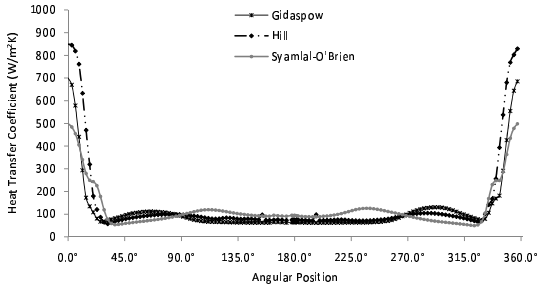

FIGURE 5.17: Local heat transfer coefficient using the molecular thermal conductivity model at 0.3 s for the full 360° circumference of the immersed tube comparing the three drag models.

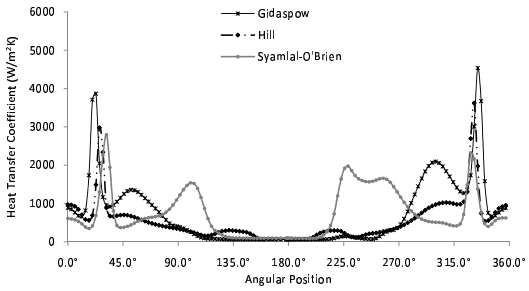

FIGURE 5.18: Local heat transfer coefficient using the complete effective thermal conductivity model at 0.3 s for the full 360° circumference comparing the three drag models.

5.2.4 Average heat transfer coefficients

The average heat transfer coefficient were extracted from the circumference of all the tubes at a distance of $6.25\text{x}10^{-5}$ m away and averaged for each of the three models. The results were plotted over a 3.0 s period for the standard Gidaspow drag model and the modified Hill-Koch-Ladd drag model and given in Fig. 5.19. These two drag models were chosen to highlight the differences between the standard Gidaspow drag model [65] which has been extensively used in the works of hydrodynamic and heat transfer modelling and the recently developed kinetic-based Hill-Koch-Ladd drag model which was derived from Lattice-Boltzmann theory [73–75]. The average for all the tubes in each model was calculated, namely the average of one tube for the 1-tube simulation, two tubes for the 2-tube simulation and three tubes for the 3-tube simulation.

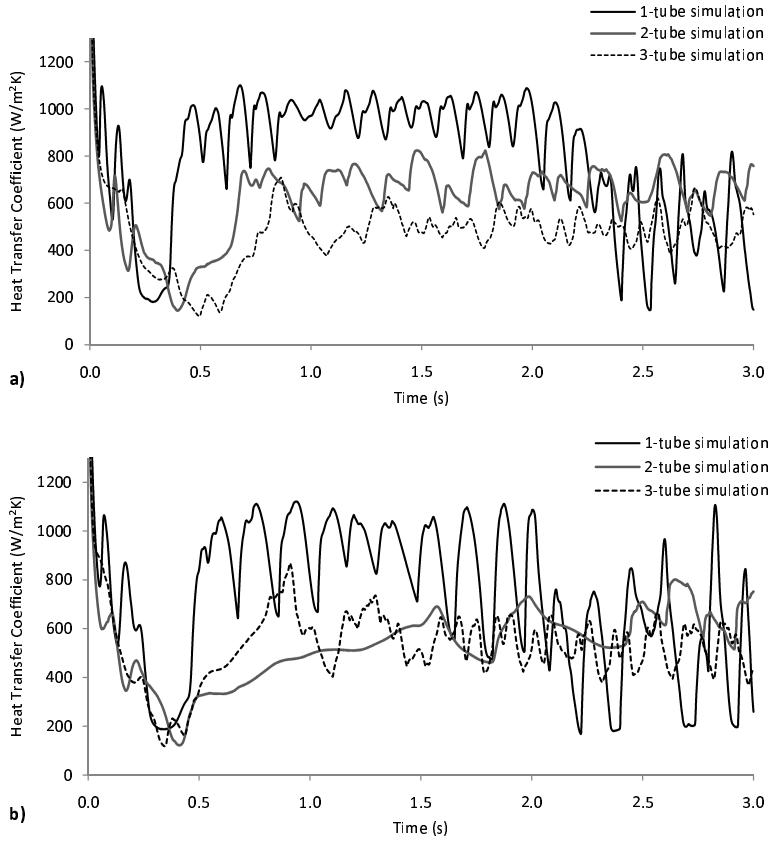

FIGURE 5.19: The average heat transfer coefficients for the three models using a) the Gidaspow drag model and b) the Hill-Koch-Ladd model over a period of 3.0 s.

The initially high value of heat transfer coefficient, seen with both models, is due to the simulation initial conditions assuming the bed is set to 293 K. In experimental conditions this would not occur as the wall initially heats up to the constant temperature of 373 K therefore the region near the wall would heat up with it. Within the first 0.5 s the average heat transfer coefficients decrease due to the build up of an air bubble below the tubes which leads to the encasement of the large air bubble. This was previously

observed in the contour plots in Fig. 5.12. By 0.5 s, for the 1-tube simulation, the bubble has completely passed the tube resulting in a sharp increase in the average heat transfer coefficient. As the number of tubes increases, there is a delay in the increase in average heat transfer coefficient also agreeing with Fig. 5.12 as the bubbles ascended the bed later with each additional tube. Furthermore, the average heat transfer of the 3-tube simulation is lower than the 1-tube and 2-tube simulations for both the Gidaspow and eventually the Hill-Koch-Ladd model. This could be due to the additional tube being positioned directly above the inlet leading to a build up of air on a more continuous basis hence reducing the average heat transfer coefficient.

Fluctuations occur in the average heat transfer coefficients for both models as air bubbles form below, blanket and break away from the tubes leading varying dense and dilute regions. The Hill-Koch-Ladd model shows a strong fluctuation in heat transfer coefficient for the single and triple immersed tube reactors indicating the model's sensitivity to the presence of excess air. However, the Hill-Koch-Ladd model for the dual immersed reactor shows a more smooth average heat transfer coefficient probably due to the tubes not being positioning directly above the fast air inlet. This allows the air flow to find an easier path past the tubes rather than being obstructed and having to break up leading to the majority of the tube being continually encased by a bubble. The Gidaspow model however picks up more fluctuations than the Hill-Koch-Ladd drag model for the 2-tube simulations.

Figure 5.20 shows the volume fraction contour plots of both models at intervals of 0.25 s after 2.0 s for the 1-tube simulation. The sudden drop in the average heat transfer coefficient, observed in Fig. 5.19, for the single immersed tube using both the Gidaspow and the Hill-Koch-Ladd models, respectively, would be due to the collection of air which forms above the tube and appears to remain as seen in Fig. 5.20. Air will travel around the tube, continually supplying more air to the region above it leaving a dilute region in constant contact against the top. Since Fig. 5.14 shows that the particle contact with the tubes in the 2-tube simulation does not appear to change dramatically and the continuous production of the smaller voidages in the 3-tube simulation from as early as 0.9 s, in Fig. 5.12; the average heat transfer coefficients in these two reactors remains generally similar magnitude for both the Gidaspow and Hill-Koch-Ladd models in Fig. 5.19. After 2.0 s the average heat transfer coefficient has a similar magnitude for all three reactors at approximately 500-600 W/m^2K.

The frequency of the fluctuations for the 1-tube simulation appear to be approximately 4 cycles in every 0.5 s for the Gidaspow model whereas the Hill-Koch-Ladd model has approximately 3 cycles in every 0.5 s. By looking at the volume fraction distribution between the two drag models in Fig. 5.15 the Hill-Koch-Ladd model shows a higher volume fraction of particles covering the 0-45° area of the tube compared to the Gidaspow model which only covers 0-22°. This larger particle contact area at 0.3 s could suggest that the model is delaying the release of the bubble from the tube or that the bubble

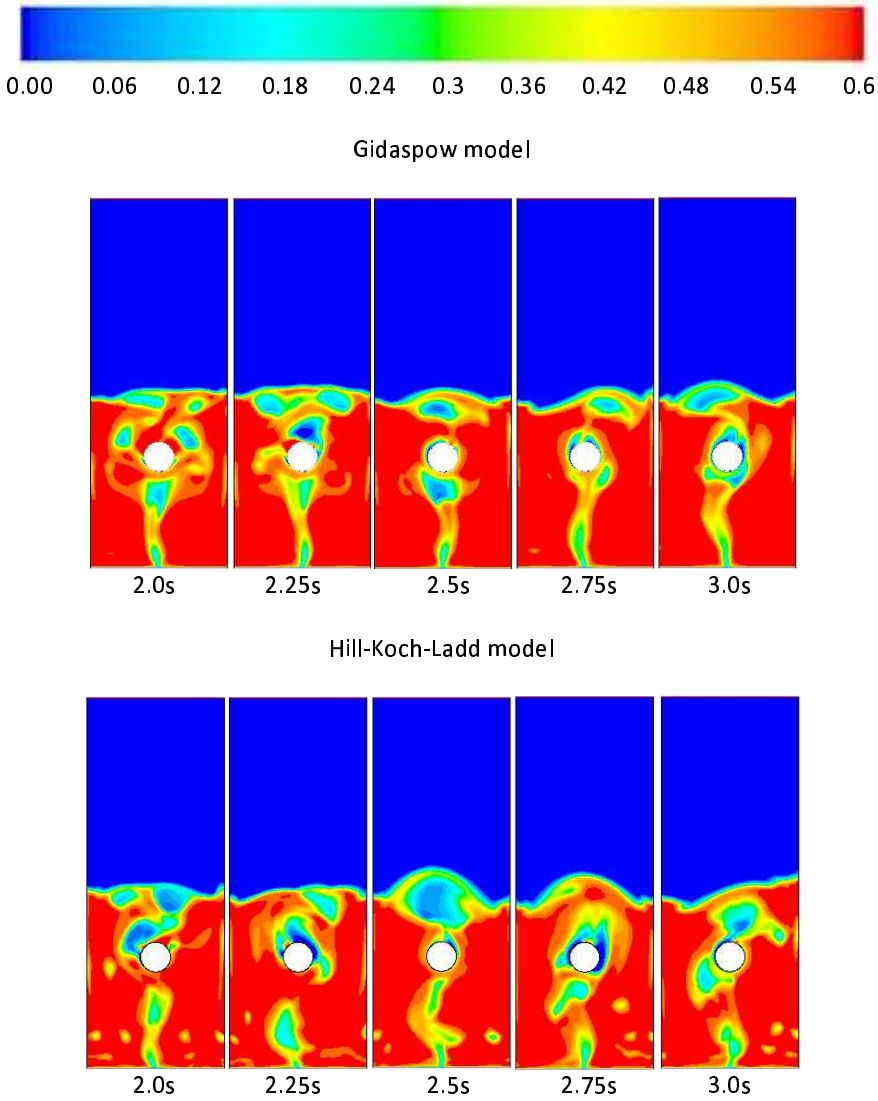

FIGURE 5.20: Contour plots of the particle volume fractions for the 1-tube simulation over the 2.0-3.0 s period using the Gidaspow and Hill-Koch-Ladd drag model.

does not encase around as much of the tube as the Gidaspow model does. Either way, this would explain the different frequency as the bubbles would be released less regularly and the slightly higher magnitude in the average heat transfer coefficient would be due to a larger area of particle contact with the wall.

Figure 5.21 shows the local heat transfer coefficient around the tube for the 1-tube model for both drag models at 3.0 s. The repositioning of the bubble above the tube shows the maximum heat transfer is reduced to approximately 280 W/m^2K for the Gidaspow drag model and approximately 850 W/m^2K for the Hill-Koch-Ladd drag model. Furthermore, the maximum heat transfer coefficient appears to have moved round the tube to around 45°, from 0° previously in Fig. 5.15, since the region above the tube is a dilute region resulting in a lower heat transfer in this area. The value given by the Gidaspow model agrees very well with the calculated maximum heat transfer coefficient from a tube

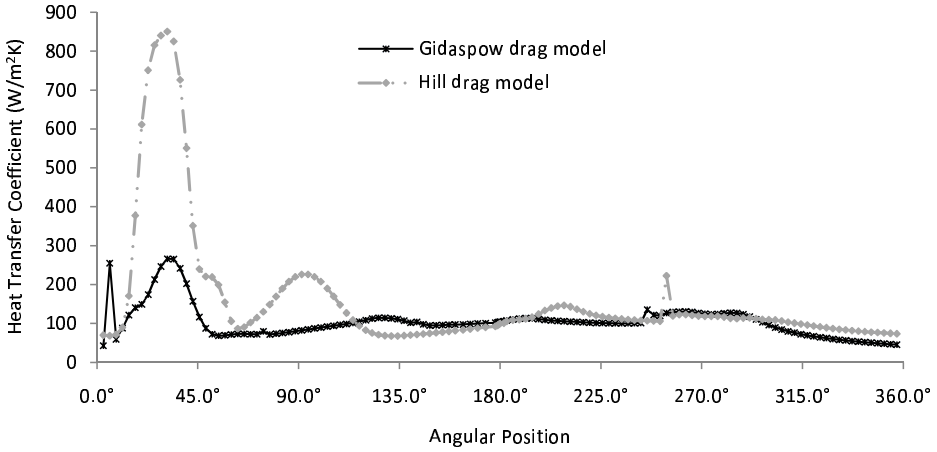

FIGURE 5.21: Local heat transfer coefficient around the tube for the 1-tube model for both drag models at 3.0 s.

determined by applying the correlation by Zabrodsky [149] who proposed:

$$\begin{aligned} \alpha_{t_{max}} &= 35.7 \lambda_g^{0.6} d_s^{-0.36} \rho_s^{0.2} \\ &= 296.466 \text{ W/m}^2\text{K} \end{aligned} \tag{5.1}$$

The average heat transfer coefficients from the individual tubes in the 3-tube simulation over a 3.0 s period are displayed for both the Gidaspow and Hill-Koch-Ladd drag models in Fig. 5.22 (a) and (b), respectively. The first 1.0 s show a decline on all three tubes as the air pockets gradually build up below each tube therefore reducing the average heat transfer coefficient. With both drag models, tube 3 starts to increase in heat transfer coefficient before tube 1 and tube 2 as the bubbles break away from tube 3 resulting in an increase in particle-wall contact around that tube. The average heat transfer coefficients from tube 1 and tube 2 are similar in frequency and wave amplitude due to their positions. However, there are small differences between the results of tubes 1 and 2, despite their symmetric positions, confirming further that the bed dynamics are not completely symmetric.

After 1.0 s, fluctuations settle into a regular pattern as the gas-particle flow mixes and regulates. The average heat transfer coefficient from tube 3 shows a stronger drop in heat transfer coefficient compared to the other two tubes due to its position directly above the fast air inlet collecting air around the tube hence suppressing the heat transfer. This explains the previous assumption in Section 5.2.4 for the lower average heat transfer coefficient from the 3-tubes simulation shown in Fig. 5.19. During a period of low heat transfer from tube 3, there is an increase of average heat transfer from the other two tubes. Once the air bubble around tube 3 increases sufficiently, it breaks away from the tube and ascends towards tubes 1 and 2 resulting in a decrease in the average heat transfer from those. At the same time, particles occupy the spaces left by the bubble that broke away from tube 3 leading to an increase in heat transfer from that tube.

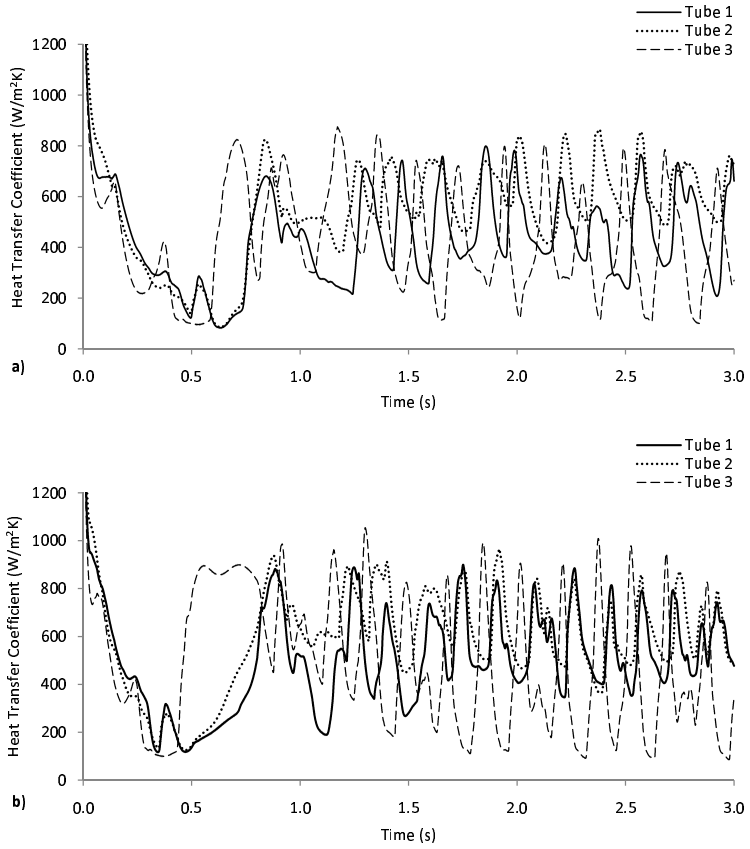

FIGURE 5.22: Average heat transfer coefficients from the individual tubes in the 3-tubes simulation with a) the Gidaspow drag model and b) the Hill-Koch-Ladd model over a period of 3.0 s.

5.2.5 Temperature distributions

Figure 5.23 displays the contour plots of the particle temperature distributions at 1.0 s for a reactor with one, two and three immersed tubes using the Gidaspow drag model. After 1.0 s there is a clear indication that more immersed tubes increases the temperature of the particles within the bed due to an increase in the heat transfer area. The higher temperatures are observed in the presence of dilute regions as the active particles travel from the heated walls through the voids. In the 3-tube simulation, the increase in the number of heated tubes along with the presence of more smaller particle carrying voidages results in a much higher temperature of particles compared to the other two reactors. The temperature distribution within the double tube reactor clearly shows the circulation of particles carrying higher temperatures.

The contour plot in Fig. 5.23 at 1.0 s does not display in detail the different temperatures in the near region of the tubes. The results are expanded in Fig. 5.24-Fig. 5.26 to display the particle and air temperature at 1.0 s at the five different distances from the tubes (given in Fig. 5.11 (c)) for the 1-, 2- and 3-tube simulation, respectively. Figure 5.24 displays the local results for the 1-tube simulation. A clear observation is that the particle and air temperatures are higher when closer to the tubes as expected. As the

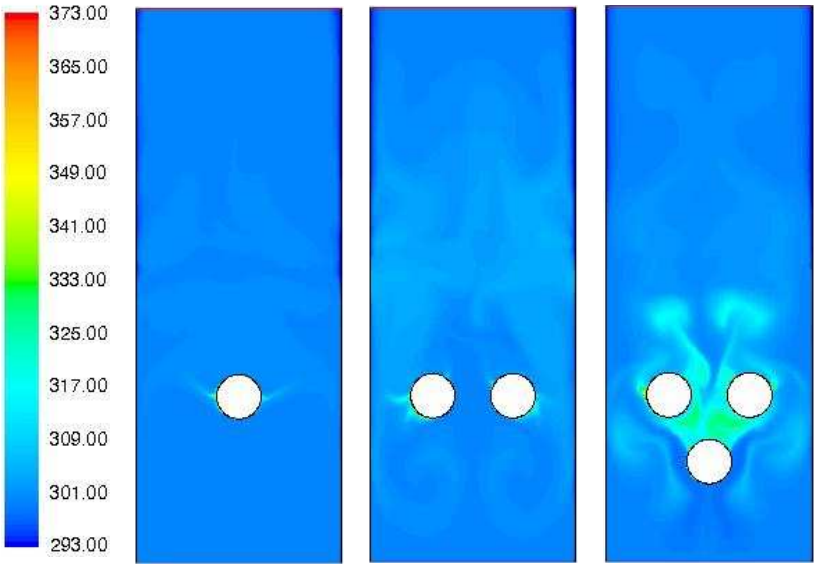

FIGURE 5.23: Contour plots of the particle temperature distribution within the three reactors at 1.0 s using the Gidaspow drag model.

distance from the tube increases the temperature change reduces until in there appears to be little change between the distances. The local temperature of the air however appears to be slightly higher than that of the particles. This could be due to the air voidages between compact particles and the tube being influenced by not only the heat from the tube but also the heat from the local particles.

The local particle volume fraction is also shown in Fig. 5.24. The peak temperatures for both particles and air can be seen during the transitions from dense to dilute regions. This will be due to the increased movement of particles in the vicinity of the tube as the air carries particles away from the wall. This mixing allows heated particles to travel and be replaced with cooler particles allowing the mixing heated particles to carry the heat to other local regions. At 135°, the volume fraction results show a transition from dilute to dense conditions however instead of an increased particle temperature there is a reduction. This would be due to the re-introduction of cooler particles against the bottom the tubes which are forced up by the fast air inlet. Whilst the local particles, one particle diameter away, heat up there is little room for particle movement leading to the confinement of the acquired heat to the local area near the tube.

Figure 5.25 and Fig. 5.26 display the local particle, air and volume fraction results for tube 1 and tube 2 in the 2-tube simulation respectively. As seen for the 1-tube simulation results in Fig. 5.24 the temperature of the particles and air is higher closer to the heated tube. Also the results show a relatively symmetrical distribution in the near-wall regions for the temperatures and volume fractions due to the symmetrical positioning of the tubes. The results again point to higher temperatures in the regions where the mixture is dilute and sufficient mixing is taking place. It can also be seen at approximately 45° on tube 1 and 315° on tube 2 that there is a significant peak in the

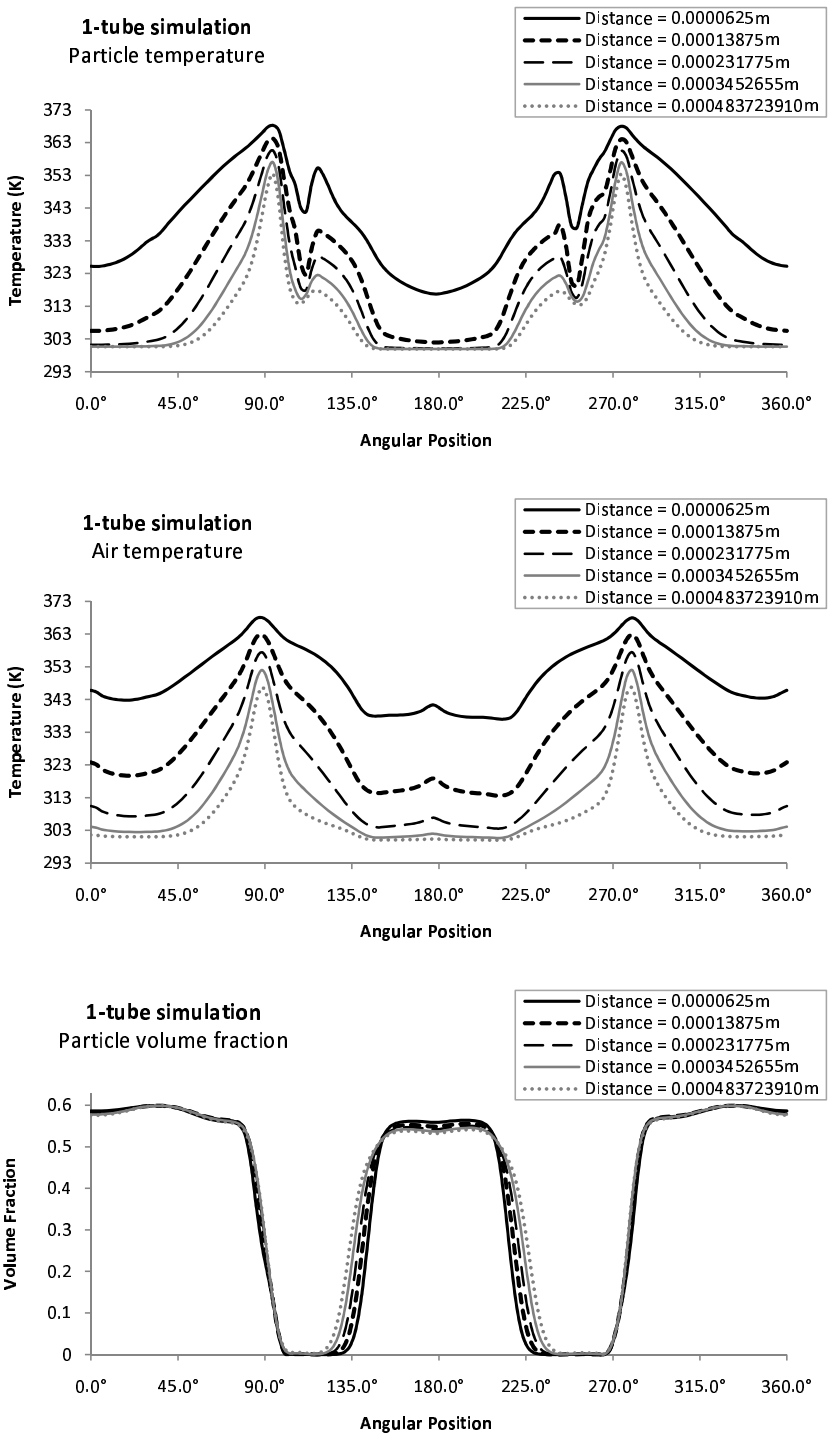

FIGURE 5.24: The local temperature particle temperature, air temperature and particle volume fraction at the five distances from the tube in the 1-tube simulation with the Gidaspow drag model at 1.0 s.

temperature of both the particles and the air whereas there is a very dense region of particles. This was not observed with the 1-tube simulation. It can be seen in Fig. 5.12 that the trajectory of the air bubbles appear to travel around the outside of the two tubes in the 2-tube simulation so the compacted particles against the wall at approximately 45° on tube 1 and 315° on tube 2 do not mix well. Therefore the increased residence time of the local particles against the wall would be the reason for this significant increase in temperature.

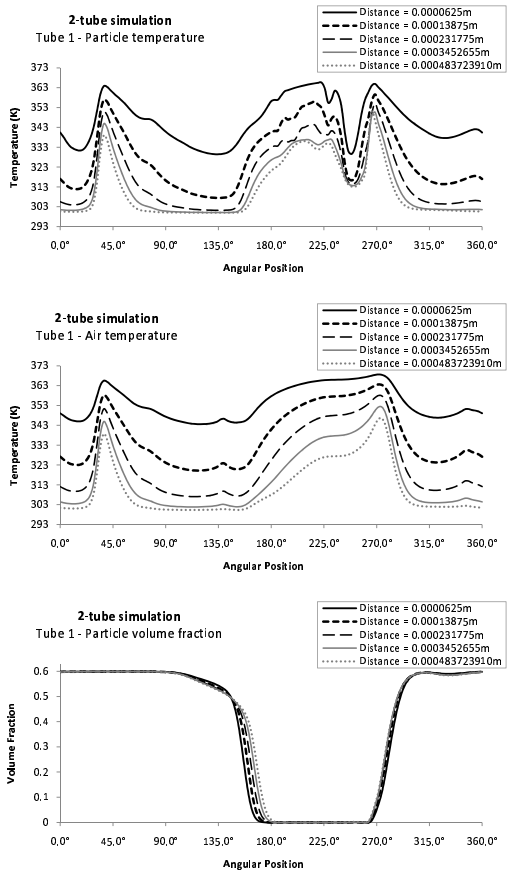

FIGURE 5.25: The local temperature particle temperature, air temperature and particle volume fraction at the five distances from tube 1 in the 2-tube simulation with the Gidaspow drag model at 1.0 s.

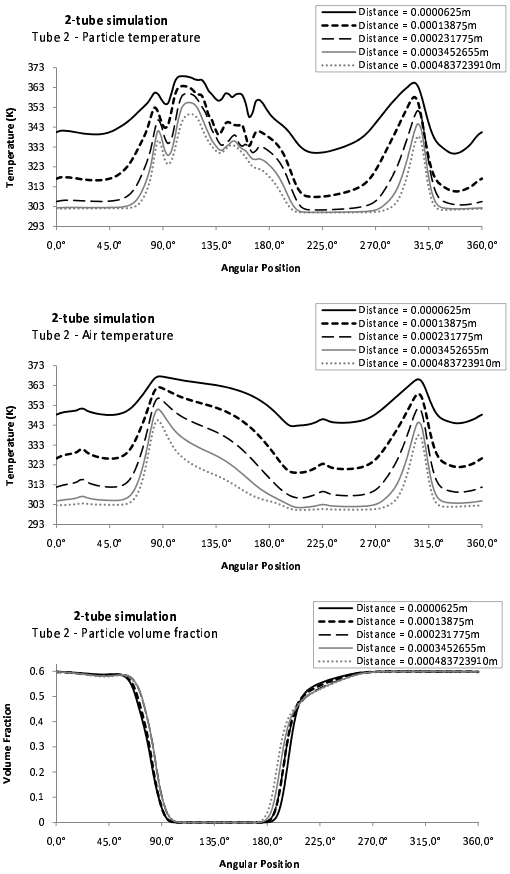

FIGURE 5.26: The local temperature particle temperature, air temperature and particle volume fraction at the five distances from tube 2 in the 2-tube simulation with the Gidaspow drag model at 1.0 s.

The particle temperature and volume fraction at the different distances from the tubes in the 3-tube simulation at 1.0 s are given in Fig. 5.27 and Fig. 5.28, respectively. The third tube shows a general symmetrical distribution for both the particle temperature and volume fraction results whereas tube 1 and tube 2 shows significant asymmetry from both tube 3 and each other. This is because increasing the tubes lead to the break up of larger bubbles into smaller ones particularly in the region between the three tubes. Resulting in increased mixing which would produce an unpredictable distribution of particles within the vicinity of the tubes. As seen in the previous reactors and as

expected the temperature is highest closer to the heated tube. However, compared with the results from the 1-tube and 2-tube simulations the results for the furthest distances from all three tubes show a overall increase in particle temperature. This is again a consequence of the increased mixing between the tubes and is explained further with the volume fraction results in Fig. 5.28. It is clear that other than the tops of the tubes, approx 315° - 45°, there are very few dense particle regions enhancing the movement of the particles to distribute the heat more effectively.

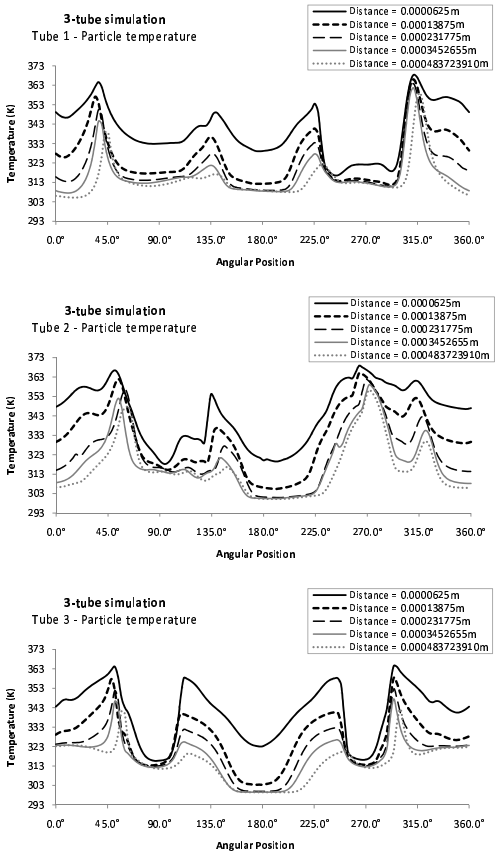

FIGURE 5.27: The local temperature particle temperature at the five distances from the tube in the 3-tube simulation with the Gidaspow drag model at 1.0 s.

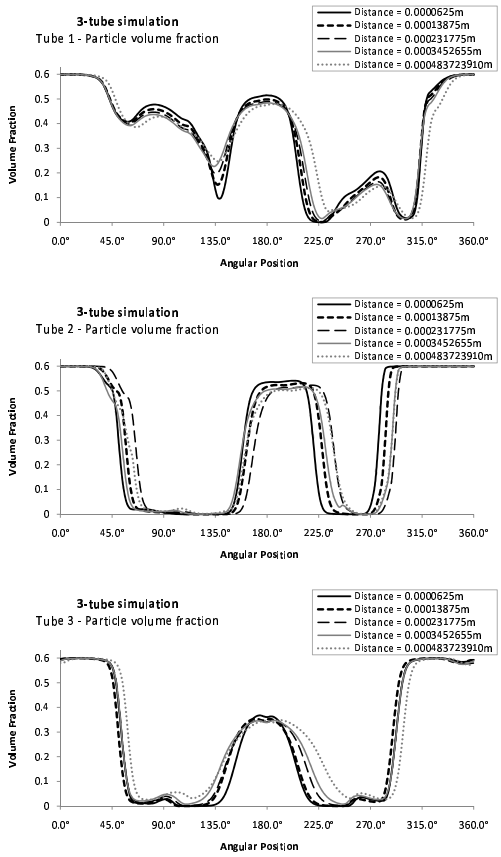

FIGURE 5.28: The local particle volume fraction at the five distances from each of the tubes in the 3-tube simulation using the Gidaspow drag model at 1.0 s.

In order to display the effect of varying particle volume fractions in the near-tube regions with varying time the results in Fig. 5.29 show the instantaneous average particle temperature collectively taken from all the tubes in the 1-, 2- and 3-tube simulations from the furthest distance of 0.000483723910 m from the tubes over a period of 3.0 s with the Gidaspow drag model. The initial 0.75 s indicate the simulations forming a regular pattern as the gas-particle flow mixes and regulates. The average temperature from all the tubes in the 3-tube reactor is significantly higher than those of the other two reactors agreeing with the instantaneous results at 1.0 s in Fig. 5.27. It can also be seen that the results of the 2-tube simulation show a slight increase over the results

of the 1-tube model. This would confirm that increasing the number of tubes would increase the temperature in the reactor faster. However since these results are only in the near-tube region of the tubes where the temperature from the other tubes would not directly influence these results it could also indicate that improved mixing within the near-tube regions have a significant influence on temperature distribution.

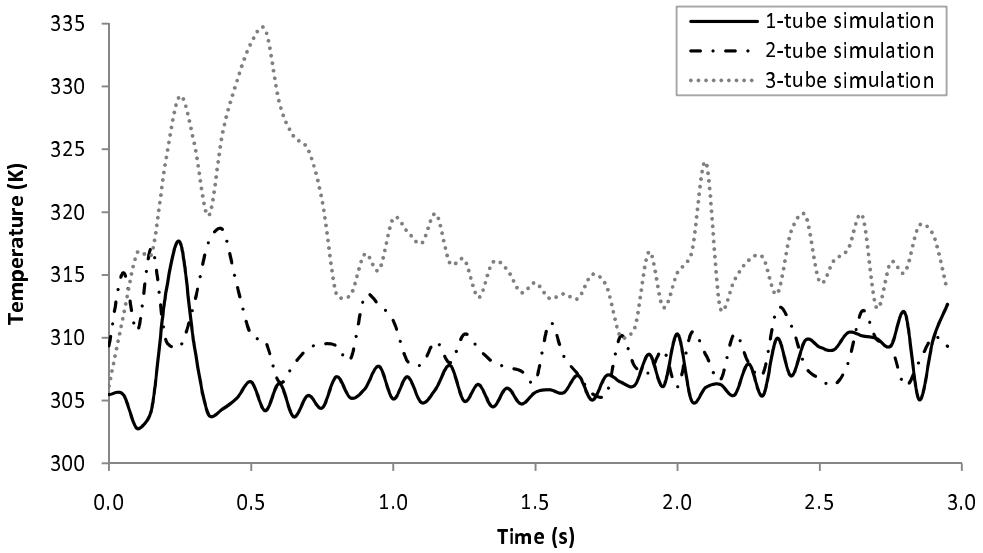

FIGURE 5.29: Instantaneous collective average particle temperature from all the tubes in the 1-, 2- and 3-tube simulations at the furthest distance from the tube over a period of 3.0 s with the Gidaspow drag model.

5.3 Conclusions

A two-fluid Eulerian-Eulerian model simulation has been carried out applying the kinetic theory of granular flow (KTGF) to a wall-to-bed bubbling fluidised bed. The local heat transfer coefficients were compared against experimental data for two drag models, namely the Gidaspow and the Syamlal-O'Brien drag models. Contour plots comparing the two drag models showed very similar features during the passage of the bubble up the wall. However differences were observed in the local near-wall region as the different drag models showed different clustering effects at the wall. The dependence of the heat transfer coefficient on the volume fraction was proven where regions of higher particle volume fraction resulted in a higher heat transfer. Both drag models gave a local heat transfer coefficient at a specific point in the bed which was agreeable with experimental data. Multiple bubble formation occurred due to the partitioning of the bubbles from the recirculating particle bed back towards the wall. Both models picked up the presence of multiple bubble formation from the start but the Syamlal-O'Brien model took approximately 1.5 s to displays these peaks to be periodically of a similar magnitude and time. The coefficient of restitution was varied but led to very little variation in the local

heat transfer coefficient. However, increasing the particle diameter greatly reduced the local heat transfer coefficient due to an increased porosity between the compact particles which was taken into account in the models. Increasing the velocity gave reasonable results however the development of multiple bubble formation was detected more at an early stage by both models and appeared to affect the local heat transfer coefficient more with increasing time. This suggests that the simulation should be extended and compared with data taken for a longer period. A simulation was allowed to run for 8.0 s to determine if periodic behaviour occurred. The results showed a gradual decrease in local heat transfer coefficient and multiple bubble formations occurring during the time that the fast inlet was supplying air. This is due to the bed becoming more regular and the circulating particles partitioning the elongated bubble along the wall. These effects were observed after 1.5 s simulation time confirming that previous simulations in the literature were not run long enough to allow the flow to fully develop.

Three tube-to-bed heated fluidised bed reactors have been modelled using an Eulerian-Eulerian kinetic theory of granular flow model. A reactor containing one immersed tube was set up based on a model from the literature [3] and compared with their predicted results. The models looked at the flow characteristics and local heat transfer coefficients using multiple drag models including the modified Hill-Koch-Ladd drag model derived from kinetic theory and modified for the incorporation into two-fluid modelling. The flow characteristics showed a close resemblance to the symmetrical results in literature. Increasing the number of tubes improved the heat transfer into the bed due to the increased heat transfer area and the break up of bubbles to form smaller particle carrying voidages. Moreover, extending the simulation time from the previously carried out 0.45 s to 3.0 s shows an increasingly asymmetric distribution. The local heat transfer coefficients for all the drag models agreed reasonably well with the results obtained in the literature for an effective thermal conductivity consisting of only a molecular contribution. The results from the kinetic contribution greatly overestimated the values of the heat transfer coefficients due to the strong influence that the granular temperature has on the kinetic theory of granular flow. The local instantaneous volume fraction distribution varied greatly from the predicted results observed in the literature yet the present time-averaged particle volume fraction results followed the expected trend determined experimentally [4], thus confirming that the previous assumption made in the literature [3] to use a symmetric bed would not correctly capture the correct flow dynamics. The average heat transfer coefficient extracted from the circumference of the tube for the three models were taken and plotted over a 3.0 s period for the standard Gidaspow drag model and the modified Hill-Koch-Ladd drag model. The results showed that the Gidaspow model detected the passage of the bubble around the tube before the Hill-Koch-Ladd model however their average heat transfer coefficient values were of similar magnitude. Furthermore, for multiple immersed tubes the average heat transfer coefficient differed in magnitude for each tube, again confirming the asymmetric flow

distribution and the effect of tube positioning. A contour plot for the temperature distribution of the particles showed that increasing the number of tubes increases heat transfer from the tubes to the particles and the flow around the tubes resulting in increased temperature. The local particle temperature and particle volume fractions at different distances from the tube were analysed for the three reactors and found that increased particle temperature occurred in the transition from dense particle-laden regions to dilute region as the particles experience mixing. The transition from dilute to dense particle regions resulted in local temperature reduction as new cooler particles are introduced to the local vicinity. The instantaneous average particle temperature for the three reactors showed that increasing the number of tubes resulted in an increase in the local particle temperature where improved mixing was shown to be a contribution.

Chapter 6

Reaction Modelling

This chapter incorporates reaction kinetics into an Eulerian-Eulerian model of a bubbling fluidised beds coal gasifier. The chapter is categorised into two sections; the first carries out a two-dimensional parametric study for different model conditions and the effects such variations have on the emission compositions and temperatures; the second section expands the work further into three-dimensional modelling by analysing the effects of different inlet compositions and velocities and the modification of fuel properties to that of wood with different composition ratios of coal:wood. The results presented in the two-dimensional modelling section of this chapter are quite extensive and available in two separate papers journal papers. The first paper introduces the initial results of this model and is published in the Chemical Engineering Journal [16]. A second paper is based on the parametric study within the two-dimensional model and is under review in the Industrial and Engineering Chemistry Research journal [17]. Finally, conclusions are made based on the results observed throughout this chapter.

6.1 Two-dimensional modelling

The model was set up according to the experimental study of Colombian coal by Ocampo et al. [5]. Figure 6.1 displays a sketch of the experimental set up used. The reactor had an internal diameter of 0.22 m and height of 2 m with a screw-feeder located at 0.3 m for the introduction of the coal and limestone mixture. A mixture of air and steam was introduced into a bed at different rates and temperatures as given in Table 6.1.

In the model, an initial bed of limestone and char was set to the height of 1.0 m with a volume fraction of 0.48; an equal volume fraction was used for the two solid phases set to 0.24 each. The solids properties for the coal, limestone and char are given in Table 6.2. The simulation considers four separate phases, a gaseous phase and three solid phases, limestone, coal and char. The gaseous phase consists of a mixture of 8 species, namely,

TABLE 6.1: Operating conditions and experimental results for the 2D BFB gasifier.

Operating Conditions	Model 1	Model 2
Air supply (kg/h)	21.9	17.0
Steam supply (kg/h)	4.7	4.7
Coal feed (kg/h)	8.0	8.0
Limestone feed (kg/h)	0.8	0.8
Air and steam		
temp at entrance (K)	693.15	686.15
Temperature of reactor (K)	1128.15	1085.15
Experimental results		
H_2 (%)	8.53	8.84
CO_2 (%)	19.31	18.38
N_2 (%)	60.37	61.10
CH_4 (%)	0.84	1.07
CO (%)	10.94	10.59

H_2O, O_2, CO_2, CO, H_2, CH_4, tar and N_2. As carried out by previous researcher [63, 150], the tar is regarded as C_6H_6 since the composition of tar is usually regarded as condensed nuclei aromatics. The limestone consists of two pseudo-species - $CaCO_3$ and CaO. When limestone calcination is considered, calcium carbonate, $CaCO_3$, breaks down to produce calcium oxide, CaO, and carbon dioxide, CO_2. The CaO produced would then become the active solid in the absorption of sulphur dioxide, SO_2, should the inclusion of SO_2 be considered leading to limestone desulphurisation. However, due to the low amount of sulphur and nitrogen within the coal, the inclusion of an additional phase species based on the low amounts of these compounds would not be computationally beneficial therefore the present model does not account for their presence in the chemical processes. Limestone calcination is considered but not limestone desulphurisation.

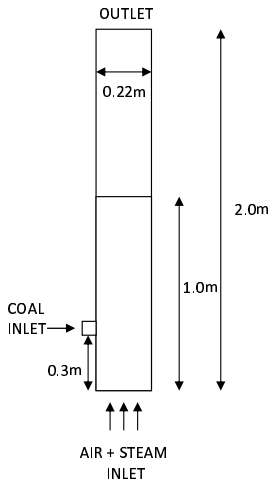

FIGURE 6.1: Experimental setup of the BFB gasifier taken from Ocampo et al. [5].

TABLE 6.2: Characteristics of solids phases in the BFB coal gasifier.

Coal Properties			
Proximate Analysis (wt%)			
Moisture		2.6	
Volatile matter		41.8	
Fixed carbon		54.1	
Ash		1.5	
Ultimate Analysis (wt%)			
Carbon		75.3	
Hydrogen		5.4	
Oxygen		15.6	
Nitrogen		1.8	
Sulphur		0.4	
Ash		1.5	
Others	*Limestone*	*Coal*	*Char*
Mean particle size (m)	0.0006	0.00062	0.00060
Apparent density (kg/m^3)	2700	1250	450
Specific heat (J/kg K)	840	1600	1600
Thermal conductivity (W/m K)	1.33	0.107	0.107

6.1.1 Mesh generation

A mesh was created using 2215 quadrilateral cells. The cells near the walls were not refined further as the purpose of the model was to capture the gasification processes within the bed and not the near wall behaviour. Boundary conditions for the gas phase were set to no-slip and for the particulate phase a tangential slip condition was imposed which was developed by Johnson and Jackson [146] using the previously utilised specularity coefficient of 0.25. The cell size in the horizontal direction was 0.01 m whilst the vertical direction was set to 0.02 m replicating a domain of (22x100) cells as used previously [63, 151]. The present model however refines the region near the coal inlet further to a minimum of 0.0004 m horizontally and 0.0008 m vertically to correctly capture the devolatilisation characteristics near the fuel inlet as the fuel is introduced.

6.1.2 Phase segregation

A brief analysis of the gas-solid dynamics in the bed is considered before the effects of the reaction kinetics are studies. Figure 6.2 displays the volume fraction of the gases for model 1 over a 0.5 s period after steady state conditions were achieved. There are a number of observations that can be seen including the formation of bubbles along the

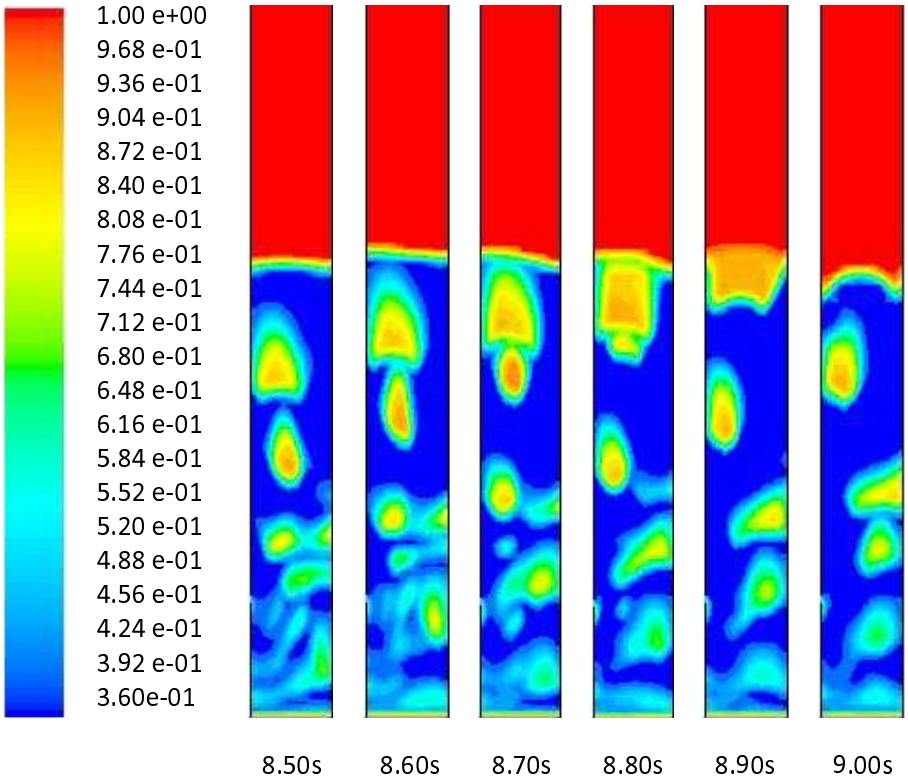

FIGURE 6.2: Gas volume fraction within the BFB for model 1 over a period of 0.5 s.

left side of the reactor, formation of bubbles in the lower region of the bed and also the variation of bed height. The formation of bubbles up the left wall is due to the build up of gaseous products after devolatilisation has taken place near the fuel inlet on the left hand side of the reactor. As the gases build up, the bubbles increase in size and continue to rise up through the bed. The formation of larger bubbles near the top of the bed is a result of the coalescence of smaller bubbles. It is due to the movement of these bubbles through the bed that mixing is enhanced within a bubbling fluidised bed. The bubbles formed in the lower section of the bed are small in comparison to those observed at the top of the bed. Their formation originates endogenously from the build up of the gaseous products due to the heterogeneous reactions. At the inlet the oxygen concentration is highest and combustion takes place immediately upon impact with the char particles in the bed. The gases form small bubbles that continue up the bed increasing in size as further reactions and coalescence take place.

Figure 6.3 displays the gas, limestone and char volume fractions within the bed. The gaseous bubbles are seen in Fig. 6.3 (a) to begin formation at the base of the reactor, increasing with size as the bubbles rise and coalesce. The bubble coalescing phenomenon can be seen half way up the bed where two smaller bubbles are on the verge of merging into a larger one. Also near the fuel inlet a small collection of pyrolysis products has formed and is awaiting the passage of a larger bubble from below to merge with and

travel up the bed. This phenomena can be seen in the early stages of Fig. 6.2.

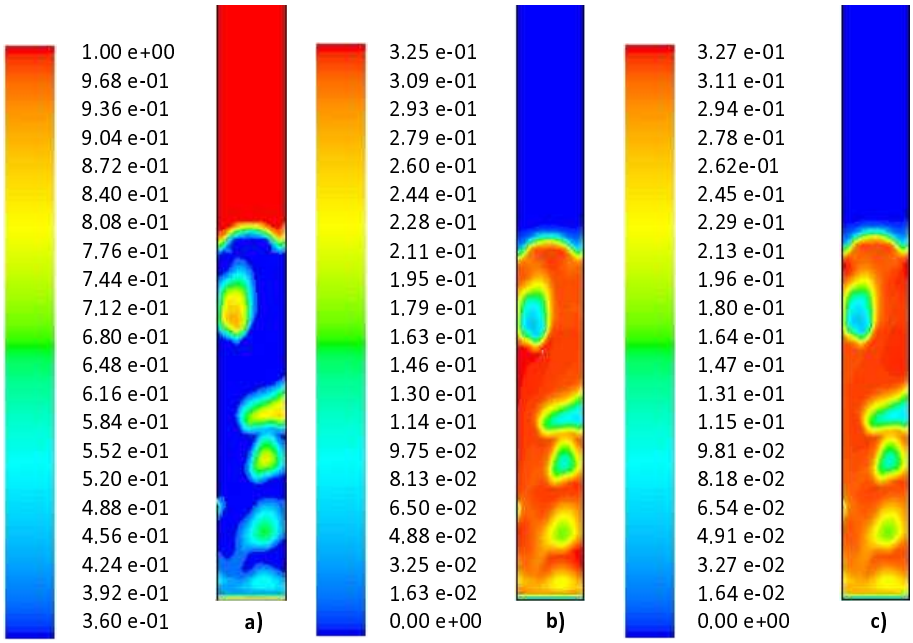

FIGURE 6.3: Volume fraction distribution within the bed at 9.0 s for a) gases, b) limestone and c) char.

The volume fraction of the limestone and char in Fig. 6.3(b) and Fig. 6.3 (c), respectively, show a similar distribution of particles within the bed. Gerber et al. [114] displayed particle segregation of two phases with different particle diameters and the same particle densities. In this case, the particle diameters remain the same however the densities of the limestone and char differ greatly. Although no clear distinction is observed with regards to segregation in Fig. 6.2 closer inspection indicates that the lower density particles, namely char, are segregating to the top of the bed. In order to observe these variations more effectively the relative volume fraction of the char and the limestone were compared in the bed by removing the volume fraction of char from limestone in each cell ($\alpha_l - \alpha_{ch}$). Therefore, positive values indicate a higher presence of limestone within the cell whereas negative values indicate a higher volume fraction of char. The result for the limestone $(\alpha_l - \alpha_{ch}) > 0$ and the char $(\alpha_l - \alpha_{ch}) < 0$ are displayed in Fig. 6.4. The results show a collection of limestone towards the base of the bed whilst the char phase slightly dominates the centre and the top of the bed. The limestone has a higher density than the char which would result in its settlement at the base of the bed whereas the smaller char particles segregate to the top of the bed.

A higher presence of char seen in the centre of the bed can be explained by looking at the positioning of the gaseous bubbles, more specifically the smaller bubbles near the base of the bed. An increased volume fraction of char within the bubbles indicates that the

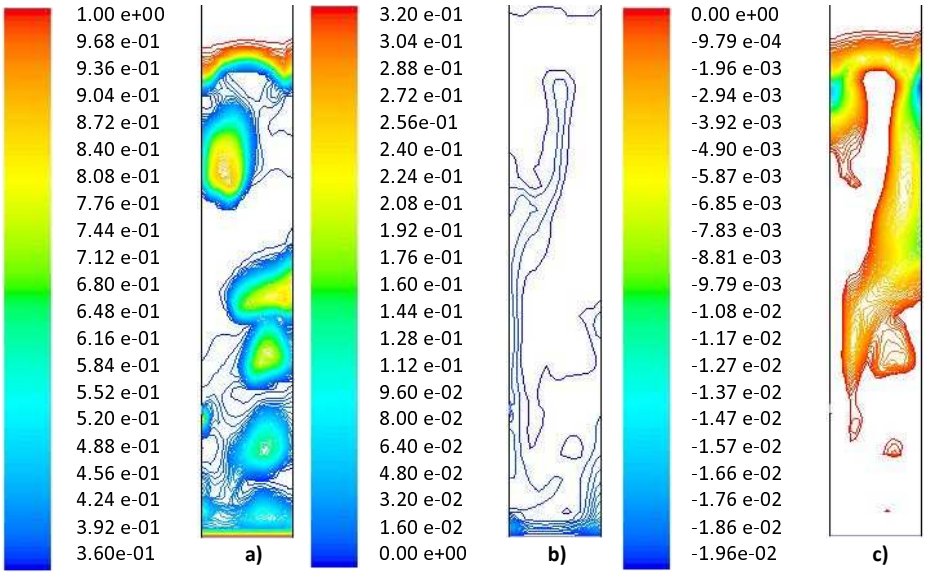

FIGURE 6.4: a) Gaseous volume fraction and the relative volume fraction distribution in the bed for b) limestone $(\alpha_l - \alpha_{ch}) > 0$ and c) char $(\alpha_l - \alpha_{ch}) < 0$.

bubbles have a strong impact on these lower density particles compared to the higher density limestone particles. The variation in particle properties would be responsible for these slight changes as different sized particles and different densities are influenced greatly by the flow dynamics. This is confirmed by the different minimum fluidisation velocities for the char and limestone phases, i.e., $U_{mf,ch} \approx 0.055$ m/s and $U_{mf,l} \approx 0.33$ m/s, respectively, and their different terminal velocities, i.e., $V_{t,ch} \approx 5.05$ m/s and $V_{t,l} = 30.3$ m/s. The ascending bubbles continually transport char particles through the bed resulting in a build up at the top of the bed. This mixing behaviour is a reason why a bubbling bed allows for excellent heating properties as the higher temperatures observed at the base of the bed, discussed further in Section 6.1.8, can be carried through the bed via the char particles in the bubbles.

6.1.3 Devolatilisation models

Two devolatilisation models, namely, the Badzioch model [119] and the Kobayashi model [137], were tested and the mole fraction of the gaseous species, averaged over a period of 80.0 s, are compared with experimental data in Fig. 6.5. Both models agree fairly well with the experimental data although there is a distinct variation in the mole fraction of CO_2 as the composition of CO is higher than that of CO_2 unlike the experimental results. This is expected as the bed in the present model was formed of both char and limestone whereas the majority of the experimental bed was limestone until coal was slowly added and mixed before gasification was began. As a result, the catalytic behaviour of the char consumed the CO_2 faster via the Boudouard reaction (R3) leading to an increase in the concentration of CO. The concentrations of CH_4 in Fig. 6.5 are extremely low and not

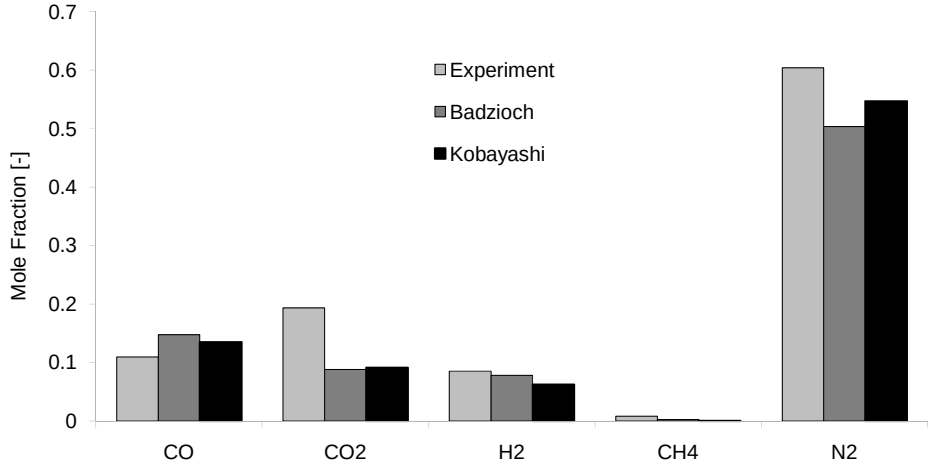

FIGURE 6.5: Mole fraction comparison of the gaseous products from the Badzioch and Kobayashi models with experimental data from Ocampo et al. [5].

clear, therefore Fig. 6.6 focuses on the CH_4 compositions. Both models under predict the mole fraction of CH_4 which could be down to the low mass fraction of CH_4 given by the Loison and Chauvin correlation [122] for the yield of volatiles released during devolatilisation. A study of the various yield correlations would be highly advantageous as different yields would be given for different yield correlations.

FIGURE 6.6: The mole fraction comparison of methane, CH_4, from the two devolatilisation models with the experimental data from Ocampo et al. [5].

Figure 6.7 displays the instantaneous mole fraction of the exiting gaseous products over a 100.0 s period through the outlet for both devolatilisation models. It can be seen that the Kobayashi devolatilisation model appears to have reached steady state conditions for all gaseous species whereas the Badzioch model does not. The species CO and H_2 appear to increase in mole fraction with time whereas CO_2 and H_2O decrease slightly. This could be due to the Kobayashi model's incorporation of yield factors which modify the volatile release based on local temperatures whereas the Badzioch model does not.

Since particles can migrate due to the mixing behaviour of the bed the local temperature would change. The Kobayashi model would recognise this change in temperature and choose its volatile release accordingly whereas the Badzioch model would assume the same volatile release for lower temperatures as for higher temperatures. The increased concentration of these volatile species in regions of lower temperatures would promote more heterogeneous reactions leading to a slight increase in their products, namely CO and H_2 as observed in Fig. 6.5.

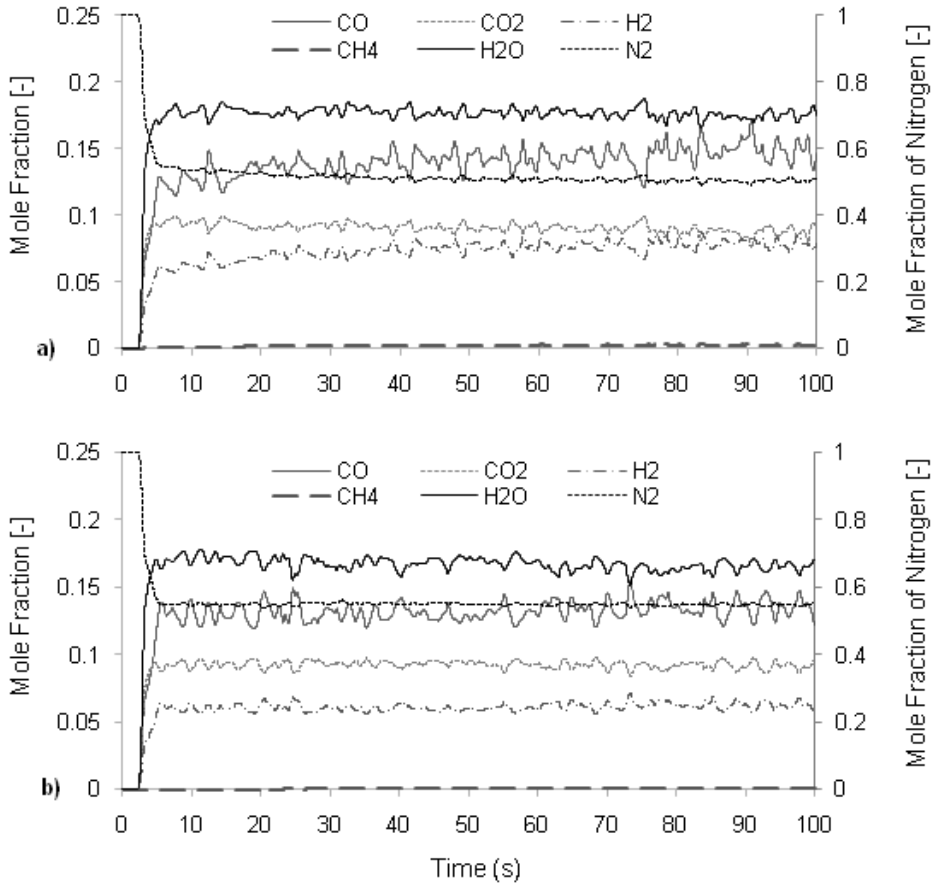

FIGURE 6.7: The instantaneous mole fraction of the gaseous products over a 100.0 s period through the outlet for the a) Badzioch and b) Kobayashi devolatilisation model.

The increase in H_2 would explain why the concentration of CH_4 in Fig. 6.6 is higher for the Badzioch model compared to the Kobayashi model. A higher concentration of H_2 would influence the methanation heterogeneous reaction (R4) resulting in an increase in CH_4. Since the Badzioch devolatilisation model does not appear to have reached steady state conditions after 100.0 s with regards to the mole fraction compositions the Kobayashi model was carried out for the remaining models.

6.1.4 Heterogeneous and homogeneous reactions

Figure 6.8 displays the reaction rates of the different heterogeneous reactions that take place in model 1. It is apparent that the mole fraction of O_2 is confined to the vicinity of the air inlet where it is immediately consumed with the combustion reaction (R1). The steam gasification reaction (R2) is also dominating the lower region of the bed as steam is introduced through the base of the reactor and gradually consumed. In the case of the combustion reaction, O_2 is completely consumed within the local area of the inlet as it is not the product of any further reactions unlike the H_2O which is the product of a number of homogeneous reactions.

It can be seen that the combustion reaction takes place faster than the remaining reactions. This is because the concentration of O_2 is much higher in the vicinity of the air/steam inlet compared to the other species throughout the bed. As a consequence of the fast reaction rate there is a fast production of CO_2. The Boudouard reaction takes place throughout the bed but predominantly within the lower region indicating that although the combustion reaction is the dominant reaction within the vicinity of the inlet, CO_2 as its product immediately reacts with the surrounding chars. With increasing bed height CO_2 and H_2O are consumed because the species continually interact with more of the char phase leading to slow heterogeneous reactions higher in the bed.

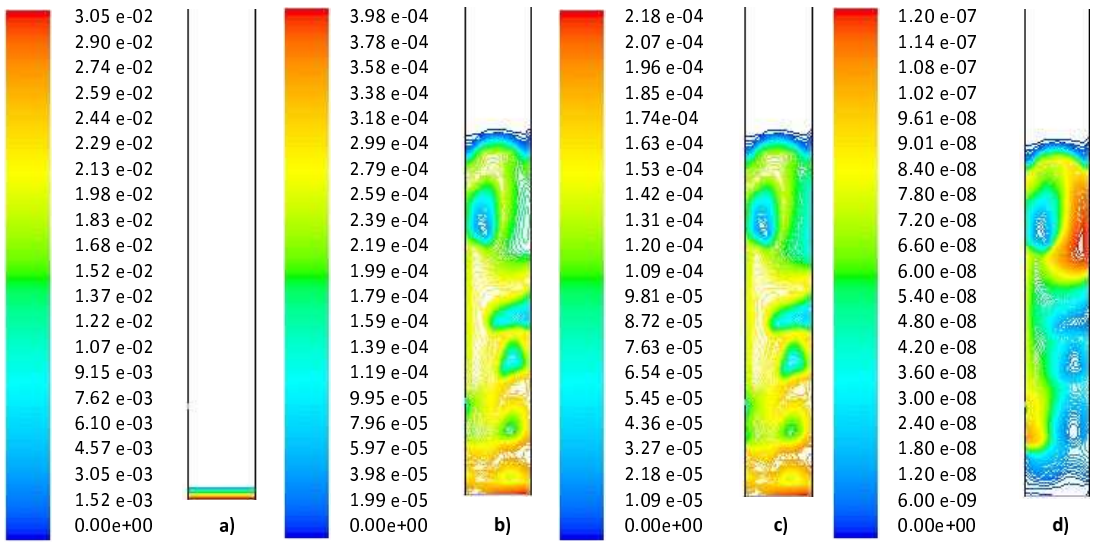

FIGURE 6.8: The reaction rates of the heterogeneous reactions **a)** C - O_2, **b)** C - H_2O, **c)** C - CO_2 and **d)** C - $2H_2$.

It can be seen in Fig. 6.8 (d) that the methanation reaction takes place much slower than the other heterogeneous reactions. There is a large region at the top of the bed where the methanation reaction is seen to be taking place faster. Whilst comparing Fig. 6.8 (d) with Fig. 6.3 (a) this area is a particle laden region therefore the presence of char

would suggest that the steam gasification reaction could have previously dominated this region leading to an increase in the H_2 species. Near the fuel inlet there appears to be a region with a slightly increased methanation reaction rate. This could be due to the release of H_2 as a devolatilisation product and the gradual accumulation of H_2 as a product of the steam gasification heterogeneous reaction within the vicinity.

Figure 6.9 shows the oxidation of CO, H_2 and CH_4 all take place within the vicinity of the primary inlet where the concentration of O_2 is highest. It is observed that the CO oxidation reaction took place much faster than the H_2 and CH_4 oxidation reactions due to the fast reaction rate of the Boudouard reaction (R3) leading to a higher concentration of CO near the air inlet as seen in Fig. 6.8. The reaction rate for the CH_4 oxidation reaction is much lower than the other homogeneous reactions as the only heterogeneous reaction that produces CH_4 is the methanation reaction which takes place extremely slowly, especially in the lower regions where there is a limited concentration of H_2 to activate the reaction in the first place.

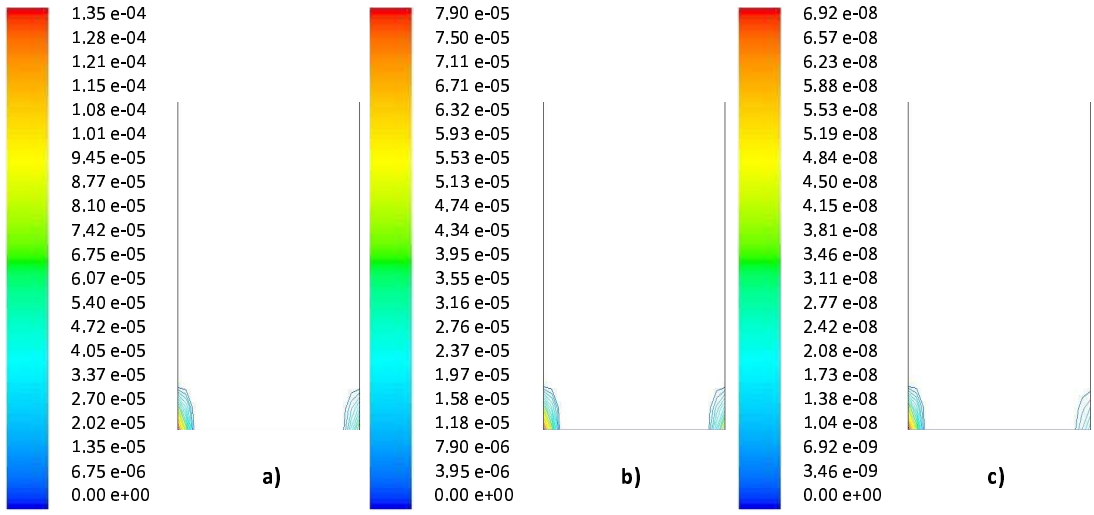

FIGURE 6.9: The reaction rates of the homogeneous oxidation reactions **a)** CO - $0.5O_2$, **b)** H_2 - $0.5O_2$, **c)** CH_4 - $2O_2$.

6.1.5 Comparisons with experimental data

The mole fraction composition of the exiting gases for model 1 and model 2, where limestone calcination was not activated, are compared to the experimental results given in the literature [5] and given in Fig. 6.10. The models both provide a reasonably good representation of the experimental compositions however it can be seen, particularly in model 1, that the composition of CO is higher than that of CO_2 unlike the experimental results. As explained previously, this is due to the bed in the present model being formed of both char and limestone whereas the experimental bed consisted primarily of limestone

until coal was slowly added and mixed before gasification had begun. Resulting in the Boudouard reaction taking place faster producing more CO. However, the results of model 2 display similar mole fractions of CO and CO_2 due to the initial set up having a lower temperature distribution. A lower bed temperature would reduce the Boudouard reaction rate, along with other reaction rates, due to the high temperature dependency of the reactions leading to lower production of CO and lower consumption of CO_2. For further comparison, the average mole fractions for model 1 and model 2 are also given in numerical form in Table 6.3 along with the experimental results.

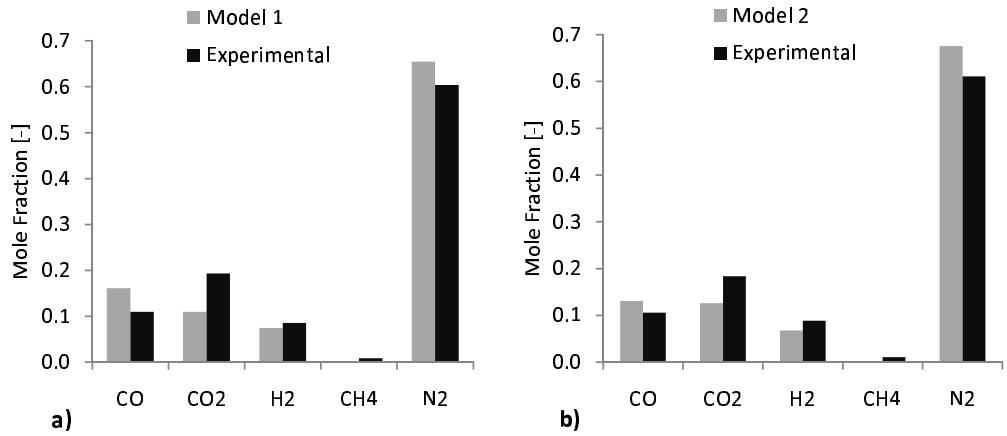

FIGURE 6.10: Average mole fraction of the exiting gaseous products for a) model 1 and b) model 2 calcinating limestone.

Model 1 and 2 were both rerun without the inclusion of limestone calcination and compared to the calcinating included model to determine its effect on the composition of the exiting gases. The comparison between an inert limestone and a calcinating limestone bed are given in Fig. 6.11. From these graphs there does not appear to be a great deal of variation between the compositions of the gaseous products. This is due to the slow conversion rate of limestone decomposition. Wang et al. [115] investigated the effects of temperature and residence time on the decomposition of limestone of similar sized particles in a CO_2 atmosphere and found that with a BFB temperature of 1193.15 K, the residence time for over 73% conversion of $CaCO_3$ to CaO was approximately 70mins. Therefore, the 100.0 s run time presented here would not lead to a significant CO_2 production.

It is easier to observe the differences between the average mole fractions for both model 1 and model 2 with both an inert bed and a calcinating bed in table-form, therefore they are given in Table 6.3. The difference between the average exiting mole fractions (inert - calcinating) are also given to highlight the impact that limestone calcination has on a gaseous composition. In both cases there is a slight increase in the mole fraction of CO_2 as expected due to the release of CO_2 during limestone decomposition however the

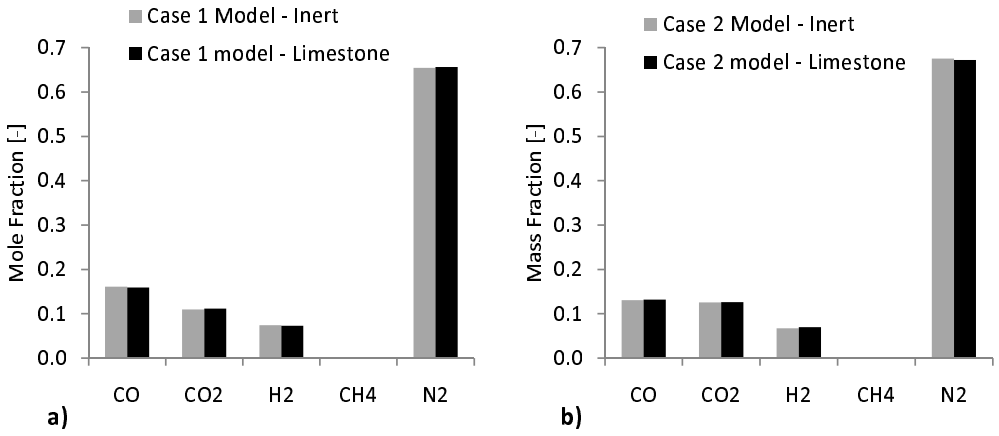

FIGURE 6.11: Average mole fraction of the exiting gaseous products for a) model 1 with inert and calcinating limestone and b) model 2 with inert and calcinating limestone.

impact is different between the two models. In model 1, the results show a slight decrease in the mole fraction of CO and H_2 whilst H_2O increases with CO_2. This suggests that the limestone model impacts the water-gas shift reaction as a result of further introduction of CO_2.

Model 2 shows an increase in all species except H_2O which decreases. It can be observed that model 1 and model 2 vary significantly in H_2O due to the variation in reactor temperature. The water-gas shift reaction is dependent on temperature and gaseous concentration and since the temperature distribution of the bed remains the same between an inert bed and the calcinating bed it can be assumed that the impact would be due to a slight increase in gaseous compositions. This is plausible as a lower temperature results in a lower mole fraction of CO compared to model 1 since the temperature dependent Boudouard reaction rate is reduced. An increase in CO_2 due to calcination would help promote the Boudouard reaction causing a slight increase in CO. Increasing the composition of the CO would accelerate the forward water-gas shift reaction leading to a reduction in H_2O and an increase in the products CO_2 and H_2. As the reaction continues the species compromise and adjust according to the local species concentration. It is interesting that the species CH_4 and tar do not vary between the inert model and a calcinating model. In addition to their low mole fraction within the bed this would be due to their non-involvement with the water-gas shift reaction.

A further point to emphasise is the use of a char and limestone bed would not display a great impact due to limestone calcination as the heterogeneous reaction rates with char dominates over the limestone reactions. The effects of different bed material on the gaseous compositions is investigated further in Section 6.1.11.

TABLE 6.3: Average mole fraction of gas species for an inert and calcinating limestone bed and the differences.

Model 1	CO	CO_2	H_2	CH_4	N_2	H_2O	Tar
Inert	0.13464	0.09150	0.06226	0.00020	0.54675	0.16428	0.00037
Calcinating	0.13249	0.09279	0.06094	0.00020	0.54671	0.16649	0.00037
Difference	-0.00214	0.00130	-0.00132	0.00000	-0.00003	0.00220	0.00000
Model 2	CO	CO_2	H_2	CH_4	N_2	H_2O	Tar
Inert	0.10135	0.09742	0.05230	0.00014	0.52268	0.22584	0.00026
Calcinating	0.10268	0.09818	0.05422	0.00014	0.52379	0.22073	0.00026
Difference	0.00132	0.00076	0.00192	0.00000	0.00111	-0.00511	0.00000
Experiment	CO	CO_2	H_2	CH_4	N_2	H_2O	Tar
Exp 1	0.1094	0.1931	0.0853	0.0084	0.6037	N/A	N/A
Exp 2	0.1059	0.1838	0.0884	0.0107	0.6110	N/A	N/A

6.1.6 Gas compositions

The gaseous mole fraction distributions within the reactor for model 1 are given in Fig. 6.12. There is a clear distinction between the species introduced through the gaseous inlet and combustion processes as they are more concentrated towards the base of the reactor compared to those which increase in concentration with increasing height. The species N_2, H_2O and CO_2 show a larger mole fraction at the base of the reactor since N_2 and H_2O are introduced through the lower air/steam inlet. The CO_2 is introduced endogenously as the product of the combustion heterogeneous reaction. These gaseous species decrease with height as they are consumed by further reactions. CH_4, H_2 and CO build up in concentration with increasing height as they are the products of heterogeneous reactions thus accumulate as further reactions take place.

The region near the fuel inlet shows a particularly concentrated region for most of the gaseous species. This region signifies the accumulation of devolatilisation products as the fuel is introduced to the bed at this point. The products then mix through the bed along with the products of heterogeneous reactions from the lower bed region to continually trigger further reactions, i.e., heterogeneously within the bed as seen in Fig. 6.8 and finally with the water-gas shift which dominates above the bed.

It is apparent that the heterogeneous reactions result in a strong variation in the mole fraction within the bed. This is because the reactions depend on the local concentrations of the species which consequently influence further reactions as increased concentrations of their products accumulate. An example of this would be the large region at the top right of the bed which, as was previously discussed in Section 6.1.4, which consists of a very low concentration of H_2O yet an increased mole fraction of H_2 and CO. This would confirm the previous assumption that the steam gasification reaction had previously dominated this region leading to an increased concentration of its products. It can also

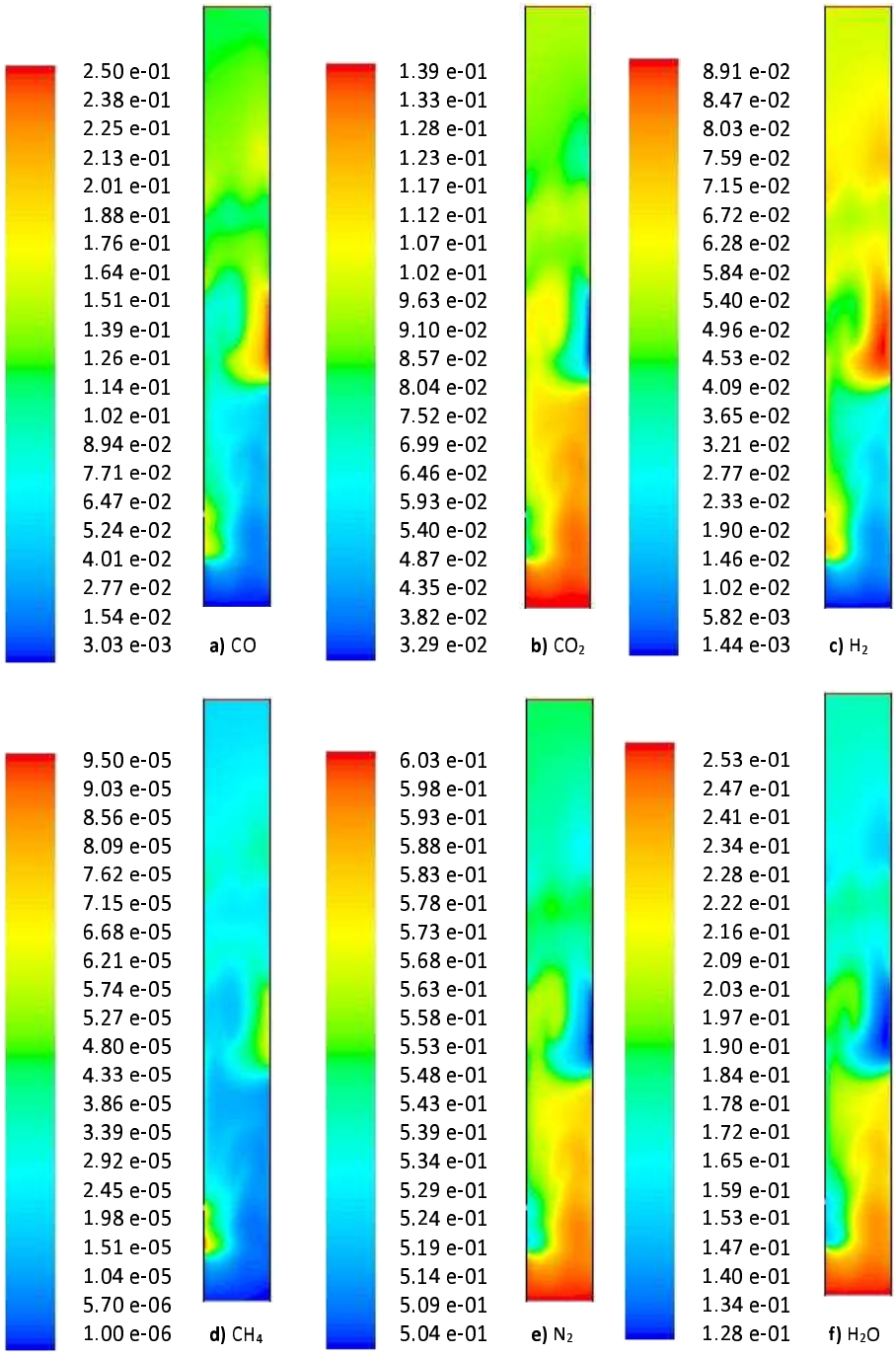

FIGURE 6.12: The mole fractions of the different gaseous products for model 1.

be seen that the mole fraction of CH_4 is gradually increasing which agrees with Fig. 6.8 (d) where an increase in the methanation reaction rate can be seen.

Above the bed the mole fractions in all cases regulate as the water-gas shift reaction takes place. An ideal case would be for the water-gas shift reaction to reach equilibrium leading to very little fluctuations in the average mole fraction of the gaseous products through the outlet as seen in Fig. 6.13. Whilst extensive work has been carried out with regards to the kinetics of the water-gas shift reaction it has been widely accepted that equilibrium is attainable whilst maintaining temperatures of 1073.15-1123.15 K for tall large scale beds. Unfortunately, this is highly unlikely within lab-scale reactors as the freeboard is not tall enough for equilibrium to be completely achieved. This is the case seen here in model 1 (Fig. 6.13) as stronger fluctuations are observed for the four species involved in the water-gas shift reaction, namely H_2O, CO, CO_2 and H_2.

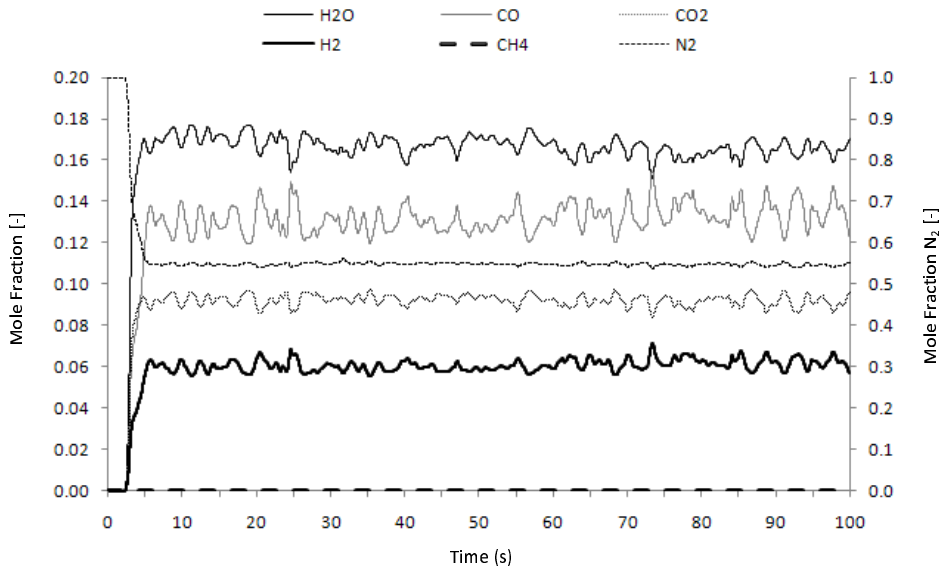

FIGURE 6.13: The average mole fraction of each gaseous product through the outlet over a period of 100.0 s.

From as early as 5.0 s the composition of the species through the outlet remains relatively steady with fluctuations occurring as the water-gas shift reaction continually compromises between the dominating species. The mole fraction of N_2 and CH_4 appears more consistent with average mole fractions of 54.7% and 0.02%, respectively, although CH_4 is so low that it is not as apparent in the graph. This is due to their non-participation in any of the reactions except for the methanation heterogeneous reaction where the reaction rate is so small and its participation taking place lower in the reactor therefore it would not greatly influence the CH_4 fluctuations.

The fluctuations of the remaining products appear strongly correlated with the mole fraction of its species. For H_2O and CO, averages of 16.4% and 13.5%, respectively, display larger fluctuations than CO_2 and H_2. It can be seen that the fluctuations of

these different groups reflect each other showing a decrease in CO whilst H_2O increases. The same can be seen for the other two species. This is a result of the water-gas shift reaction not reaching equilibrium and the species having to compromise with an increased concentration of one of the species on each side of the reaction.

6.1.7 Variation in bed height

It was observed in the last section, Section 6.1.6, that the water-gas shift had not reached equilibrium for a bed height of 100 cm so simulations were carried out with various bed heights of 0.5 m, 0.75 m, 1.0 m and 1.25 m. The results given in Fig. 6.14 show the instantaneous mole fraction of the gaseous species over a 100.0 s period for the different bed heights. The increased magnitude of the fluctuations with increasing bed height indicate that the water-gas shift has not had sufficient time to reach equilibrium before exiting the reactor. As explained previously, it is commonly acknowledged that it is highly unlikely for water-gas shift reaction to reach equilibrium within lab scale reactors due to the reduced area of freeboard space. A bed height of 0.5 m in Fig. 6.14 (a) shows a significant reduction in the fluctuation of the gaseous species upon exit. This lower bed height increases the area of the freeboard providing more space for the relevant species, namely CO, CO_2, H_2 and H_2O, to compete in the water-gas shift reaction thus indicating that equilibrium could be obtained in a small scale reactor providing the freeboard is sufficiently tall enough. The bed height of 1.25 m shows very strong fluctuations since the average mole fraction results are taken at 2.0 m leaving limited space for the species to adapt through the water-gas shift reaction.

From as early as 5.0 s the composition of the species through the outlet remains relatively steady with the fluctuations varying depending on bed height. The mole fractions of N_2 and CH_4 appear more consistent with average mole fractions of approximately 55% and 0.02%, respectively, due to their non-participation in the water-gas shift reaction. It can be seen however that lower bed heights, 0.5 m and 0.75 m, display a gradual increase in CO and H_2 species over time indicating that for such small bed heights the compositions do not reach steady state conditions compared to higher bed heights. This is due to smaller bed heights containing less char therefore CO_2 and H_2O would not be consumed as effectively by heterogeneous reactions. Such high concentrations of CO_2 and H_2O would affect the water-gas shift reaction leading to the gradual increase in their opposing species H_2 and CO. The average mole fractions of CO_2 and H_2 in Fig. 6.15 decrease with increasing bed height as increasing char levels lead to more exposure of gases to heterogeneous reactions whilst products of such reactions, CO and H_2, increase with increasing bed height.

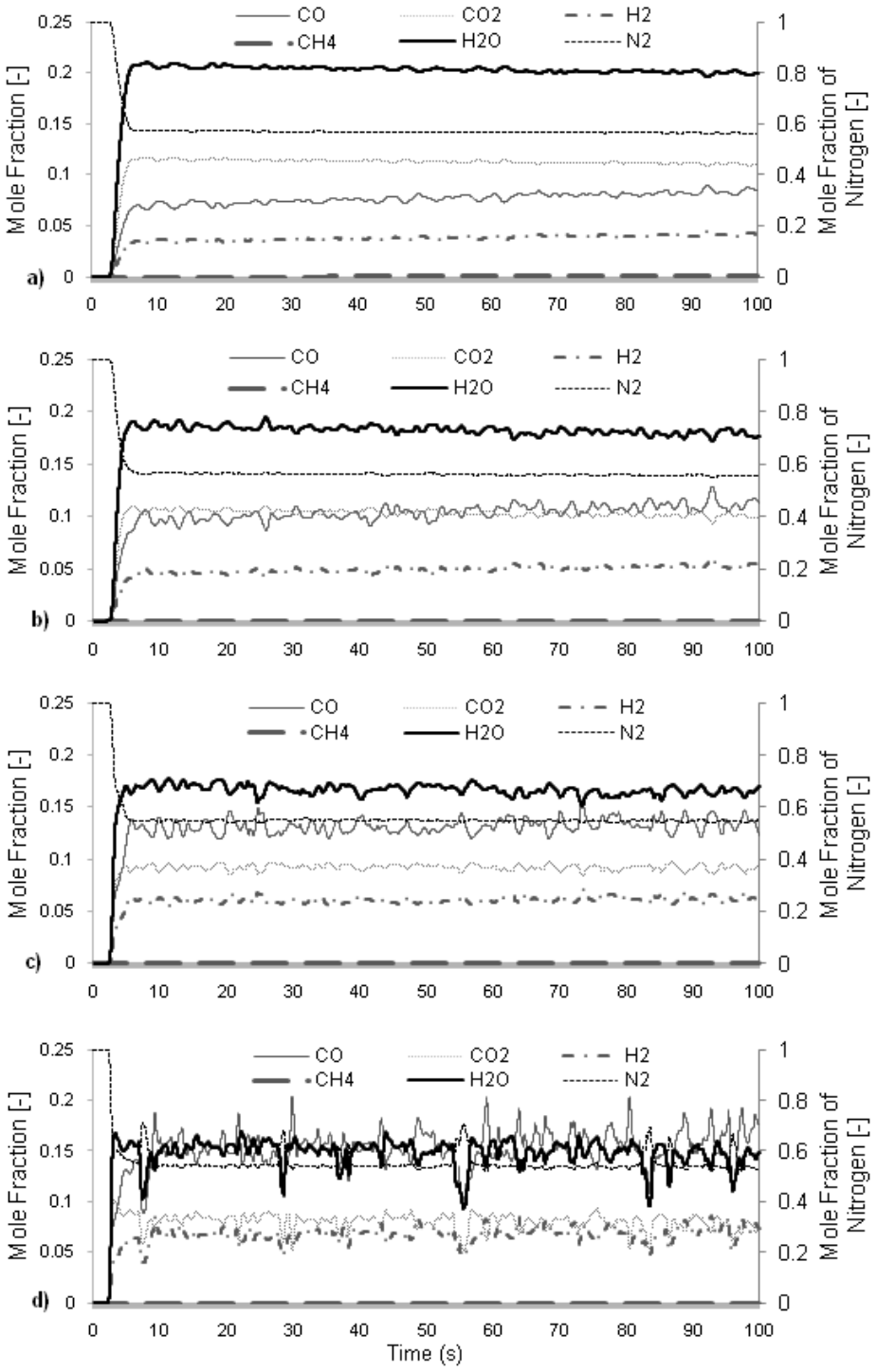

FIGURE 6.14: The instantaneous average mole fraction of the gaseous species over a 100.0s period for bed heights a) 0.5 m, b) 0.75 m, c) 1.0 m and d) 1.25 m.

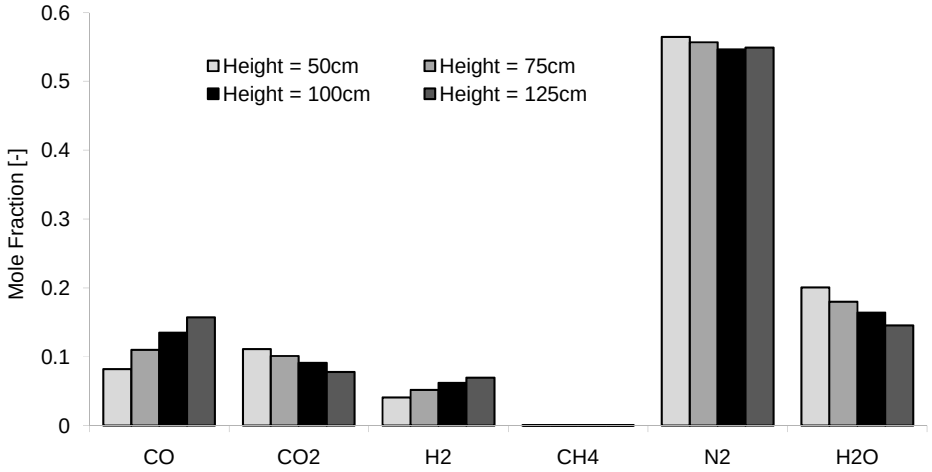

FIGURE 6.15: The average mole fraction of each gaseous product through the outlet over a period of 100.0 s for varying bed heights.

6.1.8 Temperature distributions

Figure 6.16 displays the contour plots of the gaseous temperature distribution for model 1 with two scales. In Fig. 6.16 (a) it is clear that the highest temperature is observed at the base of the reactor where the exothermic combustion reaction dominates. Figure 6.16 (b) displays a modified scale of Fig. 6.16 (a) for the benefit of observing the temperatures in different regions of the bed. There is a clear difference in temperature throughout the bed depending on position and local reactions. The temperatures near the wall remain similar to that of the reactor walls, 1128.15 K, whilst the centre of the bed varies. A region near the top of the bed on the right hand side shows a significantly lower temperature than the remaining bed. This region was brought up previously as having a significantly higher methanation reaction rate (Fig. 6.8 (d)) and showing a low mole fraction of H_2O (Fig. 6.12 (f)). The previous assumption was that previously this region was exerted to strong steam gasification activity. This is confirmed with the lower temperature as the steam gasification reaction is endothermic therefore a reduction in local gaseous temperature would indicate the presence of this reaction previously. The methanation reaction is slightly exothermic, however the methanation reaction rate in this region is significantly lower than the other heterogeneous reactions simultaneously taking place for it to make a significant impact on the temperature.

A slight temperature increase is observed near the top of the bed on the left. It can be seen in Fig. 6.3 (a) that there is a large gaseous bubble within this region. An increase in temperature would indicate that the water-gas shift reaction is taking place within the vicinity particularly within the bubble where the endothermic heterogeneous reactions rates are lower (Fig. 6.8(b),(c)) due to the reduced char concentration. Therefore a homogeneous reaction would be responsible for this temperature increase. As with all the homogeneous reactions, the water-gas shift reaction is slightly exothermic and since

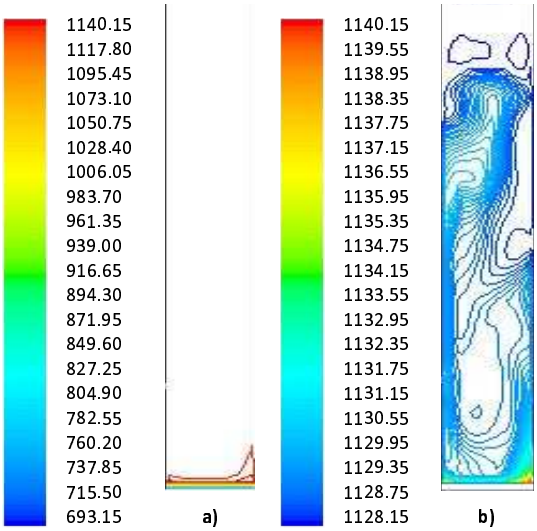

FIGURE 6.16: The gaseous temperature distribution (K) within the reactor for model 1 a) with a complete scale and b) a modified scale to highlight the temperature distribution within the bed.

the remaining oxidation reactions take place at the base of the bed it must be this reaction causing this temperature change.

6.1.9 Variation in temperature

The effect of bed temperature on the compositions of the exhaust gases was studied with models using temperatures lower (1078.15 K) and higher (1178.15 K) than the base case (1128.15 K). The average mole fraction of the gaseous species are given in Fig. 6.17. Results show that bed temperature is an important influence on the gasification processes. Increasing the temperature results in an increase in CO and H_2 species and a decrease in CO_2 and H_2O. This is due to the highly temperature dependent heterogeneous reactions. As the temperature increases the reactions take place faster leading to a faster consumption of the reactants H_2O and CO_2 through the steam gasification reaction and Boudouard reaction, respectively. This subsequently leads to an increase in their products CO and H_2, which is apparent in Fig. 6.17.

Figure 6.18 displays the instantaneous mole fraction of gaseous species through the outlet over a 100.0 s period. The fluctuations of the four water-gas shift species increased in magnitude as the bed temperature increased. For the 1178.15 K bed the fluctuations were highly erratic possibly due to the levels of CO and H_2O being the dominating species. These species react together as the forward reactants of the water-gas shift reaction therefore their dominance within the freeboard compared to the lower levels of the competing backward reactants would not allow for equilibrium to be achieved easily, especially in such a small freeboard area. Therefore, it can be assumed from

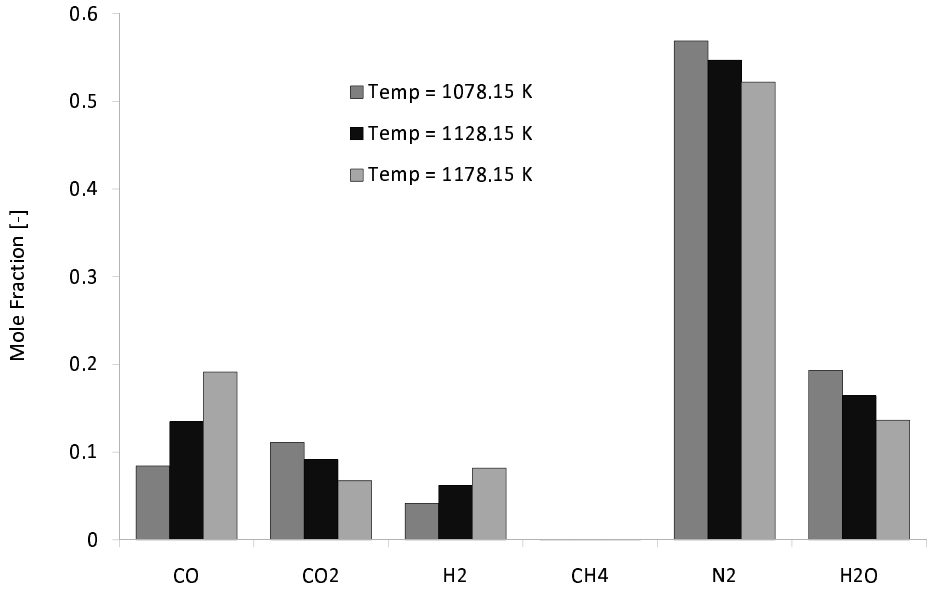

FIGURE 6.17: The average mole fraction of each gaseous product through the outlet over a period of 100.0 s for varying temperatures.

Fig. 6.14 and Fig. 6.18 that should the two dominating species in the freeboard be the reactants on the same side of the water-gas shift reaction, e.g., CO and H_2O being the reactants for the forward reaction, then the attainability of equilibrium would be very difficult. Having dominating species on both sides of the reversible reaction displays smaller fluctuations in the instantaneous mole fractions indicating an improved chance of reaching equilibrium state.

The water-gas shift reaction is dependent on concentration as well as temperature therefore as the concentration of the forward reactants peaks the reaction takes place faster. This increases the concentration of their products, CO_2 and H_2, whilst causing a sharp decrease in CO and H_2O due their conversion. The continual supply of increased forward shift reactants by heterogeneous reactions and as products of the backward shift reaction then leads to a peak in their mole fractions again starting the cycle once more. Occasionally, there appears to be a dramatic peak in CO and H_2O, for example at approx 38.0 s and 72.0 s in Fig. 6.18 (c). This could be due to bubble eruptions from the bed releasing concentrated products of the heterogeneous reactions into the freeboard.

6.1.10 Variation in heat transfer coefficient

The model was adjusted to incorporate heat transfer at the walls with four different heat transfer coefficients, 2, 4, 6 and 8 W/m^2 K. The inclusion of heat transfer coefficients has a strong impact on the average gaseous temperature leaving the reactor as seen in Fig. 6.19. Higher temperatures are observed with lower heat transfer coefficients as the

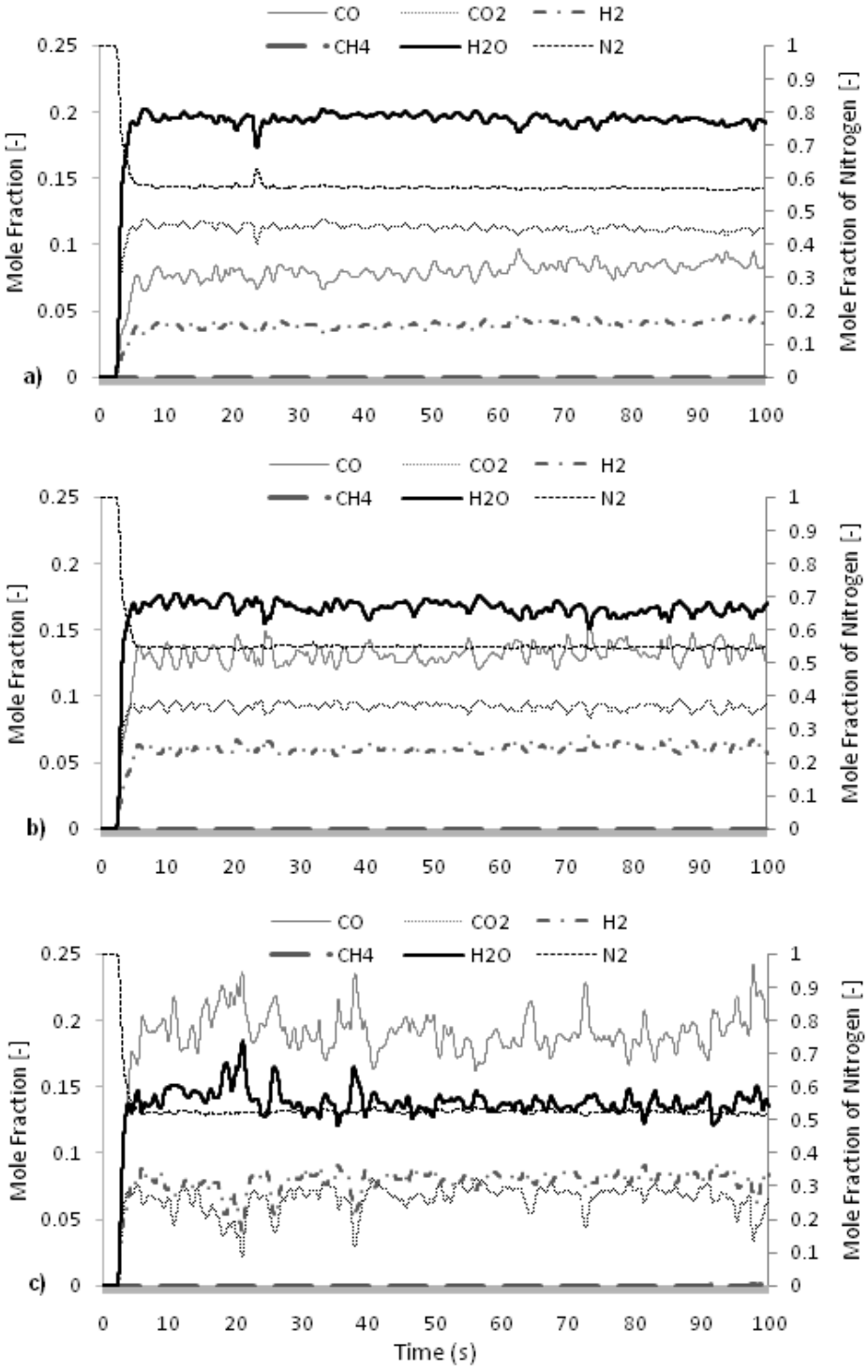

FIGURE 6.18: The instantaneous mole fraction of gaseous species through the outlet over a 100.0 s period for bed temperatures a) 1078.15 K, b) 1128.15 K and c) 1178.15 K.

heat loss through the walls is reduced. This was also previously observed by Gerber et al. [114] who further found, which can also be seen in Fig. 6.19, that lower heat transfer coefficients did not reach steady state conditions whilst higher ones did.

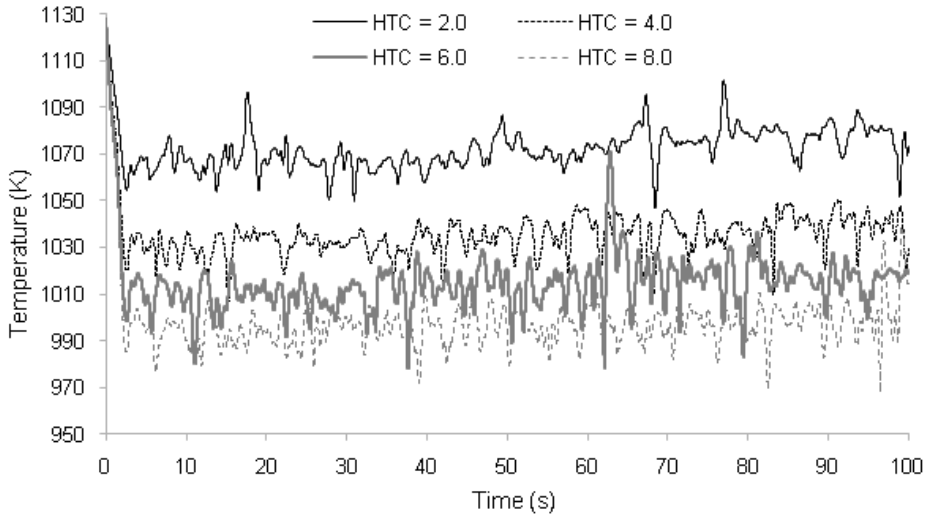

FIGURE 6.19: The instantaneous average temperature through the outlet over a period of 100.0 s for varying heat transfer coefficients (W/m^2 K).

The influence that temperature has on the gasification and homogeneous reaction rates were observed previously in Section 6.1.8. However it can be seen in Fig. 6.20 that although the variation of heat transfer coefficient greatly affects the exiting gaseous temperatures it does not affect the composition of the exiting gases. The average mole fraction of the gaseous products for the four different heat transfer coefficients does not show a great deal of variation. This is due to the heat transfer coefficients only effecting the local wall regions and in the dense particulate bed this is neglected since the high bed temperature dominates. However, in the freeboard the temperature from the walls are transported via convection through the gases therefore increasing the temperature in this region. The slight fluctuations observed in Fig. 6.20 could be due to the variation in freeboard temperature which affects the reaction rate of the water-gas shift reaction. The higher temperature from lower heat transfer coefficients would accelerate the reaction rate of the water-gas-shift reaction which is slightly exothermic leading to a further increase in local temperature. This could explain the unsteady temperature profile for lower heat transfer coefficients compared to the remaining coefficients in Fig. 6.19.

6.1.11 Variation in bed material

The composition of char and limestone can greatly influence the concentration of the gaseous products. Additional models were carried out modifying the base case which

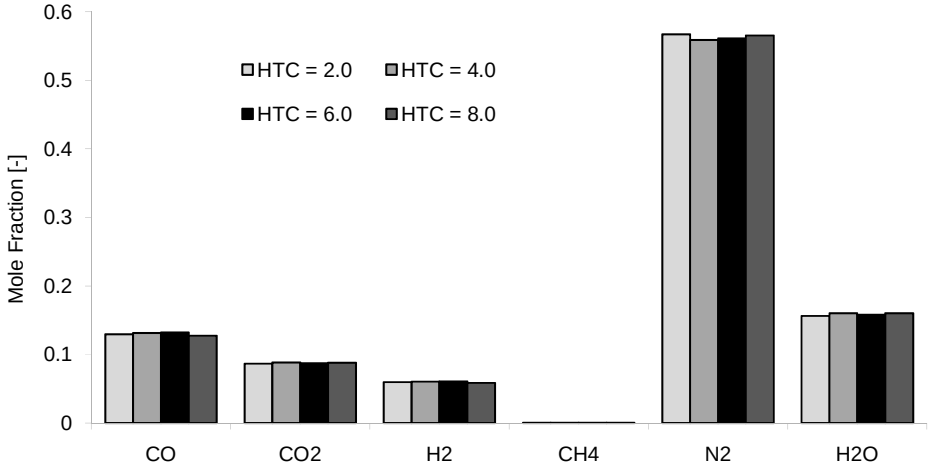

FIGURE 6.20: The average mole fraction of the exiting gaseous products for the four different heat transfer coefficients (W/m^2 K).

initially had a bed with a 50:50 ratio (char:limestone) to a limestone dominating bed (25:75) and char dominating bed (75:25). The mole fraction of the gaseous products are given in Fig. 6.21. It is clear that increasing the percentage of char in the bed results in an increase in CO and decrease in CO_2. An increased presence of char promotes the combustion reaction leading to more CO_2 being produced. The CO_2 is then consumed through the Boudouard reaction to produce more CO. Increasing the amount of char would increase the instances of heterogeneous reactions taking place, including further up the bed where the steam gasification reaction produces further CO and H_2. This is also observed in Fig. 6.21 where there is an increase in the concentration of CO and H_2 with increasing char content and a decrease in the heterogeneous reactants CO_2 and H_2O. It is worth pointing out that the bed containing a limestone majority (25:75) closely resembles the experimental results which is as expected since the experimental bed contained a limestone bed with coal supplied before the air and steam was introduced, therefore was a limestone dominating bed however the exact ratio of coal to limestone was not given in the literature [5].

Figure 6.22 shows the average mole fraction of O_2 at different heights in close proximity to the air inlet for the three bed ratios of char:limestone, namely 25:75, 50:50 and 75:25. It can be seen that the bed with the 25:75 ratio model has a higher mole fraction of O_2 at all three heights 0.01 m, 0.015 m and 0.02 m. The average mole fraction decreases with increasing char quantity as more char is available to participate in the heterogeneous combustion reaction. Since a lower char to limestone ratio has a higher O_2 concentration further up the bed, oxidation reactions can take place more over a great area which could also increase the concentration of CO_2 and H_2O in the bed.

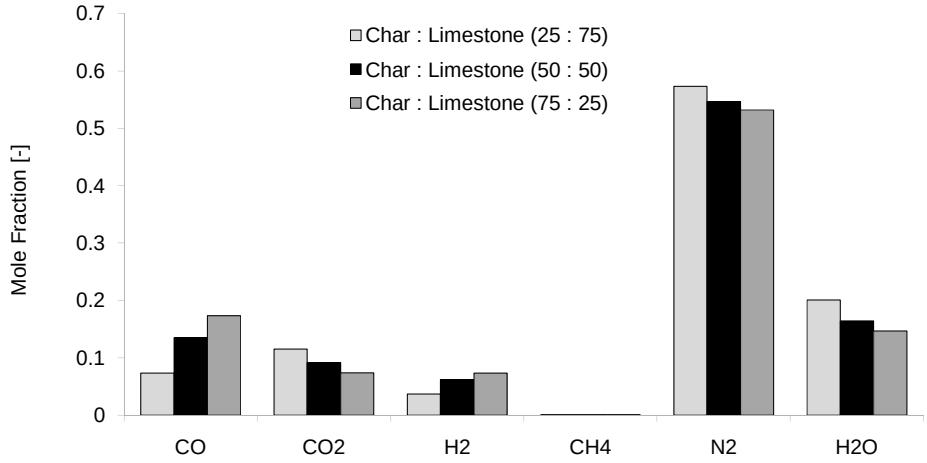

FIGURE 6.21: Average mole fraction of the gaseous products through the outlet for varying bed compositions.

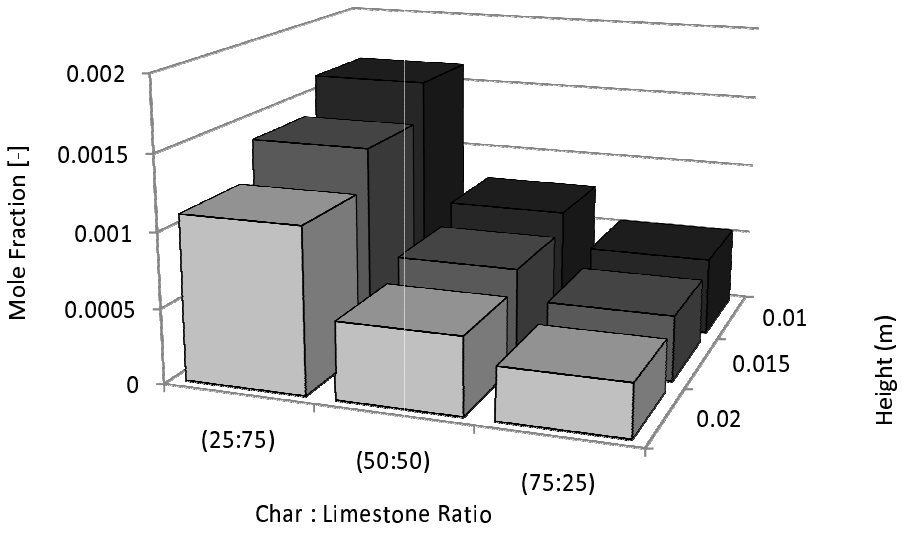

FIGURE 6.22: Average mole fraction of O_2 at different heights near the air inlet for the three bed compositions.

It is worth highlighting that the limestone calcination model was carried out in all instances therefore an assumption could be made that increasing the amount of limestone would result in an increase in CO_2 due to its release during the calcination process. To further highlight the effects of limestone calcination a bed consisting of 100% limestone was modelled with inert limestone and calcinating limestone. The results given in Fig. 6.23 show a completely different composition compared to that given with char present. This is due to the heterogeneous reactions only taking place with the limited char produced during devolatilisation.

A close up of the products, CO, CO_2, H_2 and CH_4 in Fig. 6.24 shows low concentrations of CO, H_2 and CH_4, which are due to the homogeneous reactions taking place

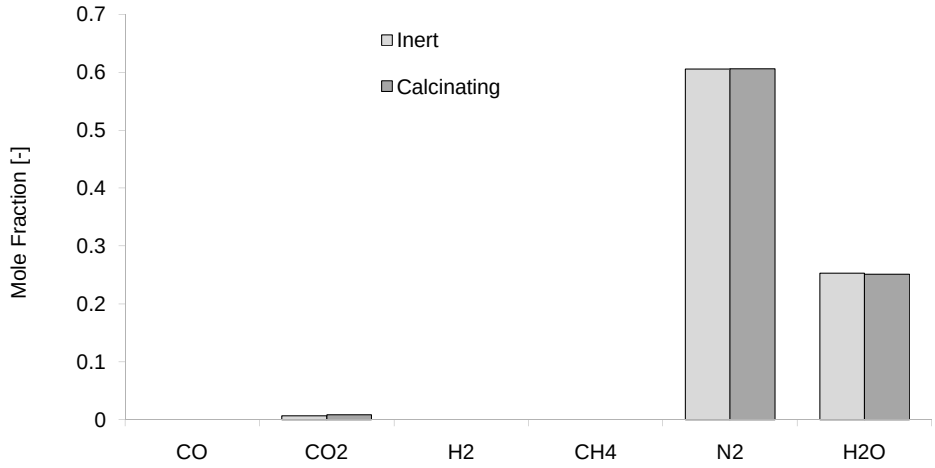

FIGURE 6.23: Average mole fraction of the gaseous products with a bed containing only inert limestone or calcinating limestone.

throughout the bed as opposed to beds containing char where the reactions are limited to O_2 enriched near-inlet region. Since there is very little char in the bed O_2 does not get consumed therefore the volatile products released near the fuel inlet are immediately consumed via the oxidation homogeneous reactions producing CO_2 and H_2O (Fig. 6.23). A significant increase in the concentration of CO_2 can be seen due to both the additional CO_2 produced through limestone calcination but also through the oxidation reactions of CO immediately after devolatilisation has taken place. However, this increase is only slight compared to the influence heterogeneous reactions has on the gaseous compositions, particularly in the early stages of the limestone calcination process.

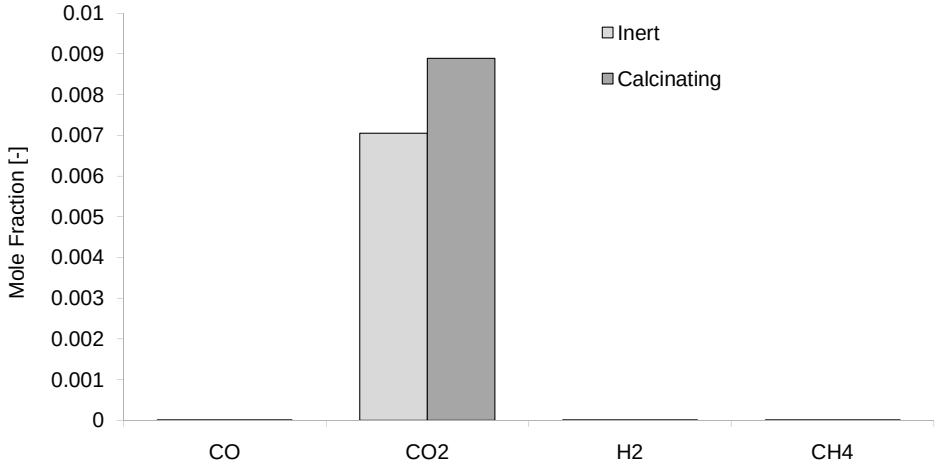

FIGURE 6.24: Close up of the gaseous composition of the products for a bed of inert and calcinating limestone.

6.1.12 Extended simulation times

The instantaneous gaseous compositions taken from the outlet given in Fig. 6.13 suggest that the gaseous compositions reach steady state by 100.0 s however extending the runs further would confirm this assumption. Unfortunately, due to the extensive time such reaction models require a grid dependency check is performed to determine appropriate cell sizes and time steps which would carry out the simulations in a faster time without too much loss of accuracy. Table 6.4 displays the twelve separate cases consisting of three grid sizes; a refined grid - 0.01 m x 0.01 m, the base case grid - 0.01 m x 0.02 m and a coarse grid - 0.02 m x 0.02 m; that were modelled using four different time steps: 0.00005 s, 0.0001 s (the base case), 0.0005 s and 0.001 s. The cases were run for 20.0 s using the model set up of Model 1, given in Table 6.1. For reference, the initial base case carried out throughout this work, which was applied previously for a different model in the literature [63, 151], is given as case 6 in Table 6.4.

TABLE 6.4: Grid dependency carried out with different cell sizes and time steps.

Case	Cell size Horizontal (m) x Vertical (m)	Time step (s)
1	0.01 x 0.01	0.00005
2	0.01 x 0.01	0.0001
3	0.01 x 0.01	0.0005
4	0.01 x 0.01	0.001
5	0.01 x 0.02	0.00005
6	0.01 x 0.02	0.0001
7	0.01 x 0.02	0.0005
8	0.01 x 0.02	0.001
9	0.02 x 0.02	0.00005
10	0.02 x 0.02	0.0001
11	0.02 x 0.02	0.0005
12	0.02 x 0.02	0.001

Figure 6.25 displays the performance of the different cases showing the time taken in hours to run to 20.0 s along with the number of cells involved in the calculations using 8 processors. As expected, as the grid becomes coarser the number of cells reduces and the time taken to run the simulations to 20.0 s reduces. The variation in time step impacts the duration of the run times greatly as smaller time steps require more time steps within the same period of 20.0 s to complete. Increasing the time step reduces the number of time steps to be carried out but increases the number of iterations per time steps required to ensure convergence is achieved. This is observed by looking at the time difference between the models run with 0.0005 s and 0.001 s time steps. The time duration display very little difference even though the number of time for the 0.001

s time steps required half the number of time steps within the 20.0 s period. Due to the large time steps the model requires more iterations before reaching convergence therefore time is not necessarily gained to benefit these large time steps.

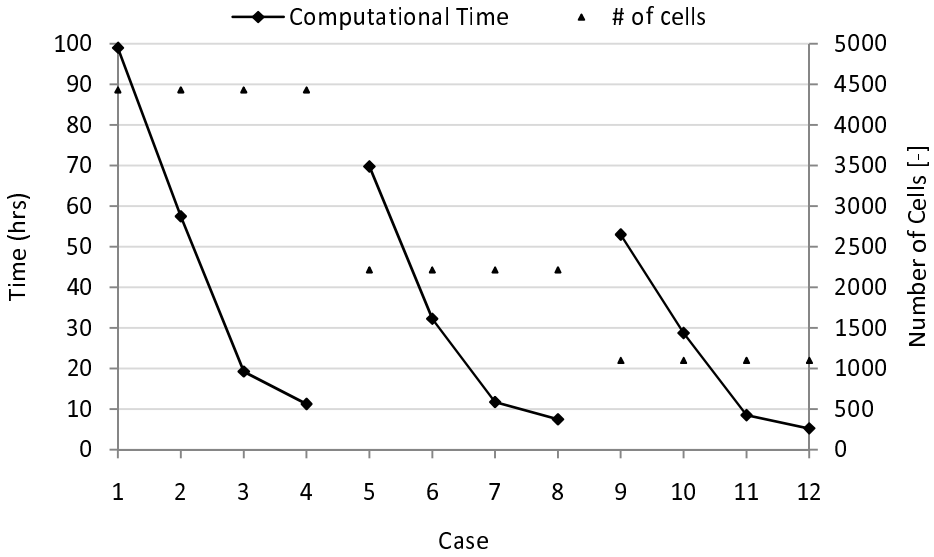

FIGURE 6.25: Performance of the different grid dependency cases which ran for 20.0 s.

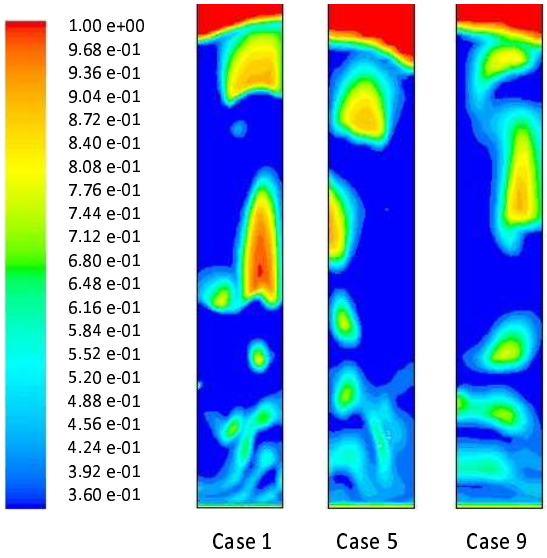

FIGURE 6.26: Gas volume fractions taken at 20.0 s for three different mesh sizes using the smallest time step: case 1, case 5 and case 9.

The effect of different grid sizes can be seen in Fig. 6.26 which compares the volume fraction of the gases at 20.0 s for the smallest time step models: case 1, case 5 and case 9. The smallest time step allows for very fast convergence therefore discrepancies seen would be due to grid size instead of a coarse time step. The finest grid, case 1, shows clear defined bubbles for both small and large bubbles with the interaction between the bubbles and dense particulate phase being refined and the bubbles containing higher gas

volume fractions. The coarsest grid, case 9, however displays similar bubble structures except the bubbles appear larger as the interaction of the bubble with the bed appears thicker and also the bubbles appear to have lower volume fractions. This is again due to the rough estimations made in local area, a smaller grid cell would detect a gas volume fraction of say 0.99 whereas a grid cell with twice the size would average this value with the surrounding values in the cell which could be lower leading to a reduction in the value. The effects of coarser averaging is particularly seen at the base of the bed were there are small bubble formations due to the endogenous products of heterogeneous reactions. The refined bed captures these small bubble formations whereas increasing the grid size reduces the ability to capture of them as rougher estimations are made with regards to the local behaviour within the vicinity.

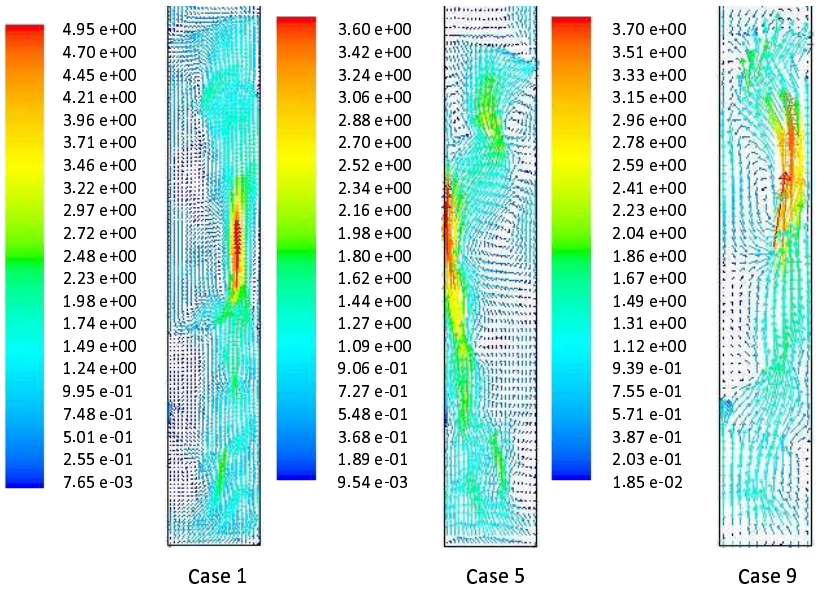

FIGURE 6.27: Gas velocity vectors taken at 20.0 s for three different mesh sizes using the smallest time step: case 1, case 5 and case 9.

The mesh used in case 5 contains a horizontal grid size which is the same as case 1 but the same vertical grid size as case 9. The formation of some smaller bubbles can be seen and the large bubble at the top of the bed shows refinement for the bubble interaction with the bed on the left and right side of the bubble however the top of this bubble and the base of the react show the effects of the coarser grid in the vertical direction as the results appear less refined. It is explaining the different flow distributions achieved at the same time by the three models. As coarser grids produce rougher estimations for the flow dynamics these less accurate values would then be used to calculate the results at the next time step. Continuation like this would subsequently lead to a different flow distribution in an already heterogeneously bubbling bed.

The corresponding gas velocity vectors are given in Fig. 6.27 showing how much more refined the mesh in case1 is compared to the mesh in case 9. Each node gives the velocity value and which is scaled according to the local velocity of the gases. Comparison with Fig. 6.26 shows the gas travelling faster in the dilute regions, i.e., through the bubbles, as the gas travels the easiest route possible with the least resistance. Since bubbles contain a low concentration of particles, which act as obstacles, the gas prefers to travel via this route. Although the flow displays a different distribution for the three cases at 20.0 s, the gas velocities are very similar regardless of the grid size. A peak velocity is observed in case 1 within a bubble which is significantly faster compared to the velocities observed in the other two cases however this would be due to the volume fraction of the gases in this region being very dilute (in Fig. 6.26). Furthermore, it could also just be specific to the flow distribution captured at this specific point in time.

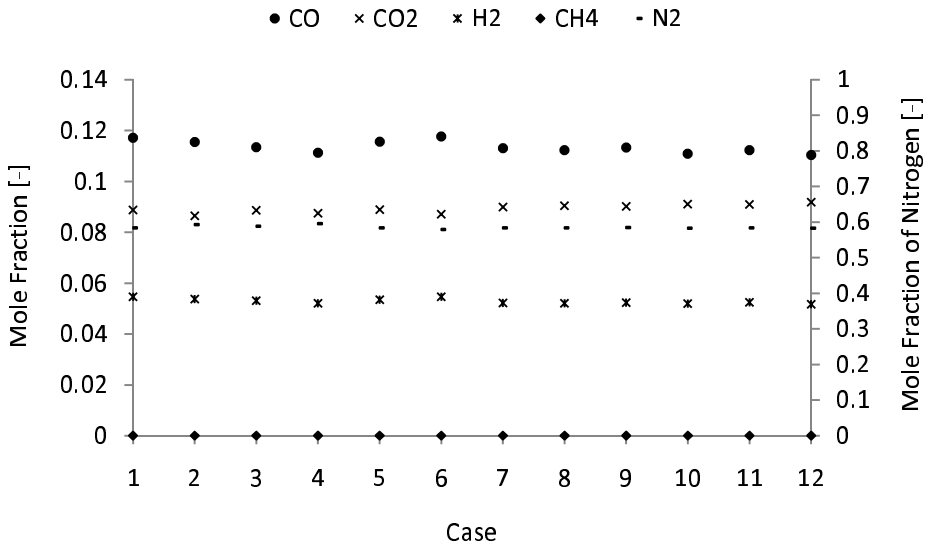

FIGURE 6.28: Mole fraction of exiting gases for the different models.

Whilst the flow dynamics display slight differences between the grid sizes it is worth comparing the average gaseous compositions for all cases to determine the effects grid size has on the reaction kinetics. Figure 6.28 shows the exiting gaseous compositions which were average over a period of 10.0 s for each of the twelve cases. There appears to be very little variation in the average gaseous compositions across all the models probably because any difference in gaseous composition produced within the bed as a result of averaging over coarser grids, would probably be negligible by the time the gases reach the outlet because the water-gas shift reaction would adjust the compositions accordingly leading to similar compositions.

For the benefit of modelling the gaseous composition alone, a coarse grid would work just as effectively as a refined grid. The coarser grid of 0.02 m x 0.02 m will be utilised in the extended simulation models as the gaseous compositions is the main focus of

this study however the time step chosen will be 0.0005 s, i.e., case 11, allowing for a faster simulation time than the previously used case 6 without compromising too much accuracy by increasing the time step. A limestone dominated bed (char:limestone = 25:75) was chosen as the results shown in the previous section, Section 6.1.11 closely resembled the experimental results given in the literature [5]. The extended model ran for 2000.0 s and the instantaneous average mole fractions of the gases leaving the reactor are given in Fig. 6.29.

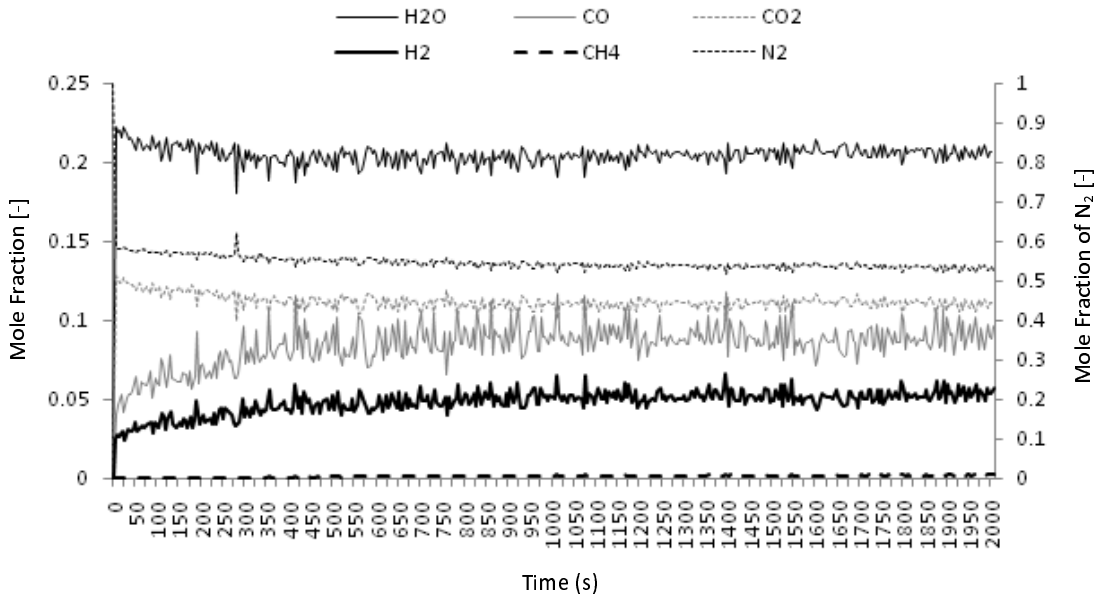

FIGURE 6.29: Instantaneous average gaseous composition over a period of 2000.0 s using case 11 from Table 6.4.

The results in Fig. 6.29 were obtained at 5.0 s intervals which explains the dramatic peaks that can be seen, especially in the water-gas shift species where the compositions are expected to vary as the reactants try to reach an equilibrium. It can be seen that the results reach steady state however this seems to occur after about 400.0 s suggesting that whilst the previous models which were carried out to 100.0 s may appear to have reached steady state due to the smaller time intervals, 0.005 s, at which the data was extracted which would suppress the increasing trend, they had not and in order to obtain sufficient time averaged composition results the simulation time needs to be extended further. The compositions were averaged for the last 50% of the 2000.0 s simulation and the 100.0 s simulation times, i.e., averaged between 1000.0-2000.0 s and 50.0-100.0 s, respectively. The results are compared to the experimental data given from Ocampo et al. [5] in Fig. 6.30.

The simulation that ran for 2000.0 s is averaged over a larger time period therefore the results would provide a better representation of the compositions over this extended

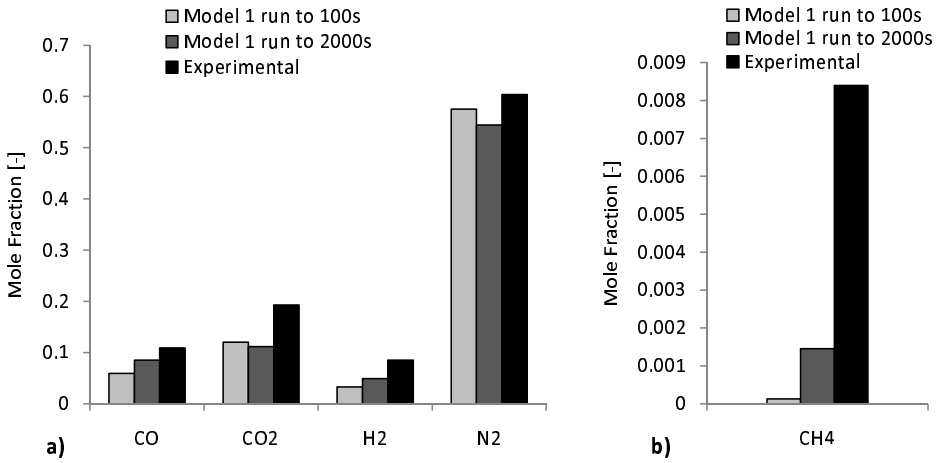

FIGURE 6.30: Average mole fraction of a) the dominant exiting gases and b) CH_4 after 100.0 s and 2000.0 s of simulation time.

time period whereas the results from the 100.0 s are not only taken before steady state has been achieved but averaged over a shorter time period hence reducing the accuracy. The bar chart shows clear differences between the different simulations. The longer simulation shows an increase in the CO, H_2 and CH_4 due to the continual build up after the 100.0 s period of these products from the heterogeneous reactions. The CO_2 and H_2O, which gave an average mole fraction of 0.2113 for the 100.0 s simulation and 0.2049 for the 2000.0 s, reduces slightly which would be due to the water-gas shift being strongly influenced by the significant increase in CO and H_2. The results for N_2 throughout this work is given as the remaining composition once the other species had been accounted for.

6.1.13 Mass variations

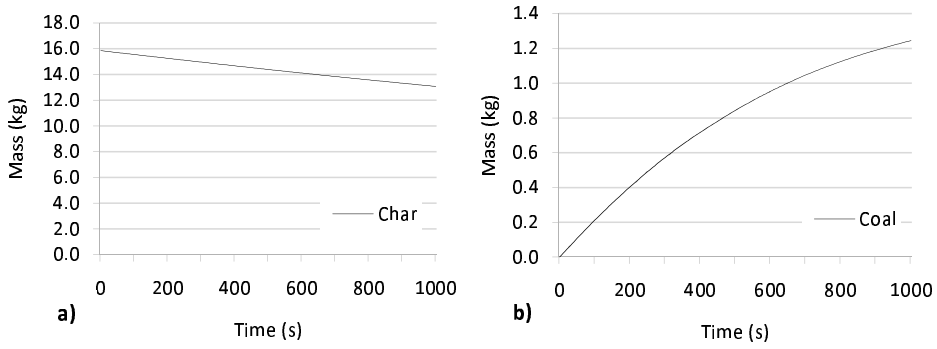

FIGURE 6.31: Mass of a) the char and b) the coal in the reactor during the first 1000.0 s of simulation time.

The mass of the char and coal in the reactor for the first 1000.0 s of the limestone dominating bed and grid case 11 are given in Fig. 6.31. As expected, the char shows a gradual decrease as the char gets consumed by heterogeneous reactions. Since the mass

of the char depends on the consumption of the char through heterogeneous reactions as well as its production during the devolatilisation process the continual decrease in the char mass indicates the consumption takes place fast than the production. Therefore the reactor would eventually run out of char. The coal however increases quite fast at the beginning of the simulation and levels off gradually. This is due to the coal being introduced into the reactor at the beginning and building up. As coal degradation takes place the coal gradually breaks down into its constituents, namely volatiles and char, reducing the mass of coal leading to total mass levelling out as the reactor becomes accustomed to the introduction and degradation rates of the total coal in the bed.

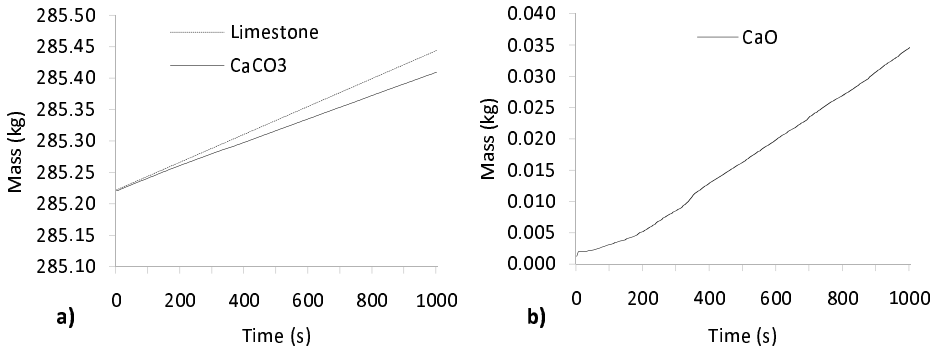

FIGURE 6.32: Mass of a) the complete limestone phase and the mass contribution from $CaCO_3$ and b) the contribution of CaO in the reactor during the first 1000.0 s of simulation time.

The masses of the total limestone, $CaCO_3$ and CaO are provided in Fig. 6.32 for the first 1000.0 s for the limestone dominating bed. The mass of the limestone phase shows a steady increase which is expected as the bed in continually being supplied limestone through the fuel inlet at a rate of 0.8 kg/h. The mass of $CaCO_3$ is the only component of the limestone at the beginning of the simulation before limestone calcination takes place. As the calcination reaction starts converting $CaCO_3$ into CaO and CO_2 there is a gradual decrease in the mass of $CaCO_3$ whilst the CaO gradually increases. The graph of the CaO mass shows a different behaviour at the beginning of the simulation as the reactor attempts to reach steady state but once steady state appears to be achieved at around 350.0-400.0 s the CaO increases at what appears to be a steady rate. This time period agrees well with the results shown previously in Fig. 6.29 also displaying steady state behaviour for the mole fraction of the exiting gases.

6.2 Three-dimensional modelling

The two-dimensional mesh was extended to a three-dimensional mesh which is the main focus of this section. A mesh was created using 66243 cells. The cell size in the horizontal direction was taken to be the 0.02 m whilst the vertical direction was set to 0.02

m replicating the coarser mesh carried out in the two-dimensional modelling, in Section 6.1.12, as it was shown to capture the basic bubbling dynamics and little variation in gaseous compositions. Similarly, the three-dimensional mesh refines the region near the coal inlet further to a minimum of 0.0004 m horizontally and 0.0008 m vertically to correctly capture the devolatilisation characteristics near the fuel inlet as the fuel is introduced.

TABLE 6.5: Operating conditions and experimental results for the 3D BFB gasifier.

Operating Conditions	Model 1	Model 2	Model 3	Model 4
Air supply (kg/h)	21.9	17.0	19.4	21.9
Steam supply (kg/h)	4.7	4.7	4.7	4.7
Coal feed (kg/h)	8.0	8.0	8.0	8.0
Limestone feed (kg/h)	0.8	0.8	0.8	0.8
Air and steam				
temp at entrance (K)	693.15	686.15	695.15	708.15
Temperature of reactor (K)	1128.15	1085.15	1114.15	1139.15
Experimental results				
H_2 (%)	8.53	8.84	9.36	7.88
CO_2 (%)	19.31	18.38	14.40	15.60
N_2 (%)	60.37	61.10	64.62	64.52
CH_4 (%)	0.84	1.07	1.34	1.01
CO (%)	10.94	10.59	9.97	10.94

The model was set up as the two-dimensional model only without the inclusion of limestone calcination as the previous results displayed a minimal influence on the gas composition results. The same properties for the coal, limestone and char are used and are given in Table 6.2 however, this section later looks at the modification of the model to test a different fuel, namely, wood. Therefore an additional biomass phase is introduced. The wood properties along with the devolatilisation model used are taken from the literature [114] and given previously in Section 3.3.6. Additional case set ups are carried out for the three-dimensional models to compare different gaseous inlet velocities and temperatures to further experimental results from the literature [5]. The model conditions and experimental results are given in Table 6.5.

6.2.1 Gas inlet velocity variation

Three-dimensional models were carried out for models 1, 2, 3 and 4, in Table 6.5, for 10.0 s as simulation times took almost two weeks to reach 10.0 s on 8 processors using a time step of 0.0005 s. The gas distribution within the four beds are given in Fig. 6.33. Iso-values for a gaseous volume fraction of 0.8 are visible displaying the presence of the bubble in their irregular distorted shapes at different positions within the reactor.

Typical characteristics can be seen in all three models including the formation of gases

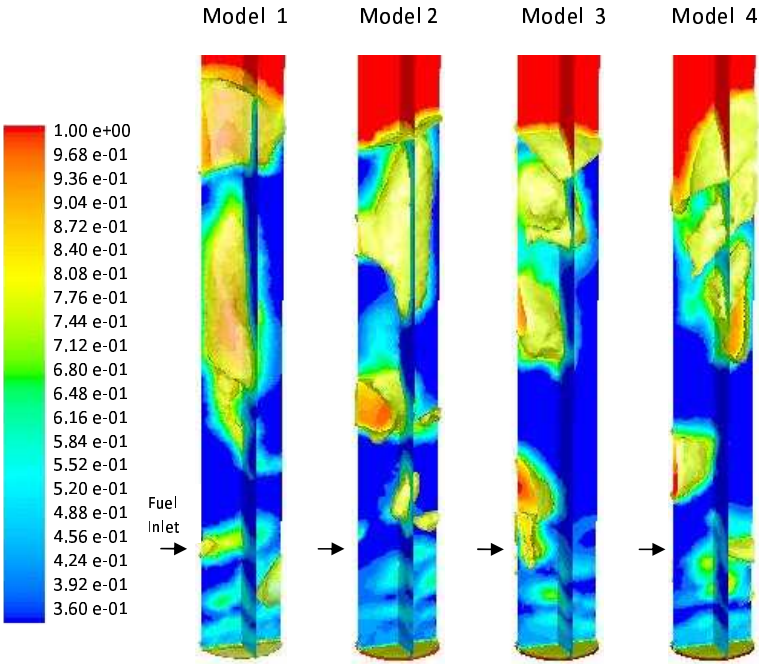

FIGURE 6.33: Gaseous volume fraction with a gas volume fraction iso-value of 0.8 for the four different models.

near the fuel inlet due to the build up of volatile gases, the elongation of bubbles near the walls, the formation of endogenously formed bubbles resulting from the heterogeneous reactions at the base of the reactor and the eruption of bubbles at the top of the bed. The bubbles appear to be larger with increasing height as coalescence takes place - particularly seen in case 4 of Fig. 6.33 where bubbles are in the process of merging. Although the velocity of the inlet gases vary the bubbles appear to display similar bubble diameters. It is hard to determine whether this is just what appears at this particular instant or whether the bubbles are generally of a similar diameter. However the inlet velocities do not vary a great deal therefore it can be assumed that the bubble diameters would be relatively similar.

The instantaneous composition of the individual gaseous species taken averaged from the outlet for each model is given in Fig. 6.34. The first observation is that the species CO, CO_2, H_2 and H_2O display steady compositions after about 5.0 s whereas CH_4 and tar do not. This is expected because the amount of CH_4 and tar present is very small and continually build up following the devolatilisation process. The tar is building up due to the devolatilisation alone as it does no participate in any further reactions. On the other hand, CH_4 is a reaction of the oxidation reaction (R7) and is the product of the methanation reaction (R4). However it was shown in Section 6.1.4 that these two reactions take place very slowly and closer inspection of Fig. 6.34 (d) and (f) shows that the CH_4 and tar graphs look almost identical with regards to the peaks and troughs. This suggests that regardless of the reactions CH_4 participates in they are negligible

as the main contribution to the CH_4 is the same as that for the tar, namely from the devolatilisation process.

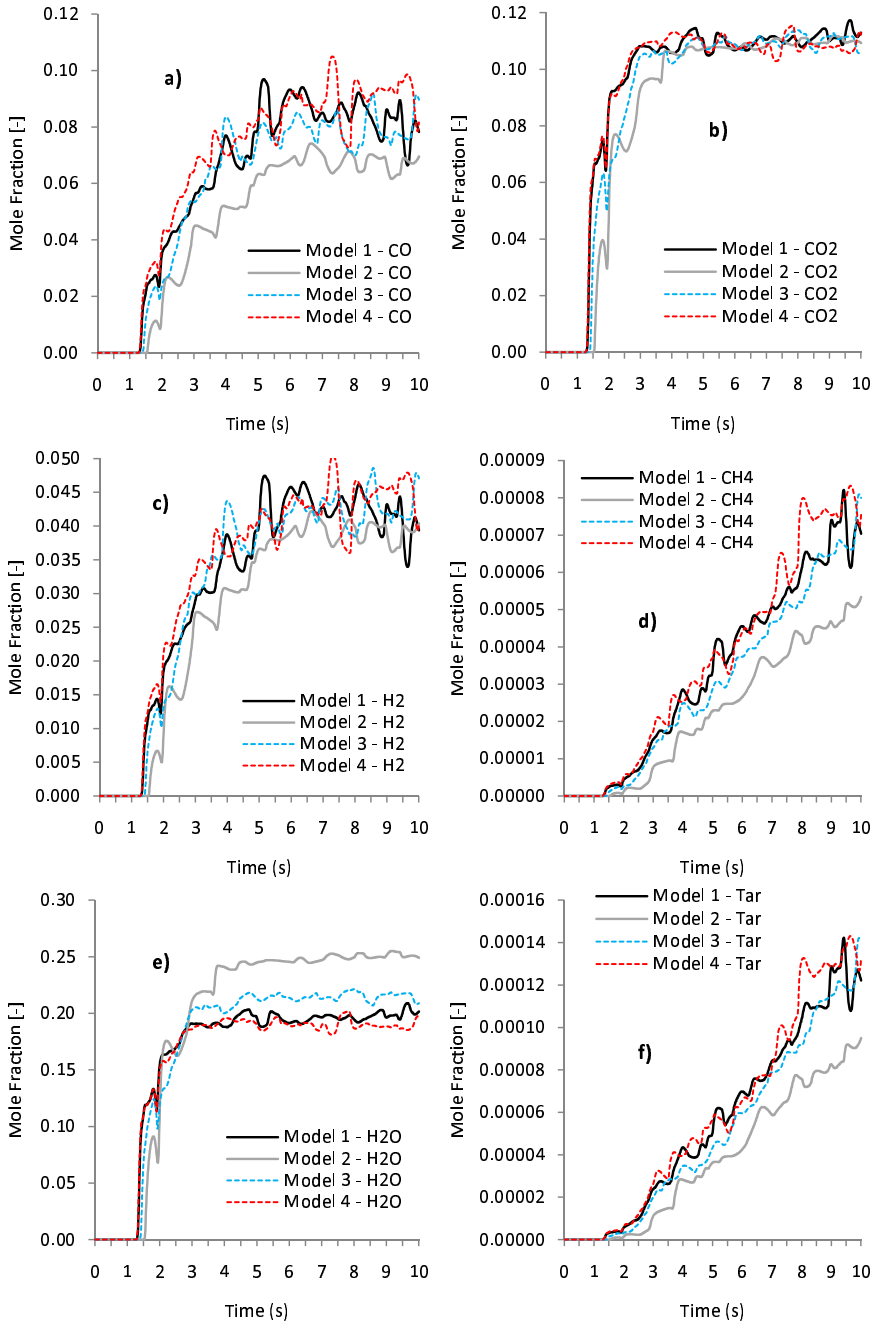

FIGURE 6.34: Instantaneous average composition of the individual gaseous species a) CO, b) CO_2, c) H_2, d) CH_4, e) H_2O and f) tar for each model.

Model 1 and model 4, in Fig. 6.34, display similar magnitudes which is quite expected since their model set ups are almost identical except for an increase in bed and inlet temperatures. Therefore any variation between these two models would be a result of temperature differences. Figure 6.35 displays the average temperature of the gases

leaving the reactor over the 10.0 s period and there is a clear difference due to the initial temperature set ups. The trend that the temperatures show in Fig. 6.35 appear to replicate the mole fractions of the individual gaseous species in Fig. 6.34. The mole fractions of CO, H_2, CH_4 and tar appear to increase with increasing temperatures whilst the mole fraction of H_2O shows a decrease with increasing temperatures. The reason for the CH_4 and tar increases with increasing temperature is due to the strong temperature dependence of the devolatilisation model so the higher the bed temperature the faster the rate of volatile release leading to a faster accumulation of the respective species. The reason for the increase in mole fraction of CO and H_2 and decrease of H_2O with temperature is due to the effects that temperature has on the heterogeneous reactions. Similarly with the devolatilisation reactions, the heterogeneous reactions are strongly temperature dependent therefore the reactant of the steam gasification reaction (R2), H_2O, would be consumed faster leading to the reduction in this species with increasing temperature. The products of this reaction, CO and H_2, would be produced faster leading to an increase in their mole fraction with increasing temperature.

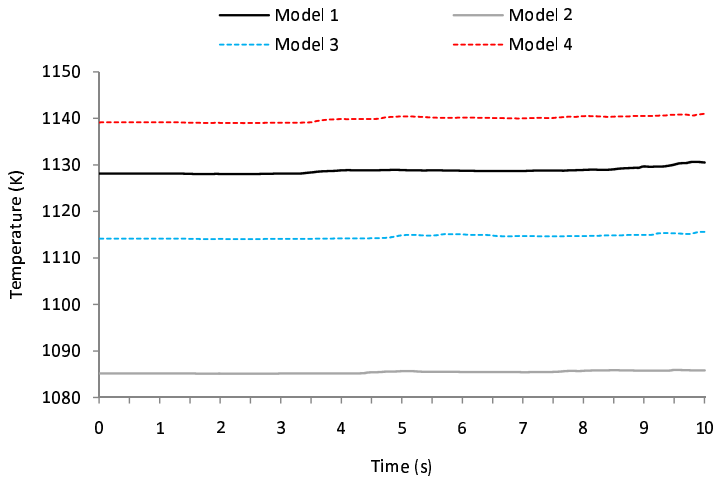

FIGURE 6.35: Instantaneous average gas temperature for each model taken at the exit of the reactor.

The average mole fraction of CO_2 does not show a definitive increase or decrease in mole fraction with increasing temperature. CO_2 is the product of the dominant combustion reaction (R1) therefore increasing the temperature would produce CO_2 much faster. It can be seen from Table 6.5 that the ratio of air to steam increases with increasing bed temperatures therefore with higher temperatures there is more O_2 available for consumption through the combustion reaction leading to an increase in CO_2. Furthermore, CO_2 is one of the dominant species of the devolatilisation process therefore CO_2 would also be supplied faster from the fuel inlet. Therefore it would be assumed that the mole fraction of CO_2 would increase with increasing temperature. This can be seen in the initial stages of Fig. 6.34 b) however after about 4.0 s the mole fraction for all models

do not show any distinctive variation between the different models. CO_2 is also the reactant of the Boudouard reaction (R3) so any additional CO_2 with increasing temperatures would promote this reaction leading to an increase in CO, as was observed. Therefore, whilst CO_2 is being produced faster with increasing temperatures is it also being consumed faster leading to the similar average composition between the models.

Figure 6.35 appears to show a gradual increase in the average temperatures of the gas leaving the reactor. Table 6.6 provides the temperature increase from the temperatures taken at the beginning and the end of the 10.0 s simulation. Although the highest temperature does not have the largest temperature increase the results seems to suggest higher temperatures result in larger temperature increases. This is because an increase in the temperature would lead to an increase in the water-gas shift reaction rate. Since this reaction is slightly exothermic increased activity would gradually increase the temperature in the freeboard. The water-gas shift reaction is also dependent on the concentration of its reactants so a possible reason for the slightly higher increase in temperature in model 1 compared to model 4 could be due to a distinctive variation in the mole fraction of the relevant reactants, namely CO, CO_2, H_2 and H_2O; between the two models which is seen in Fig. 6.34.

At around 9.5 s there is a large difference between the mole fractions of CO and H_2

TABLE 6.6: Temperature increases from average temperature taken at the beginning and at the end of the simulation.

Temperature (K)	Model 1	Model 2	Model 3	Model 4
At 0.0 s	1128.15	1085.15	1114.15	1139.15
At 10.0 s	1130.5116	1085.8207	1115.6143	1141.0187
Increase	2.3616	0.6707	1.4643	1.8687

for the two models moreover, model 1 there shows a stronger drop these mole fraction compared to any other previous times. This change in mole fraction would affect the water-gas shift reaction significantly as the species compete to reach equilibrium hence accelerating the equilibrium reaction leading to the generation of more exothermic heat. This would explain the sudden jump in the instantaneous average temperature in Fig. 6.35 around this time for model 1 and hence the slight increase in temperature of this model compared to model 4 at 10.0 s which was seen in Table 6.6.

Since the majority of the species in Fig. 6.34 appear to display steady compositions after 5.0 s the mole fraction of the exiting gases were averaged over the final 5.0 s and compared to the relevant experimental data given in the literature [5] in Fig. 6.36. In all cases the species show similar trends to the experimental results. Model 3 and model 4 provide close representations of the experimental data for the majority of the species. As expected CH_4 is significantly lower in all cases since it continues to increase in concentration with time as seen previously. The mole fraction of CO_2 shows a significant under prediction for model 1 and model 2. Assumptions have been made on the amount

of limestone in the bed compared to char, as specific information was not provided in the literature, therefore this would lead to variations in the predicted results. All the species underpredict the experimental data which is expected as H_2O was found in the simulated results to constitute the largest fraction of the exiting gases and the information for this species was not available in the literature for the experimental results, similarly with tar information. Therefore if this fraction were considered in the experimental data then the experimental values would decrease which would potentially lead to an improved in the comparison with the simulated results. For a closer comparison of the average mole fractions of the species the simulated and experimental data is also provided in Table 6.7.

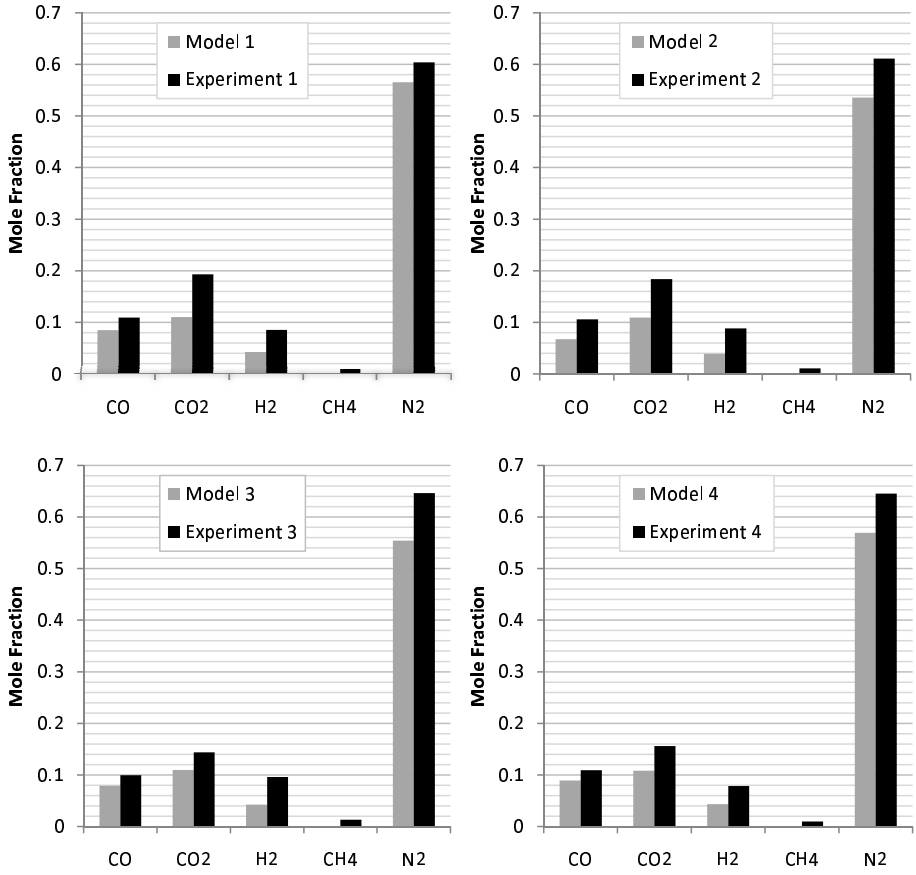

FIGURE 6.36: Average mole fraction of the exiting gases for the four different models.

6.2.2 Fuel variation

The present section looks at the models application to a different fuel, namely wood. Model 1 is extended further to include an additional biomass phase with three different ratios. Case 1 - coal only (the results given for Model 1 in Table 6.7; Case 2 - a wood to coal ratio of 25:75; Case 3 - a wood to coal ratio of 50:50 and Case 4 - wood only.

TABLE 6.7: Comparison of the simulated and experimental mole fraction of the exiting gases for the four different models.

	CO	CO_2	H_2	CH_4	N_2	H_2O	Tar
Model 1	0.08503	0.11023	0.04261	0.00006	0.56551	0.19647	0.00009
Experiment 1	0.10940	0.19310	0.08530	0.00840	0.60370	Not given	Not given
Model 2	0.06748	0.10906	0.03898	0.00004	0.53538	0.24900	0.00007
Experiment 2	0.10590	0.18380	0.08840	0.01070	0.61100	Not given	Not given
Model 3	0.07904	0.10987	0.04230	0.00005	0.55385	0.21480	0.00009
Experiment 3	0.09970	0.14400	0.09630	0.01340	0.64620	Not given	Not given
Model 4	0.08919	0.10833	0.04350	0.00006	0.56919	0.18963	0.00010
Experiment 4	0.10940	0.15600	0.07880	0.01010	0.64520	Not given	Not given

TABLE 6.8: Operating conditions for the co-gasification modelling in the 3D BFB gasifier.

Operating Conditions	Case 1	Case 2	Case 3	Case 4
Air supply (kg/h)	21.9	21.9	21.9	21.9
Steam supply (kg/h)	4.7	4.7	4.7	4.7
Coal feed (kg/h)	8.0	6.0	4.0	0.0
Wood feed (kg/h)	0.0	2.0	4.0	8.0
Limestone feed (kg/h)	0.8	0.8	0.8	0.8
Air and steam				
temp at entrance (K)	693.15	693.15	693.15	693.15
Temperature of reactor (K)	1128.15	1128.15	1128.15	1128.15

Table 6.8 displays the set up for each case. The properties for the biomass particles are given in Table 6.9.

TABLE 6.9: Table of Parameters: Biomass properties for 3D modelling.

Biomass	
Particle diameter (m)	0.004
Particle density (kg/m^3)	585
Specific heat (J/kg K)	2380
Thermal conductivity (W/m K)	0.158

Figure 6.37 displays the gaseous compositions of the species, averaged between the period 5.0 s and 10.0 s, leaving the reactor. The results show that the inclusion of wood into the reactor influences the compositions of the emissions. Case 4, which models wood only, shows an increase in all species compared to case 1 which models coal only. Whilst these increases are only slight in the CO, CO_2, H_2 and H_2O species there is a dramatic increase in the mole fractions of CH_4 and tar.

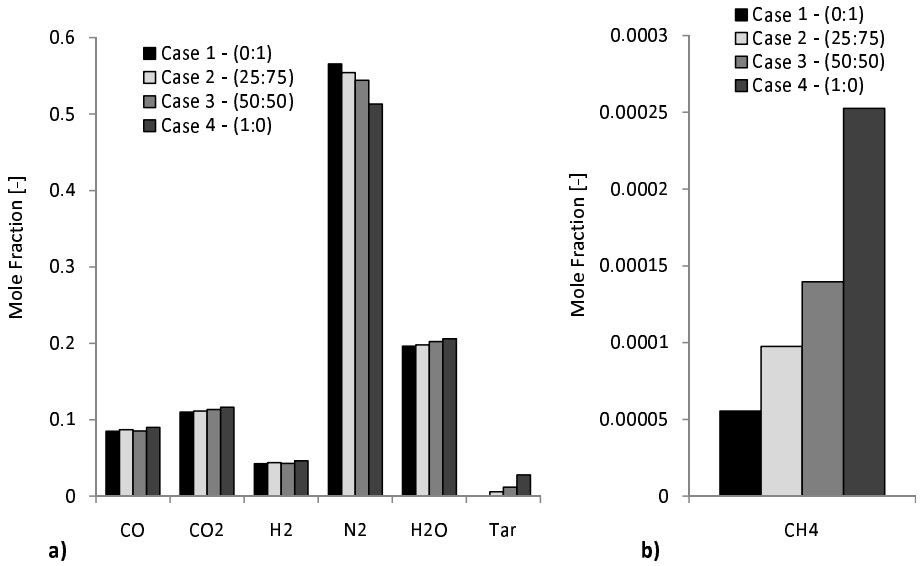

FIGURE 6.37: Average gas compositions of a) the dominating species and b) CH_4 for the four fuel composition cases.

The composition of the devolatilisation gases, given in Table 6.10, shows a larger composition of CH_4 and CO_2 in the wood gases than in the coal whilst the remaining species have a lower content. Since the formation of CH_4 was shown previously in Section 6.2.1 to primarily develop from the devolatilisation process its increase in mole fraction with increasing wood content would be due to the significantly higher CH_4 content in the wood. Although the average mole fractions of CO, CO_2, H_2 and H_2O show a slight increase with increasing wood ratio in Fig. 6.37 this trend is not always observed as the CO and H_2 display lower average mole fractions for case 3 compared to case 2. This would be due to the water-gas shift reaction amending the concentrations as expected. However regardless of this, there is still a general increase in the average mole fraction for each of all species with increasing wood content, including the CO and H_2, when compared with the coal only model. This includes species with lower composition in the wood compared to coal shown in Table 6.10. This would be due to the volatile content in wood being higher than coal therefore a larger proportion of the gaseous species would be released through the wood devolatilisation process which would lead to higher mole fractions of the gaseous products.

TABLE 6.10: Composition of the different gaseous products released during the devolatilisation process for wood and coal.

Fuel	**CO_2**	**CO**	**CH_4**	**H_2**	**H_2O**
Wood	0.386	0.270	0.056	0.032	0.256
Coal	0.142	0.273	0.028	0.059	0.314

The average mole fraction of tar shows a dramatic increase with increasing wood content in Fig. 6.37. This is because the wood devolatilisation model [142] used in the present model only models the primary stage and does not include tar cracking which further breaks the tar down into inert tar and additional gaseous compositions. Therefore the tar produced would be higher than that given in the coal devolatilisation model as the tar cracking stage would usually be reduced further during the secondary stage. In order to accommodate for the tar cracking stage an additional inert tar species would need to be incorporated into the gaseous phase.

6.3 Conclusions

Two-dimensional Eulerian-Eulerian modelling was carried out on a coal bubbling fluidised bed gasifier with a char and limestone bed with the introduction of limestone calcination to determine its impact on the composition of the gases leaving the reactor. The compositions of the gaseous species were validated with experimental data from the literature and a full parametric study was carried out to determine different conditions that impact the exiting gaseous compositions.

The formation of bubbles formed both exogenously and endogenously as a result of the reaction kinetics were observed. Multiple phases were used for the different bed phases, char and limestone, and their different material properties led to phase segregation as lower density char particles were transported not only through the mixing behaviour of the bed but also within the ascending bubbles. The denser limestone particles descended to the base of the reactor.

Two different devolatilisation models were compared and both agreed well with the available experimental data. However after 100.0 s the Kobayashi model displayed steady conditions whilst the Badzioch model had not. This was down to the inclusion of yield factors in the Kobayashi model which modifies the volatile release based on the local temperature. This is not included in the Badzioch model therefore whilst coal particles would migrate to lower temperature regions the change in volatile yields would not be correctly accounted for. The Kobayashi model was applied to the remaining calculations due to its improved adaptability leading to earlier steady state achievement hence a reduction in computational time and cost.

An investigation into the heterogeneous reactions showed the complete consumption of oxygen near the air/steam inlet as a result of the dominating combustion reaction. The remaining gasification heterogeneous reactions took place in different regions of the reactor depending on the local concentration of the gasifying species. H_2O and CO_2 dominated the lower region of the bed due to the introduction of H_2O and CO_2 being a product of the combustion reaction. Such species decreased in mole fraction with increasing height as they got consumed by further reactions. The methanation reaction

took place higher in the bed after an accumulation of H_2 as a product of heterogeneous reactions and from the devolatilisation process. The homogeneous oxidation reactions took place near the air/steam inlet where there was O_2 present. Above the bed and in large gaseous bubbles, the water-gas shift reaction took place.

The mole fraction of the gaseous species were taken at the exit of the reactor over time and, as expected in lab-scale reactors, fluctuations indicated that the water-gas shift reactor had not reached equilibrium. The average mole fractions were compared to experimental results for two different experimental setups. Reasonable results were achieved however an increase in CO and decrease in CO_2 was observed in the models compared to experimental data. This is due to the present expansion of previous work to include char in the bed compared to limestone being the dominating bed material in the experimental reactor. A lower mole fraction of CO_2 was observed as its reaction took place more readily throughout the bed increasing the mole fraction of CO.

Variation of bed height influenced both the water-gas shift reaction and mole fraction of the products from heterogeneous reactions. A lower bed height provided additional freeboard space for the gaseous species meaning equilibrium was more attainable. The composition of the gaseous species showed an increase in the products of heterogeneous reactions and decrease in their reactants as the bed height increased. This was because increased bed height allowed for additional char to consume the reactants more effectively to produce more CO, H_2 and CH_4.

The temperature distribution within the bed was presented more extensively than previous CFD models of gasification processes. As seen previously, higher temperatures were observed in the vicinity of the air/steam inlet as the exothermic combustion of oxygen took place however reducing the temperature scale displayed varying temperatures throughout the bed as a result of the different reactions taking place locally. The Boudouard and steam gasification reactions are endothermic and their presence throughout the bed at different rates resulted in temperature reductions. Whereas the homogeneous reactions including the water-gas shift are exothermic and in regions of low solid volume fraction, namely, the bubbles, there appeared to be a slight increase in temperature due to the water-gas shift reaction taking place.

The temperature of the bed was varied and an increase in temperature led to an increase in the reaction products and decrease in their reactants. This was due to the acceleration of the reaction rate since the heterogeneous reactions are highly temperature dependent. Increasing the temperature displayed erratic instantaneous average mole fractions of the species indicating the water-gas shift reaction was unstable and far from reaching equilibrium. It was assumed that should the two dominating species in the freeboard be the reactants on the same side of the water-gas shift reaction then the attainability of reaching equilibrium would be very difficult. Having dominating species on both sides

displayed smaller fluctuations in the instantaneous mole fractions leading to an improved chance of reaching an equilibrium state.

Heat transfer coefficients were introduced on the walls and showed the convective transport of heat within the freeboard affected the average gaseous temperature leaving the reactor but did not influence the average mole fraction of the gaseous species. Since the temperature of the particulate bed dominates compared to the convective temperatures from the walls there would be no variation in bed temperature leading to similar mole fractions of the heterogeneous products.

Limestone calcination was introduced to a computational fluid dynamic model with results showing only slight effects. A reason could be the relatively short simulation time, which does not show the full effects of limestone calcination. However, slight changes were observed in the gaseous compositions due to the introduction of further CO_2 as a result of limestone decomposition. Its impact affected the water-gas shift reaction as the species adjust to reach an equilibrium.

Different ratios of coal to limestone volume fractions in the bed were studied and additional char led to an increase in the products of heterogeneous reactions, as such reactions took place more often. Since increased levels of char enabled more heterogeneous reactions to take place the reactants, CO_2 and H_2O, decreased with increasing char content. The mole fraction of O_2 at different heights near the air inlet for the different char:limestone ratios were analysed showing O_2 decreases with height and with increased char content in the bed.

Two models were carried out for a bed with limestone only, one treating the limestone as inert whilst the other calcinated. The results showed that after a short period of time the contribution of additional CO_2 through calcination was only small. In addition to this there were very low gaseous composition of all species as the only char taking place in heterogeneous reactions was that produced through the devolatilisation process. Furthermore, the combustion reaction was limited to this region meaning more O_2 was present throughout the bed. Increased O_2 enabled oxidation homogeneous reactions to take place near the top of the bed consuming the devolatilisation products and those produced through the heterogeneous reactions immediately.

The simulations were extended to 2000.0 s using a coarser grid which appropriately captured the basic bubbling characteristics however a slight loss of accuracy was observed during the transition from dilute to dense phases. The mole fraction of the exiting gaseous appeared consistent between fine and coarse grids. Furthermore, the extended simulations showed steady gaseous compositions were achieved after approximately 400.0 s suggesting that previous coal gasification results obtained both in the present chapter and in the literature [63, 113] which ran upto 100.0 s were not ran for a sufficient period of time.

The mass of the solid phases were analysed showing a reduction in char due to heterogeneous reaction and an increase in coal which levelled off as the bed became accustomed to the introduction of fresh coal and the consumption due to the devolatilisation processes. The limestone showed a gradual increase due to an inflow of limestone in the fuel inlet. Its constituents, $CaCO_3$ and CaO, showed a decrease and increase, respectively, due to the calcination reaction.

Three-dimensional models were also carried out which tested different gas inlet velocities and temperatures which agreed well with experimental data from the literature. The model was also changed to incorporate different fuel properties, namely, wood. The simulations displayed an increase in the average mole fraction of the species with increasing wood content due to the larger volatile content in wood compared to coal.

Chapter 7

Conclusions

This chapter summises the conclusions that were drawn throughout the thesis and the novelties made as a result of this work. Finally, suggestions are made for the future application of this work to the field of fluidisation technologies along with its extension into further fields of research.

7.1 Conclusions

7.1.1 Hydrodynamic modelling

Two-dimensional and three-dimensional simulations were carried out on a circulating fluidised bed taken from the literature [2]. A parametric study carried out in the riser under a bubbling regime considered variations in drag model, coefficients of restitution, inlet velocity and particle diameter. The transition from a bubbling bed regime to a fast fluidising regime was observed once the inlet velocity exceeded the terminal velocity.

Bubble sizes increased with height, increasing inlet velocity and particle diameter. Lower velocities led to a greater collection of particles settling back to the base of the riser. The results of the variation in coefficient of restitution showed that the particles with the larger coefficient of restitution, 0.98, displayed reduced particle agglomeration at the base of the bed as a higher coefficient of restitution conserves more energy during the collisions of particles resulting in a move active movement of particles.

The complete CFB geometry was simulated for a fast fluidising regime using two drag models, the Gidaspow and the energy minimisation multiscale (EMMS) model. The EMMS model correctly predicted the particle clusters which the Gidaspow model was unable to take into account.

The 3D EMMS models showed the magnitude of the particle velocities agreed fairly well with the experimental results taken from literature [2]. The 3D Gidaspow results did

not show the core-annulus structure and over estimated the velocity. This was not only because of the models inability to capture the correct cluster formation but also a much coarser grid was used in the 3D model reducing the accuracy.

Improvements were made on the EMMS downflow velocity of the particles at the walls as the shear on the wall was slightly increased compared to previous simulations in the literature which imposed a free slip condition. The volume fraction distribution of particles at different heights showed an increase in the volume fraction at the walls due to the segregation of particles from the core towards the walls; this further increased down the bed as the particles descend and accumulate. The 3D results agreed that higher volume fractions of particles are found at the walls, as seen experimentally and in the 2D models.

Increasing the airflow to a transitional turbulent state along with the presence of the secondary inlet affects the flow of particles within the bed to produce an irregular flow lower down the riser becoming more symmetrical with height.

7.1.2 Heat transfer modelling

Different drag models were compared in a parametric study of two beds with two heat sourses, i.e., a heated wall and heated tubes. Contour plots comparing drag models showed very similar features however differences were observed in the local near-wall region as the different drag models showed different clustering effects at the wall. Higher particle volume fractions due to clustering resulted in a higher heat transfer due to improved conduction. It is difficult to distinguish the best drag model since each drag model varied in heat transfer coefficients and volume fractions for both reactors but the results were of similar behaviours and magnitudes.

The local heat transfer coefficients for all the drag models in both reactors agreed reasonably well with the results obtained in the literature for an effective thermal conductivity consisting of only a molecular contribution. The results from the kinetic contribution greatly overestimated the values of the heat transfer coefficients due to the strong influence that the granular temperature has from the kinetic theory of granular flow. The heat transfer coefficient reduced with increasing the particle diameter due to an increased porosity between the compact particles.

Multiple bubble formations occurred due to the partitioning of the bubbles from the recirculating particle bed back towards the wall. An extended simulation time showed a gradual decrease in local heat transfer coefficient and multiple bubble formations whilst the fast inlet was supplying air. This is due to the bed becoming more regular and the circulating particles partitioning the elongated bubble along the wall. Such results confirmed that previous simulations in the literature were not run long enough to allow the flow to fully develop.

Whilst the tube-to-bed reactor displayed similar resemblances in the early stages to the symmetrical results from the literature extending the simulation time led to a more asymmetric distribution. Increasing the number of tubes improved the heat transfer due to the increased heat transfer area and the break up of bubbles to form smaller particle carrying voidages. Temperature distributions of the particles showed that increasing the number of tubes increases heat transfer from the tubes to the particles and the flow around the tubes resulting in an increase in temperature. Increased particle temperature occurred during the transition from dense particle-laden regions to dilute regions due to mixing whereas the transition from dilute to dense particle regions led to a local temperature reduction due to the introduction of new cooler particles.

7.1.3 Reaction modelling

Reaction models were incorporated into a two-dimensional Eulerian-Eulerian model of a coal bubbling fluidised bed gasifier with a char and limestone bed and the introduction of limestone calcination to determine the its impact on the composition of the gases leaving the reactor. Bubbles formed both exogenously and endogenously as a result of the reaction kinetics. Multiple phases for the bed phases, char and limestone, led to phase segregation as lower density char particles migrated towards the top of the bed and the denser limestone particles descended to the base of the reactor.

The average compositions of the gaseous species were validated with experimental data from the literature and agreed well. The composition of the species in the bed showed H_2O and CO_2 dominated the lower region of the bed due to the introduction of H_2O and CO_2 being a product of the combustion reaction which consumed the O_2 immediately. These species were consumed further up the bed as opposed to the methanation reaction took place higher in the bed after an accumulation of H_2 as a product of heterogeneous reactions. The homogeneous oxidation reactions were confined to O_2 enriched areas whilst the water-gas shift reaction dominated the freeboard. Higher temperatures were observed near the inlet where the exothermic combustion reaction took place whereas slight temperature increases in bubbles were due to the slightly exothermic water-gas shift reaction.

A full parametric study looking at the variation of bed height, bed material, bed temperature and heat transfer coefficients from the walls was carried out. The variation of bed height was seen to influence both the water-gas shift reaction and mole fraction of the products from heterogeneous reactions as the freeboard space was increased with lower heights. However, a lower bed height led to less char in the bed leading to an inefficient consumption of CO_2 and H_2O through heterogeneous reactions. Increased char levels in the bed led to an increase in the products of heterogeneous reactions, as such reactions took place more readily. Increasing bed temperature led to an increase in the highly temperature dependant heterogeneous reaction rates leading to an increase in

the reaction products and decrease in their reactants. Finally, heat transfer coefficients showed negligable effects on the average composition of species leaving the reactor as the heterogeneous reactions dominated, however the convective transport of heat within the freeboard affected the average gaseous temperatures leaving the reactor.

Limestone calcination was introduced to a computational fluid dynamic model with results showing only slight effects due to the relatively short simulation time, which does not show the full effects of limestone calcination. A bed containing only limestone displayed very low gaseous composition of all species since heterogeneous reactions were confined to the char produced through the devolatilisation process. Increased O_2 in the bed consuming the devolatilisation products and those produced through the heterogeneous reactions immediately through oxidation homogeneous reactions.

Extended simulations showed steady gaseous compositions were achieved after approximately 400.0 s suggesting that previous coal gasification results obtained, which ran up to 100.0 s, were not run for a sufficient period of time. The masses of the solid phases over time showed a reduction in char due to heterogeneous reaction and an increase in coal which levelled off as the bed became accustomed to the introduction of fresh coal and its consumption during the devolatilisation process. The limestone showed a gradual increase due to an inflow of limestone in the fuel inlet. Its constituents, $CaCO_3$ and CaO, showed a decrease and increase, respectively, as a result of the calcination process.

Three dimensional models were also carried out which tested different gas inlet velocities and temperatures and agreed well with experimental data from the literature. The model was also changed to incorporate different fuel properties, namely, wood. The simulations displayed an increase in the average mole fraction of the species with increasing wood content due to the larger volatile content in wood compared to coal.

7.2 Summary of contributions

This thesis has presented contributions to the fields of multiphase flow dynamics, heat transfer and reaction kinetics. The following contributions were made:

- An extensive review was carried out on the coal gasification processes in a lab-scale bubbling fluidised bed using an Eulerian-Eulerian kinetic theory of granular flow model with the incorporation of reaction kinetics, via C-subroutines, in the commerical software ANSYS 12.0. Whilst the use of multiple solid phases displays improved flow dynamics over previous models an extensive review highlights the models ability to correctly incorporate variations to the model set up which is essential for the determination of optimal reactor designs and operating conditions which will improve performance whilst reducing emissions.

- The introduction of limestone calcination is an encouraging step forward in the aim for improved emissions as reagents such as limestone are applied to reactors to help reduce SOx emissions. The present model can now be expanded further to include SOx and NOx modelling along with the inclusion of desulphurisation kinetics.

- The heat transfer from multiple immersed tubes was carried out and highlighted a number of important factors which were not considered previously. Whilst the positions of the tubes may be symmetrical, the heterogeneous behaviour of the bed requires that a complete bed should be modelled over previous symmetrical beds. Whilst heat transfer has been seen previously to accelerate in particle-laden regions it was also found in the present work that the heat transfer in the near regions of immersed tubes was improved in the presence of dilute bubbles where heated particles were mixed and transported to cooler regions transporting heat with them. This was also improved with additional tubes where additional heat sources along with the improved mixing led to improved bed temperatures.

- The transition from a bubbling bed to a fast fluidising bed was captured effectively using an Eulerian-Eulerian model. The air inlet was varied within the region of the terminal velocity for different particle properties. The advantage of an Eulerian-Eulerian model being able to capture this transition means that should the variation of phase diameters or densities be included in such models due to the reaction processes, i.e., particle shrinkage, then appropriate inlet velocities can be chosen to avoid potential entrainment.

7.3 Future work

The developed gasification code can be applied to Eulerian-Eulerian models of both bubbling and circulating beds. With substantial research being carried out in the advancement and incorporation of multiscale modelling to circulating fluidised bed technologies, the inclusion of reaction modelling alongside such models would allow the simulated gasification process to be carried out in large-scale circulating reactors which are utilised in industry for the product of energy. The use of sub-grid scale models to capture the multiple scales observed in circulating beds allows for coarser grids which means the model can be expanded to include further reactions without influencing the computational time too much.

The code can be modified easily to consider a vast number of pyrolysis, gasification and combustion reactions. In the near future the aim is to expand the code to include a database with a number of available reaction kinetics which also includes SOx and NOx reactions such that when the code is integrated into the commerical software the user needs to just choose the relevant reaction rate from the drop down list according to the

model they are carrying out. This would also include the reaction kinetics for a variety of fuels including different biomasses, e.g., wood, straw etc.

Computational fluid dynamics is emerging as an important tool in both academic and industrial research with improvements in the hydrodynamic, heat transfer and reaction models continuing to be made. Furthermore the continual advancement in computational performance allows for reduced computational times and expense. The application of CFD to the future research of fluidised bed technologies will be vital due to the expense of experimental modifications compared with preliminary simulations which could potential determine optimal reactors designs and operating conditions for the improvement of energy production and emissions reduction. Finally, the incorporation of reaction kinetics into Eulerian-Eulerian granular flows could also apply to other fields other than fluidised bed technologies e.g. biological and medical engineering.

Appendix A

Momentum Interphase Equations

For the majority of the drag model, unless stated otherwise, the particle Reynolds number, Re, is calculated as follows:

$$Re_s = \frac{\rho_g d_s \left| \vec{v_s} - \vec{v}_g \right|}{\mu_g} \tag{A.1}$$

A.1 The Ergun equation

The frictional pressure drop coefficient for a particle size, d_s and particle sphericity, ϕ_s was correlated by Ergun [64] for densely packed beds as follows:

$$\frac{\Delta P}{\Delta x} = 150 \frac{\varepsilon_s^2 \mu_g U_0}{\varepsilon_g^3 (\phi_s d_s)^2} + 1.75 \frac{\varepsilon_s \rho_g U_0^2}{\varepsilon_g^3 \phi_s d_s} \tag{A.2}$$

where

$$U_0 = \varepsilon_g \left(v_g - v_s \right) \tag{A.3}$$

Now the friction coefficients between the fluid and the solid are obtained from correlations when the acceleration is negligable. Therefore in a steady state and neglecting acceleration, gravity and wall friction the following expression is obtain from the gas momentum balance:

$$-\varepsilon_g \frac{\partial P}{\partial x} - K_{gs} \left(v_g - v_s \right) = 0 \tag{A.4}$$

Comparison of Equation A.2 and Equation A.4 then gives the following drag model which is only valid for $\varepsilon_g \leq 0.8$:

$$K_{gs} = 150\,\frac{\varepsilon_s^2 \mu_g}{\varepsilon_g \left(\phi_s d_s\right)^2} + 1.75 \frac{\varepsilon_s \rho_g \left|\upsilon_g - \upsilon_s\right|}{\phi_s d_s} \tag{A.5}$$

A.2 The Wen-Yu drag function

Unfortunately, fluidised regimes also contain gas rich regions due to bubbles and the gas above the bed in the freeboards so a model needed to be developed that accounted for the drag within these regions. The Wen and Yu drag function [19] was developed and has been widely accepted for $\varepsilon_g > 0.8$:

$$K_{gs} = \frac{3}{4}\,C_D\,\frac{\varepsilon_s \varepsilon_g \rho_g \left|\vec{\upsilon_s} - \vec{\upsilon}_g\right|}{d_s}\,\varepsilon_g^{-2.65} \tag{A.6}$$

where

$$C_D = \frac{24}{\varepsilon_g Re_s}\left[1 + 0.15\left(\varepsilon_g Re_s\right)^{0.687}\right] \tag{A.7}$$

A.3 The Gidaspow drag function

The Gidaspow drag model [65] is a standard model which has been used for many fluidised bed simulations and incorporates the two drag models for the dense and dilute regions of the bed using the models from Ergun [64] and Wen and Yu [19], respectively:

$$K_{gs} = \frac{3}{4}\,C_D\,\frac{\varepsilon_s \varepsilon_g \rho_g \left|\vec{\upsilon_s} - \vec{\upsilon}_g\right|}{d_s}\,\varepsilon_g^{-2.65} \quad \text{for } \varepsilon_g > 0.8 \tag{A.8}$$

$$K_{gs} = 150\,\frac{\varepsilon_s^2 \mu_g}{\varepsilon_g d_s^2} + 1.75 \frac{\varepsilon_s \rho_g \left|\vec{\upsilon_s} - \vec{\upsilon}_g\right|}{d_s} \quad \text{for } \varepsilon_g \leq 0.8 \tag{A.9}$$

where

$$C_D = \frac{24}{\varepsilon_g Re_s}\left[1 + 0.15\left(\varepsilon_g Re_s\right)^{0.687}\right]$$

A.4 The Syamlal-O'Brien drag function

Syamlal and O'Brien [68] developed a drag function which was based on a single particle's terminal velocity. They considered that under terminal velocity conditions, the drag force on a particle was equal to its buoyant weight thus determined the following drag function:

$$K_{gs} = \frac{3}{4}\,\frac{\varepsilon_s \varepsilon_g \rho_g}{\upsilon_{r,s}^2 d_s}\,C_D\left(\frac{Re_s}{\upsilon_{r,s}}\right)\left|\vec{\upsilon_s} - \vec{\upsilon}_g\right| \tag{A.10}$$

where

$$C_D = \left(0.63 + \frac{4.8}{\sqrt{Re_s}\upsilon_{r,s}}\right)^2 \tag{A.11}$$

The terminal velocity correlation $\upsilon_{r,s}$ of the particles was taken from a correlation for the velocity and voidage from Garside and Al-Dibouni [152]:

$$\upsilon_{r,s} = 0.5\left(A - 0.06Re_s + \sqrt{(0.06Re_s)^2 + 0.12Re_s\,(2B - A) + A^2}\right) \tag{A.12}$$

with

$$A = \varepsilon_g^{4.14} \quad B = \varepsilon_g^{2.65} \quad \text{for } \varepsilon_g > 0.85$$

or

$$A = \varepsilon_g^{4.14} \quad B = 0.8\varepsilon_g^{1.28} \quad \text{for } \varepsilon_g \leq 0.85$$

A.5 The Energy Minimisation Multiscale (EMMS) drag model

The energy minimisation multiscale (EMMS) approach was developed by Yang et al. [81] which can identified the different multiple scales present in a circulating fluidised bed and correctly account for the clustering effects which would not be accounted for in standard non-filtered drag models:

$$K_{gs} = 150\,\frac{\varepsilon_s^2\mu_g}{\varepsilon_g^2 d_s^2} + 1.75\frac{\varepsilon_s\rho_g\left|\vec{\upsilon_s} - \vec{\upsilon_g}\right|}{\varepsilon_g d_s} \qquad \text{for } \varepsilon_g \leq 0.74 \tag{A.13}$$

$$K_{gs} = \frac{3}{4}\,C_D\,\frac{\varepsilon_s\rho_g\left|\vec{\upsilon_s} - \vec{\upsilon_g}\right|}{d_s}\,\omega(\varepsilon) \qquad \text{for } \varepsilon_g > 0.8 \tag{A.14}$$

$$\omega(\varepsilon) = \begin{cases} -0.5760 + \frac{0.0214}{4(\varepsilon_g - 0.7463)^2 + 0.0044} & (0.74 < \varepsilon_g \leq 0.82) \\ -0.0101 + \frac{0.0038}{4(\varepsilon_g - 0.7789)^2 + 0.0040} & (0.82 < \varepsilon_g \leq 0.97) \\ -31.8295 + 32.8295\varepsilon_g & (\varepsilon_g > 0.97) \end{cases} \tag{A.15}$$

where

$$C_D = \frac{24}{Re_s}\left[1 + 0.15\,(Re_s)^{0.687}\right] \qquad \text{for } \mathrm{Re_s} \leq 1000$$

$$C_D = 0.44 \qquad \text{for } \mathrm{Re_s} > 1000$$

A.6 The Hill-Koch-Ladd drag function

Hill et al. [74, 75] developed a drag model based on Lattice-Boltzmann theory which provided different formulas for the drag function at varying Reynolds numbers and particle volume fraction. Unfortunately, the transition between the different equations were very sudden which caused problems with regards to modelling the transitions. Therefore, Benyahia et al. [73] extended their work further to develop a single formula that smoothly covers the varying range of Reynolds numbers and volume fraction without jumps or gaps such that it can be applied to multiphase models:

$$K_{gs} = 18\mu_g \left(1-\varepsilon_s\right)^2 \varepsilon_s \frac{F}{d_s^2} \tag{A.16}$$

The force is defined by:

$$F = 1 + \frac{3}{8} Re_s \qquad \varepsilon_s \leq 0.01 \;\text{ and }\; Re_s \leq \frac{F_2 - 1}{(3/8) - F_3} \tag{A.17}$$

$$F = F_0 + F_1 Re_s^2 \qquad \varepsilon_s > 0.01 \;\text{ and }\; Re_s \leq \frac{F_3 + \sqrt{F_3^2 - 4F_1\left(F_0 - F_2\right)}}{2F_1} \tag{A.18}$$

$$F = F_2 + F_3 Re_s \begin{cases} \varepsilon_s \leq 0.01 \;\text{ and }\; Re_s > \frac{F_2 - 1}{(3/8) - F_3} \\ \\ \varepsilon_s > 0.01 \;\text{ and }\; Re_s > \frac{F_3 + \sqrt{F_3^2 - 4F_1(F_0 - F_2)}}{2F_1} \end{cases} \tag{A.19}$$

Where the parameters are set as follows:

$$F_0 = \begin{cases} (1-w)\left[\frac{1+3\sqrt{(\varepsilon_s/2)}+\frac{135}{64}\varepsilon_s \ln(\varepsilon_s)+17.14\varepsilon_s}{1+0.681\varepsilon_s-8.4\varepsilon_s^2+8.16\varepsilon_s^3}\right] + w\left[\frac{10\varepsilon_s}{(1-\varepsilon_s)^3}\right] & \\ & 0.01 < \varepsilon_s < 0.4 \\ \\ \frac{10\varepsilon_s}{(1-\varepsilon_s)^3} & \varepsilon_s \geq 0.4 \end{cases} \tag{A.20}$$

$$F_1 = \begin{cases} \frac{\sqrt{(2/\varepsilon_s)}}{40} & 0.01 < \varepsilon_s \leq 0.1 \\ \\ 0.11 + 0.00051 \exp\left(11.6\varepsilon_s\right) & \varepsilon_s > 0.1 \end{cases} \tag{A.21}$$

$$F_2 = \begin{cases} (1-w)\left[\frac{1+3\sqrt{(\varepsilon_s/2)}+\frac{135}{64}\varepsilon_s \ln(\varepsilon_s)+17.89\varepsilon_s}{1+0.681\varepsilon_s-11.03\varepsilon_s^2+15.41\varepsilon_s^3}\right] + w\left[\frac{10\varepsilon_s}{(1-\varepsilon_s)^3}\right] & \varepsilon_s < 0.4 \\ \\ \frac{10\varepsilon_s}{(1-\varepsilon_s)^3} & \varepsilon_s \geq 0.4 \end{cases} \tag{A.22}$$

$$F_3 = \begin{cases} 0.9351\varepsilon_s + 0.03667 & \varepsilon_s < 0.0953 \\ 0.0673 + 0.212\varepsilon_s + \frac{0.0232}{(1-\varepsilon_s)^5} & \varepsilon_s \geq 0.0953 \end{cases} \tag{A.23}$$

Where

$$w = \exp\left(-10\left(\frac{0.4-\varepsilon_s}{\varepsilon_s}\right)\right)$$

The Reynolds number for the particles is calculated as follows:

$$Re_s = \frac{\rho_g\left(1-\varepsilon_s\right)d_s\left|\vec{v_s} - \vec{v}_g\right|}{2\mu_g} \tag{A.24}$$

Appendix B

Discretisation

Solving flow problems analytically is very difficult due to the complexity and non-linearity of the governing equations. ANSYS 12.0 is designed to simplify this by separating the domain into discrete volumes and solving for each individual algebraic equation. This is known as the finite volume method.

To explain the process of discretisation it is good to start with the general scalar equation:

$$\underbrace{\frac{\partial(\rho\phi)}{\partial t}}_{\text{Transient term}} + \underbrace{\nabla\cdot(\rho\phi\overline{\nu})}_{\text{Convection term}} = \underbrace{\nabla\cdot(\Gamma\nabla\phi)}_{\text{Diffusion term}} + \underbrace{S}_{\text{Source term}} \tag{B.1}$$

The discretisation of a basic example would be a one-dimensional case for the steady convection and diffusion terms in the absence of sources:

$$\frac{d(\rho\phi u)}{dx} = \frac{d}{dx}\left(\Gamma\frac{d\phi}{dx}\right) \tag{B.2}$$

During the discretisation process, the scalar quantity, ϕ is determined and stored at each of the grid points **P**, **W** and **E**, which can be seen in Fig. B.1. ANSYS 12.0 would carry out the calculations, repeat the iterations and adjusts these values accordingly until convergence has been reached.

Integrating these equations over the control volume in Fig. B.1 gives:

$$\int_w^e \frac{d(\rho\phi u)}{dx}dx = \int_w^e \frac{d}{dx}\left(\Gamma\frac{d\phi}{dx}\right)dx \tag{B.3}$$

$$(\rho\phi uA)_e - (\rho\phi uA)_w = \left(A\Gamma\frac{d\phi}{dx}\right)_e - \left(A\Gamma\frac{d\phi}{dx}\right)_w \tag{B.4}$$

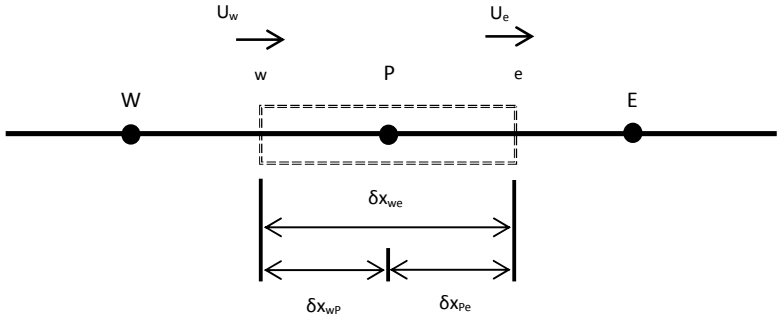

FIGURE B.1: Example of the control volume used in the discretisation process. The grid points are shown for the storage of the scalar quantity, ϕ.

The gradient, $d\phi/dx$, in the diffusion term is calculated using central differencing, e.g., through the east face, e, of the control volume in Fig. B.1:

$$\frac{d\phi_e}{dx} = \frac{\phi_E - \phi_P}{\delta x_{PE}} \tag{B.5}$$

The central differencing is applied and the convective mass flux per unit area and the diffusion conductance is defined at the cell faces as two separate variables, as $F = \rho u$ and $D = \frac{\Gamma}{\delta x}$, respectively. Therefore, Equation B.4 can be written as:

$$F_e A_e \phi_e - F_w A_w \phi_w = D_e A_e \left(\phi_E - \phi_P\right) - D_w A_e \left(\phi_P - \phi_W\right) \tag{B.6}$$

and this process will also be applied to the continuity as the flow must satisfy this condition:

$$\left(\rho u A\right)_e - \left(\rho u A\right)_w = 0. \tag{B.7}$$

Since the area of the west and east faces are assumed the same, i.e., $A_w = A_e = A$, the algebraic equations simplify down to:

$$F_e \phi_e - F_w \phi_w = D_e \left(\phi_E - \phi_P\right) - D_w \left(\phi_P - \phi_W\right) \tag{B.8}$$

and

$$\left(\rho u\right)_e - \left(\rho u\right)_w = 0. \tag{B.9}$$

Applying a linear interpolation to the convective terms can determine the cell face values of ϕ on the west and east faces of the control volume:

$$\phi_e = \frac{\phi_P + \phi_E}{2} \tag{B.10}$$

and

$$\phi_w = \frac{\phi_W + \phi_P}{2} \tag{B.11}$$

Therefore, Equation B.8 can now be re-written as:

$$\frac{F_e}{2}(\phi_P + \phi_E) - \frac{F_w}{2}(\phi_W + \phi_P) = D_e(\phi_E - \phi_P) - D_w(\phi_P - \phi_W) \tag{B.12}$$

These terms in Equation B.12 can be re-arranged to give the following algebraic equation:

$$a_P\phi_P = a_E\phi_E + a_W\phi_W \tag{B.13}$$

where the coefficients are represented by:

$$A_E = D_e - \frac{F_e}{2}, \quad A_W = D_w + \frac{F_w}{2}, \quad A_P = A_E + A_W + (F_e - F_w).$$

Unfortunately, applying a linear interpolation for the convective term in a strongly convective flow would not identify the flow direction because the value of ϕ is influenced by the the values on either side of it. An example would be a strong flow from west to east where central differencing would mean ϕ_w is dependent on both ϕ_W and ϕ_P however there would be a stronger influence from ϕ_W compared to that at ϕ_P.

The upwind scheme is a profile that takes the transportiveness of the problem into account. Where the linear interpolation was applied in Equation B.10 and Equation B.11, the upwind scheme sets the values of the cell faces, ϕ_e and ϕ_w, according to whether the flow is in the positive direction of $u_e > 0$ and $u_w > 0$; or a negative direction of $u_e < 0$ and $u_w < 0$. In a positive direction the values at the cell faces are given as:

$$\phi_e = \phi_P \quad \text{and} \quad \phi_w = \phi_W \tag{B.14}$$

and for a flow in the negative direction:

$$\phi_e = \phi_E \quad \text{and} \quad \phi_w = \phi_P \tag{B.15}$$

Therefore in the positive direction the discretised equation (Equation B.12) now becomes:

$$F_e\phi_P - F_w\phi_W = D_e(\phi_E - \phi_P) - D_w(\phi_P - \phi_W) \tag{B.16}$$

and in the negative direction it becomes:

$$F_e\phi_E - F_w\phi_P = D_e(\phi_E - \phi_P) - D_w(\phi_P - \phi_W) \tag{B.17}$$

As carried out previously for the linear interpolation, these discretised equations can be manipulated into the algebraic form in Equation B.13. The coefficients of the central coefficient in the algebraic equation, A_P, is the same as that given in Equation B however the neighbouring coefficients differ depending on the direction of the flow:

$$\begin{aligned} \text{Positive}: \quad & A_E = D_e \qquad & A_W = D_w + F_w \\ \text{Negative}: \quad & A_E = D_e - F_e \quad & A_W = D_w \end{aligned}$$

Which can be written simply as:

$$A_E = D_e + \max(0, -F_e) \quad A_W = D_w + \max(F_w, 0)$$

There are a number of other schemes which can be used examples include the hybrid scheme, [153] which is a combination of central and upwind differencing schemes; and the quadratic upwind differencing scheme (QUICK) [154] which is higher order scheme which minimises numerical errors through the incorporation of additional neighbouring points. For further information on the different schemes available, the reader is advised to refer to discussions in the literature [155].

Bibliography

[1] World Coal Institute: http://www.worldcoal.org/.

[2] A. Samuelsberg and B.H. Hjertager. An experimental and numerical study of flow patterns in a circulating fluidized bed reactor. *Int. J. Multiphase Flow*, 22: 575–591, 1995.

[3] A. Schmidt and U. Renz. Eulerian computation of heat transfer in fluidized beds. *Chem. Eng. Sci*, 54:5515–5522, 1999.

[4] F. Di Natale, P. Bareschino, and R. Nigro. Heat transfer and void fraction profiles around a horizontal cylinder immersed in a bubbling fluidised bed. *Int J Heat Mass Transfer*, 53:3525–3532, 2010.

[5] A. Ocampo, E. Arenas, F. Chejne, J. Espinel, C. Londono, J. Aguirre, and J.D. Perez. An experimental study on gasification of Colombian coal in fluidised bed. *Fuel*, 82:161–164, 2003.

[6] Intergovernment panel on climate change (IPCC) 2007: http://www.ipcc.ch/.

[7] BP reports: http://www.bp.com/.

[8] H.H. Lowry. *Chemistry of Coal Utilization*. John Wiley, New York, 1945.

[9] A. Williams, M. Pourkashanian, and J.M. Jones. The combustion of coal and some other solid fuels. *Proceedings of the Combustion Institute*, 28:2141–2162, 2000.

[10] L-M. Armstrong, K.H. Luo, and S. Gu. Three-dimensional modelling on the hydrodynamics of a circulating fluidised bed. In *Proceedings of the Inaugural US-EU-China Thermophysics Conference, Beijing, China*, 2009.

[11] L-M. Armstrong, K.H. Luo, and S. Gu. Two-dimensional and three-dimensional computational studies of hydrodynamics in the transition from bubbling to circulating fluidised bed. *Chem. Eng. J.*, 160:239–248, 2010.

[12] L-M. Armstrong, K.H. Luo, and S. Gu. Drag model study of the wall-to-bed heat transfer in a gas-solid bubbling fluidised bed using the kinetic theory of granular flow. *Int J Heat Mass Transfer*, 53:4949–4959, 2010.

[13] L-M. Armstrong, K.H. Luo, and S. Gu. The influence of multiple tubes on the tube-to-bed heat transfer in a fluidised bed. *Int. J. Multiphase Flow*, 36:916–929, 2010.

[14] L-M. Armstrong, K.H. Luo, and S. Gu. CFD modelling of the gasification of coal particles in fluidised beds. In *Proceedings of the International Heat Transfer Conference, Washington, DC, USA*, 2010.

[15] L-M. Armstrong, K.H. Luo, and S. Gu. CFD modelling of the co-gasification of biomass and coal particles in fluidised beds. In *BioTen Conference, Birmingham, UK*, 2010.

[16] L-M. Armstrong, K.H. Luo, and S. Gu. Effects of limestone calcination on the gasification processes in a BFB coal gasifier. *In press: Chem. Eng. J.*, 2011. doi: 10.1016/j.cej.2011.01.102.

[17] L-M. Armstrong, K.H. Luo, and S. Gu. A parametric study of the gasification processes in a BFB coal gasifier. *Under review: Ind. Eng. Chem. Res.*, 2011.

[18] D. Gidaspow. *Multiphase flow and fluidization, continuum and kinetic theory descriptions.* Academic Press, Inc., 1994.

[19] Y.C. Wen and Y.H. Yu. Mechanics of fluidization. *Chem. Eng. Prog. Symp. Ser.*, 62:100, 1966.

[20] D. Kunii and O. Levenspiel. *Fluidization Engineering.* Elsevier, 1991.

[21] D. Geldart. Types of gas fluidization. *Powder Technol.*, 7:285–292, 1973.

[22] D. Gidaspow, M. Syamlal, and Y. Seo. Hydrodynamics of fluidization of single and binary size particles: Supercomputer modelling. In *Proceedings of the fifth Engineering Foundation Conference on Fluidization. New York: AIChE Engineering Foundation.*, volume 5, pages 1–8, 1986.

[23] D. Liu, M. Kwauk, and H. Li. Aggregative and particulate fluidization-the two extremes of a continuous spectrum. *Chem. Eng. Sci.*, 51:4045, 1996.

[24] D. Gera, M. Gautam, Y. Tsuji, T. Kawaguchi, and T. Tanaka. Computer simulation of bubbles in large-particle fluidized beds. *Powder Technol.*, 98:38–47, 1998.

[25] D. Gera, M. Syamlal, and T.J. O'Brien. Hydrodynamics of particle segregation in fluidized beds. *Int. J. Multiphase Flow*, 30:419–428, 2004.

[26] C.H. Ibsen, E. Helland, B.H. Hjertager, T. Solberg, L. Tadrist, and R. Occelli. Comparison of multifluid and discrete particle modelling in numerical predictions of gas particle flow in circulating fluidised beds. *Powder Technol.*, 149:29–41, 2004.

[27] M.A van der Hoef, M. van Sint Annaland, N.G. Deen, and J.A.M. Kuipers. Numerical simulation of dense gas-solid fluidized beds: A multiscale modeling strategy. *Annu. Rev. Fluid Mech.*, 40:47–70, 2008.

[28] K. Papadikis, A.V. Bridgwater, and S. Gu. CFD modelling of the fast pyrolysis of biomass in fluidised bed reactors, part a: Eulerian computation of momentum transport in bubbling fluidised beds. *Chem. Eng. Sci.*, 63 (16):4218–4227, 2008.

[29] K. Papadikis, S. Gu, and A.V. Bridgwater. CFD modelling of the fast pyrolysis of biomass in fluidised bed reactors. part b: Heat, momentum and mass transport in bubbling fluidised beds. *Chem. Eng. Sci.*, 64:1036–1045, 2009.

[30] K. Papadikis, H. Gerhauser, A.V. Bridgwater, and S. Gu. CFD modelling of the fast pyrolysis of an in-flight cellulosic particle subjected to convective heat transfer. *Biomass and Bioenergy*, 33(1):97–107, 2009.

[31] K. Papadikis, S. Gu, and A.V. Bridgwater. CFD modelling of the fast pyrolysis of biomass in fluidised bed reactors: Modelling the impact of biomass shrinkage. *Chem. Eng. J*, 149:417–427, 2009.

[32] K. Papadikis, S. Gu, A.V. Bridgwater, and H. Gerhauser. Application of CFD to model fast pyrolysis of biomass. *Fuel Processing Technology*, 90:504–512, 2009.

[33] K. Papadikis, S. Gu, and A.V. Bridgwater. Computational modelling of the impact of particle size to the heat transfer coefficient between biomass particles and a fluidised bed. *Fuel Processing Technology*, 91(1):68–79, 2010.

[34] K. Papadikis, A.V. Bridgwater, and S. Gu. A CFD approach on the effect of particle size on char entrainment in bubbling fluidised bed reactors. *Biomass and Bioenergy*, 34(1):21–29, 2010.

[35] K. Papadikis, S. Gu, A. Fivga, and A.V. Bridgwater. Numerical comparison of the drag models of granular flows applied to the fast pyrolysis of biomass. *Energy and Fuels*, 24 (3):2133–2145, 2010.

[36] K. Papadikis, S. Gu, and A.V. Bridgwater. 3D simulation of the effects of sphericity on char entrainment in fluidised beds. *Fuel Processing Technology*, 2010. doi: doi:10.1016/j.fuproc.2010.02.008.

[37] S. Chapman and T.G. Cowling. *The Mathematical Theory of Non-Uniform Gases.* 3rd Edition, Cambridge, UK.: Cambridge University Press, 1970.

[38] R.A. Bagnold. Experiments on a gravity-free dispersion of large solid spheres in a newtonian fluid under shear. *Proc. Roy. Soc.*, A225:49, 1954.

[39] S. Ogawa, A. Umemura, and N. Oshima. On the equations of fully fluidized granular materials. *Z. Angew. Math. Phys.*, 31:483–493, 1980.

[40] J.T. Jenkins and S.B. Savage. A theory for the rapid flow of identical, smooth, nearly elastic, spherical particles. *J. Fluid Mech.*, 130:187–202, 1983.

[41] S.B. Savage and D.J. Jeffrey. The stress tensor in a granular flow at high shear rates. *J. Fluid Mech.*, 110:255–272, 1981.

[42] S.B. Savage. *Granular Flows at High Shear Rates.* in R. E. Meyer, Ed. Theory of Dispersed Multiphase Flow. New York: Academic Press, 1983.

[43] M.J.V. Goldschmidt, J.A.M. Kuipers, and W.P.M. van Swaaij. Hydrodynamic modelling of dense gas-fluidized beds using the kinetic theory of granular flow: effect of restitution coefficient on bed dynamics. *Chem. Eng. Sci.*, 56:571, 2001.

[44] F. Taghipour, N. Ellis, and C. Wong. Experimental and computational study of gas-solid fluidized bed hydrodynamics. *Chem. Eng. Sci.*, 60:6857–6867, 2005.

[45] H. Kim and H. Arastoopour. Extension of the kinetic theory to cohesive particle flow. *Powder Technol.*, 122:83, 2002.

[46] J. Sun and F. Battaglia. Hydrodynamic modeling of particle rotation for segregation in bubbling gas-fluidized beds. *Chem. Eng. Sci.*, 61:1470–1479, 2006.

[47] J.L. Sinclair and R. Jackson. Gas-particle flow in a vertical pipe with particle-particle interactions. *AIChE J.*, 35:1473, 1989.

[48] A. Samuelsberg and B.H. Hjertager. Computational modeling of gas/particle flow in a riser. *AIChE J.*, 42:1536–1546, 1996.

[49] B. Sun and D. Gidaspow. Computation of circulating fluidized-bed riser flow for the fluidization viii benchmark test. *Ind. Eng. Chem. Res.*, 38:787–792, 1999.

[50] S. Benyahia, H. Arastoopour, T.M. Knowlton, and H. Massah. Simulation of particles and gas flow behaviour in the riser section of a circulating fluidized bed using the kinetic theory approach for the particulate phase. *Powder Technol.*, 112: 24–33, 2000.

[51] A. Almuttahar and F. Taghipour. Computational fluid dynamics of high density circulating fluidized bed riser: Study of modeling parameters. *Powder Technol.*, 185:11–23, 2008.

[52] A. Neri and D. Gidaspow. Riser hydrodynamics: simulation using kinetic theory. *AIChE*, 42:1801–1815, 2000.

[53] Y. Zheng, X. Wan, Z. Qian, and Y. Wei, F.and Jin. Numerical simulation of the gas-particle turbulent flow in risers reactor based on $k-\epsilon-kp-\epsilon p-\theta$ two-fluid model. *Chem. Eng. Sci.*, 56:6813–6822, 2001.

[54] M.S. Detamore, M.A. Swanson, K.R. Frender, and C.M. Hrenya. A kinetic-theory analysis of the scale-up of circulating fluidized beds. *Powder Technol.*, 116:190–203, 2001.

[55] C. Chan, Y. Guo, and K. Lau. Numerical modelling of gas-particle flow using a comprehensive kinetic theory with turbulent modulation. *Powder Technol.*, 150: 42–55, 2005.

[56] S. Benyahia, M. Syamlal, and T.J. O'Brien. Evaluation of boundary conditions used to model dilute, turbulent gas/solid flows in a pipe. *Powder Technol.*, 156: 62–72, 2005.

[57] V. Jiradilok, D. Gidaspow, and R.W. Breault. Computation of gas and solid dispersion coefficients in turbulent risers and bubbling beds. *Chem. Eng. Sci.*, 62: 3397–3409, 2007.

[58] G. Balzer, A. Boelle, and O. Simonin. Eulerian gas-solid flow modelling of dense fluidized beds. *Fluidization, Engineering Foundation*, 8:409, 1996.

[59] A. Boemer, H. Qi, and U. Renz. Eulerian simulation of bubble formation at a jet in a two-dimensional fluidized bed. *Int. J. Multiphase Flow*, 23:927–944, 1997.

[60] H. Enwald and A.E. Almstedt. Fluid dynamics of a pressurized fluidized bed: comparison between numerical solutions from two-fluid models and experimental results. *Chem. Eng. Sci.*, 54:329–342, 1999.

[61] S.J. Gelderbloom, D. Gidaspow, and R.w. Lyczkowski. CFD simulations of bubbling/collapsing fluidized beds for three geldart groups. *AIChE J.*, 49:844–858, 2003.

[62] J. Jung and D. Gidaspow. Measurement of two kinds of granualr temperatures, stresses and dispersion in bubbling beds. *Ind. Eng. Chem. Res.*, 44:1329–1341, 2005.

[63] L. Yu, J. Lu, X. Zhang, and S. Zhang. Numerical simulation of the bubbling fluidized bed coal gasification by the kinetic theory of granular flow (KTGF). *Fuel*, 86:722–734, 2007.

[64] S. Ergun. Fluid flow through packed columns. *Chem. Eng. Prog.*, 48(2):89–94, 1952.

[65] D. Gidaspow, R. Bezburuah, and J Ding. Hydrodynamics of circulating fluidized beds: Kinetic theory approach. In *Proceedings of the 7th Fluidization Conference*, 1992.

[66] J.F. Richardson and Zaki W.N. Sedimentation and fluidization: part i. *Trans Chem Eng.*, 32:35–53, 1954.

[67] L.G. Gibilaro, R. Di Felice, and S.P. Waldram. Generalized friction factor and drag coefficient correlations for fluid-particle interactions. *Chem. Eng. Sci.*, 40: 1817–1823, 1985.

[68] M. Syamlal and T.J. O'Brien. Derivation of a drag coefficient from velocity-voidage correlation. In *U.S. Dept. of Energy, Office of Fossil Energy, National Energy Technology Laboratory, Morgantown, West Virginia April*, 1987.

[69] H. Arastoopour, P Pakdel, and M. Adewumi. Hydrodynamic analysis of dilute gas-solids flow in a vertical pipe. *Powder Technol.*, 62(2):163–170, 1990.

[70] R. Di Felice. The voidage functions for fluid-particle interaction systems. *Int. J. Multiphase Flow.*, 20(1):153–159, 1994.

[71] Y.H. Zhang and J.M. Reese. The drag force in two-fluid models of gas-solid flows. *Chem. Eng. Sci.*, 58:1641–1644, 2003.

[72] E. Cruz, F.R. Steward, and T. Pugsley. New closure models for CFD modeling of high-density circulating fluidized beds. *Powder Technol.*, 169:115–122, 2006.

[73] S. Benyahia, M. Syamlal, and T.J. O'Brien. Extension of Hill-Koch-Ladd drag correlation over all ranges of reynolds number and solids volume fraction. *Powder Technol.*, 162:166–174, 2006.

[74] R.J. Hill, D.L. Koch, and A.J.C. Ladd. The first effects of fluid inertia on flows in ordered and random arrays of spheres. *J. Fluid Mech.*, 448:213–241, 2001.

[75] R.J. Hill, D.L. Koch, and A.J.C. Ladd. Moderate-Reynolds-number flows in ordered and random arrays of spheres. *J. Fluid Mech.*, 448:243–278, 2001.

[76] D.J. Gunn and A.A. Malik. The structure of fluidized beds in particulate fluidization. In *Proceedings of the International Symposiumon Fluidization; Dringkenbrug, A.A., Ed.; Netherlands University Press: Eindhoven, The Netherlands.*, pages 52–65, 1967.

[77] T.J. O'Brien and M. Syamlal. Particle cluster effects in the numerical simulation of a circulating fluidized bed. *In Preprint Volume for CFB-IV; Avidan, A.A.; Ed.; AIChE: New York.*, pages 430–435, 1993.

[78] J.H. Li, A. Chen, Z. Yan, G. Xu, and X. Zhang. Particle-fluid contacting in circulating fluidized beds. *In Preprint Volume for CFB-IV; Avidan, A. A., Ed.; AIChE: New York*, pages 49–54, 1993.

[79] J.H. Li, C. Cheng, Z. Zhang, J. Yuan, A. Nemet, and F.N. Fett. The EMMS model-its application, development and updated concepts. *Chem. Eng. Sci.*, 54: 5409–5425, 1999.

[80] J.H. Li, L. Wen, W. Ge, H. Cui, and J. Ren. Dissipative structure in concurrent-up gas-solid flow. *Chem. Eng. Sci.*, 53:3367–3379, 1998.

[81] N. Yang, W. Wang, W. Ge, and L. Wang. Simulation of heterogeneous structure in a circulating fluidized-bed riser by combining the two-fluid model with the EMMS approach. *Ind. Eng. Chem. Res.*, 43:5548–5561, 2004.

[82] V. Jiradilok, D. Gidaspow, S. Damronglerd, W.J. Koves, and R. Mostofi. Kinetic theory based CFD simulation of turbulent fluidization of FCC particles in a riser. *Chem. Eng. Sci.*, 61:5544–5559, 2006.

[83] S. Sundaresan. Perspective: Modeling the hydrodynamics of multiphase flow reactors: current status and challenges. *AIChE J.*, 46:1102–1105, 2000.

[84] V. Mathiesen, T. Solberg, E. Manger, and B. Hjertager. Modelling and predictions of multiphase flow in a pilotscale circulating fluidised beds. In *Circulating Fluidized Bed Technology, vol 5. J. Kwauk and J.Li, eds. Science Press, Beijing, China*, 1997.

[85] V. Mathiesen, T. Solberg, and B. Hjertager. An experimental and computational study of multiphase flow behavior in a circulating fluidised bed. *Int J Multiphase Flow*, 22:575–591, 2000.

[86] C.H. Ibsen, T. Solberg, and B.H. Hjertager. The influence of the number of phases in eulerian multiphase simulations. In *14th International Congress of Chemical and Progress Engineering, Praha, Czech Republic*, 2000.

[87] V. Mathiesen, T. Solberg, and B.H. Hjertager. A numerical study of three-dimensional multiphase flow pattern in a riser. In *J. Werther (Ed). 6th International Conference on Circulating Fluidized Beds, Würzburg, Germany, August 24-27*, pages 249–254, 1999.

[88] D.Z. Zhang and W.B. VanderHeyden. High-resolution three dimensional numerical simulation of a circulating fluidized bed. *Powder Technol.*, 116:133–141, 2001.

[89] J.A.M. Kuipers and W.P.M. van Swaaij. Simulation of three dimensional (3d) riser flow using kinetic theory of granular flow. In *J. Werther (Ed). 6th International Conference on Circulating Fluidized Beds, Würzburg, Germany, August 24-27*, 1999.

[90] C.H. Ibsen, T. Solberg, and B.H. Hjertager. Evaluation of a three-dimensional numerical model of a scaled circulating fluidized bed. *Ind. Eng. Chem. Res.*, 40 (23):5081–5086, 2001.

[91] K.G. Hansen, T. Solberg, and B.H. Hjertager. A three-dimensional simulation of gas/particle flow and ozone decomposition in the riser of a circulating fluidized bed. *Chem. Eng. Sci.*, 59:5217–5224, 2004.

[92] J. S. M. Botterill and J. R. Williams. The mechanism of heat transfer to gas fluidized beds. *Trans. Instn. Chem. Engrs.*, 41:217, 1963.

[93] E. U. Schlünder. Wärmeübergang an bewegte kugelschüttungen bei kurzfristigem kontakt. *Chemie Ing. Tech.*, 43:651, 1971.

[94] H. S. Mickley and D. F. Fairbanks. Mechanism of heat transfer to fluidized beds. *AIChE J.*, 1(3):374, 1955.

[95] J.A.M. Kuipers, W. Prins, and W.P.M. van Swaaij. Numerical calculation of wall-to-bed heat transfer coefficients in gas-fluidized beds. *AIChE J.*, 38:1079–1091, 1992.

[96] P. Zehner and E.U. Schlünder. Wärmeleitfähigkeit von schüttungen bei mäβigen temperaturen. *Chem. Ing. Tech.*, 42:933–941, 1970.

[97] D.J. Patil, J. Smit, M. van Sint Annaland, and J.A.M. Kuipers. Wall-to-bed heat transfer in gas-solid bubbling fluidized beds. *AIChE J.*, 52:58–74, 2006.

[98] V.V.R. Natarajan and M.L. Hunt. Kinetic theory analysis of heat transfer in granular flows. *Int J Heat Mass Transfer*, 41:1929–1944, 1998.

[99] M.L. Hunt. Discrete element simulations for granular material flows: Effective thermal conductivity and self diffusivity. *Int J Heat Mass Transfer*, 40:3059–3068, 1997.

[100] V.N. Korolev, N.Y. Syromyatnikov, and E.M. Tolmachev. Structure of a fixed bed of granular material near an immersed surface (wall). *J. Eng. Phys.*, 21:1475–1478, 1971.

[101] H. Martin. Low péclet number particle-to-fluid heat and mass transfer in packed beds. *Chem. Eng. Sci.*, 33:913–919, 1978.

[102] D.J. Gunn. Transfer of heat or mass to particles in fixed and fluidised beds. *Int J Heat Mass Transfer*, 21:467–476, 1978.

[103] L. Smoot. Modeling of coal-combustion processes. *Prog. Energy Combust. Sci.*, 10:229–272, 1984.

[104] M.L. de Souza-Santos. Comprehensive modeling and simulation of fluidized bed boilers and gasifiers. *Fuel*, 68:1507–1521, 1989.

[105] L. Huilin, B. Rushan, Y. Lidan, Z Guangbo, and T. Xiu. Numerical computation of a circulating fluidized bed combustor. *Int. J. Energy Res.*, 22:1351–1364, 1998.

[106] H.M. Yan, C. Heidenreich, and D.K. Zhang. Modelling of bubbling fluidised bed coal gasifiers. *Fuel*, 78:1027–1047, 1999.

[107] L. Huilin, Z. Guangbo, B. Rushan, C. Yongjin, and D. Gidaspow. A coal combustion model for circulating fluidized bed boilers. *Fuel*, 79:165–172, 2000.

[108] F. Chejne and J.P. Hernandez. Modeling and simulation of coal gasification process in fluidized bed. *Fuel*, 81:1687–1702, 2002.

[109] A. Gungor and N Eskin. Two-dimensional coal combustion modeling of CFB. *Int. J. Thermal Sci.*, 47:157–174, 2008.

[110] M. Gräbner, S. Ogriseck, and B. Meyer. Numerical simulation of coal gasification at circulating fluidised bed conditions. *Fuel Proc. Tech.*, 88:948–958, 2007.

[111] H. Zhou, G. Flamant, and D. Gauthier. DEM-LES of coal combustion in a bubbling fluidized bed. Part I: gas-particle turbulent flow structure. *Chem. Eng. Sci.*, 59:4193–4203, 2004.

[112] M. Oevermann, S. Gerber, and F. Behrendt. Euler-Lagrange/DEM simulation of wood gasification in a bubbling fluidized bed reactor. *Particuology*, 4:307–316, 2009.

[113] X. Wang, B. Jin, and W. Zhong. Three-dimensional simulation of fluidized bed coal gasification. *Chem. Eng. Proc.*, 48:695–705, 2009.

[114] S. Gerber, F. Behrendt, and M. Oevermann. An Eulerian modeling approach of wood gasification in a bubbling fluidized bed reactor using char as bed material. *Fuel*, 89(10):2903–2917, 2010.

[115] Y. Wang, S Lin, and Y Suzuki. Study of limestone calcination with CO_2 capture: decomposition behavior in a CO_2 atmosphere. *Energy and Fuels*, 21:3317–3321, 2007.

[116] D.P. Ross, C.A. Heidenreich, and D.K. Zhang. Devolatilisation times of coal particles in a fluidised-bed. *Fuel*, 79:873–883, 2000.

[117] M. M. Baum and P. J. Street. Predicting the combustion behavior of coal particles. *Combust. Sci. Tech.*, 3(5):231–243, 1971.

[118] K. K. Pillai. The influence of coal type on devolatilization and combustion in fluidized beds. *J. Inst. Energy*, page 142, 1981.

[119] S. Badzioch and P. G. W. Hawksley. Kinetics of thermal decomposition of pulverized coal particles. *Ind. Eng. Chem. Process Design and Development*, 9:521–530, 1970.

[120] D. B. Stickler, R. E. Gannon, and H. Kobayashi. Rapid devolatilization modeling of coal. In *Eastern States Section, Fall Meeting of the Combustion Institute, Applied Physics Laboratory, Maryland, Nov 12-13,*, 1974.

[121] H. Kobayashi. *Devolatilization of Pulverized Coal at High Temperatures*. PhD thesis, Department of Mechanical Engineering, Massachusetts Institute of Technology, Cambridge, Mass., 1976.

[122] R. Loison and R. Chauvin. Pyrolise rapide du charbon. *Chimie et Industrie*, 91: 269, 1964.

[123] R.P. Ma, R.M. Felder, and J.K. Ferrell. Evolution of hydrogen sulfide in a fluidized bed coal gasification reactor. *Ind. Eng. Chem. Res.*, 28:27–33, 1989.

[124] A. Goyal and A. Rehmat. Modeling of a fluidised bed coal carbonizer. *Ind. Eng. Chem. Res.*, 32:1396–1410, 1993.

[125] J.M. Lee, Y.J. Kim, W.J. Lee, and S.D. Kim. Coal-gasification kinetics derived from pyrolysis in a fluidized bed reactor. *Energy*, 23:475–488, 1998.

[126] B.H. Song, Y.W. Jang, S.D. Kim, and S.K. Kang. Gas yields from coal devolatilization in a bench-scale fluidized bed reactor. *Korean J. Chem. Eng.*, 18:770–774, 2001.

[127] R.H. Hurt. Structure, properties and reactivity of solid fuels. In *27th Symposium (International) on combustion*, 1998.

[128] R.H. Hurt and J.M. Calo. Semi-global intrinsic for char combustion modeling. *Combustion and Flame*, 125:1138–2114, 2001.

[129] M.L. Hobbs, P.T. Radulovic, and L.D. Smoot. Modeling fixed-bed coal gasifiers. *AIChE J.*, 38:681–702, 1992.

[130] P.L. Walker, F. Rusinko, and L.G. Austin. *Advances in catalysts*. Academic Press, New York, 1959.

[131] C.Y. Wen and T.Z. Chaung. Entrainment coal gasification modeling. *Ind. Eng. Chem. Process Des. Dev.*, 18:684, 1979.

[132] J. Ding and D. Gidaspow. A bubbling fluidization model using kinetic theory of granular flow. *AlChE J.*, 36:523–538, 1990.

[133] C.K.K. Lun, S.B. Savage, D.J. Jeffrey, and N. Chepurniy. Kinetic theories for granular flow: Inelastic particles in Couette flow and slightly inelastic particles in a general flow field. *J. Fluid Mech.*, 140:223–256, 1984.

[134] D.G. Schaeffer. Instability in the evolution equations describing incompressible granular flow. *J. Diff. Equ.*, 66:19–50, 1987.

[135] M. Syamlal. The particle-particle drag term in a multiparticle model of fluidization. In *National Technical Information Service, Springfield, VA.*, 1987. doi: DOE/MC/21353-2373,NTIS/DE87006500.

[136] B. E. Launder and D. B. Spalding. *Lectures in mathematical models of turbulence.* Academic Press, Inc., 1972.

[137] H. Kobayashi, J. B. Howard, and A. F. Sarofim. Coal devolatilization at high temperatures. *Symposium (International) on Combustion*, 16:411–425, 1977.

[138] I.B. Ross and J.F. Davidson. The combustion of carbon particles in a fluidized bed. *Chem. Eng. Res. Des.*, 60a:108–114, 1982.

[139] B. Magnussen and B. H. Hjertager. On mathematical models of turbulent combustion with special emphasis on soot formation and combustion. In *16th Symp. (Int'l.) on Combustion*, 1976.

[140] R. H. Borgwardt. Kinetics of the reaction of SO_2 with calcined limestone. *Environ. Sci. Technol.*, 4:59–63, 1970.

[141] R. H. Borgwardt and R. D. Harvey. Properties of carbonate rock related to SO_2 reactivity. *Environ. Sci. Technol.*, 6:350–360, 1972.

[142] F. Thurner and U. Mann. Kinetic investigation of wood pyrolysis. *Ind. Eng. Chem. Process Des. Dev.*, 20:482–488, 1981.

[143] M.G. Grϕnli and M.C. Melaan. Mathematical model for wood pyrolysis-comparison of experimental measurements with model predictions. *Energy Fuels*, 14:791–800, 2000.

[144] J. Larfeldt, B. Leckner, and M.C. Melaaen. Modelling and measurements of the pyrolysis of large wood particles. *Fuel*, 79:1637–43, 2000.

[145] V. Seebauer. *Experimentelle Untersuchungen zur Pyrolyse von Kohle und Holz.* PhD thesis, Graz University of Technology, 1999.

[146] P. Johnson and R. Jackson. Frictional-collisional constitutive relations for granular materials, with application to plane shearing. *J. Fluid Mech.*, 176:67–93, 1987.

[147] J.R. Grace and J. Tuot. A theory for cluster formation in vertically conveyed suspensions of intermediate density. *Trans. Inst. Chem. Engrs.*, 57:49–54, 1979.

[148] K. Agrawal, P.N. Loezos, M. Syamlal, and S. Sundaresan. The role of meso-scale structures in rapid gas-solid flows. *J. Fluid Mech.*, 445:151–185, 2001.

[149] S.S. Zabrodsky. Analysis of experimental data on heat transfer in fluidized beds (in russian). *Inzh.-Fiz. Zhurn.*, 1(4):22–30, 1958.

[150] I. Petersen and J. Werther. Experimental investigation and modeling of gasification of sewage sludge in the circulating fluidized bed. *Chem. Eng. Proc.*, 44(7):717–736, 2005.

[151] H. Enwald, E. Peirano, A.E. Almstedt, and B. Leckner. Simulation of the fluid dynamics of a bubbling fluidized bed experimental validation of the two-fluid model and evaluation of a parallel multiblock solver. *Chem. Eng. Sci.*, 54:311–328, 1999.

[152] J. Garside and M.R. Al-Dibouni. Velocity-voidage relationship for fluidization and sedimentation. *Ind. Eng. Chem. Proc. Des. Dev.*, 16(2):206–214, 1977.

[153] D.B. Spalding. A novel finite-differencing formulation for differential expressions involving both first and second derivatives. *Int. J. Numer. Methods Eng.*, 4:551, 1972.

[154] B.P. Leonard. A stable and accurate convective modelling procedure based on quadratic upstream interpolation. *Comput. Methods Appl. Mech. Eng.*, 19:59–98, 1979.

[155] H.K. Versteeg. *An introduction to computational fluid dynamics*. Pearson Education Limited, 2007.